

**PREDICTION OF REFLECTION CRACKING IN
HOT MIX ASPHALT OVERLAYS**

A Dissertation

by

FANG-LING TSAI

Submitted to the Office of Graduate Studies of
Texas A&M University
in partial fulfillment of the requirements for the degree of

DOCTOR OF PHILOSOPHY

December 2010

Major Subject: Civil Engineering

**PREDICTION OF REFLECTION CRACKING IN
HOT MIX ASPHALT OVERLAYS**

A Dissertation

by

FANG-LING TSAI

Submitted to the Office of Graduate Studies of
Texas A&M University
in partial fulfillment of the requirements for the degree of

DOCTOR OF PHILOSOPHY

Approved by:

Chair of Committee,	Robert Lytton
Committee Members,	Amy Epps Martin
	Anastasia Muliana
	Zachary Grasley
Interim Department Head,	John Niedzwecki

December 2010

Major Subject: Civil Engineering

ABSTRACT

Prediction of Reflection Cracking in Hot Mix Asphalt Overlays. (December 2010)

Fang-Ling Tsai, B.S., China University of Science and Technology;

M.S., I-Shou University

Chair of Advisory Committee: Dr. Robert Lytton

Reflection cracking is one of the main distresses in hot-mix asphalt (HMA) overlays. It has been a serious concern since early in the 20th century. Since then, several models have been developed to predict the extent and severity of reflection cracking in HMA overlays. However, only limited research has been performed to evaluate and calibrate these models. In this dissertation, mechanistic-based models are calibrated to field data of over 400 overlay test sections to produce a design process for predicting reflection cracks. Three cracking mechanisms: bending, shearing traffic stresses, and thermal stress are taken into account to evaluate the rate of growth of the three increasing levels of distress severity: low, medium, and high. The cumulative damage done by all three cracking mechanisms is used to predict the number of days for the reflection crack to reach the surface of the overlay. The result of this calculation is calibrated to the observed field data (severity and extent) which has been fitted with an S-shaped curve.

In the mechanistic computations, material properties and fracture-related stress intensity factors are generated using efficient Artificial Neural Network (ANN) algorithms. In the bending and shearing traffic stress models, the traffic was represented by axle load spectra. In the thermal stress model, a recently developed temperature model was used to predict the temperature at the crack tips. This process was developed to analyze various overlay structures. HMA overlays over either asphalt pavement or jointed concrete pavement in all four major climatic zones are discussed in this dissertation. The results of this calculated mechanistic approach showed its ability to efficiently reproduce field observations of the growth, extent, and severity of reflection cracking. The most important contribution to crack growth was found to be thermal stress. The computer running time for a twenty-year prediction of a typical overlay was between one and four minutes.

DEDICATION

To my parents,
Zong-Biao Tsai and Jin-Lan Ciou,
My sister and brother,
Yan-Ling and Yu-Ping,
and my friends
who made all this possible
for their support and love.

ACKNOWLEDGEMENTS

I would like to thank my committee chair, Dr. Robert Lytton, for his continuous support, guidance, patience, and encouragement. I am also grateful to my committee members, Dr. Amy Epps Martin, Dr. Zachary Grasley, and Dr. Anastasia Muliana, for their guidance and support throughout the course of this research.

I appreciate the financial support provided by the National Cooperative Highway Research Program (NCHRP), and by the Benson Chair Foundation from Dr. Robert Lytton, that made this work possible. In addition, this research was materially aided by the assistance of Dr. Amir Hanna, Mr. Jagannath Mallela, Dr. Arif Chowdhury, Dr. Halil Ceylan, Dr. Charles J. Glover, Dr. Reynaldo Roque, Dr. Sheng Hu, Dr. Fujie Zhou, Dr. SangIck Lee, Dr. Rong Luo, Rongbin Han, and Xin Jin.

I would also like to acknowledge the Zachry Department of Civil Engineering at Texas A&M University and the Texas Transportation Institute (TTI), where this research was conducted, and Mrs. Cathy Bryan, Dr. Jeongho Oh, Dr. Eyad Masad, Mr. Troy Brown, and Dr. Wenting Liu, for their advice and assistance, and the Transportation Research Board (TRB) that the material (Journal of the Transportation Research Board, No. 2155, pp. 43-54) is reproduced from. This work would not have been possible without the support of my friends and colleagues. I am thankful to Jonathan Howson, with whom I worked closely and who made my stay in College Station more enjoyable.

Finally, thanks to my family for their patience, support, and love. Also thanks to my friends, whether in the U.S. or back in Taiwan, for their encouragement and support.

TABLE OF CONTENTS

CHAPTER	Page
I	INTRODUCTION 1
1.1	Background 1
1.2	Approach Outline 2
II	LITERATURE REVIEW 8
2.1	Introduction 8
2.2	Available Reflection Cracking Models 8
2.3	Reflection Cracking Models Comparison 42
III	MODEL CHARACTERISTICS AND DEVELOPMENT 46
3.1	Introduction 46
3.2	Definition of Three Mechanisms 48
3.3	Pavement Structure Data Collection 51
3.4	Categorization of Traffic Loads 55
3.4.1	Classification of Vehicles 56
3.4.2	Axle Load Distribution Factor 56
3.4.3	Estimation of Annual Number of Axle Loads for Each Category with AADTT 63
3.4.4	Normalized Vehicle Class Distribution 64
3.4.5	Number of Axle Types per Vehicle 65
3.5	Tire Patch Length and Cumulative Axle Load Distribution 70
3.5.1	Tire Patch Length 70
3.5.2	Determination of Cumulative Axle Load Distribution on Tire Length 71
3.5.3	Modeling of Cumulative Axle Load Distribution (CALD) 76
3.6	Determination of Hourly Number of Traffic Load 89
3.6.1	Probability Density on Tire Patch Length 89
3.6.2	Calculating Hourly Number of Traffic Load 91
3.7	Climatic Data Collection 103
3.7.1	Hourly Climatic Input Data Collection 105
3.7.2	Obtaining Site-Specific Model Parameters 110

CHAPTER	Page
3.8	Reflection Cracking Amount and Severity Model..... 112
3.8.1	System Identification Process 113
3.8.2	Parameter Adjustment and Adaption Algorithm 115
3.8.3	Calibrated Observed Reflection Cracking Length 117
3.9	Viscoelastic Thermal Stress Computation 123
3.9.1	Collocation Matrix 125
3.9.2	Shift Factors..... 126
3.10	Stress Intensity Factor Computation by Finite Element Method 128
3.10.1	Background of the Fracture Mechanics Approach and Associated SIF Computation Tools..... 129
3.10.2	SA-CRACKPRO: A New Crack Propagation Analysis Tool 131
3.10.3	Isoparametric Quadratic "Quarter-Point" Element..... 132
3.10.4	Thin-Layer Elements for Simulating Pavement Layer Contact Condition and Load Transfer Efficiency at Joints/Cracks 135
3.10.5	Automatic Meshing and Re-meshing Technique for Crack Propagation..... 135
3.11	Temperature Prediction Model in Hot Mix Asphalt Overlay 136
3.11.1	Heat Transfer in Pavement..... 139
3.11.2	The Surface Boundary Condition 140
3.11.3	The Bottom Boundary Condition 143
3.11.4	Optimization and Interpolation of Model Parameters 144
3.12	Mixture Properties Determination 153
3.12.1	Complex Modulus by Artificial Neural Network..... 154
3.12.2	Calculation of G_g for Level 2 Input..... 164
3.12.3	Paris' Law - Fracture Properties A and n 168
3.12.4	Healing Coefficients 174
3.12.5	Stress Wave Pattern Correction 174
3.13	Stress Intensity Factor Models by Artificial Neural Network 185
3.13.1	Thermal Reflection Cracking Cases 191
3.13.2	Shearing Reflection Cracking Cases 202
3.13.3	Bending Reflection Cracking Cases 213
IV	FIELD OBSERVED DISTRESS CALIBRATION AND CALIBRATION COEFFICIENTS DETERMINATION 223
4.1	Introduction 223
4.2	Calibration of Calculated Overlay Life to the Observed Distress 225
4.3	Calibrated Model and Calibrated Coefficients Determination 233

CHAPTER	Page
V REFLECTION CRACKING PREDICTION AND SENSITIVITY ANALYSIS	248
5.1 Introduction	248
5.2 Predictions of Overlay Reflection Cracking	249
5.3 Comparison of Predicted Overlay Life and Observed Data	259
5.4 Sensitivity Analysis Scale Parameter, ρ	272
VI CONCLUSION AND FUTURE WORK	289
6.1 Summary and Conclusion	289
6.1.1 The Model Development Process	291
6.1.2 Mechanistic Prediction of Crack Growth	292
6.1.3 Hot Mix Asphalt Overlay Material Properties	292
6.1.4 Climatic Data and Temperature Prediction	293
6.1.5 Consistent Description of Reflection Cracking Distress	294
6.1.6 Calibration of Calculated Overlay Life to the Observed Distress	295
6.1.7 Sensitivity Analysis of Scale Parameter, ρ	295
6.2 Future Work	296
REFERENCES	299
VITA	308

LIST OF FIGURES

FIGURE	Page
1.1 Mechanisms of reflection cracking. (a) Mechanisms of reflection cracking, (b) Traffic mechanisms	3
1.2 Definitions of the numbers of days and two-phase crack growth	4
1.3 Computation processes for reflection cracking. (a) Crack growth computation due to thermal stress, (b) Crack growth computations due to bending stress, (c) Crack growth computations due to shearing stress	5
2.1 Different failure modes considered for the reflection cracking model	14
2.2 Overall reflection cracking analysis procedure	15
2.3 Three modes of crack opening displacement: (a) Mode I–Opening Mode, (b) Mode II–Shearing Mode, (c) Mode III–Tearing Mode	20
2.4 Predicted vs. observed reflection cracking (Days)	24
2.5 Predicted vs. measured reflection cracking at LTPP GPS-7 sections	27
2.6 Random microstructure, scatter of microstresses, and crack band or sharp crack model	32
2.7 Effective width of existing crack	33
2.8 Finite element model	34
2.9 Comparative effect of various treatments	34
2.10 Cohesive cracking model analogy	35
2.11 Damage field and crack pattern after 396,000 load applications	40
2.12 Flow chart of the proposed overlay design procedure against reflective cracking	42
3.1 Mechanisms of reflection cracking	50

FIGURE	Page
3.2 Bending and shear mechanisms	50
3.3 Sketch of an asphalt overlay system	51
3.4 Annual normalized single axle load distribution for vehicle class 4 to 7 (LTPP section in Tippecanoe, Maryland 2004)	59
3.5 Vehicle class related to axle and tire categories	62
3.6 Tire load applied to pavement surface	70
3.7 Procedure for determination of cumulative axle load distribution on tire patch length	73
3.8 Cumulative annual axle load distribution on tire length (category 1 of LTPP section Tippecanoe, Maryland in 2004)	76
3.9 Typical cumulative axle load distribution curve	77
3.10 Gompertz model curve	78
3.11 Cumulative axle load distribution for LTPP section Tippecanoe, Maryland (2004). (a) Category 1 (Single axle/single tire), (b) Category 2 (Single axle /dual tires), (c) Category 3 (Tandem axle/single tire), (d) Category 4 (Tandem axle/dual tires), (e) Category 5 (Tridem axle/single tire), (f) Category 6 (Tridem axle/dual tires), (g) Category 7 (Quad axle /single tire), (h) Category 8 (Quad axle/dual tires)	81
3.12 Probability density function of tire length (category 1, LTPP section in Tippecanoe, Maryland)	90
3.13 Probability density functions for LTPP section in Tippecanoe, Maryland (2004). (a) Category 1 (Single axle/single tire), (b) Category 2 (Single axle /dual tires), (c) Category 3 (Tandem axle/single tire), (d) Category 4 (Tandem axle/dual tires), (e) Category 5 (Tridem axle/single tire), (f) Category 6 (Tridem axle/dual tires), (g) Category 7 (Quad axle /single tire), (h) Category 8 (Quad axle/dual tires)	99
3.14 Typical daily pavement temperature prediction using improved model	104
3.15 Seasonal trend decomposition of hourly air temperature. (a) For a whole year, (b) Magnified view of 5 days period	108

FIGURE	Page
3.16 Daily air temperature patterns at 6 different pavement sites	109
3.17 Distribution map of 29 SMP pavement sites studied	112
3.18 Methods for system identification process	114
3.19 Scheme of system identification process	115
3.20 Calibrated model on measured reflective crack for LTPP section 340503	121
3.21 Calibrated model on measured reflective crack for LTPP section 270506	122
3.22 Calibrated model on measured reflective crack for LTPP section 240563	122
3.23 Calibrated model on measured reflective crack for LTPP section 55B901	123
3.24 Generalized Maxwell model for relaxation	125
3.25 m_{mix} at different temperatures	128
3.26 (a) Quadrilateral (b) Collapsed quadrilateral quarter-point element	133
3.27 Finite elements meshing around crack tip	134
3.28 Typical daily pavement temperature prediction using EICM model	138
3.29 Typical daily pavement temperature prediction using improved model	139
3.30 Schematic representation of heat transfer model of pavement	141
3.31 Optimized albedo values in: (a) Summer and (b) Winter, (c) Winter optimized albedo values on an annual average snowfall map	147
3.32 Optimized values of the algebraic difference between emissivity and absorption coefficients: (a) Summer (b) Winter	150
3.33 Optimized values of absorption coefficients	152
3.34 Comparison of Witczak 1999 model with artificial neural network algorithm	163

FIGURE	Page
3.35 Comparison of Witczak 2006 model with artificial neural network algorithm	164
3.36 Loading time under stress free temperature	170
3.37 Method to evaluate the m_{mix} of fracture properties for thermal case	171
3.38 Method to evaluate the m_{mix} of fracture properties for traffic case	171
3.39 Method to evaluate the $m_{mix-FWD}$	173
3.40 Load wave shape for single axle in bending crack propagation	177
3.41 Load wave shape for tandem axle in bending crack propagation	178
3.42 Load wave shape for triple axle in bending crack propagation	179
3.43 Load wave shape for quad axle in bending crack propagation	180
3.44 Load wave shape for single axle in shearing crack propagation	181
3.45 Load wave shape for tandem axle in shearing crack propagation	182
3.46 Load wave shape for triple axle in shearing crack propagation	183
3.47 Load wave shape for quad axle in shearing crack propagation	184
3.48 Artificial neural network models for stress intensity factors	188
3.49 Interlayer reinforcing stiffness (MN-mm/m ²) versus reinforcing thickness (mm)	189
3.50 Diagrams of HMA overlay on asphalt concrete pavement-thermal	191
3.51 ANN Model of thermal stress intensity factors for asphalt overlays over cracked asphalt surface layer	192
3.52 Diagrams of HMA overlay on jointed concrete pavement-thermal	193

FIGURE	Page
3.53 ANN model of stress intensity factors of asphalt overlay on jointed concrete pavement	193
3.54 Diagram of HMA overlay on asphalt concrete pavement with SC or FC-thermal	195
3.55 ANN model of stress intensity factor for asphalt overlay over seal coat or open graded friction course over cracked asphalt surface layer	196
3.56 Diagram of HMA overlay on asphalt concrete pavement with reinforcing interlayer beneath overlay-thermal	197
3.57 ANN models for stress intensity factors for overlays over cracked asphalt surface layer–low interlayer reinforcing stiffness level-thermal	199
3.58 ANN models for stress intensity factors for asphalt overlays over cracked asphalt surface layer–medium interlayer reinforcing stiffness level-thermal ·	200
3.59 ANN Models for stress intensity factors for asphalt overlays over cracked asphalt surface layer–high interlayer reinforcing stiffness level-thermal	201
3.60 Diagram of HMA overlay on asphalt concrete pavement-shearing	202
3.61 ANN model of the shearing part of the shearing stress intensity factors for asphalt overlays over cracked asphalt surface layer (single axle-single tire) ·	204
3.62 ANN model of the bending part of the shearing stress intensity factors for asphalt overlays over cracked asphalt surface layer (single axle–single tire)·	205
3.63 ANN model of the shearing part of the shearing stress intensity factors for asphalt overlays over cracked asphalt surface layer (single axle–dual tire)··	207
3.64 ANN model of the bending part of the shearing stress intensity factors for asphalt overlays over crack asphalt surface layer (single axle–dual tire)····	208
3.65 Diagram of HMA overlay on jointed concrete pavement-shearing	209
3.66 ANN model of the shearing stress intensity factors for asphalt overlays over jointed concrete surface layer (single axle–single tire)	210
3.67 ANN model of the shearing stress intensity factors for asphalt overlays over jointed concrete surface layer (single axle – dual tire)······	212

FIGURE	Page
3.68 Diagram of HMA overlay on asphalt concrete pavement-bending.....	213
3.69 ANN model of the positive part of the bending stress intensity factors for asphalt overlays over cracked asphalt surface layer (single axle–single tire)	214
3.70 ANN model of the positive and negative parts of the bending stress intensity factors for asphalt overlays over cracked asphalt surface layer (single axle–single tire)	215
3.71 ANN model of the positive part of the bending stress intensity factors for asphalt overlays over cracked asphalt surface layer (single axle–dual tire)	217
3.72 ANN model of the positive and negative parts of the bending stress intensity factors for asphalt overlays over cracked asphalt surface layer (single axle–dual tire)	218
3.73 Diagram of HMA overlay on jointed concrete pavement-bending.....	219
3.74 ANN model of positive part of the bending stress intensity factors for asphalt overlays over jointed concrete surface layer (single axle–single tire)	219
3.75 ANN model of positive and negative parts of the bending stress intensity factors for asphalt overlays over jointed concrete surface layer (single axle–single tire)	221
4.1 Illustration of amount and severity of reflection cracking distress curves.....	224
4.2 Definition of the number of days of crack growth.....	233
4.3 LMH Regression results of ρ and β for AC over AC pavement and Wet-Freeze climatic zone.....	240
4.4 MH Regression results of ρ and β for AC over AC pavement and Wet-Freeze climatic zone.....	240
4.5 H Regression results of ρ and β for AC over AC pavement and Wet-Freeze climatic zone.....	240

FIGURE	Page
4.6 LMH Regression results of ρ and β for AC over JPC/JRC pavement and Wet-Freeze climatic zone	241
4.7 MH Regression results of ρ and β for AC over JPC/JRC pavement and Wet-Freeze climatic zone	241
4.8 H Regression results of ρ and β for AC over JPC/JRC pavement and Wet-Freeze climatic zone	241
4.9 LMH Regression results of ρ and β for AC over FC/SC pavement and Wet-Freeze climatic zone	242
4.10 MH Regression results of ρ and β for AC over FC/SC pavement and Wet-Freeze climatic zone	242
4.11 H Regression results of ρ and β for AC over FC/SC pavement and Wet-Freeze climatic zone	242
4.12 LMH Regression results of ρ and β for AC over CRC pavement and Wet-Freeze climatic zone	243
4.13 MH Regression results of ρ and β for AC over CRC pavement and Wet-Freeze climatic zone	243
4.14 LMH Regression results of ρ and β for AC over AC pavement and Wet-No Freeze climatic zone	243
4.15 MH Regression results of ρ and β for AC over AC pavement and Wet-No Freeze climatic zone	244
4.16 LMH Regression results of ρ and β for AC over FC/SC pavement and Wet-No Freeze climatic zone	244
4.17 LMH Regression results of ρ and β for AC over AC pavement and Dry-Freeze climatic zone	244
4.18 MH Regression results of ρ and β for AC over AC pavement and Dry-Freeze climatic zone	245
4.19 H Regression results of ρ and β for AC over AC pavement and Dry-Freeze climatic zone	245
4.20 LMH Regression results of ρ and β for AC over AC pavement and Dry-No Freeze climatic zone	245

FIGURE	Page
4.21 MH Regression results of ρ and β for AC over AC pavement and Dry-No Freeze climatic zone	246
4.22 H Regression results of ρ and β for AC over AC pavement and Dry-No Freeze climatic zone	246
4.23 LMH Regression results of ρ and β for AC with reinforcing over PCC pavement and Wet-No Freeze climatic zone	246
4.24 LMH Regression results of ρ and β for AC with reinforcing over AC pavement and Dry-Freeze climatic zone	247
4.25 LMH Regression results of ρ and β for AC with Reinforcing over PCC pavement and Wet- Freeze climatic zone	247
4.26 MH Regression results of ρ and β for AC with Reinforcing over PCC pavement and Wet- Freeze climatic zone	247
5.1 Development of transverse reflection cracking distress extent and severity for HMA overlay over asphalt surface in wet-freeze zone (Lincoln, Maine)	251
5.2 Development of transverse reflection cracking distress extent and severity for HMA overlay over jointed reinforced concrete in wet-freeze zone (Beaver, Pennsylvania)	251
5.3 Development of transverse reflection cracking distress extent and severity for HMA overlay over friction course over asphalt surface in wet-freeze zone (Frederick, Maryland)	252
5.4 Development of transverse reflection cracking distress extent and severity for HMA overlay over continuously reinforced concrete pavement in wet-freeze zone (Minnesota, Washington)	252
5.5 Development of transverse reflection cracking distress extent and severity for HMA overlay with reinforcing geosynthetic over jointed concrete in wet-no freeze zone (Waco, Texas)	254
5.6 Development of transverse reflection cracking distress extent and severity for HMA overlay with reinforcing geosynthetic over asphalt surface in dry-freeze zone (Amarillo, Texas)	254

FIGURE	Page
5.7 Development of transverse reflection cracking distress extent and severity for HMA overlay over asphalt surface in wet-no freeze zone (Pittsylvania, Virginia)	255
5.8 Development of transverse reflection cracking distress extent and severity for HMA overlay over friction course over asphalt surface in wet-no freeze zone (Yazoo, Mississippi)	255
5.9 Development of transverse reflection cracking extent and severity for HMA overlay over asphalt pavement surface in dry-freeze zone (Deaf Smith County, Texas)	257
5.10 Development of transverse reflection cracking extent and severity for HMA overlay over asphalt pavement surface in dry-no freeze zone (Pinal, Arizona)	257
5.11 Development of transverse reflection cracking distress extent and severity for HMA overlay with reinforcing geosynthetic over jointed concrete pavement in wet-freeze zone (New York, New York)	258
5.12 The comparison between field and predicted results for LMH severity distress (AC over AC pavement structure, Wet-Freeze climatic zone)	260
5.13 The comparison between field and predicted results for LMH severity distress (AC over JPC pavement structure, Wet-Freeze climatic zone)	261
5.14 The comparison between field and predicted results for MH severity distress (AC over JPC pavement structure, Wet-Freeze climatic zone)	261
5.15 The comparison between field and predicted results for LMH severity distress (AC over FC pavement structure, Wet-Freeze climatic zone)	262
5.16 The comparison between field and predicted results for MH severity distress (AC over FC pavement structure, Wet-Freeze climatic zone)	262
5.17 The comparison between field and predicted results for LMH severity distress (AC over CRC pavement structure, Wet-Freeze climatic zone)	264
5.18 The comparison between field and predicted results for MH severity distress (AC over CRC pavement structure, Wet-Freeze climatic zone)	264

FIGURE	Page
5.19 The comparison between field and predicted results for LMH severity distress (AC over reinforcing interlayer over PCC pavement structure, Wet-Freeze climatic zone)	265
5.20 The comparison between field and predicted results for MH severity distress (AC over reinforcing interlayer over PCC pavement structure, Wet-Freeze climatic zone)	265
5.21 The comparison between field and predicted results for LMH severity distress (AC over AC pavement structure, Wet-No Freeze climatic zone) ...	266
5.22 The comparison between field and predicted results for MH severity distress (AC over AC pavement structure, Wet-No Freeze climatic zone) ...	266
5.23 The comparison between field and predicted results for LMH severity distress (AC over FC pavement structure, Wet-No Freeze climatic zone)	267
5.24 The comparison between field and predicted results for LMH severity distress (AC over reinforcing interlayer over PCC pavement structure, Wet-No Freeze climatic zone)	267
5.25 The comparison between field and predicted results for LMH severity distress (AC over AC pavement structure, Dry-Freeze climatic zone)	269
5.26 The comparison between field and predicted results for MH severity distress (AC over AC pavement structure, Dry-Freeze climatic zone)	269
5.27 The comparison between field and predicted results for H severity distress (AC over AC pavement structure, Dry-Freeze climatic zone)	270
5.28 The comparison between field and predicted results for LMH severity distress (AC over reinforcing interlayer over AC pavement structure, Dry-Freeze climatic zone)	270
5.29 The comparison between field and predicted results for LMH severity distress (AC over AC pavement structure, Dry-No Freeze climatic zone)	271
5.30 The comparison between field and predicted results for MH severity distress (AC over AC pavement structure, Dry-No Freeze climatic zone)	271
5.31 Sensitivity analysis of ρ_{LMH} for AC over AC pavement structure in a Wet-Freeze climatic zone	274

FIGURE	Page
5.32 Sensitivity analysis of ρ_{MH} for AC over AC pavement structure in a Wet-Freeze climatic zone	275
5.33 Sensitivity analysis of ρ_H for AC over AC pavement structure in a Wet-Freeze climatic zone	275
5.34 Sensitivity analysis of ρ_{LMH} for AC over JPC pavement structure in a Wet-Freeze climatic zone	276
5.35 Sensitivity analysis of ρ_{MH} for AC over JPC pavement structure in a Wet-Freeze climatic zone	276
5.36 Sensitivity analysis of ρ_H for AC over JPC pavement structure in a Wet-Freeze climatic zone	277
5.37 Sensitivity analysis of ρ_{LMH} for AC over FC (SC) pavement structure in a Wet-Freeze climatic zone	277
5.38 Sensitivity analysis of ρ_{MH} for AC over FC (SC) pavement structure in a Wet-Freeze climatic zone	278
5.39 Sensitivity analysis of ρ_H for AC over FC (SC) pavement structure in a Wet-Freeze climatic zone	278
5.40 Sensitivity analysis of ρ_{LMH} for AC over CRC pavement structure in a Wet-Freeze climatic zone	280
5.41 Sensitivity analysis of ρ_{MH} for AC over CRC pavement structure in a Wet-Freeze climatic zone	280
5.42 Sensitivity analysis of ρ_{LMH} for AC over AC pavement structure in a Wet-No Freeze climatic zone	281
5.43 Sensitivity analysis of ρ_{MH} for AC over AC pavement structure in a Wet-No Freeze climatic zone	281
5.44 Sensitivity analysis of ρ_{LMH} for AC over FC (SC) pavement structure in a Wet-No Freeze climatic zone	282
5.45 Sensitivity analysis of ρ_{LMH} for AC over AC pavement structure in a Dry-Freeze climatic zone	282

FIGURE	Page
5.46 Sensitivity analysis of ρ_{MH} for AC over AC pavement structure in a Dry-Freeze climatic zone	283
5.47 Sensitivity analysis of ρ_H for AC over AC pavement structure in a Dry-Freeze climatic zone	284
5.48 Sensitivity analysis of ρ_{LMH} for AC over AC pavement structure in a Dry-No Freeze climatic zone	284
5.49 Sensitivity analysis of ρ_{MH} for AC over AC pavement structure in a Dry-No Freeze climatic zone	285
5.50 Sensitivity analysis of ρ_H for AC over AC pavement structure in a Dry-No Freeze climatic zone	285
5.51 Sensitivity analysis of ρ_{LMH} for AC over Reinforcing over PCC pavement structure in a Wet-Freeze climatic zone	287
5.52 Sensitivity analysis of ρ_{MH} for AC over Reinforcing over PCC pavement structure in a Wet-Freeze climatic zone	287
5.53 Sensitivity analysis of ρ_{LMH} for AC over Reinforcing over PCC pavement structure in a Wet-No Freeze climatic zone	288
5.54 Sensitivity analysis of ρ_{LMH} for AC over Reinforcing over AC pavement structure in a Dry-Freeze climatic zone	288

LIST OF TABLES

TABLE	Page
2.1 Reflection cracking model parameters	10
2.2 Comparison of reflection cracking modeling approaches	44
3.1 Overlay sections for model development	52
3.2 LTPP test sections used for calibration	53
3.3 FHWA vehicle classification	58
3.4 Load intervals for each axle type	59
3.5 Number of single axle loads for vehicle class 4 to 7 (LTPP section at Tippecanoe, Maryland in 2004)	60
3.6 Normalized vehicle class distribution factor	65
3.7 Number of axles for each vehicle class	67
3.8 Average number of axles for each vehicle	68
3.9 Results of number of axle loads for a section with AADTT = 1,500	69
3.10 Typical characteristics for each axle type	72
3.11 Tire patch length increment for each load category	74
3.12 Model parameters and CALD on tire length (category 1 of LTPP section at Tippecanoe, Maryland in 2004)	79
3.13 Model parameters and CALD on tire length of LTPP section at Tippecanoe, Maryland (2004)	80
3.14 Minimum values to be considered for load related distress	85
3.15 CALD model parameter default values determined based on LTPP data	86

TABLE	Page
3.16 Default cumulative axle load distribution for each load category	87
3.17 Default probability density for each load category	92
3.18 Default hourly truck traffic distribution values	94
3.19 Hourly number of traffic for LTPP section in Tippecanoe, Maryland within category 1	96
3.20 Collected reflection crack information of LTPP test sections	119
3.21 Predicted reflective cracking development of L+M+H severity for LTPP test sections	120
3.22 Calibrated model parameters of LTPP sections	121
3.23 Loading times for different axles	156
3.24 Load times for different categories	157
3.25 Mean CAM model parameters for the four climatic regions	159
3.26 1999 ANN relaxation model input format	162
3.27 2006 ANN relaxation model input format	163
3.28 G_g database at different PG grading and climatic zones	167
3.29 Fatigue calibration coefficients for four climatic zones	170
3.30 Tensile strength of asphalt mixtures	173
3.31 Upper limit of integration of a_k in different axles	175
3.32 Number of computer runs of SIF	186
3.33 Thermal stress variables in HMA overlay on asphalt concrete pavement system	191

TABLE	Page
3.34 Thermal stress variables in HMA overlay on jointed concrete pavement system	194
3.35 Thermal stress-variables in HMA overlay on asphalt concrete pavement with SC or FC system	195
3.36 Thermal stress variables in HMA overlay on asphalt concrete pavement with reinforcing interlayer on level-up and beneath overlay system	198
3.37 Shearing stress variables in HMA overlay on asphalt concrete pavement system	203
3.38 Shearing stress variables in HMA overlay on asphalt concrete pavement system	206
3.39 Shearing stress variables in HMA overlay on jointed concrete pavement system	209
3.40 Shearing stress variables in HMA overlay on jointed concrete pavement system	211
3.41 Bending stress variables in HMA overlay on asphalt concrete pavement system	213
3.42 Bending stress variables in HMA overlay on asphalt concrete pavement system	216
3.43 Bending stress variables in HMA overlay on jointed concrete pavement system	220
3.44 Bending stress variables in HMA overlay on jointed concrete pavement system	222
4.1 Observed coefficients ρ and β for each calibration section	226
4.2 Summary of modeling coefficients for different pavement structures and climatic zones	237
5.1 Figures showing calculated reflection cracking distress curves	250
5.2 Summary of sensitivity analytic sections in different climatic zones and pavement structures	272

CHAPTER I

INTRODUCTION

1.1 Background

Reflection cracking is one of the primary distresses in hot-mix asphalt (HMA) overlays for flexible and rigid pavements. It permits the penetration of water and foreign objects into the cracks and deteriorates the pavement structure and reduces the ride quality, thus shortening the service life of the pavement. In order to improve the resistance of overlays to reflection cracking, it is necessary to analyze and predict the reflection cracking phenomenon in HMA overlays. Several researchers have studied methods to predict reflection cracking (1, 2, 3). In most cases, the researchers focused on only one of the three cracking mechanisms instead of combining them as is done in this dissertation.

Reflection cracking occurs due to existing cracks or joints in the overlaid pavement surface layer growing through the overlay as illustrated in Figure 1.1. The crack growth is induced by bending or shearing from passing traffic loads or by temperature changes. Every pass of a traffic load would induce two peak shearing stresses and one bending peak stress in the HMA overlay (Figure 1.1b). In addition, mixture properties, the degree of load transfer at joints and cracks, etc. This dissertation

This dissertation follows the style of *Transportation Research Board (TRB)*.

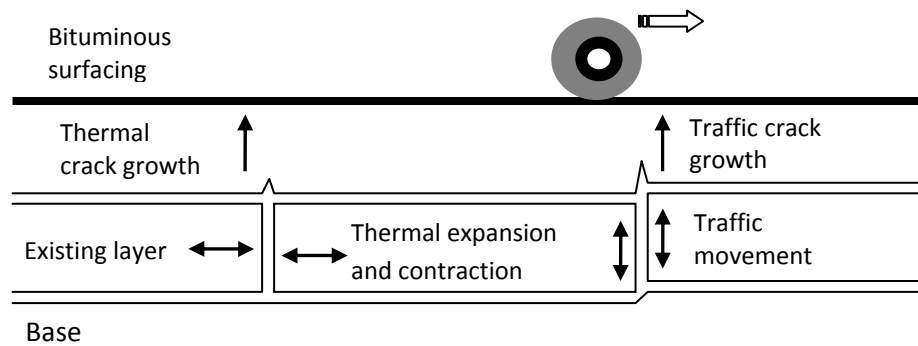
would present mechanistic-based models which would be calibrated to field data to produce a design process that is compatible with the Mechanistic-Empirical Pavement Design Guid (MEPDG) Program (4).

The first stage of predicting reflection cracking is the identification and separation of the three cracking mechanisms present in the overlay: bending, shearing, and thermal stresses. Paris' fracture law (5) would be used in this study to evaluate the length increase of the reflection cracks per day when the overlays are subjected to the three mechanisms. Each mechanism would be modeled as a two-phase process. The first phase is when the crack grows from the bottom of the overlay to "Position 1", as illustrated in Figure 1.2, and all three mechanisms contribute to crack growth. In the second phase, the crack grows from "Position 1" to the overlay surface and bending produces no additional crack growth due to a negative bending stress (i.e. compressive). Because the bending stress is negative, the only causes of further crack growth are shearing and thermal stresses.

1.2 Approach Outline

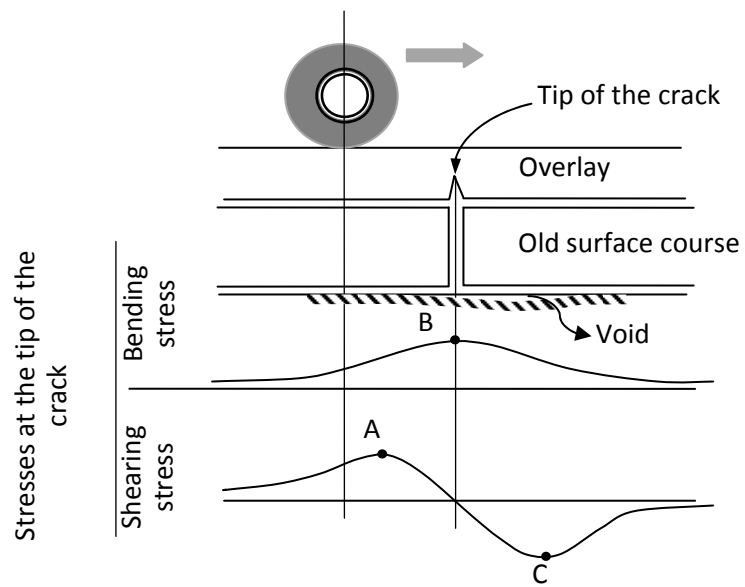
The computation flow charts shown in Figure 1.3 present the calculation processes for thermal stress and traffic stresses due to bending and shearing. Figure 1.3a illustrates an algorithm used to compute crack growth due to the thermal stress. The first step in the process would consist of calculating the pavement temperature at the current tip of the growing reflection crack. The hourly pavement temperature would be used to evaluate the properties of the binder and mixture and the viscoelastic thermal stress. The daily increments of crack length would be computed and summed each day to check the

total crack length against the thickness of the overlay, and the numbers of days for the crack to reach the overlay surface are reported. Similar processes would be used for calculating bending and shearing crack growth and are described in Figure 1.3b and Figure 1.3c, respectively. As is done in the MEPDG software, traffic load spectra would be used to characterize the daily traffic loading. After completing the calculation of the number of days for each mechanism to reach “Position 1” and then to reach the surface of the overlay, the set of five numbers of days (i.e., three numbers of days to reach “Position 1” due to bending, shearing, and thermal stresses, and two numbers of days to reach the overlay surface due to shearing and thermal stresses) would be used in calibrating all overlays of the same structural type within the same climatic zone to the observed field distress data.



(a) Mechanisms of reflection cracking (after Nunn (6))

Figure 1.1. Mechanisms of reflection cracking (7).



(b) Traffic mechanisms

Figure 1.1. continued (7).

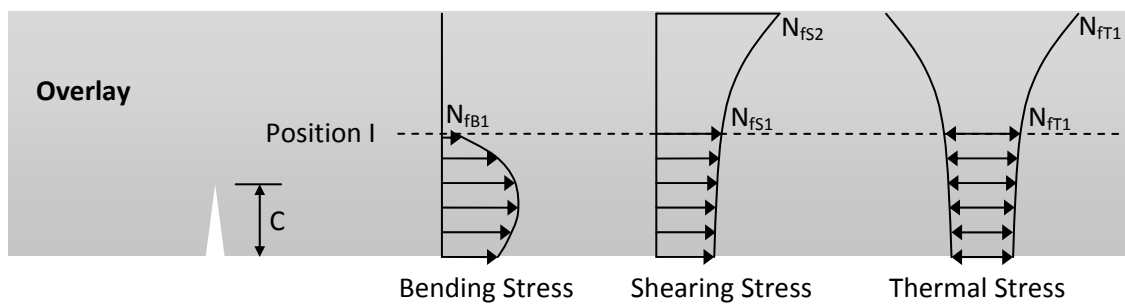
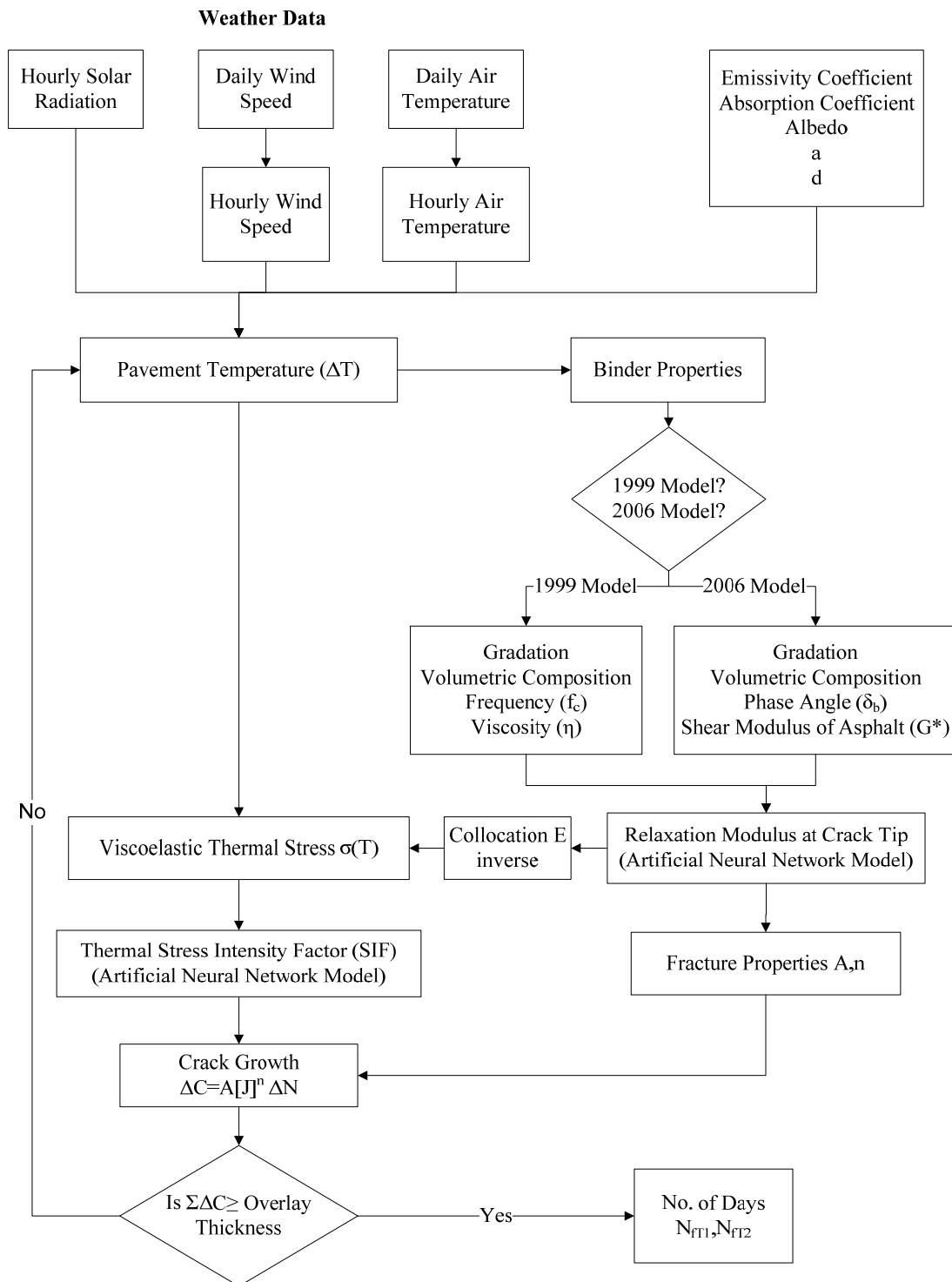
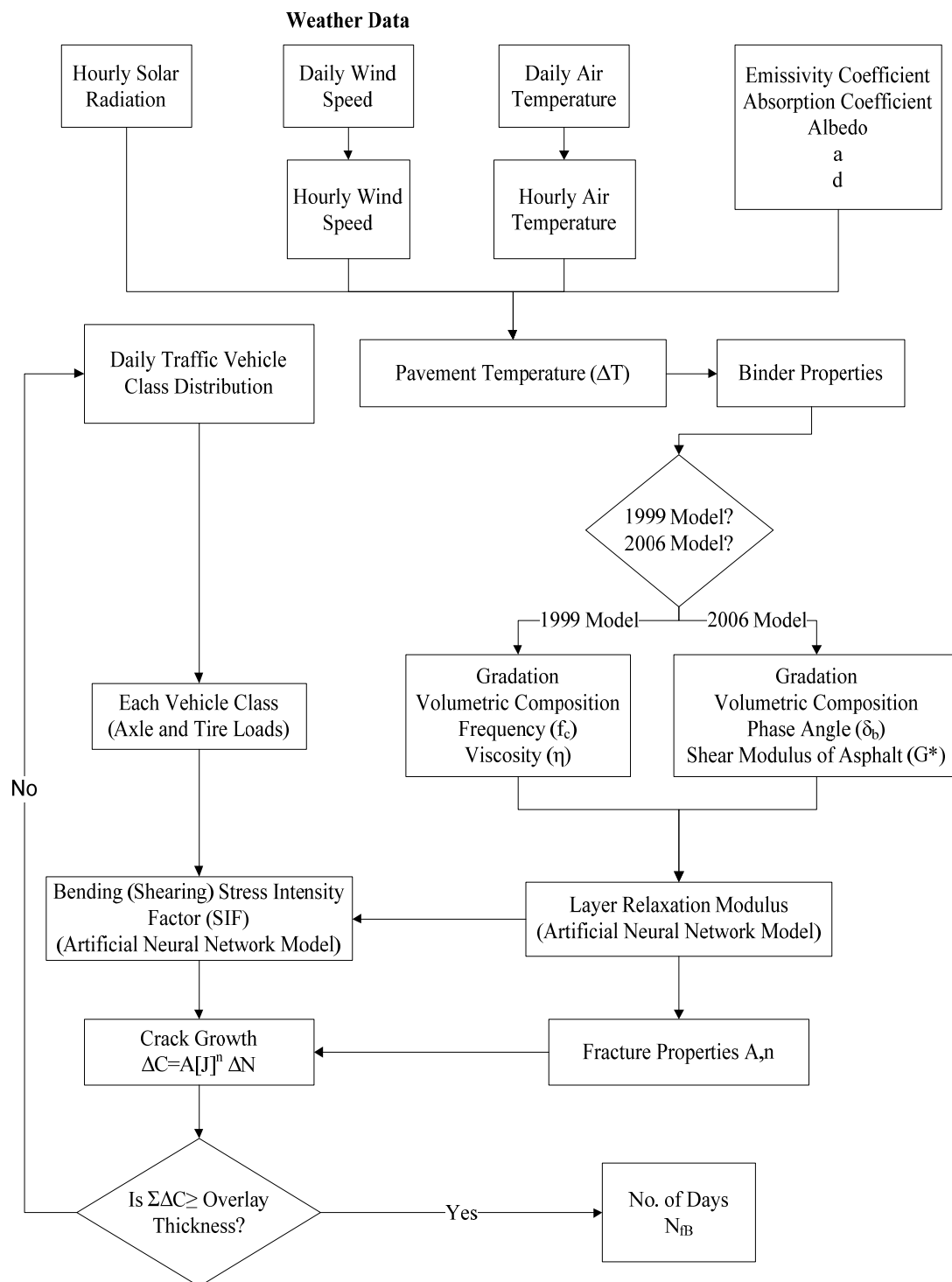


Figure 1.2. Definitions of the numbers of days and two-phase crack growth.



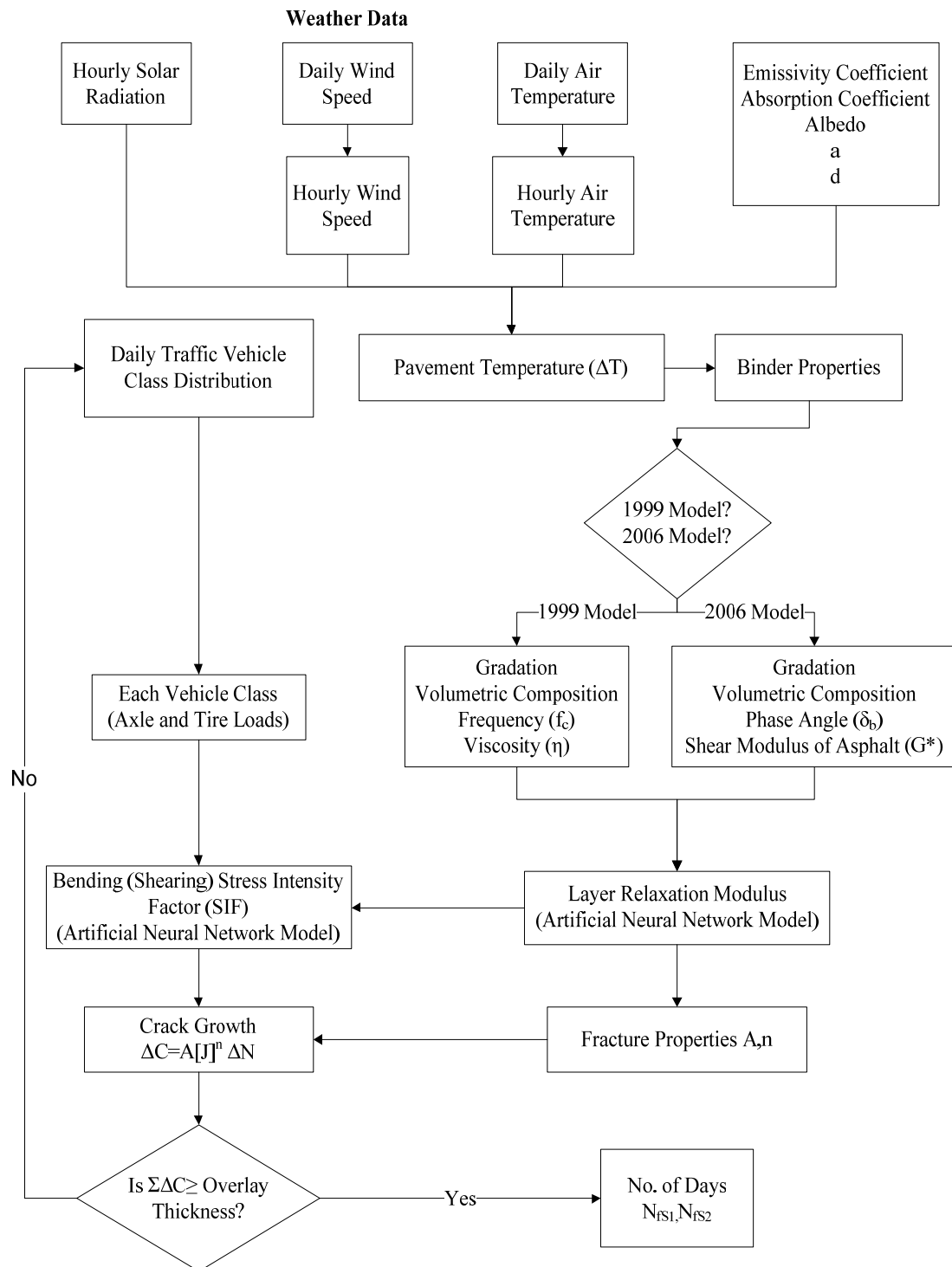
(a) Crack growth computation due to thermal stress

Figure 1.3. Computation processes for reflection cracking.



(b) Crack growth computations due to bending stress

Figure 1.3. Continued.



(c) Crack growth computations due to shearing stress

Figure 1.3. Continued.

CHAPTER II

LIERATURE REVIEW

2.1 Introduction

Reflection cracking is one of the primary forms of distress in hot-mix asphalt (HMA) overlays of flexible and rigid pavements. In addition to affecting ride quality, the penetration of water and foreign debris into these cracks accelerates the deterioration of the overlay and the underlying pavement, thus reducing service life. Preliminary models for predicting the extent and severity of reflection cracking in HMA overlays have been developed. However, only limited research has been performed to evaluate and validate these models. Research is needed to address the issues associated with reflection cracking and to identify or develop mechanics-based models for use in mechanistic-empirical procedures for the analysis and design of HMA overlays. The objective of the research is to identify or develop mechanics-based models for predicting reflection cracking in HMA overlays of flexible and rigid pavements and associated computational software for use in mechanistic-empirical procedures for overlay design and analysis.

2.2 Available Reflection Cracking Models

Reflection cracking has been a serious concern associated with asphalt overlay over existing pavements from as early as 1932, when Gary and Martin (8) studied this problem. Since then, many studies have been conducted to address this problem. Many

models have been developed to analyze or predict reflection cracking. In general, these models can be categorized as follows:

- Empirical model
- Extended multi-layer linear elastic model
- Equilibrium equations-based models
- Finite element plus traditional fatigue equation model
- Finite element plus fracture mechanics model
- crack band theory based model
- cohesive cracking/zone model
- non-local continuum damage mechanics-based model

A detailed discussion of each type of model is presented in the following sections.

1) Empirical Model

A number of empirical models have been developed for predicting reflection cracking in asphalt overlay pavements. In general, these empirical models relate several variables such as existing pavement conditions, environment, and traffic loading to the amount of reflection cracking. For example, Hall, et al. (9) developed an empirical model to predict the total length of medium and high-severity reflection cracks in HMA overlay pavements. The variables in the model include cumulative 80-kN equivalent single axle loads (ESALs), thickness of overlay, age of overlay, freezing index, and some measure of the condition of the PCC (Portland Cement Concrete) pavement prior

to overlay. Another empirical reflection cracking model was included in the research report of NCHRP (National Cooperative Highway Research Program) 1-37A project (1). This model shown in Equation 2.1 predicts the percentage of cracks that propagate through the overlay as a function of time using a sigmoidal function.

$$RC = \frac{100}{1 + e^{a+bt}} \quad (2.1)$$

where:

RC = Percent of cracks reflected, %.

t = Time, years.

a and b = Fitting parameters shown in Table 2.1.

Table 2.1. Reflection cracking model parameters (6).

Pavement type	Parameters	
	a	b
Flexible	$3.5+0.75(h_{ac})$	$0.688584-3.37302(h_{ac})^{-0.915469}$
Rigid, Good Load Transfer	$3.5+0.75(h_{ac}-1)$	$0.688584-3.37302(h_{ac}-1)^{-0.915469}$
Rigid, Poor Load Transfer	$3.5+0.75(h_{ac}-3)$	$0.688584-3.37302(h_{ac}-3)^{-0.915469}$

Note: h_{ac} = thickness of overlay in inches.

Obviously, this reflection cracking model (Equation 2.1) is a pure regression equation. The only variables that are considered are the load transfer at joints and cracks of the PCC pavements and the asphalt overlay thickness. The influences of traffic load

and traffic levels, environmental conditions, material properties of the HMA overlay, existing layers and subgrade, etc, are not considered, although these factors have a significant impact on the reflection cracking.

2) Extended Multi-layer Linear Elastic Model

Multi-layer linear elastic theory has been widely used in asphalt pavement analysis and design. In fact, the pavement response model in the current Mechanistic-Empirical Pavement Design Guide (MEPDG) is based on multi-layer linear elastic theory. Note that the multi-layer linear elastic theory is based on the following assumptions:

- Axi-symmetrical geometry
- Homogeneous, isotropic linear elastic materials
- All layers extend to infinity in the horizontal plane

Obviously, these assumptions cannot be fully satisfied when using the multi-layer linear elastic theory to analyze an HMA overlay over cracked pavements. Thus, the multi-layer linear elastic theory is not suitable to analyze the reflection cracking issue. However, several trials have been made to analyze the crack propagation in a simplified manner.

The approach used in the MOEBIUS software (10) assumes the pavement as initially sound. The HMA overlay layer is divided in as many sublayers as possible, each

of which has the initial properties of new asphalt. The first crack at the bottom is supposed to be initiated by fatigue. After the crack initiation stage, the properties of the different sublayers are progressively reduced from the bottom to the top with a rate of propagation determined from the knowledge of Paris' law. Such a procedure cannot perfectly model the complexity of the cracking phenomena. The accuracy of the predictions is, of course, limited by the oversimplification and is also dependent on the input data.

Another trial to use a multi-layer linear elastic program for crack propagation from an existing pavement through a new overlay was made by Van Gurp and Molenaar (11). First of all, Van Gurp and Molenaar compared analysis results from finite element analysis with those from the BISAR multi-layer linear elastic program. Based on the comparison, the finite element meshes were determined given that the critical tensile strain for an uncracked pavement structure was equal to the one calculated from the BISAR program. A study of a cracked pavement structure was then conducted in order to determine an effective modulus value for the BISAR program. It was concluded that providing that reliable effective modulus values are chosen, the multi-layer linear elastic model could be used for asphalt overlay thickness design purposes.

It is clear however that this type of extension of the multi-layer linear elastic model is merely a way to use an existing tool in a field for which it was not initially developed.

3) Equilibrium Equations Based Models

An asphalt overlay design procedure has been developed for the Federal Highway Administration (FHWA) and later for the Arkansas State Highway and Transportation Department by McCullough and his associates (12, 13, 14). This procedure was based on a simple mechanistic approach in which equilibrium equations were used to estimate the stress and strain in an asphalt overlay. Moreover, this procedure has been implemented in the forms of computer programs and charts for practical overlay design. The detailed procedure is described as follows.

Austin Research Engineers (ARE) (12, 13) has developed an analytical procedure for reflection crack analysis based on simple static equilibrium equations without using fracture mechanics or finite element techniques. Two different failure modes are considered. The first is an opening mode (Figure 2.1) due to horizontal movements of the existing concrete pavement resulting from a temperature reduction. The second is a shearing mode (Figure 2.1) resulting from a differential deflection across the joint or crack as the traffic load moves across the discontinuity. Figure 2.2 presents the flow diagram of the overall reflection cracking analysis procedure. Note that the contribution to failure through the opening mode caused by bending when the traffic load is centered above the crack is not included in the procedure. In developing the models, a number of assumptions have been made, including:

- Linear elasticity and all the assumptions associated with it are applicable to this problem,
- The governing equation of static equilibrium is applicable to pavements: i. e. $\Sigma F_x=0, \Sigma F_y=0, \Sigma F_z=0$ (sum of the force in each direction equal to zero),
- Temperature variations are uniformly distributed in the existing concrete slab,
- Concrete movement is continuous with slab length,
- Movement of a layer is constant through the layer thickness, and
- Material properties are independent of space.

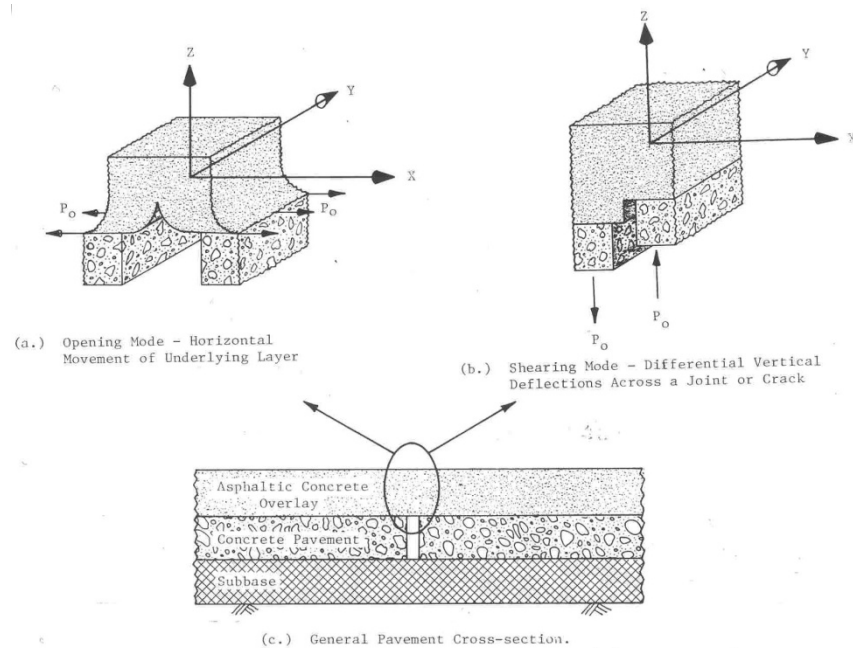


Figure 2.1. Different failure modes considered for the reflection cracking model (5).

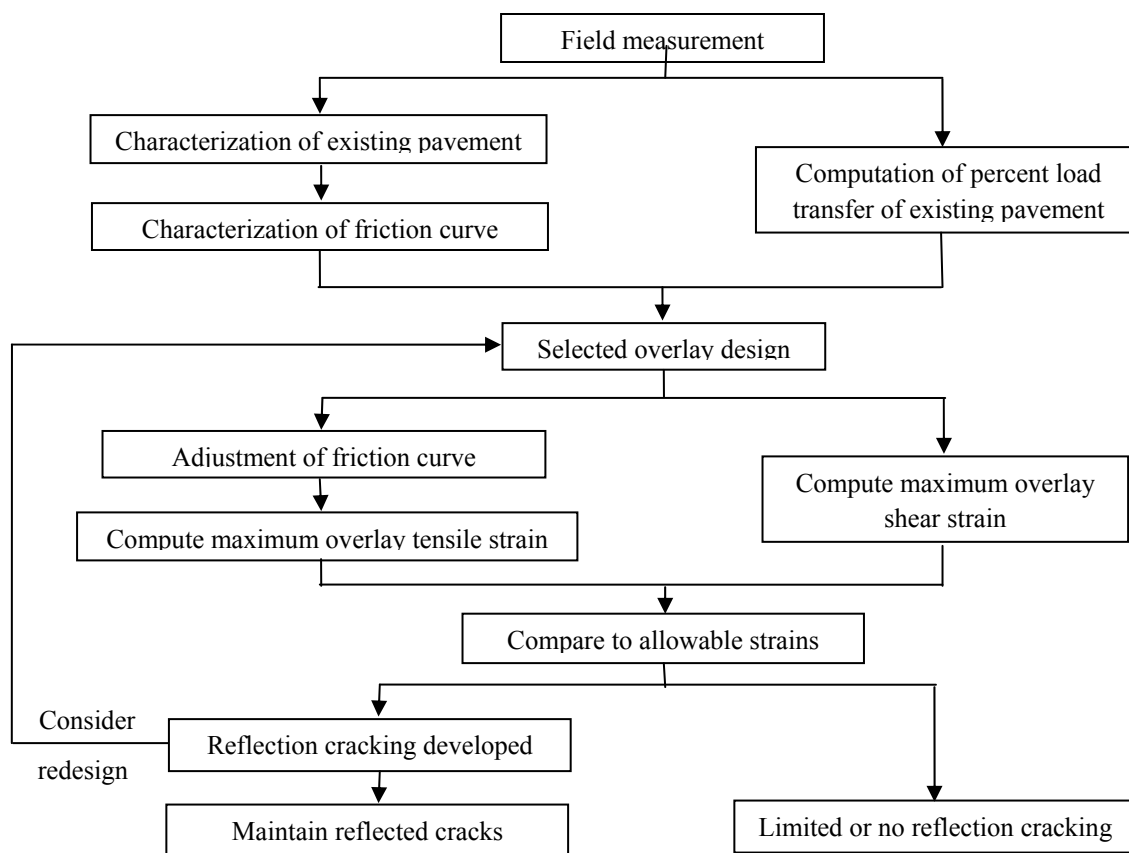


Figure 2.2. Overall reflection cracking analysis procedure (12).

Later, the ARE procedure was then extended and calibrated for the Arkansas State Highway and Transportation Department (14). It was recognized that the tensile strains that induce reflection cracking result the direct thermal stresses and the temperature-drop-related movements of the underlying slab, the temperature variations are cyclic in nature, and the reflection cracking in asphalt overlays must be attributed to fatigue or the accumulation of damage brought about by cyclic loading.

4) Finite Element Plus Traditional Fatigue Equation Model Approach

Finite element (FE) techniques have been widely used to analyze reflection cracking of asphalt overlays. Coetzee and Monismith (15, 16) have utilized the 2-D finite element procedure to examine the distribution of stresses in an overlay in the vicinity of a crack with and without an asphalt rubber membrane (Stress Absorbing Membrane Interlayer), and then recommended that use the standard FE to examine the state of stress/strain rather than the stress intensity factor (SIF) at a crack in the existing pavement. The most recent work on reflection cracking done by Monismith and his associates (15, 16) was to calculate strains under traffic loads at the bottom of thicker overlays, then to relate those to strains leading to long fatigue life in beam fatigue tests.

In the early 1980s, Chen et al. (17) also used 2-D linear plane strain FE program to analyze the Arizona's three-layer overlay system of rigid pavements under moving traffic loads. The analysis results indicated that shearing action is more inductive to reflection cracking of overlays than bending action when traffic loading is moving from one side of a joint to the other.

In the early 1990s, Francken and Vanelstraete (18,19) used 2-D FE methodology to analyze the effect of interface systems on preventing reflection cracking and then compare the 2-D FE results with those of 3-D FE. The result showed that 2-D plane strain FE provides a much higher strain, which is understandable because the load is assumed to act on the entire pavement cross-section.

In 2002, Kim and Buttlar (20) also conducted a detailed analysis of the critical response in an asphalt overlay system for Taxiway E at the Greater Peoria Regional

Airport (GPRA) using a 3-D nonlinear FE program. As expected, a very high longitudinal tensile stress occurs at the bottom of the overlay, directly above the existing crack site. The tensile stress in the overlay under these conditions [17,065 kPa (2,475 psi)] would exceed the tensile strength of a typical HMA by a factor of 5 to 6. This result clearly demonstrates the necessity of reflection crack treatment. Otherwise, rapid reflective crack propagation would be expected.

In 2005, Sousa et al. (21, 22, 23) presented a mechanistic-empirical based overlay design method for reflective cracking. A methodology was proposed for two asphalt overlay materials: dense graded mixes with PG70-10 binders (HMA-DG) or gap graded mixes with asphalt rubber modified binders (AR-HMA-GG), cracked flexible pavements to minimize the risk of premature reflective cracking. The proposed overlay design method consists of the seven steps presented below.

- Determination of the Moduli and Thicknesses of the Pavement Section Layers

This can be accomplished using FWD (Falling Weight Deflectometer) backcalculation methods or other forms of estimating cracked pavement section moduli.

- Determination of Representative Air Temperatures

The maximum and minimum air temperature determined with the desired reliability should be obtained for the location where the pavement is to be overlaid in order to compute the mean average monthly air temperature.

- Selection of Design Cracking Percentage

The value selected should be in keeping with an agencies overlay policy.

- Determination of Adjustment Factors

During the process of model calibration, several adjustment factors were developed: an aging adjustment factor (AAF), a temperature adjustment factor (TAF), and a field adjustment factor (FAF). These three adjustment factors need to be considered for the location where the overlay will be placed and for the desired cracking level at the end of the overlay's design life.

- Selection of Overlay Material Modulus

The modulus and flexural fatigue life are obtained through flexural fatigue tests, and other moduli can be computed and introduced in the method based on actual tests performed on other types of materials.

- Determination of the Design Value, ϵ_{VM}

A 3-D FE program was used to analyze the state of stress/strain in the zone above a crack.

- Determination of ESALs (Design Equivalent Standard Axle Loads)

Using the appropriate flexural fatigue equation from last step, determine the number of (ESALs).

5) Finite Element (FE) Plus Fracture Mechanics Model

Since Majidzadeh (24) introduced fracture mechanics concepts into the field of pavements, the fracture mechanics approach has been widely used in predicting pavement cracking, especially reflection cracking analysis. As stated by Monismith et al. (15), "Fracture mechanics applications are conceptually appealing and undoubtedly have

the potential to provide solutions for crack reflection through pavement overlays.”

Different from continuum mechanics, the fracture mechanics approach focuses on crack propagation. The occurrence of reflection cracking is a crack propagation process caused by a combination of the three modes of loading (Figure 2.3):

- Mode I loading (opening mode, K_I) results from loads that are applied normally to the crack plane (thermal and traffic loading).
- Mode II loading (sliding mode, K_{II}) results from in-plane shear loading, which leads to crack faces sliding against each other normal to the leading edge of the crack (traffic loading).
- Mode III loading (tearing mode, K_{III}) results from out-of plane shear loading, which causes sliding of the crack faces parallel to the crack leading edge.
- Compared to Modes I and II, Mode III is rare and is often neglected for simplicity.

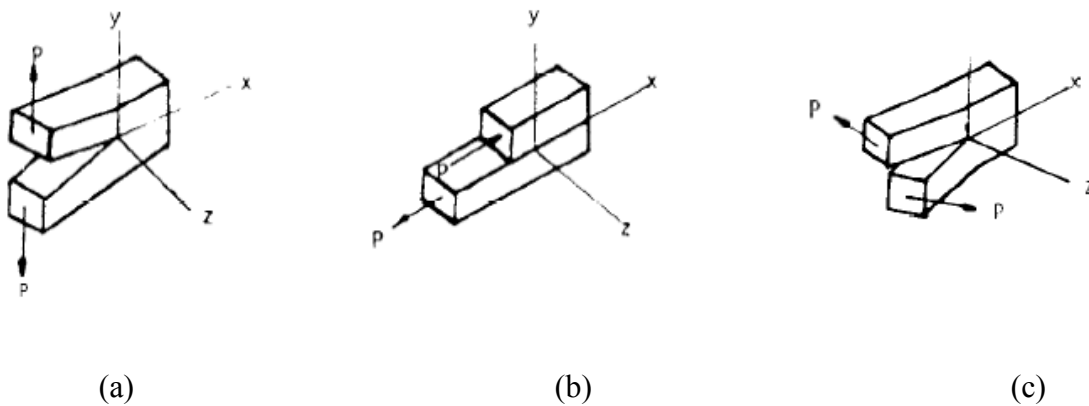


Figure 2.3. Three modes of crack opening displacement: (a) Mode I—Opening Mode, (b) Mode II—Shearing Mode, (c) Mode III—Tearing Mode (25).

The fact that the mechanisms of reflection cracking (bending, shearing, and thermal stresses) discussed previously can be exactly modeled by fracture Modes I and II makes the fracture mechanics approach the best option for modeling reflection cracking.

The generally accepted crack propagation law was proposed by Paris and Erdogan (5) in the form of Equation 2.2. It has successfully been applied to asphalt concrete by many researchers, for the analysis of experimental tests and prediction of reflection cracking and low temperature cracking.

$$\frac{dc}{dN} = A * (\Delta K)^n \quad (2.2)$$

where:

- c = Crack length,
 N = Number of loading cycles,

- A, n = Fracture properties of asphalt mixture determined by the experimental test, and
- ΔK = Stress intensity factor (SIF) amplitude, depending on the geometry of the pavement structure, fracture mode, and crack length.

The number of load cycles N_f needed to propagate a crack through an asphalt overlay of thickness h can be estimated by numerical integration in the form of Equation 2.3.

$$N_f = \int_0^h \frac{dc}{A(\Delta K)^n} \quad (2.3)$$

It is apparent that the SIF (Stress Intensity Factor), material fracture properties (A and n), and interlayer properties (if used) must be known in order to predict the reflection cracking performance of an asphalt overlay.

Lytton and his associates (25, 26, 27, 28, 29, 30, 31) have successfully applied fracture mechanics to predict reflection cracking of asphalt overlays since the mid-1970s. The same fracture mechanics concept was also used by Owusu-Antwi et al. (32) and Al-Qadi and his associates (33, 34). A briefly introduction from these researches would be shown as follows.

- **Reflection Cracking Model Proposed by Jayawickrama and Lytton (26)**

TTI (Texas Transportation Institute) has found that the thermal stress is the main contributor to the occurrence of reflection cracking, followed by the shear mode, and then the bending mode. Based on this finding, Jayawickrama and Lytton (26) first proposed a combined reflection cracking model shown in Equation 2.4. In this model, crack propagation calculated from Equation 2.3 is repeated until the crack either stops growing for bending stress, or reaches the surface of the overlay for thermal tensile stress and/or shear stress. In this way the number of days for a crack to propagate in the bending, shearing or thermal mode is calculated separately. Then, the three modes of reflection cracking are combined together to predict the actual number of days for a reflected crack to appear at the surface of the overlay as follows:

$$N_f = N_{T1} \left(\alpha_1 - \alpha_2 * \frac{N_{T1}}{N_B} - \alpha_3 * \frac{N_{T1}}{N_{S1}} \right) + N_{T2} \left(\alpha_4 - \alpha_5 * \frac{N_{T2}}{N_{S2}} \right) \quad (2.4)$$

where:

N_f = Actual number of days for a reflection crack to reach the surface of the overlay,

N_{T1}, N_{T2} = Number of days for a thermal reflection cracking to reach the neutral axis (N_{T1}) and the additional number of days for thermal reflection cracking to break through the overlay (N_{T2}),

- N_B = Number of days for bending reflection cracking to reach the neutral axis. The “neutral axis” is the point where bending stresses no longer cause crack propagation. Its location depends on the level of load transfer and moduli of pavement layers,
- N_{S1}, N_{S2} = Number of days for shearing reflection cracking to reach the neutral axis (N_{S1}) and from there to break through the overlay (N_{S2}), and
- $\alpha_1 \sim \alpha_5$ = Calibration factors.

It is known that the crack propagation length is related to the total amount of cracking that reaches the overlay surface by way of a crack length distribution function. The idea is that material variability along the length of the pavement section will result in different crack propagation lengths, even for the same exposure conditions. The crack length distribution governs how much cracking is observed in a particular section that has a specific crack length computed on the basis of average material properties. Jayawickrama and Lytton (26) proposed an S-shaped empirical model (Equation 2.5) to describe the severity development of reflection cracking in an asphalt overlay. This reflection cracking severity model is based on the number of load repetitions (or days). Combining with the Equation 2.4, Jayawickrama and Lytton (26) developed three sets of calibration factors (α_1 - α_5) for three levels of severity of reflection cracking: 0.33, 0.40, and 0.50, corresponding to low, medium, and high severity levels, respectively. Figure

2.4 shows an example of the prediction results from Jayawickrama and Lytton's model.

It should be also noted that it is the only model that dealt with reflection cracking severity.

$$g = e^{-\left(\frac{\rho}{N}\right)^\beta} \quad (2.5)$$

where:

g = Damage rating of the pavement, ranging from 0 to 1.

N = Number of load repetitions (or days).

ρ, β = Calibration coefficients.

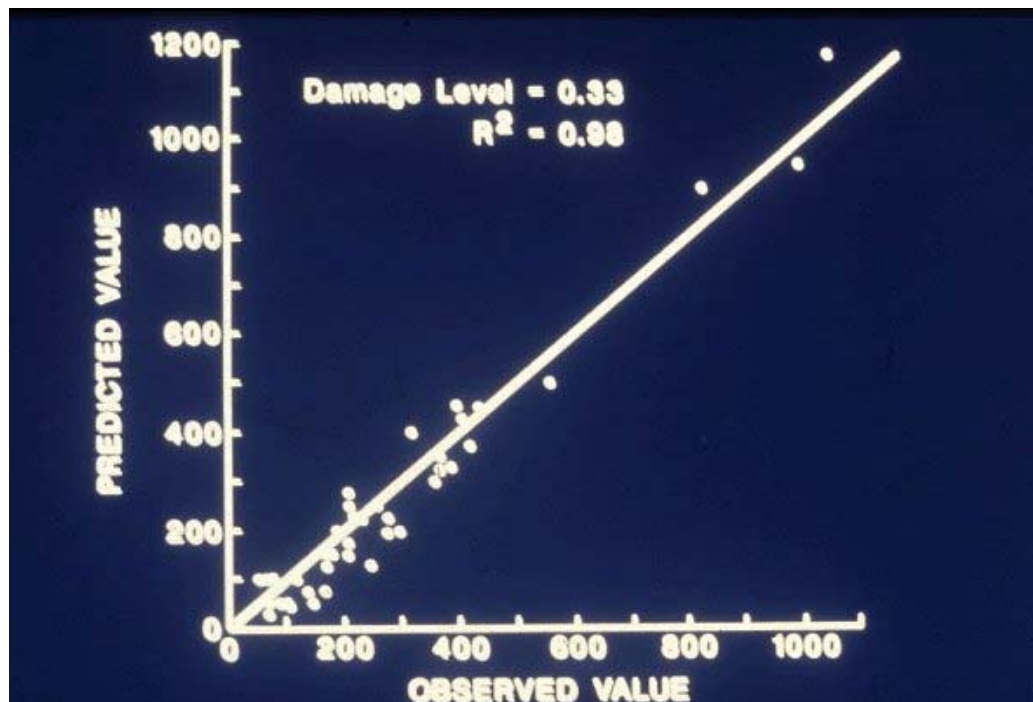


Figure 2.4. Predicted vs. observed reflection cracking (Days) (26).

- **Reflection Cracking Model Proposed by Owusu-Antwi, et al. (32)**

Owusu-Antwi et al. (32) also developed a mechanistic based reflection cracking model for asphalt concrete-overlaid pavements. They also used Paris' law (Equation 2.2) to describe crack propagation. Then, a similar form of Equation 2.3 was used to estimate the number of load repetitions (N_i) needed to propagate a crack through an asphalt overlay of thickness, h_{OL} . However, a simplified approximation, as expressed in Equation 2.6, was proposed to estimate N_i . For any level of temperature or traffic loads with known SIF (K_C), the number of load applications to failure N_i can be calculated. With N_i known, the contribution of each load application to the total damage can then be determined.

$$N_i = \frac{h_{OL}}{AK_C^n} \quad (2.6)$$

where:

N_i = Number of load repetitions (N_i) needed to propagate a crack through the asphalt overlay thickness, h_{OL} ,

h_{OL} = Asphalt overlay thickness,

K_C = Stress intensity factor at the crack tip when the crack has propagated to the middle of the asphalt concrete overlay, and

A, n = Material constants determined experimentally.

The damage accumulated from temperature and traffic variations are then calculated as follows. The damage accumulated from traffic load can then be calculated using Miner's cumulative damage approach (35).

$$TEMPDAMAGE = \frac{AGE}{N_{temp}} \quad (2.7)$$

$$TRAFDAMAGE = \sum \frac{n_i}{N_i} \quad (2.8)$$

where:

AGE = Age of the pavement after overlay, in years, and

N_{temp} = Number of temperature load applications to failure.

n_i = Actual number of axle passes for axle weight i , and

N_i = Allowable number of axle passes calculated from Equation 2.6.

For each axle load level i , the number of applications to failure $N_{i, traffic}$ can also be estimated from Equation 2.6. It should be noted that only mode II shearing loading was considered in the Owusu-Antwi et al. model (32). Then, the total damage, DAMTOT, from both temperature and traffic loading was calculated using the Equation 2.9 obtained after calibration of the model with the Long Term Pavement Performance (LTPP) (36) GPS-7 data, where n_i , AGE , N_i , and N_{temp} are defined before, and FI is the freezing index.

$$DAMTOT = 0.0132 \sum \frac{n_i}{N_i} + \frac{AGE}{N_{temp}} (8.79 + 0.000795 * FI * AGE) \quad (2.9)$$

With the above total damage model (Equation 2.9), Owusu-Antwi, et al. (32) developed the following Equation 2.10 through optimization techniques to predict the percentage of reflection cracking, %RCRACKS, in a composite asphalt concrete-overlaid pavement. The predicted vs. measured reflection cracking on the 33 LTPP GPS-7 sections is plotted in Figure 2.5, and the R^2 is 0.61.

$$\%RCRACKS = \frac{100 * DAMTOT^{1.9}}{DAMTOT^{1.9} + 1} \quad (2.10)$$

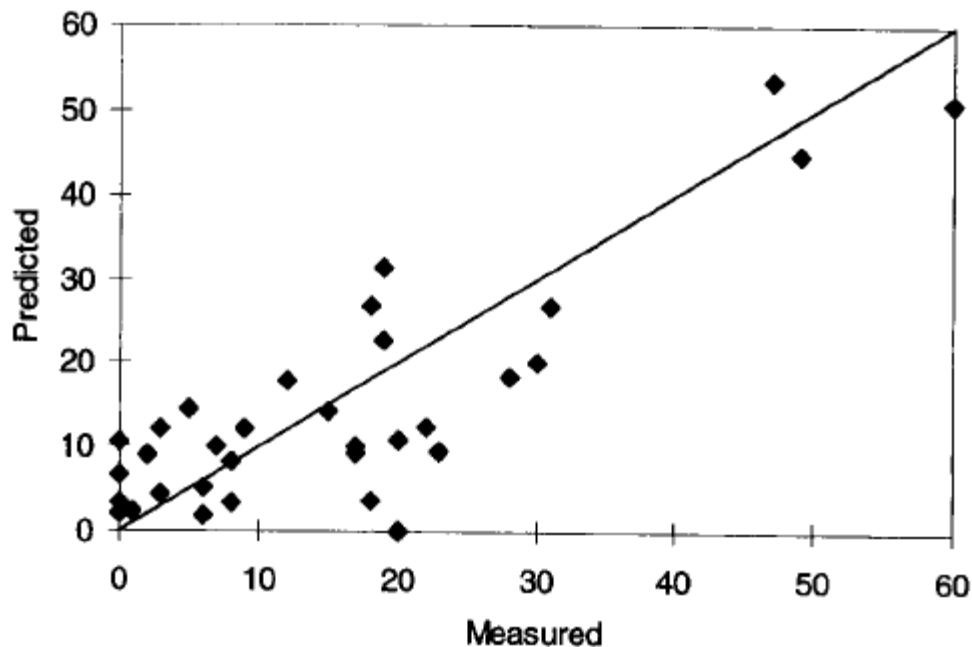


Figure 2.5. Predicted vs. measured reflection cracking at LTPP GPS-7 sections (32).

- **Simplified Overlay Design Model Proposed by Al-Qadi and his Associates (33, 34)**

Al-Qadi and his associates developed a simplified overlay design model to predict the service life of rehabilitated flexible pavement structures against reflective cracking, which was based on linear elastic fracture mechanics principles (33, 34). It was assumed that reflection cracking includes three stages: crack initiation, stable crack propagation, and unstable crack propagation. The last stage was neglected because the crack growth rate increases rapidly in this stage as global instability is approached. The crack initiation phase is described using a traditional fatigue law (Equation 2.11) developed by the Belgium Road Research Center (BRRC)(37), and the crack propagation phase is described using Paris's law (Equation 2.2). Three contour lines were used around the crack front to calculate the path independent J-integral. Then, calculations of the stress intensity factors (SIF) were determined based on the J-integral using 3-D commercial FE software ABAQUS 5.8-1 (33, 34).

$$N = 4.856 \times 10^{-14} \gamma_{zx}^{-4.76} \quad (2.11)$$

where:

N = Number of cycles before crack initiation, and

γ_{zx} = Shear strains 10mm above the existing crack.

The total number of cycles before a crack reflects to the pavement surface is defined as follows (assuming that global instability is reached when the crack front is at 12.7 mm from the pavement surface):

$$N_{\text{total}} = N_{\text{initiation}} + N_{\text{propagation}} \quad (2.12)$$

where:

N_{total} = Total number of cycles before the crack reaches 12.7 mm from the surface of the overlay,

$N_{\text{initiation}}$ = Number of cycles for crack initiation at the bottom of the overlay, and

$N_{\text{propagation}}$ = Number of cycles for the crack to propagate from the bottom of the overlay to 12.7mm from the surface of the overlay.

Although this analysis is capable of effectively evaluating the overlay service life against reflective cracking, it is very time consuming. Thus, a simplified regression model was developed to predict the number of cycles as a function of the significant variables.

$$\log W_{t80} = \frac{1}{10^4} \left[255H_{\text{overlay}} + 2.08E_{\text{overlay}} + 45.3H_{\text{HMA}} + 8.73E_{\text{HMA}} + 1.34H_{\text{base}} + 6.93E_{\text{base}} + 1.49E_{\text{subgrade}} \right] \quad (2.13)$$

where:

W_{t80} = Total number of 80-kN single-axle load applications,

$H_{overlay}$ = Thickness of HMA overlay (mm),

$E_{overlay}$ = Modulus of resilience of HMA overlay (MPa),

H_{HMA} = Thickness of existing HMA layer (mm),

E_{HMA} = Modulus of resilience of existing HMA layer (MPa),

H_{base} = thickness of base layer (mm),

E_{base} = Modulus of resilience of base layer (MPa),

$H_{subgrade}$ = Modulus of resilience of subgrade (MPa), and

It should be kept in mind that the influence of temperature variations on reflection cracking was not taken into account in this regression (Equation 2.13).

In summary, the FE plus fracture mechanics based reflection cracking model is conceptually sound, and the three mechanisms of reflection cracking (bending, shearing, and thermal loading) can be easily described with a fracture mechanics based model. Furthermore, this type of model, as discussed previously, has been successfully employed to predict the reflection cracking in asphalt overlays by different researchers. Moreover, specific software such as CRACKTIP, CAPA-3D, CAPAm, are available for automatically calculating the SIF, which once was the most difficult part in the use of fracture mechanics. Another advantage of this type of model is that empirical equations, based on Schapery's theory, have been developed to estimate the fracture properties of

asphalt concrete mixes. Thus, the FE plus a fracture mechanics based reflection cracking model, compared to the other models, is most suitable, as an adjunct to the MEPDG approach, to model reflection cracking in asphalt overlays.

6) Crack Band Model

The crack band model was developed based on the “smeared crack concept” introduced by Rashid (38, 39, 40). In this approach, a single discrete crack is replaced by infinitely many parallel cracks of infinitely small opening continuously distributed (smeared) over the finite element. Also, the effect of this smeared cracking can be modeled by reducing the material modulus in the direction normal to the cracks after the peak strength of the material has been reached.

Joseph et al. (38) discussed the reasonableness and necessity of the application of a crack band model to analyze low-temperature reflection cracking. First of all, asphalt concrete is a heterogeneous material. The stresses and strains in the equivalent homogeneous continuum are defined as the average of the micro stresses and micro strains over the selected representative volume which is shown in Figure 2.6. This definition is based on the theory of randomly inhomogeneous materials (41, 42). It implies that the detailed distributions of stress or strain over distances less than the size of several aggregates are meaningless. Consequently, the geometry of the microstructure with the difference in the elastic constants between the aggregate and the binder is not taken into account. Only the stress resultants and the accumulated strain

over the cross-section of the characteristic volume as represented by the crack band will be of interest.

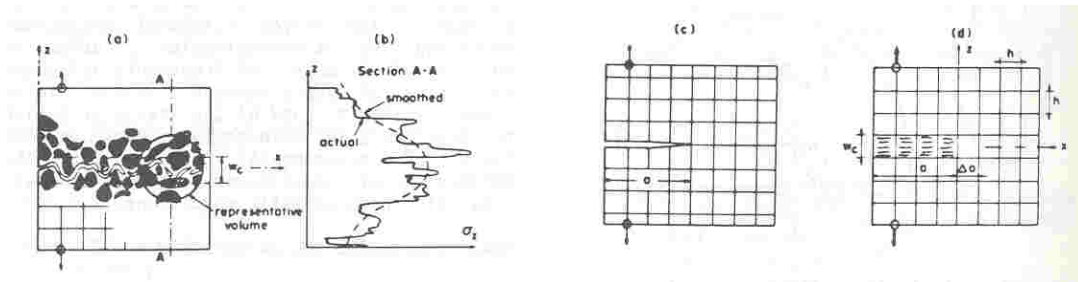


Figure 2.6. Random microstructure, scatter of microstresses, and crack band or sharp crack model (40, 41).

Secondly, the crack tends to curve around the hard aggregate pieces and randomly deviate to each side of the overall fracture axis by distances approximately equal to the aggregate size (Figure 2.6). The scatter in the location of visible microcracks relative to the path of crack propagation is better characterized by the crack band concept than the usual sharp crack approximation.

Thirdly, it has been proven (41, 42) that the line crack and the crack band models yield the same results for cases when the stress at failure drops suddenly to zero without undergoing any strain softening as a result of micro cracking. However, the assumption of abrupt stress drop is inadequate for cross-section dimensions that are not sufficiently large compared to the aggregate size (41, 42). Therefore, a gradual strain softening due to progressive micro cracking must be taken into account and this can be done easily by using the concept of a crack band model.

Finally, the FE method can be easily implemented particularly for crack propagation analysis. This can be done by simply reducing the material stiffness in the direction normal to the cracks in the band. In addition, this concept reflects the reality of densely distributed cracks in heterogeneous materials.

Based on the discussion above, Joseph et al. defined the effective width of an existing crack as shown in Figure 2.7. Then, a 2-D plain strain FE model (see Figure 2.8) was developed to analyze the effect of various treatments on retarding low-temperature reflection cracking. Figure 2.9 presents the analysis results. It must be mentioned here that Joseph et al. used the crack band model only to analyze the induced thermal stress at the bottom of asphalt overlays. No crack propagation was ever tried in asphalt overlays by using the crack band model.

More intensive research is needed in order to implement this approach into predicting reflection cracking in asphalt overlays. Actually, the crack band model, as discussed in detail by Bazant and Planas (39), is equivalent to the cohesive cracking model as discussed subsequently.

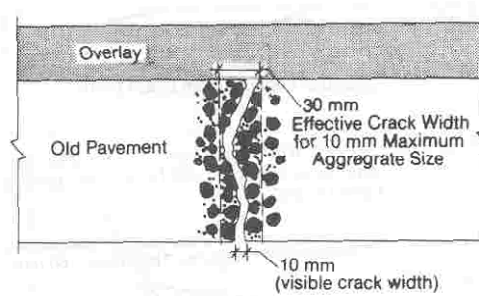


Figure 2.7. Effective width of existing crack (39).

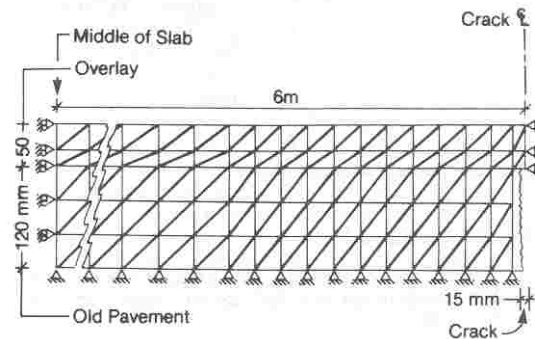


Figure 2.8. Finite element model (38).

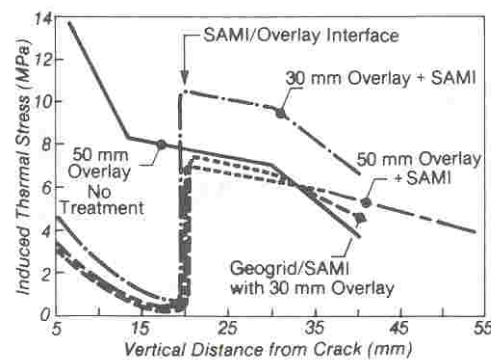


Figure 2.9. Comparative effect of various treatments (38).

7) Cohesive Crack/Zone Model

Uzan and Levenberg (43) discussed the phenomenology of asphalt concrete fracture and provided a brief overview of the cohesive crack model (CCM). There is a strongly nonlinear fracture process zone (FPZ) around the crack tip in asphalt concrete as shown in Figure 2.10. It is important to mention that in some situations, for asphalt concrete mixtures, the FPZ can extend to considerable lengths, up to a few centimeters

(44). In order to account for a relatively large plastic yield zone ahead of a crack tip, Dugdale (45) and Barenblatt (46) proposed a “correction” for the classical linear elastic fracture mechanics. Their model approximated an elastic-plastic material behavior by applying closure stresses at the model-crack’s tip. Hillerborg et al. (47) proposed a similar model to account for the relatively large FPZ that has been encountered in concrete failure. The above models are generally considered CCMs, because the models employ cohesive closure stresses at the near crack tip region.

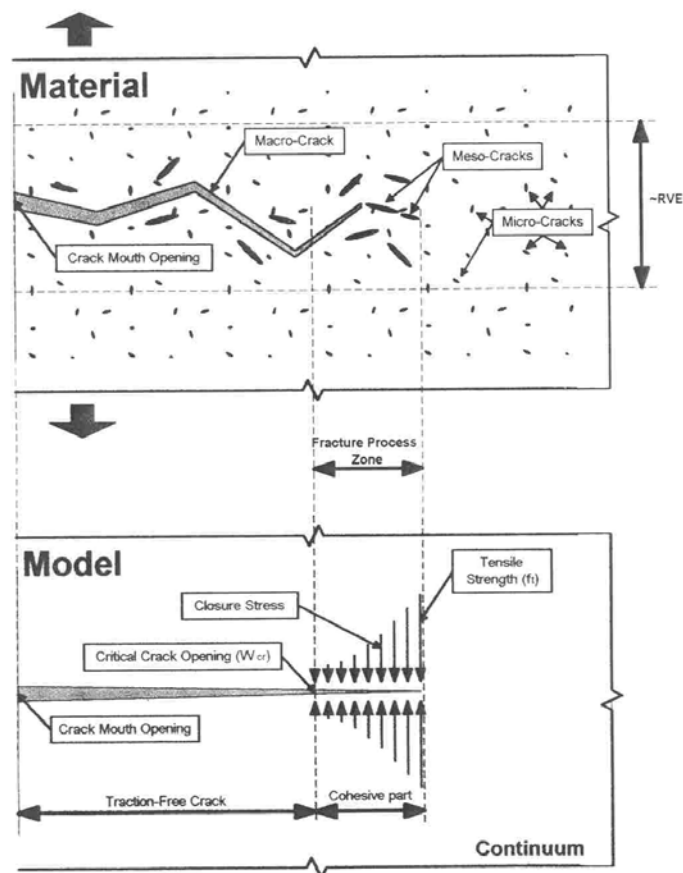


Figure 2.10. Cohesive cracking model analogy (43).

The three fundamental hypotheses of the standard CCM are as follows:

- The properties of the materials outside the process zone are governed by the undamaged state.
- A crack length can be divided into two separate regions (Figure 2.10): a traction free length, and a cohesive part. In the cohesive part, crack opening resisting tractions exist and there is still stress transfer between its faces, which is done by introducing closure stresses. The CCM postulates that the cohesive part of the crack begins to form at a point when the maximum principal stress at that point reaches the tensile strength of the material (and the crack propagation is perpendicular to the maximum stress direction) (43). Actually, this postulation is a crack initiation criterion.
- Meanwhile, the stress transfer capability of the cohesive part follows a descending path, from full transfer capability (when the cohesive crack faces just begin to depart (at peak stress conditions)) down to zero transfer capability as the displacement between the two cohesive crack faces reach a critical opening. This representation constitutes the CCM's crack propagation criterion. During the crack propagation analysis, the traction free crack is incrementally advanced whenever the calculated displacement reaches the critical opening in size. The stress transferred between the faces of the crack is described by a post-peak function (softening function). This softening curve of the material is considered to be a main component of the

CCM. Although each material has its unique softening curve, determined only by experiments, Petersson (48) first found that the softening curve is similar in shape for different mixtures of Portland cement concrete (PCC) when the softening curves are plotted in a non-dimensional form.

The latest research in this field is being led by Paulino, Buttlar, and their associates (49, 50, 51, 52). Their research focus is on developing a laboratory test such as a disk-shaped compact tension test to determine the CCM parameters and associated numerical simulation. Repeated load testing has not been touched yet.

In general, the application of the CCM to asphalt concrete mixtures is still in the preliminary stage. All studies discussed previously only applied the CCM to cracking under monotonic loading. To extend the CCM to repeated loading (such as reflection cracking), additional material parameters describing damage accumulation under unloading and reloading are needed. However, no work on this has been done yet. Therefore, the CCM is very promising, but it is not mature yet. More development is still needed.

8) Non-local Continuum Damage Mechanics Based Reflection Cracking Model (53)

The most recent research on modeling reflection cracking was conducted by Wu et al. (53). Continuum damage mechanics (CDM) allows one to describe the heterogeneous microprocesses involved during the straining of materials and structures

at the macroscale. The ultimate state of local CDM corresponds generally to macroscopic crack initiation upon which it becomes a crack propagation problem and should be considered in the framework of Fracture Mechanics. If local CDM is used to describe crack propagation, the spurious mesh dependency then comes into play. Fortunately, this mesh-dependency can be avoided by introducing non-local mechanics. A non-local continuum is a continuum in which the stress at a point depends not only on the strain history of the same point, but also on the strain history of the point's neighbor.

Non-local CDM is essentially an “enhancement” of local-CDM. Numerous ways have been proposed to incorporate non-locality into the constitutive relations of materials. The most successful ones fall into two categories: integral formulation and implicit gradient formulation. The implicit gradient formulation was recommended since it is much easier to implement in the FE code, and it is a special case of the integral formulation (54).

Implicit gradient formulation is proposed by Wu (53), in which a non-local strain $\bar{\varepsilon}$ is introduced to replace the local strain measure $\tilde{\varepsilon}$ in damage evolution. And $\bar{\varepsilon}$ and $\tilde{\varepsilon}$ are related through an additional differential equation:

$$\bar{\varepsilon} - c\nabla^2\bar{\varepsilon} = \tilde{\varepsilon} \quad (2.14)$$

where \sqrt{c} has a dimension of length and is related to the internal length scale which should be approximately equal to the maximum grain size of the material, and $\nabla^2 = \sum_i \partial^2 / \partial x_i^2$ is the Laplacian operator. Physically, Schapery's theory (55, 56)

implies that $\bar{\varepsilon}$ is a spatial average of $\tilde{\varepsilon}$ and the radius of the averaging domain is in proportion to \sqrt{c} .

The introduction of Equation 2.14 leads to a coupled problem between the displacement field and the non-local strain field. The non-local strain becomes an additional degree of freedom for each node. The evaluation of a consistent algorithmic tangent at any Gauss point requires only the current strain ε , damage ω , and non-local strain $\bar{\varepsilon}$ for that same point. In this sense, the implicit gradient formulation is mathematically local and is much easier to be incorporated into existing FE codes.

After developing the non-local CDM based reflection cracking model, the SHRP (Strategic Highway Research Program) beam-fatigue tests were conducted to calibrate the model's parameters. Frequency sweep tests were used to determine the Young's modulus master curves of two asphalt concrete mixes. Fatigue tests provided stiffness reduction curves that captured the material degradation process of the two asphalt concrete mixes under repetitive loading. FE models were established to simulate the beam fatigue test. Damage evolution law parameters were calibrated by matching the calculated and measured stiffness reduction curves. Finally, the laboratory calibrated reflection cracking model was verified by simulating reflection cracking in an HVS (Heavy Vehicle Simulator) test conducted on an asphalt concrete overlay placed on a cracked and jointed concrete pavement. The model not only recovered the most dominant crack pattern observed in the field, but it also predicted the reflection cracking life of the overlay with reasonable accuracy. Figure 2.11 shows the damage field and crack pattern after 396,000 load repetitions. In conclusion, the implicit gradient non-

local CDM, implemented in a FE program, provides a promising mechanistic model for simulating reflection cracking in asphalt concrete overlays.

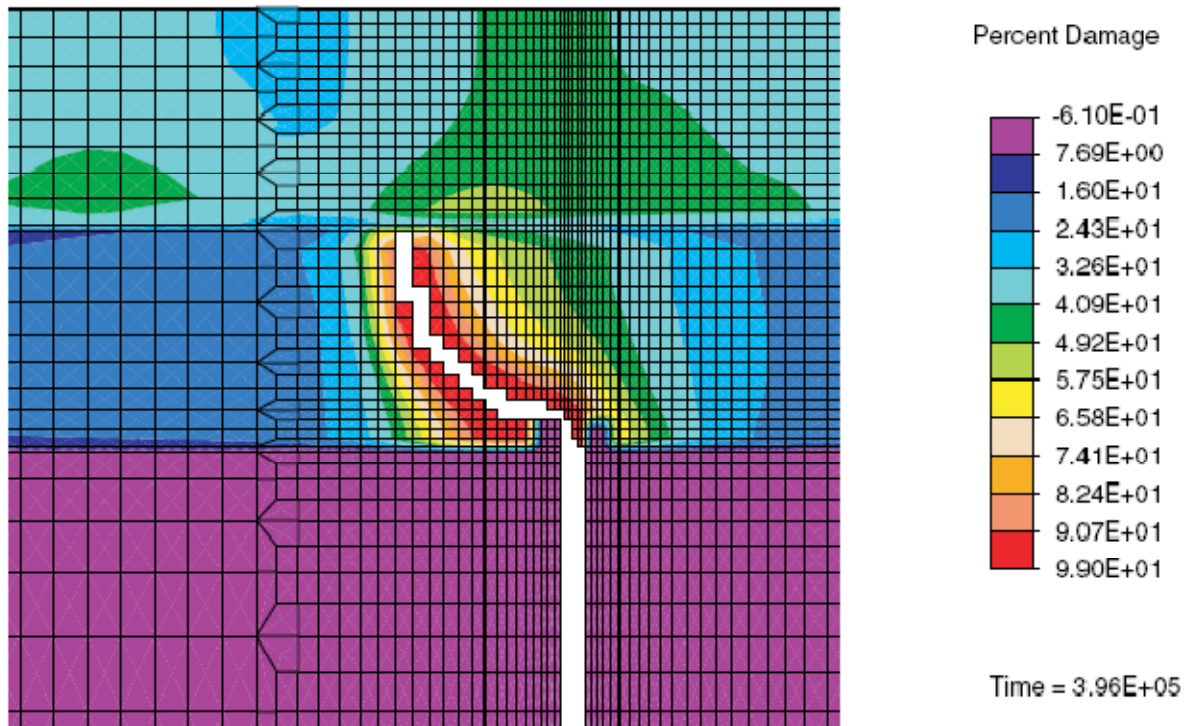


Figure 2.11. Damage field and crack pattern after 396,000 load applications (54).

In addition, Wu (57) also proposed a mechanistic-empirical design procedure against reflection cracking in asphalt concrete overlays. This procedure is intended to be used in routine design and the user is not required to know the inner workings in the FE program. The flow chart of this procedure is displayed in Figure 2.12. As shown in Figure 2.12, the proposed asphalt overlay design procedure depends on the following three models: 1) the statistical critical strain model, 2) the regression model that links the

initial conditions of an asphalt overlay to its crack through time N_{CDM} , and 3) the model for calculating the shift factor C accounting for traffic wander, aging, etc. The first model involves extensive linear elastic FE analyses. The second model requires the use of the first model as well as collecting damage evolution law parameters for typical asphalt concrete mixes and running FE simulation with non-local CDM constitutive model for thousands of overlay structures. The third model requires the use of the first two models as well as collecting extensive field performance data. Wu (57) just established the first statistical critical strain model. The other two models were left for future study.

In general, the non-local CDM reflection cracking model, similar to the CCM discussed previously, is very advanced. Wu's research results (57) demonstrated this promising model to predict reflection cracking in asphalt overlays over existing pavements. However, this non-local CDM model is still under development, and not ready for routine use. Also, the proposed asphalt overlay thickness procedure only considered reflection cracking caused by traffic loading.

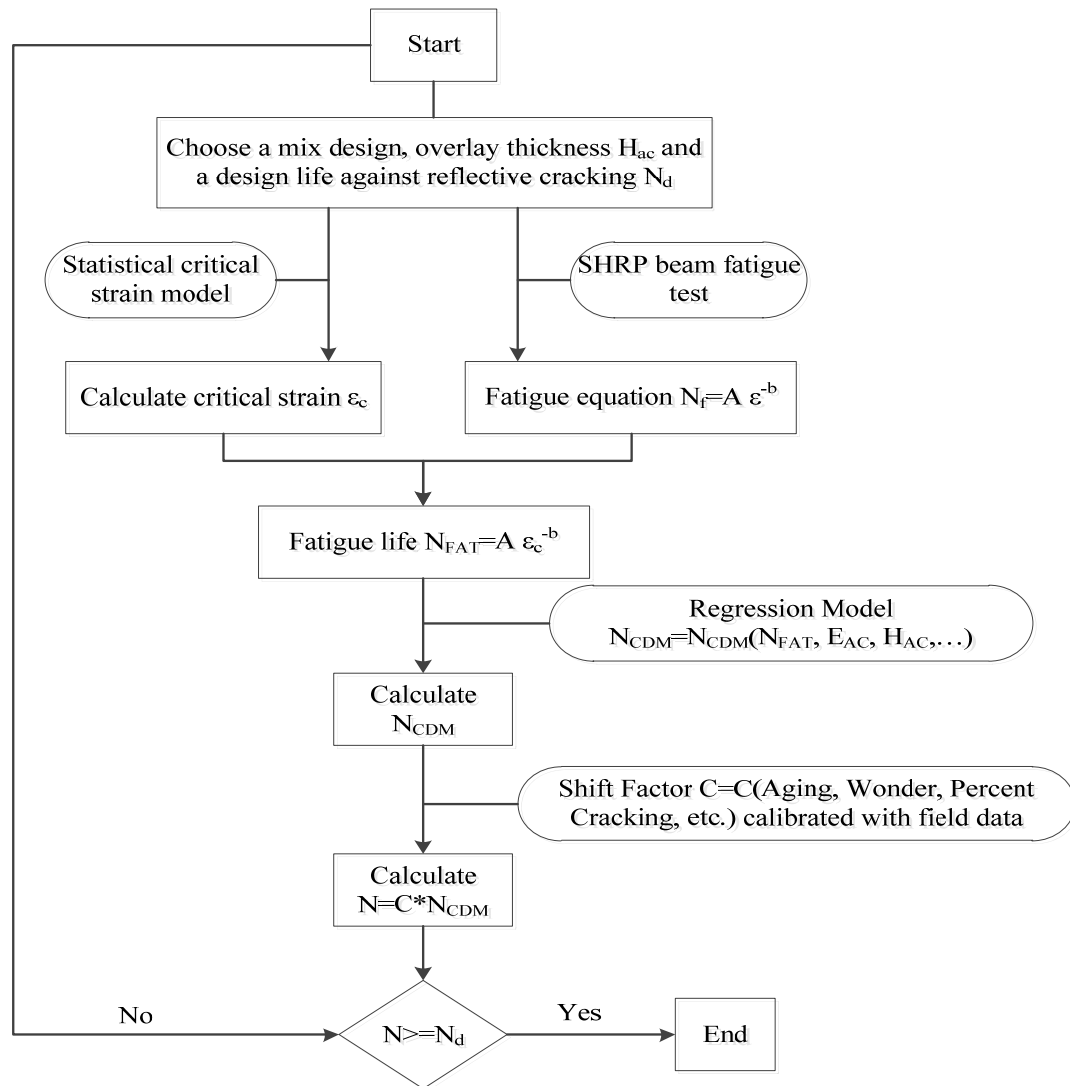


Figure 2.12. Flow chart of the proposed overlay design procedure against reflective cracking (57).

2.3 Reflection Cracking Models Comparison

Table 2.2 presents a simple comparison among the eight types of reflection cracking models based on several parameters, such as the capability of handling the factors of reflection cracking and compatibility with the MEPDG. Obviously, the

empirical approach is the simplest but the most inaccurate approach. The extended multi-layer linear elastic system and the equilibrium equation approaches are not compatible with the MEPDG. The crack band model, cohesive crack/zone model, and non-local continuum damage mechanics model are very advanced models, and the current status of these advanced models is that they are still under development, and not ready for use. Thus, the two types of models that remain are FE plus beam fatigue law and FE plus fracture mechanics. FE plus beam fatigue law model cannot directly consider the three mechanisms of reflection cracking. Also, Wu (57) compared the N_{FAT} (the fatigue life of the asphalt overlay calculated by the fatigue equation) and N_{CDM} (the crack through time of the overlay calculated by FE simulation with an advanced non-local continuum damage mechanics model). A weak relationship was found between N_{FAT} and N_{CDM} . This result indicates the necessity and importance of considering crack propagation. Compared to the empirical and FE plus beam fatigue law approaches, the FE plus fracture mechanics approach is not too complicated. Furthermore, the FE plus fracture mechanics approach has been successfully employed to accurately predict reflection cracking of asphalt overlays by different researchers, and is fully compatible with the MEPDG. Thus, the FE plus fracture mechanics approach is expected to produce the most useful results, and was the available model judged to be the most likely to successfully achieve the objectives of this research.

Table 2.2. Comparison of reflection cracking modeling approaches.

Model	Development status	Crack Propagation Mechanisms			Combined Mechanisms	Crack Prediction Method			Predicted Distress				Compatible with MEPDG	
		Thermal	Bending	Shearing		Fracture Mechanics	Phenomenological (beam) fatigue law	Empirical	Area		Severity		Yes	No
					Time				Traffic	Time	Traffic			
Empirical equation	Finished						√	√						√
Extended Multilayer linear elastic	Finished		√							√				√
Equilibrium equations	Finished	√	√	√				√		√				√
FE + fracture mechanistic	Finished	√	√	√	√	√			√	√		√	√	
FE + beam fatigue law	Finished		√						√				√	
Crack band theory	Under developing	√				√								√

Table 2.2. Continued.

Model	Development status	Crack Propagation Mechanisms			Combined Mechanisms	Crack Prediction Method			Predicted Distress				Compatible with MEPDG	
		Thermal	Bending	Shearing		Fracture Mechanics	Phenomenological (beam) fatigue law	Empirical	Area		Severity		Yes	No
									Time	Traffic	Time	Traffic		
Cohesive cracking model	Under developing		√			√								√
Non-local continuum damage mechanics model	Under developing		√	√		√								√

CHAPTER III

MODEL CHARACTERISTICS AND DEVELOPMENT*

3.1 Introduction

In this chapter, several steps of constructing a reflection cracking predicting program. The steps are briefly described in the text as follows:

- The mechanisms this dissertation use for addressing the crack growth issue are bending, shearing, and thermal stress. Based on these three mechanisms, five numbers of days would be produced.
- Select a sufficient number of overlay sections to provide a good likelihood of having a sufficient amount of good quality data (including sequential distress measurements, pavement structure and materials property data, and traffic and weather data) to permit development of a set of calibrated reflection cracking model coefficients.
- Collect pavement structure data (including layer thickness, construction dates and non-destructive testing data on each pavement section) and the mixture design data for the overlay.

*Reprinted with permission from "Prediction of Reflection Cracking in Hot-Mix Asphalt Overlays," by Fang-Ling Tsai, R. Lytton and S. Lee, Journal of the Transportation Research Board, No. 2155, pp. 43-54, to be published. 2010 TRB

- Collect traffic data on each pavement section including the input data in order to evaluate number of axle load and categorize the traffic load (Note that traffic input is a traffic load spectrum rather than the total 18-kip equivalent single axle loads).
- Develop a method of dealing with different traffic loads and tire footprints for calculating the SIF.
- Collect climatic data on each of the test sections of overlay (including the hourly air temperature, solar radiation, and surface reflectance), and determining the climatic related parameters (such as albedo, absorption, emissivity).
- Collect pavement distress data (including the total length of cracking in the old pavement surface prior to overlay and the lengths and levels of severity of reflection cracking) for at least three, and preferably more sets of sequential observations.
- Develop a program to calculate the viscoelastic thermal stresses in the overlay.
- Develop a finite element mechanistic method for calculating the SIF in overlays for thermal, bending, and shearing traffic stresses as a crack grows up through different thicknesses of overlay.
- Develop a method for accurately calculating the hourly and daily temperatures in an overlay at the current tip of the crack.
- Calculate the stiffness, tensile strength, compliance and fracture coefficients of the overlay mixture using the mixture properties of volumetric contents of the

mixture components, aggregate gradation, and binder master curve characteristics.

- Develop a computational technique for calculating the total crack growth caused by single, tandem, tridem, and quadrem axles passing over a growing crack, and include the healing shift factor that increases with the length of time between traffic loads.
- Develop a numerically accurate and computationally efficient method of predicting the SIF computed by the finite element method.

The work performed in each of the preceding steps for developing the hot mix overlay reflection cracking model would be summarized in the following sections.

3.2 Definition of Three Mechanisms

It is well known that the first effect of existing joints or cracks—stress concentration plays the dominant role in reflection cracking, which means that the basic mechanism causing reflection cracking is stress concentration in the overlay due to the movement in the existing pavements in the vicinity of joints or cracks. This movement may be induced by bending or shearing action resulting from traffic loads or daily and seasonal temperature changes. In fact, any reflection cracking is caused by the combination of these three mechanisms. Every pass of a traffic load induces two shearing plus one bending effect on the HMA overlay (Figure 3.1). Moreover, these bending and shearing stresses are affected by the daily temperature. Thus, the

combination of all three mechanisms is crucial to successfully model reflection cracking. In addition, crack initiation and propagation is also influenced by the existing pavement structure and conditions, reflection cracking countermeasures (e.g. reinforcing, interlayers), HMA mixture properties, the degree of load transfer at joints and cracks, and other factors (Figures 3.2 and 3.3). Therefore, all three mechanisms and these influence factors must be taken into account in the recommended reflection cracking model. However, only limited research has been performed to evaluate and validate these models. Research is needed to address the issues associated with reflection cracking and to identify or develop mechanics-based models for use in mechanistic-empirical procedures for the analysis and design of HMA overlays. The objective of this dissertation is to identify or develop mechanics-based models for predicting reflection cracking in HMA overlays of flexible and rigid pavements and associated computational software for use in mechanistic-empirical procedures for overlay design and analysis.

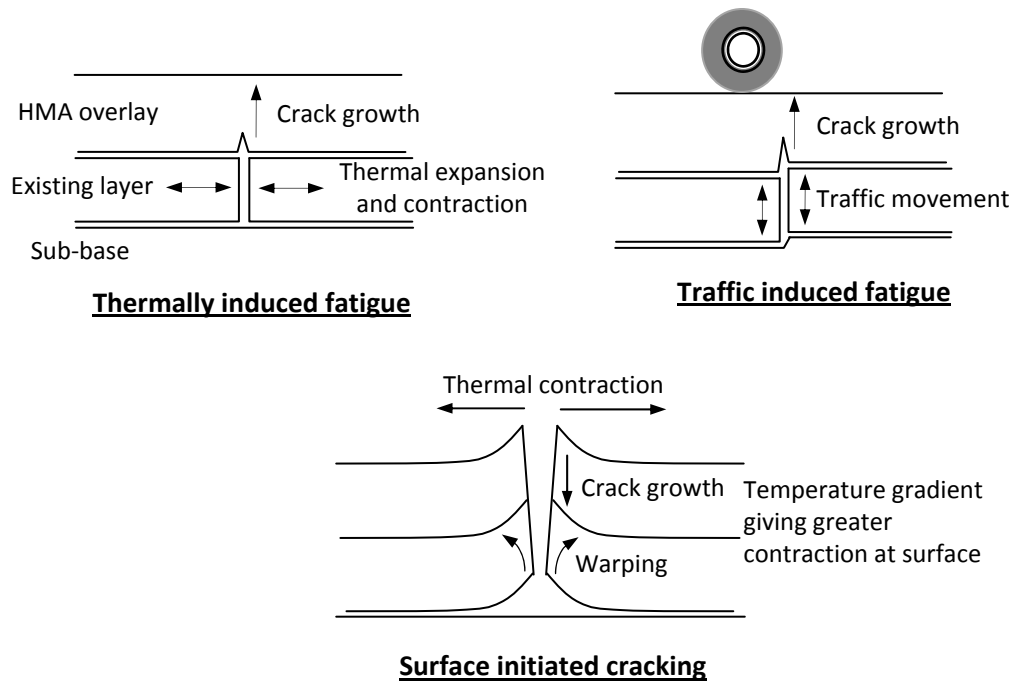


Figure 3.1. Mechanisms of reflection cracking (6).

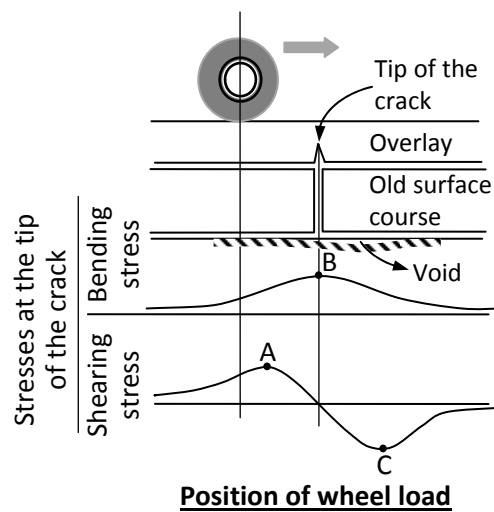


Figure 3.2. Bending and shear mechanisms (7).

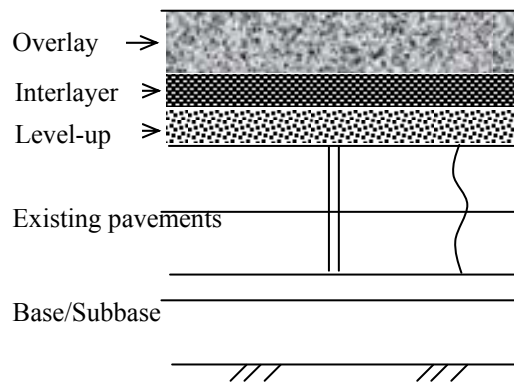


Figure 3.3. Sketch of an asphalt overlay system.

3.3 Pavement Structure Data Collection

After a thorough review of the data available from the LTPP (Long Term Pavement Performance) database (36) and for test sections in New York and Texas, the researchers concluded that there is sufficient data of high enough quality to develop sets of calibration coefficients for the reflection cracking model for each major climatic zone in the United States. Data were collected for a total of 11 pavement-structure-overlay-climatic zone sets representing 411 overlay sections, as shown in Table 3.1.

The LTPP overlay sections provided the bulk of the data that were used for modeling reflection cracking in the different types of pavement structure (36). The distribution of these sections within the different climatic zones is given in Table 3.2.

Table 3.1. Overlay sections for model development.

Data Set	Pavement Structure ¹	No. of Test Sections	Climatic Zone ²
1	AC/mill/AC OL ⁴	62	WF
2	AC/mill/AC OL	47	WNF
3	JCP/AC OL ⁴	69	WF
4	AC/AC OL	59	WF
5	AC/AC OL	33	WNF
6	AC/SAMI/AC OL ⁴	26	WF
7	CRC/AC OL ⁴	21	WF
8	AC/AC OL	16	DF
9	AC/mill/AC OL	16	DNF
10	AC/SAMI/AC OL	12	WNF
11	AC/Grid/AC OL ⁴	50	NY, Texas ³
Totals		411	

¹ The abbreviations are listed in order from the old pavement surface layer upward to the overlay.

² WF, DF, WNF, and DNF designate Wet-Freeze, Dry Freeze, Wet-No Freeze, and Dry-No Freeze, respectively.

³ The overlay test sections in Texas and New York City contributed high quality data and the unique feature of having the overlays reinforced by geosynthetic interlayers.

⁴ AC = existing HMA surface layer, JCP = jointed concrete pavement, CRC = continuously reinforced concrete surface layer, Mill = old surface layer was milled before the overlay was placed, SAMI = (Strain Absorbing Membrane Interlayer) indicates that a compliant interlayer was placed between the old surface layer and the hot mix overlay. Grid a reinforcing interlayer was placed between a leveling course and the hot mix overlay, and AC OL = hot mix asphalt overlay.

Table 3.2. LTPP test sections used for calibration.

Pavement-Overlay Structure	Description	Total Test Sections	No. of Test Sections at Each Climatic Zone			
			WF	DF	WNF	DNF
AC/AC OL	AC, then AC overlay	108	59	16	33	-
AC/Mill/AC OL	AC, then Mill+AC overlay	125	62	-	47	16
CRC/AC OL	CRC, then AC overlay	21	21	-	-	-
JRC/AC + JPC/AC OL	JRC or JPC, then AC overlay	69	69	-	-	-
AC/SC or FC/AC OL	AC, then seal coat or friction course +AC overlay	38	26	-	12	-
Total		361	237	16	92	16

The pavement data used were the layer thickness of each pavement layer and the Falling Weight Deflectometer (FWD) data for each test section prior to the placement of the overlay including the temperature at which the FWD data were obtained. The layer moduli of the old pavement were backcalculated using the program MODULUS (58). The LTPP data included the deflections measured at many equally spaced locations within each test section (36). The means of the backcalculated moduli for each layer was used as the modulus of that layer for the entire test section.

In addition to the layer thickness and the backcalculated moduli of the old pavement, the mixture design data of the overlay was available, including the volumetric composition of the HMA mixture, the gradation of the aggregate, and some indication of the grade of the asphalt binder. The grade was used to determine the six characteristics of the master curve of the binder according to the CAM model (the glassy shear modulus, G_g , the crossover frequency, ω_R , the rheological index, R , the defining temperature, T_d , and the two time-temperature shift coefficients, C_1 and C_2). These six properties of the master curve of extracted binders were measured in SHRP studies and are tabulated (4). This information was used together with the calculated temperature to determine the input to the ANN (Artificial Neural Network) models of Witczak's 1999 (2) and 2006 (3) models of the complex modulus. In these dissertation, there are two way to determine G_g according to input information. The detail of determining G_g and complex modulus is described in Section 3.12.2.

3.4 Categorization of Traffic Loads

Traffic data is a key element for the design and analysis of a HMA overlay structure as well as new pavement construction. For compatibility with the MEPDG, traffic was described by the actual load distribution (spectrum) for each axle type (single, tandem, tridem, or quad axle) for each vehicle (truck) class or number of tires (single or dual).

The daily traffic distribution data was determined based on the traffic data collected in the field over the years. However, it was found that some sections did not have enough field data to determine the traffic characteristics, while others had complete historical traffic data. In order to consider the level of collected traffic data, a hierarchical approach was adopted in the MEPDG and also is used in this project. The three levels were defined based on the availability of collected traffic data and Weigh-In-Motion (WIM) data which is used to determine the normalized axle load distribution for each axle and vehicle types (59):

Level 1: Very good knowledge of past and future traffic characteristics and site/segment specific WIM data,

Level 2: Modest knowledge of past and future traffic characteristics and regional default summaries WIM data, and

Level 3: Poor knowledge of past and future traffic characteristics and national default summaries WIM data or only Average Annual Daily Truck Traffic (AADTT) available.

In order to analyze traffic load effects for reflection cracking, annual number of axle loads for each vehicle class and axle type is entered in the analysis process. The number of axle loads can be determined using the traffic load categorized based on the FHWA vehicle class, the axle type, and the number of tires. The details are described in subsections.

3.4.1 Classification of Vehicles

FHWA defines vehicles into 13 classes depending on whether they carry passenger or commodities. Non-passenger vehicle which are from class 4 to class 13 are divided by the number of axles and the trailer units (60). While bus (vehicle class 4) is a passenger vehicle, the term truck traffic is assumed to include both trucks and buses since the proportion of buses in the traffic flow is relatively small (60). Table 3.3 presents the FHWA vehicle classification.

It is noted that since the light axle load groups, such as vehicle classes 1 to 3, do not have significant effects regarding load related distresses, the traffic analysis in this study took into account heavier load groups in which vehicle classes 4 to 13 are included.

3.4.2 Axle Load Distribution Factor

The axle load distribution is defined as the classification of traffic loading in terms of the number of load applications by each axle type (single, tandem, tridem, or quadrem) within a given range of axle load. The axle load distribution factor is the percentage of the total axle application in each load interval by an axle type for a

specific vehicle class (classes 4 to 13) (59, 61). The load intervals for each axle types are represented in Table 3.4.

The determination of the axle load distribution requires WIM data which is the number of axles measured within each axle load range by axle types of each vehicle class. In the LTPP (Long Term Pavement Performance) guideline (36), it is noted that the vehicle axle weights should be collected using WIM sensor by vehicle classes, type of axle, and axle load intervals. Using measured WIM data, the distribution is calculated by the average of the number of axles measured within each load interval of an axle type for a vehicle class divided by the total number of axles for all load intervals for a given vehicle class. The normalized axle load distribution factors are total 100 for each axle type within each truck class. Table 3.5 presents an example of FHWA W-4 Truck Weight Tables in which WIM data are typically reported for vehicle classes 4, 5, 6, and 7 for the LTPP test section in Tippecanoe, Maryland (2004). Also, Figure 3.4 shows the annual normalized single axle load distribution calculated using the data in Table 3.5.

Table 3.3. FHWA vehicle classification.










Vehicle Class	Schema	Description
4		Buses
5		Two-axle, single-unit trucks
6		Three-axle single-unit trucks
7		Four- or more than four-axle single-unit trucks
8		Four- or less than four-axle single trailer trucks
9		Five-axle single trailer trucks
10		Six- or more than six-axle single trailer trucks
11		Five- or less than five-axle multi-trailer trucks
12		Six-axle multi-trailer trucks
13	—	Seven- or more than seven-axle multi-trailer trucks

Table 3.4. Load intervals for each axle type.

Axle Type	Axle Load Interval
Single Axles	3,000 ~ 40,000 lb. at 1,000 lb. intervals
Tandem Axles	6,000 ~ 80,000 lb. at 2,000 lb. intervals
Tridem Axles	12,000 ~ 102,000 lb. at 3,000 lb. intervals
Quadrem Axles	

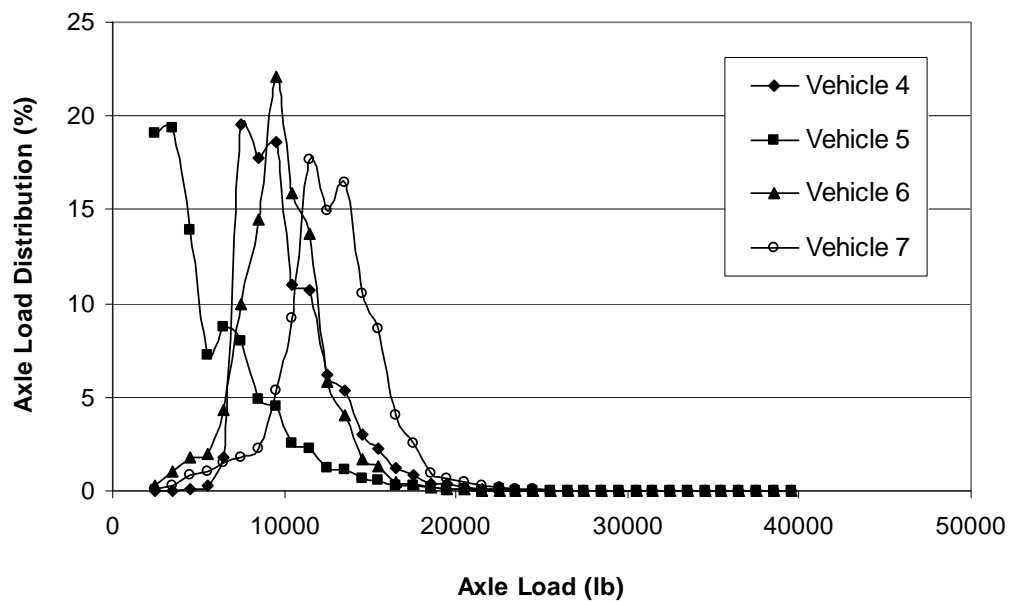


Figure 3.4. Annual normalized single axle load distribution for vehicle class 4 to 7 (LTPP section in Tippecanoe, Maryland 2004).

Table 3.5. Number of single axle loads for vehicle class 4 to 7 (LTPP section at Tippecanoe, Maryland in 2004).

Axle Load (lb.)	Vehicle Class			
	4	5	6	7
3,000	0	53,818	183	11
4,000	10	54,606	558	52
5,000	42	39,113	993	139
6,000	175	20,289	1,099	168
7,000	988	24,555	2,426	252
8,000	10,687	22,491	5,617	298
9,000	9,713	13,719	8,154	365
10,000	10,156	12,839	12,423	879
11,000	6,011	7,127	8,945	1,516
12,000	5,875	6,413	7,725	2,913
13,000	3,409	3,511	3,257	2,464
14,000	2,947	3,128	2,289	2,710
15,000	1,640	1,756	975	1,740
16,000	1,239	1,513	725	1,419
17,000	679	834	285	664
18,000	446	800	235	423
19,000	212	424	104	159
20,000	181	360	73	111
21,000	106	261	44	70
22,000	51	131	22	46

Table 3.5. Continued.

Axle Load (lb.)	Vehicle Class			
	4	5	6	7
23,000	41	135	6	26
24,000	21	85	4	9
25,000	24	90	3	12
26,000	11	43	1	7
27,000	4	33	1	2
28,000	1	12	3	1
29,000	4	25	0	1
30,000	3	13	0	0
31,000	1	16	2	0
32,000	2	8	0	0
33,000	0	5	0	0
34,000	0	2	1	0
35,000	0	0	0	0
36,000	0	0	0	0
37,000	0	2	0	0
38,000	0	0	0	0
39,000	0	0	0	0
40,000	0	0	0	0
Total	54,679	268,157	56,153	16,457

It is observed that all axles of vehicle classes 4 and 5 and single axle of class 6 and 7 vehicles have single tires while the others have dual tires. Thus, the matrix of vehicle class and axle types can be categorized according to the number of tires. When the steering and non-steering axles are put together in a single axle type, the matrix can be characterized into eight categories based on the vehicle class, the axle type, and the number of tires. The total number of axle loads for each category is used to further determine the axle load distribution factor for the analysis of the traffic load effect on reflection cracking.

Figure 3.5 shows the categorization of traffic load. The categories 1, 3, 5, and 7 have single tires and the categories 2, 4, 6, and 8 have dual tires.

Vehicle Class	Single Axle	Tandem Axle	Tridem Axle	Quad Axle
4	No. 1	No. 3	No. 5	No. 7
5		Single Tire		
6		Dual Tires		
7				
8	No. 2	No. 4	No. 6	No. 8
9				
10				
11				
12				
13				
14				

Figure 3.5. Vehicle class related to axle and tire categories.

3.4.3 Estimation of Annual Number of Axle Loads for Each Category with AADTT

The axle load distribution for each category should be calculated based on the total number of axle loads collected using WIM for each axle type within each vehicle class. However, depending on the level of data collection, some agencies might not have available WIM data to be used for evaluating reflection cracking of an asphalt overlay. In order to facilitate the use of the traffic load categorization for such agencies or Level 3 data input, Annual Average Daily Truck Traffic (AADTT) was adopted to convert it to the number of axle loads for each category.

AADTT is the annualized averaged 24-hour volume of truck traffic passing a given section of highway. The truck traffic in AADTT consists of heavy vehicles from class 4 to 13 in FHWA vehicle classification (62). AADTT is determined based on traffic counts during a given time period which is whole days greater than a day but less than a year and can be calculated simply as follows (63):

$$AADTT = \frac{\text{Number of truck for a giving time}}{\text{Number of days for a giving time}} \quad (3.1)$$

To convert AADTT into the annual number of axle loads for each vehicle and axle type, two truck-traffic adjustment factors are required: normalized vehicle class distribution and number of axles per truck.

3.4.4 Normalized Vehicle Class Distribution

The vehicle (truck) class distribution is the percentage of each vehicle class within the AADTT for the base year, and the sum of normalized distribution factors of all vehicle classes must be 100 (59). The distribution is typically determined using data collected from vehicle classification counting programs such as WIM, AVC (Automatic Vehicle Classifier), or vehicle counts. Depending on inputs at different levels, the data can be obtained from a specific site, region/statewide, or national WIM, AVC, or vehicle counts. In this study, default vehicle class distribution factor is provided, which is determined using the entire LTPP traffic data (36). The default value was obtained from the principal arterials in the roadway function class and the major multi-trailer truck route in Truck Traffic Classification (TTC) as shown in Table 3.6 (59).

The annual number of trucks for each vehicle class within a base year can be calculated as follows:

$$ANT_k = AADTT \times 365(\text{day}) \times NTP_k \quad (3.2)$$

where

k = a specific vehicle class (class 4 to 13)

ANT_k = annual number of trucks for a vehicle class, k

NTP_k = normalized vehicle class distribution percentage for a truck class, k

In calculating the number of trucks for each vehicle, the normalized truck class distribution factors are assumed to be constant from year to year or across the time of day.

Table 3.6. Normalized vehicle class distribution factor.

Vehicle Class	Distribution Factor (%)
4	1.8
5	24.6
6	7.6
7	0.5
8	5.0
9	31.3
10	9.8
11	0.8
12	3.3
13	15.3

3.4.5 Number of Axle Types per Vehicle

The number of axle types per vehicle is the average number of individual axles for each vehicle class for each axle type (single, tandem, tridem, and quadrem). This number of axles is different from the number of axles for each vehicle as shown in Table 3.7. The latter values in Table 3.7 are the typical number of axles for each vehicle based on each vehicle schema, while the former is the calculated values using WIM data measured over time. The number of axle types per truck class can be determined by

dividing the total number of a specific axle type measured for a truck class by the total number of trucks in that class.

Table 3.8 presents default values of the number of axle type per truck class which is estimated based on LTPP traffic data (59).

Using the number of axles for each vehicle and the total number of trucks for each vehicle class (ANT_k) calculated previously, the number of axle loads for each axle type and vehicle class within a year can be calculated as follows:

$$NA_{ka} = ANT_k \times NAT_{ka} \quad (3.3)$$

where

- a = a specific axle type (single, tandem, tridem, or quad)
- NA_{ka} = annual number of axle loads for a axle type under a vehicle class
- NAT_{ka} = average number of axles by axle type for each truck class

For example, when the AADTT of an asphalt overlay section is 1500, ANT_k and NA_{ka} could be calculated, using the default values in Table 3.6 and Table 3.8, as shown in Table 3.9. From the result of Table 3.9, the axle load for each category of the section having 1,500 AADTT within a year can be determined as follows:

- Category 1: $15,965 + 269,370 + 42,442 + 2,738 = 330,515$
- Category 2: $65,153 + 193,645 + 63,849 + 18,790 + 63,598 + 180,100 = 585,135$
- Category 3: 3,843

- Category 4: $41,194 + 712 + 18,341 + 330,739 + 58,484 + 1,139 + 20,597 + 178,425 = 649,631$
- Category 5: 0
- Category 6: $2,272 + 47,753 + 263 + 1,084 + 29,319 = 60,691$
- Category 7: 0
- Category 8: 0

Table 3.7. Number of axles for each vehicle class.

Vehicle Class	Number of Axles			
	Single	Tandem	Tridem	Quadrem
4	1	1		
5	2 (1)*			
6	1	1		
7	1		1	
8	3 (2)			
9	1	2		
10	1	1	1	
11	5 (4)			
12	4 (3)	1		
13	3 (2)	2		

* () is the number of non-steering single axle

Table 3.8. Average number of axles for each vehicle.

Vehicle Class	Single Axle	Tandem Axle	Tridem Axle	Quadrem Axle
4	1.62	0.39	0.00	0.00
5	2.00	0.00	0.00	0.00
6	1.02	0.99	0.00	0.00
7	1.00	0.26	0.83	0.00
8	2.38	0.67	0.00	0.00
9	1.13	1.93	0.00	0.00
10	1.19	1.09	0.89	0.00
11	4.29	0.26	0.06	0.00
12	3.52	1.14	0.06	0.00
13	2.15	2.13	0.35	0.00

Table 3.9. Results of number of axle loads for a section with AADTT = 1,500.

Vehicle Class (k)	No. of Vehicles (ANT_k)	Number of Axle Loads (NA_{ka})			
		Single Axle	Tandem Axle	Tridem Axle	Quadrem Axle
4	9,855	15,965	3,843	0	0
5	134,685	269,370	0	0	0
6	41,610	42,442	41,194	0	0
7	2,738	2,738	712	2,272	0
8	27,375	65,153	18,341	0	0
9	171,368	193,645	330,739	0	0
10	53,655	63,849	58,484	47,753	0
11	4,380	18,790	1,139	263	0
12	18,068	63,598	20,597	1,084	0
13	83,768	180,100	178,425	29,319	0

The results calculated using AADTT should be used for the sections where WIM data is not available since the number of axle loads calculated from WIM data provides more accurate data than that estimated from AADTT.

3.5 Tire Patch Length and Cumulative Axle Load Distribution

In order to analyze the traffic load effect for reflection cracking, the length of the tire patch was used to evaluate bending or shearing stress in asphalt overlay. Also, cumulative axle load distribution on tire length for each category should be determined based on collected traffic data such as WIM or AADTT.

3.5.1 Tire Patch Length

Existing practice for the evaluation of tire load effects on pavements assumes that the shape of the contact tire patch is a circle with an area which is equal to the ratio of the tire load over the tire pressure. However, a rectangular shape of tire contact area is closer to the real shape of the tire applied to pavement surface (64). Therefore, the model tire load using the rectangular tire contact area, as shown in Figure 3.6, was used to evaluate the effect of tire load on reflection cracking since the assumption can provide reasonable analysis of pavement response to tire loads.

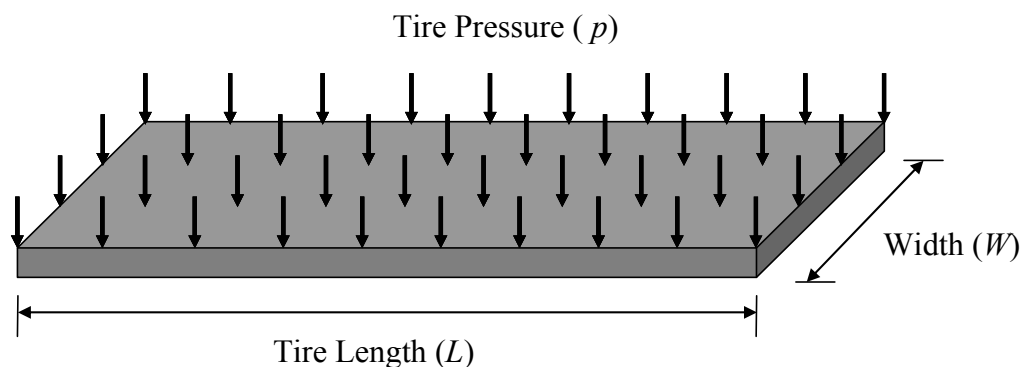


Figure 3.6. Tire load applied to pavement surface.

Tire patch length would be variable for each traffic category (vehicle class and axle type) and under different tire pressure while tire width is constant. Thus, the tire length should be calculated based on the tire pressure and width and the axle load of each vehicle class as follows:

$$\begin{aligned} \text{Tire Length (in)} &= \frac{\text{Tire load (lb)}}{\text{Tire pressure (lb/in}^2\text{)} \times \text{Tire width (in)}} \\ &= \frac{\text{Axle load (lb) / No. of tires}}{\text{Tire pressure (lb/in}^2\text{)} \times \text{Tire width (in)}} \end{aligned} \quad (3.4)$$

3.5.2 Determination of Cumulative Axle Load Distribution on Tire Length

It may be difficult to employ each tire length for axle load intervals to evaluate traffic load effects on propagation of reflection cracking. Therefore, the axle load distribution on tire length for each category was used for the evaluation of traffic load, instead of the axle load distribution on axle load mentioned previously. To convert the axle load distribution on load interval into on tire length, tire length for each load interval was determined based on the characteristics of each axle type as presented in Table 3.10.

The tire patch lengths for corresponding axle load intervals for each category could be calculated using Equation 3.4 and the characteristics of axle types. Table 3.10 lists the calculated tire lengths on axle load intervals for all traffic categories. The tire patch length increment in Table 3.11 should be used for the x -axis on the axle load distribution of the tire patch length.

Table 3.10. Typical characteristics for each axle type.

Category	Axle Type	Tires	Tire width (in.)	Tire Pressure (PSI)	Axle Load Interval (lb.)
1	Single	Single	7.874	40 (< 6,000 lb)	3,000 ~ 40,000 lb. at 1,000 lb intervals
2		Dual	8.740	120 (> 6,000 lb)	
3	Tandem	Single	7.874	120	6,000 ~ 80,000 lb. at 2,000 lb intervals
4		Dual	8.740	120	
5	Tridem	Single	7.874	120	12,000 ~ 102,000 lb at 3,000 lb intervals
6		Dual	8.740	120	
7	Quad	Single	7.874	120	12,000 ~ 102,000 lb at 3,000 lb intervals
8		Dual	8.740	120	

Using the tire patch length and collected traffic data, cumulative axle load distribution can be determined for each category. Figure 3.7 is the diagram illustrating the procedure for determining tire length and the cumulative axle load distribution of each category. The cumulative axle load distribution on tire length should be produced for all eight-categories to account for all types of vehicle and axles.

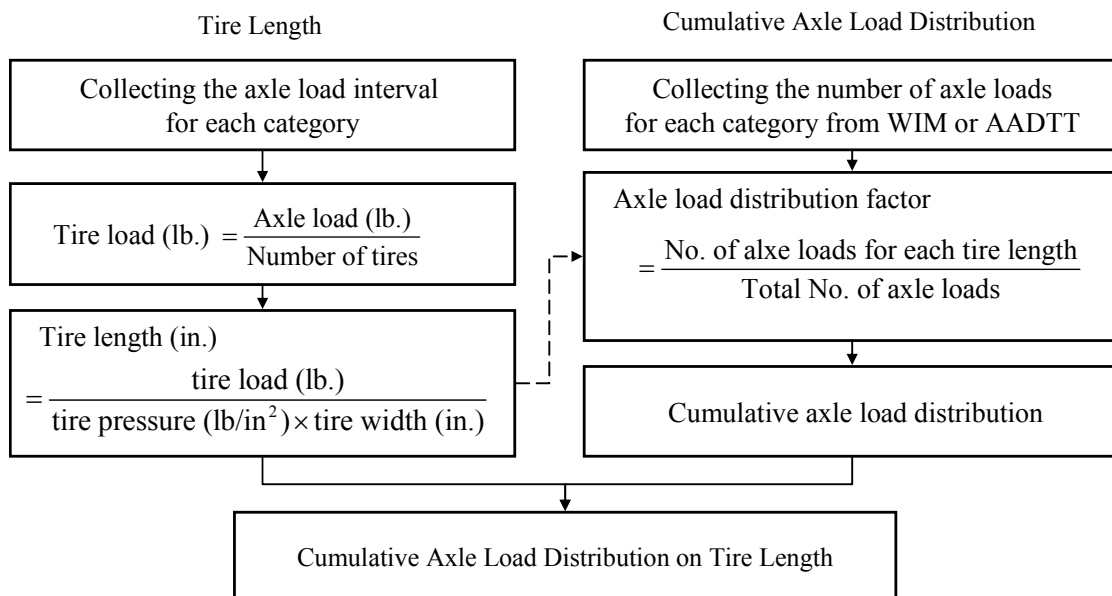


Figure 3.7. Procedure for determination of cumulative axle load distribution on tire patch length.

Figure 3.8 shows the cumulative axle load distribution for Category 1 of LTPP section Tippecanoe, Maryland, in 2004, which was determined using the data in Table 3.11.

Table 3.11. Tire patch length increment for each load category.

No.	Category							
	1	2	3	4	5	6	7	8
1	3.704	1.669	1.588	0.715	2.117	0.953	1.588	0.715
2	4.233	1.907	2.117	0.953	2.646	1.192	1.984	0.894
3	4.763	2.145	2.646	1.192	3.175	1.430	2.381	1.073
4	5.292	2.384	3.175	1.430	3.704	1.669	2.778	1.251
5	5.821	2.622	3.704	1.669	4.233	1.907	3.175	1.430
6	6.350	2.860	4.233	1.907	4.763	2.145	3.572	1.609
7	6.879	3.099	4.763	2.145	5.292	2.384	3.969	1.788
8	7.408	3.337	5.292	2.384	5.821	2.622	4.366	1.967
9	7.938	3.576	5.821	2.622	6.350	2.860	4.763	2.145
10	8.467	3.814	6.350	2.860	6.879	3.099	5.159	2.324
11	8.996	4.052	6.879	3.099	7.408	3.337	5.556	2.503
12	9.525	4.291	7.408	3.337	7.938	3.576	5.953	2.682
13	10.054	4.529	7.938	3.576	8.467	3.814	6.350	2.860
14	10.583	4.767	8.467	3.814	8.996	4.052	6.747	3.039
15	11.113	5.006	8.996	4.052	9.525	4.291	7.144	3.218
16	11.642	5.244	9.525	4.291	10.054	4.529	7.541	3.397
17	12.171	5.482	10.054	4.529	10.583	4.767	7.938	3.576
18	12.700	5.721	10.583	4.767	11.113	5.006	8.334	3.754
19	13.229	5.959	11.113	5.006	11.642	5.244	8.731	3.933
20	13.758	6.198	11.642	5.244	12.171	5.482	9.128	4.112

Table 3.11. Continued.

No.	Category							
	1	2	3	4	5	6	7	8
21	14.288	6.436	12.171	5.482	12.700	5.721	9.525	4.291
22	14.817	6.674	12.700	5.721	13.229	5.959	9.922	4.469
23	15.346	6.913	13.229	5.959	13.758	6.198	10.319	4.648
24	15.875	7.151	13.758	6.198	14.288	6.436	10.716	4.827
25	16.404	7.389	14.288	6.436	14.817	6.674	11.113	5.006
26	16.933	7.628	14.817	6.674	15.346	6.913	11.509	5.184
27	17.463	7.866	15.346	6.913	15.875	7.151	11.906	5.363
28	17.992	8.105	15.875	7.151	16.404	7.389	12.303	5.542
29	18.521	8.343	16.404	7.389	16.933	7.628	12.700	5.721
30	19.050	8.581	16.933	7.628	17.463	7.866	13.097	5.900
31	19.579	8.820	17.463	7.866	17.992	8.105	13.494	6.078
32	20.108	9.058	17.992	8.105	18.521	8.343	13.891	6.257
33	20.638	9.296	18.521	8.343	19.050	8.581	14.288	6.436
34	21.167	9.535	19.050	8.581	19.579	8.820	14.684	6.615
35	-	-	19.579	8.820	20.108	9.058	15.081	6.793
36	-	-	20.108	9.058	20.638	9.296	15.478	6.972
37	-	-	20.638	9.296	21.167	9.535	15.875	7.151
38	-	-	21.167	9.535	-	-	-	-

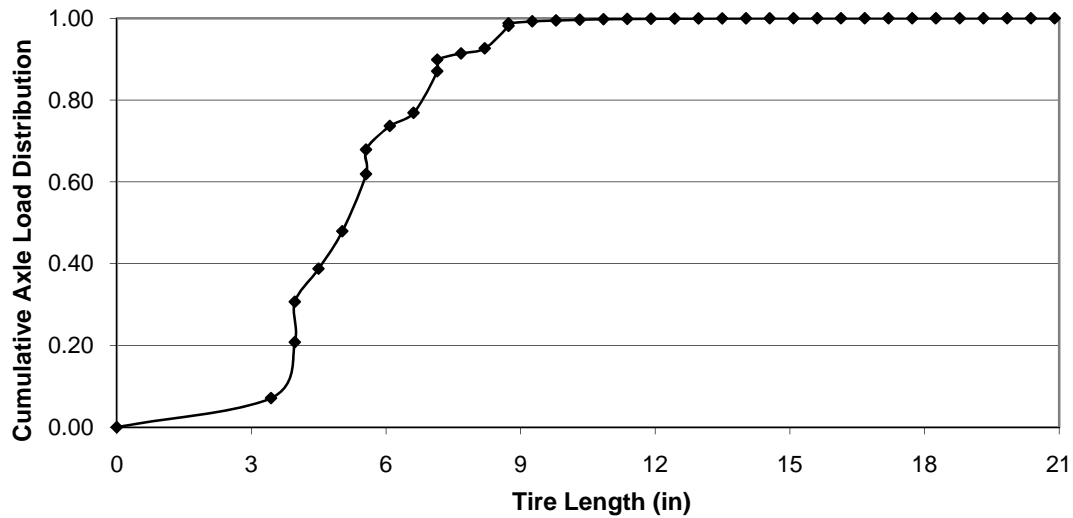


Figure 3.8. Cumulative annual axle load distribution on tire length (category 1 of LTPP section Tippecanoe, Maryland in 2004).

3.5.3 Modeling of Cumulative Axle Load Distribution (CALD)

Since the frequency distribution of each tire length of a category is used to evaluate load effects for reflection cracking propagation in this study, the cumulative axle load distribution for any pavement sections and categories should be developed along with the tire length. It is well known fact that the cumulative axle load distribution on traffic loads or tire length follows a sigmoidal curve having a lower asymptote of zero and a finite upper asymptote as shown in Figure 3.9.

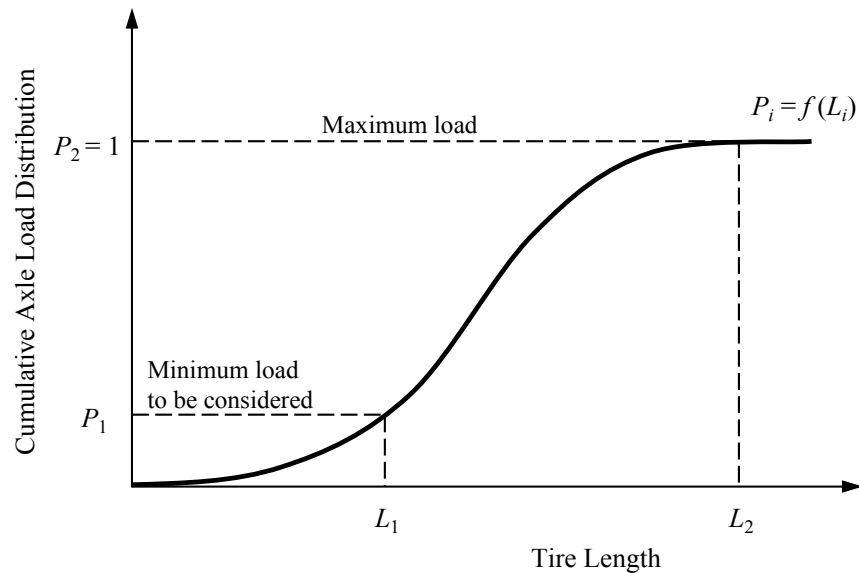


Figure 3.9. Typical cumulative axle load distribution curve.

After searching useful models which can describe the statistical properties of cumulative axle load distribution on tire length, the Gompertz model was chosen as follows:

$$y = \alpha \exp[-\exp(\beta - \gamma x)] \quad (3.5)$$

where

α , β , and γ = model parameters

The Gompertz model can describe cumulative axle load distribution curve successfully since it has a clear physical boundary condition which shows asymptotes at $y = 0$ and $y = \alpha$ and is asymmetric about its inflection point which occurs at β/γ (65).

The parameter α in the model indicates the upper asymptote which is equal to 1.00 (100

percent) for cumulative axle load distribution curve. The parameter β describes how wide the rising portion of the curve is. In addition, the parameter γ indicates the slope of the cumulative axle load distribution curve. Figure 3.10 illustrates a typical curve of the Gompertz model with the explanation of each parameter.

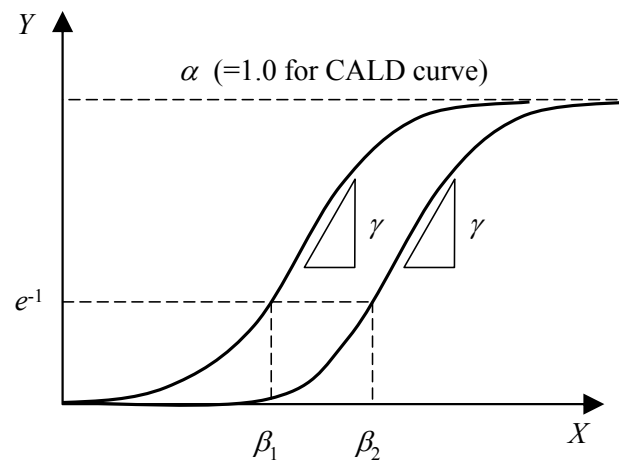


Figure 3.10. Gompertz model curve.

The parameter α should be equal to 1.00 since the cumulative axle load distribution curve has a physical boundary condition ranging from 0 to 1.00 or 0 to 100 percent. Therefore, the modified model for cumulative axle load distribution can be defined as:

$$C(L_i)_j = \exp\left[-\exp(\beta - \gamma L_{ij})\right] \quad (3.6)$$

where

- L_{ij} = i^{th} tire length in tire patch length increment at category j
 $C(L_i)_j$ = cumulative axle load distribution factor at L_i within category j
 β, γ = model parameters describing curve width and slope, respectively

The typical characteristics for each category as presented in Table 3.5 and the collected traffic data from WIM or AADTT in a given section were used to develop the model parameters β and γ in the modified Gompertz model of Equation 3.6. The results presented good data fitting along with relatively high significance. As an example, Table 3.12 presents the developed model parameters β and γ for the category 1 of LTPP section in Tippecanoe, Maryland.

Table 3.12. Model parameters and CALD on tire length (category 1 of LTPP section at Tippecanoe, Maryland in 2004).

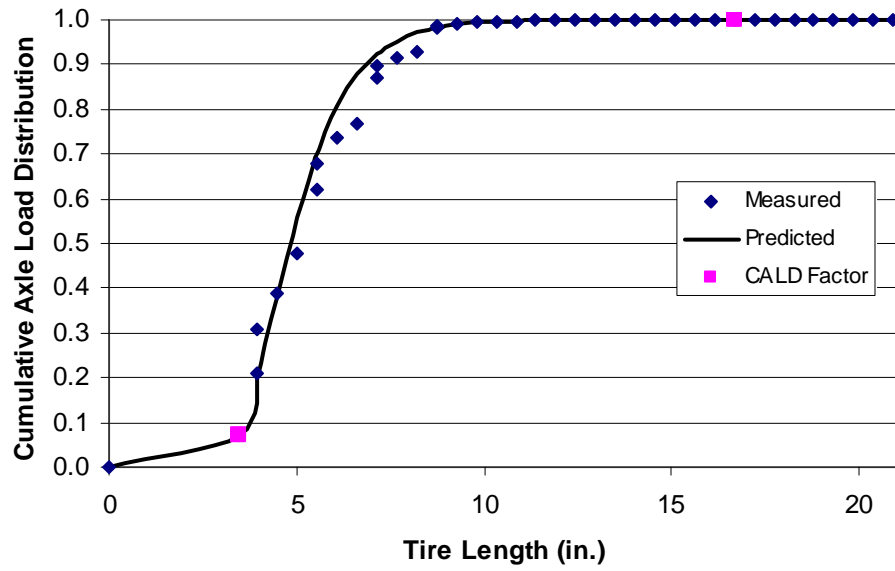
Parameter	Values	CALD Value		Tire Length (in.)	
β	4.301	C_1	0.071	L_1	3.704
γ	0.967	C_2	1.000	L_2	16.933
R^2	0.982				

Figure 3.11 illustrates the model parameters and plots of calibrated cumulative axle load distribution on tire lengths for all categories of this section (Tippecanoe, Maryland).

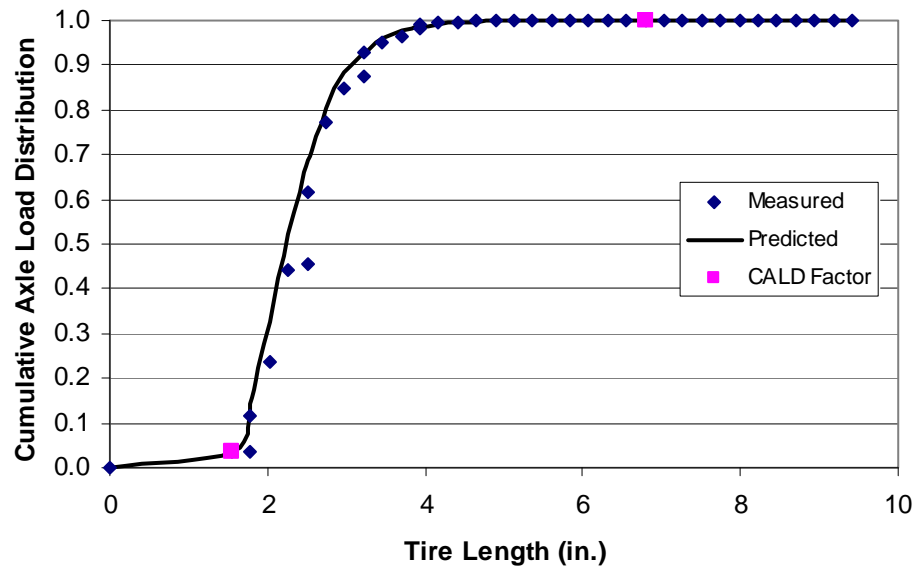
These eight cumulative axle load distributions graphs have been generated with the β and γ model parameters that are found in Table 3.13. Load categories 5 and 7 were missing and this fact is reflected in Table 3.13 which is missing the β and γ values for those two categories of traffic load.

Table 3.13. Model parameters and CALD on tire length of LTPP section at Tippecanoe, Maryland (2004).

Category	Parameter			CALD Value		Tire Length (in.)	
	β	γ	R^2	C_1	C_3	L_1	L_3
1	4.301	0.967	0.982	0.071	1.000	3.440	16.669
2	4.781	2.302	0.977	0.034	1.000	1.549	6.793
3	4.075	1.096	0.948	0.010	1.000	1.323	12.435
4	2.627	1.789	0.934	0.008	1.000	0.596	6.078
5	-	-	-	-	-	-	-
6	2.140	1.215	0.943	0.046	1.000	0.834	8.700
7	-	-	-	-	-	-	-
8	8.384	3.377	0.999	0.001	1.000	0.626	5.810

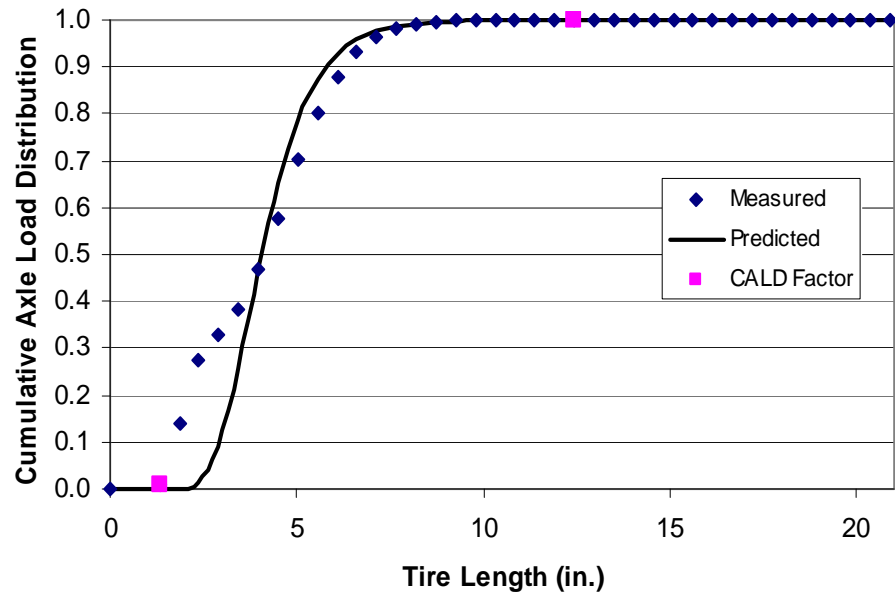


(a) Category 1 (Single axle/single tire)

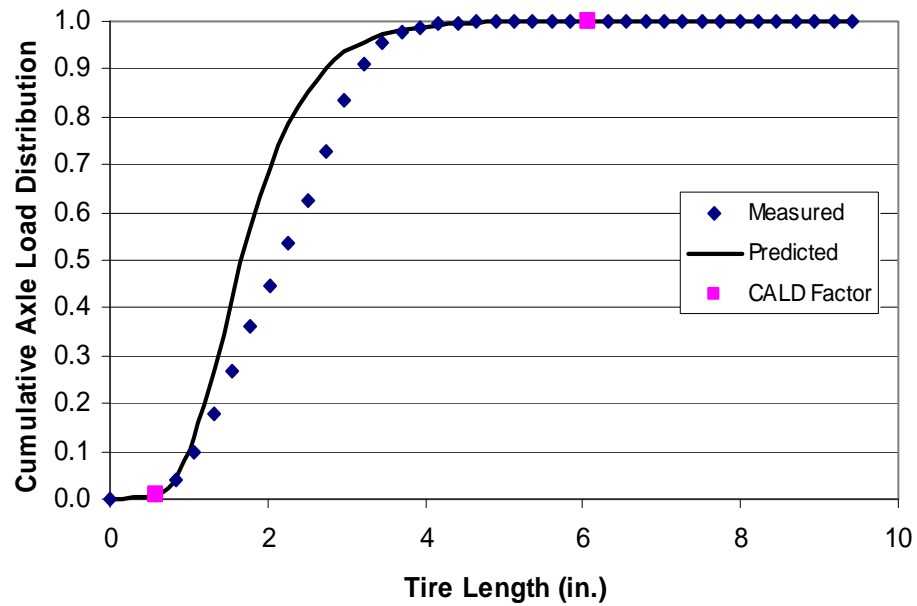


(b) Category 2 (Single axle/dual tires)

Figure 3.11. Cumulative axle load distribution for LTPP section Tippecanoe, Maryland (2004).

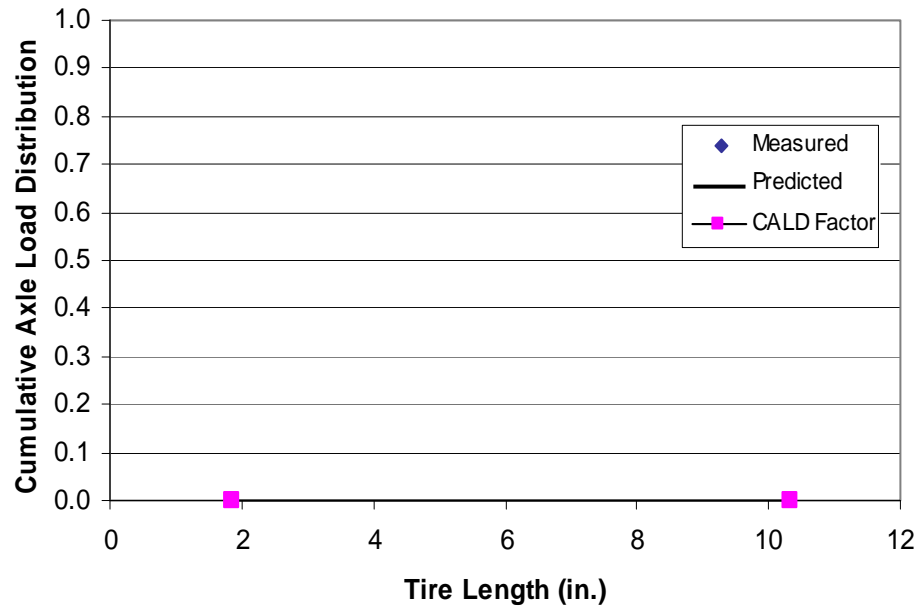


(c) Category 3 (Tandem axle/single tire)

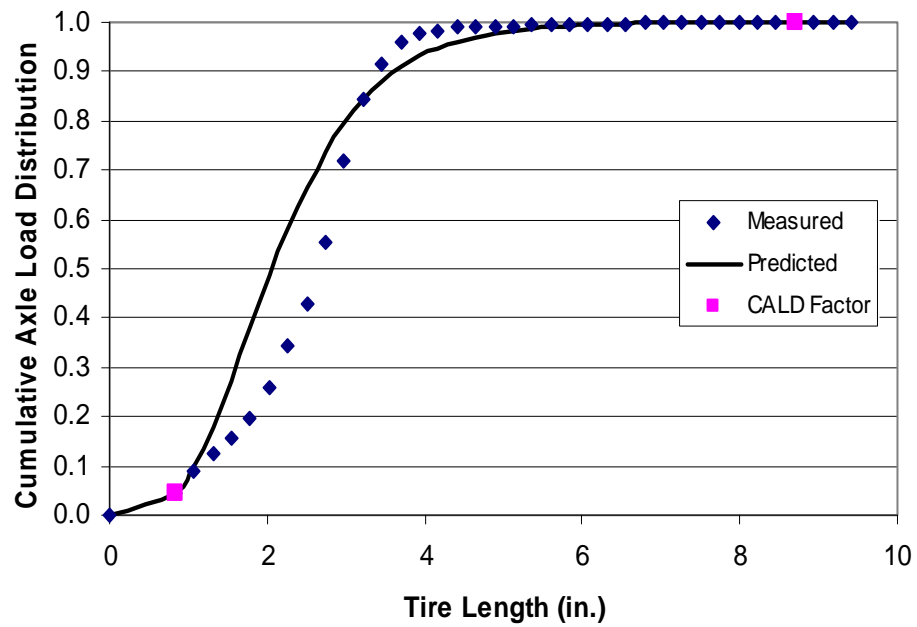


(d) Category 4 (Tandem axle/dual tires)

Figure 3.11. Continued.

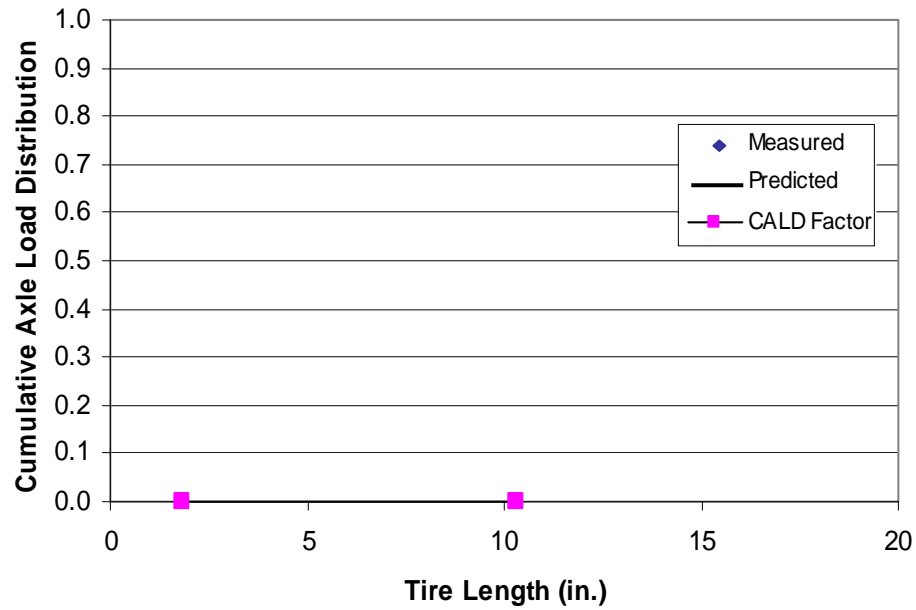


(e) Category 5 (Tridem axle/single tire)

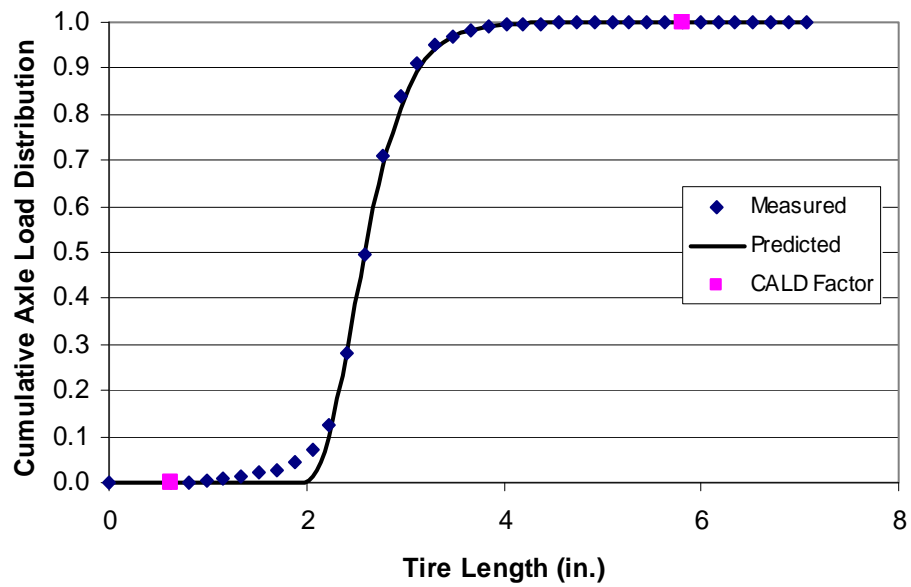


(f) Category 6 (Tridem axle/dual tires)

Figure 3.11. Continued.



(g) Category 7 (Quad axle/single tire)



(h) Category 8 (Quad axle/dual tires)

Figure 3.11. Continued.

The distribution factor C_1 represents the minimum axle load (tire length) to be considered for load related distress. The lower limits of axle load and tire length are presented in Table 3.14. C_2 is the factor at which the cumulative distribution reaches 100 percent first. L_1 and L_2 are tire lengths corresponding to C_1 and C_2 , respectively.

Table 3.14. Minimum values to be considered for load related distress.

Category	Axle Type	Minimum Values	
		Axle load (lb.)	Tire Length (in.)
1	Single	3,000	3.704
2			1.669
3	Tandem	6,000	1.588
4			0.715
5	Tridem	12,000	2.117
6			0.953
7	Quad	12,000	1.588
8			0.715

For Level 1 data inputs, the model parameters for cumulative axle load distribution can be computed using WIM data for each category, while the default values for Level 3 input are provided. The default model parameters, as shown in Table 3.15, were prepared using traffic data from the LTPP database (36). Also, Table 3.16 presents the default cumulative axle load distribution values which were determined based on the default values of the model parameters.

Table 3.15. CALD model parameter default values determined based on LTPP data.

Category	Parameters		R^2
	β	γ	
1	3.44056	0.73836	0.980
2	3.58353	1.61999	0.999
3	1.62387	0.48959	0.972
4	2.03042	1.04234	0.990
5	1.72904	1.10906	0.906
6	1.92533	1.02297	0.982
7	1.47412	0.98443	0.969
8	2.70840	1.48446	0.956

Table 3.16. Default cumulative axle load distribution for each load category.

No.*	Category							
	1	2	3	4	5	6	7	8
1	0.1320	0.0896	0.0971	0.0269	0.5835	0.0754	0.4005	0.0056
2	0.2541	0.1941	0.1654	0.0596	0.7411	0.1318	0.5384	0.0187
3	0.3958	0.3282	0.2494	0.1109	0.8465	0.2044	0.6578	0.0472
4	0.5341	0.4689	0.3424	0.1799	0.9115	0.2882	0.7532	0.0962
5	0.6542	0.5977	0.4373	0.2624	0.9498	0.3772	0.8255	0.1660
6	0.7505	0.7048	0.5281	0.3522	0.9718	0.4658	0.8783	0.2523
7	0.8235	0.7884	0.6110	0.4431	0.9842	0.5496	0.9160	0.3478
8	0.8769	0.8508	0.6837	0.5300	0.9912	0.6256	0.9423	0.4449
9	0.9149	0.8960	0.7457	0.6094	0.9951	0.6924	0.9606	0.5373
10	0.9416	0.9281	0.7973	0.6796	0.9973	0.7497	0.9732	0.6210
11	0.9601	0.9505	0.8396	0.7398	0.9985	0.7979	0.9818	0.6940
12	0.9728	0.9661	0.8738	0.7905	0.9992	0.8379	0.9876	0.7557
13	0.9815	0.9768	0.9011	0.8325	0.9995	0.8706	0.9916	0.8067
14	0.9875	0.9842	0.9228	0.8668	0.9997	0.8971	0.9943	0.8481
15	0.9915	0.9892	0.9399	0.8945	0.9999	0.9184	0.9962	0.8813
16	0.9942	0.9927	0.9533	0.9167	0.9999	0.9355	0.9974	0.9076
17	0.9961	0.9950	0.9637	0.9344	1.0000	0.9491	0.9982	0.9284
18	0.9974	0.9966	0.9719	0.9484	1.0000	0.9599	0.9988	0.9446
19	0.9982	0.9977	0.9782	0.9596	1.0000	0.9684	0.9992	0.9572
20	0.9988	0.9984	0.9832	0.9683	1.0000	0.9752	0.9995	0.9670

Table 3.16. Continued.

No.*	Category							
	1	2	3	4	5	6	7	8
21	0.9992	0.9989	0.9870	0.9752	1.0000	0.9805	0.9996	0.9746
22	0.9994	0.9993	0.9899	0.9806	1.0000	0.9847	0.9997	0.9805
23	0.9996	0.9995	0.9922	0.9848	1.0000	0.9880	0.9998	0.9850
24	0.9997	0.9997	0.9940	0.9882	1.0000	0.9906	0.9999	0.9885
25	0.9998	0.9998	0.9954	0.9907	1.0000	0.9926	0.9999	0.9911
26	0.9999	0.9998	0.9964	0.9928	1.0000	0.9942	0.9999	0.9932
27	0.9999	0.9999	0.9972	0.9944	1.0000	0.9954	1.0000	0.9948
28	0.9999	0.9999	0.9979	0.9956	1.0000	0.9964	1.0000	0.9960
29	1.0000	1.0000	0.9984	0.9966	1.0000	0.9972	1.0000	0.9969
30	1.0000	1.0000	0.9987	0.9973	1.0000	0.9978	1.0000	0.9976
31	1.0000	1.0000	0.9990	0.9979	1.0000	0.9983	1.0000	0.9982
32	1.0000	1.0000	0.9992	0.9984	1.0000	0.9987	1.0000	0.9986
33	1.0000	1.0000	0.9994	0.9987	1.0000	0.9989	1.0000	0.9989
34	1.0000	1.0000	0.9995	0.9990	1.0000	0.9992	1.0000	0.9992
35	-	-	0.9997	0.9992	1.0000	0.9994	1.0000	0.9994
36	-	-	0.9997	0.9994	1.0000	0.9995	1.0000	0.9995
37	-	-	0.9998	0.9995	1.0000	1.0000	1.0000	1.0000
38	-	-	1.0000	1.0000	-	-	-	-

* Number represents the tire patch length increment listed in Table 3.11.

3.6 Determination of Hourly Number of Traffic Load

In order to analyze reflective cracking propagation caused by bending or shearing, hourly number of traffic load should be considered in each of the tire length increments within each traffic category. The number of traffic can be calculated from probability density which is determined based on the cumulative distribution on tire length in each category.

3.6.1 Probability Density on Tire Patch Length

The probability density of tire patch length shows the frequency distribution of each tire length on a category, which is required to determine the number of traffic load during each hour of each day. The number of traffic for the one-hour time period in each day for eight traffic categories and tire length increments is used to calculate bending or shearing stress intensity factor. Also, the hourly number of traffic loads is required to calculate the modulus of the overlay at the tip of the crack for each hour of the day. They should be done before doing any reflective crack growth calculation. The calculation of the hourly number of loads for traffic categories and tire length increments are discussed subsequently in this chapter. The probability density of tire patch lengths for each category can be determined from the cumulative axle load distribution function by differentiating:

$$P(L_j) = \frac{dC(L_j)}{dL_j} \quad (3.7)$$

where

$P(L)_j$ = probability density function within category j

For instance, the probability density function for the category 1 of LTPP section 180901 (Tippecanoe, Maryland) can be determined, as shown in Figure 3.12, based on the cumulative axle load distribution of the section shown in Figure 3.11. The probability densities for all load categories of the LTPP section are showed subsequently. Default probability densities for Level 3 data input, presented in Table 3.17, are provided in the reflection cracking program, which was computed using the LTPP traffic database.

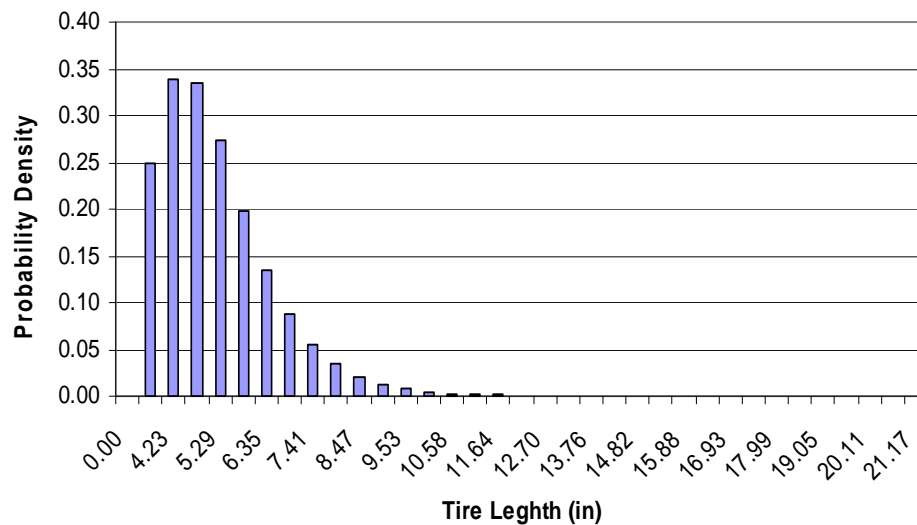


Figure 3.12. Probability density function of tire length (category 1, LTPP section in Tippecanoe, Maryland).

3.6.2 Calculating Hourly Number of Traffic Load

As described previously, since the modulus of the overlay at the tip of the crack and bending or shearing stress intensity factor are calculated at the one-hour time periods in each day, hourly number of traffic loads for each category should be determined. In order to determine the hourly number of traffic load using AADTT or the annual number of axle loads of each category, the hourly truck traffic distribution factors which represent the percentage of traffic within each hour of the day should be determined first. The hourly truck traffic distribution factors can be computed using truck traffic data measured continuously over a 24 hours period of time (59). The reflection crack software provides default values computed from the LTPP traffic database, and the values can be used for Level 3 analysis. The default hourly truck traffic distribution factors are presented in Table 3.18.

Table 3.17. Default probability density for each load category.

No.*	Category							
	1	2	3	4	5	6	7	8
1	0.1974	0.3502	0.1109	0.1014	0.3486	0.1993	0.3608	0.0429
2	0.2570	0.5155	0.1457	0.1753	0.2462	0.2733	0.3282	0.1103
3	0.2709	0.5924	0.1696	0.2542	0.1564	0.3320	0.2713	0.2140
4	0.2473	0.5753	0.1797	0.3216	0.0936	0.3668	0.2102	0.3344
5	0.2050	0.4984	0.1771	0.3659	0.0543	0.3762	0.1558	0.4426
6	0.1591	0.3994	0.1651	0.3831	0.0309	0.3640	0.1122	0.5158
7	0.1181	0.3037	0.1474	0.3759	0.0174	0.3365	0.0792	0.5453
8	0.0851	0.2227	0.1273	0.3508	0.0097	0.3002	0.0551	0.5349
9	0.0601	0.1594	0.1071	0.3146	0.0054	0.2604	0.0380	0.4954
10	0.0418	0.1122	0.0884	0.2736	0.0030	0.2209	0.0260	0.4392
11	0.0289	0.0781	0.0719	0.2324	0.0017	0.1842	0.0178	0.3763
12	0.0198	0.0540	0.0577	0.1937	0.0009	0.1516	0.0121	0.3143
13	0.0135	0.0371	0.0459	0.1591	0.0005	0.1234	0.0082	0.2573
14	0.0092	0.0254	0.0363	0.1292	0.0003	0.0997	0.0056	0.2074
15	0.0062	0.0174	0.0285	0.1040	0.0002	0.0800	0.0038	0.1653
16	0.0042	0.0118	0.0223	0.0831	0.0001	0.0638	0.0026	0.1306
17	0.0029	0.0081	0.0174	0.0661	0.0000	0.0507	0.0017	0.1024
18	0.0019	0.0055	0.0136	0.0523	0.0000	0.0402	0.0012	0.0799
19	0.0013	0.0037	0.0105	0.0413	0.0000	0.0318	0.0008	0.0621

* Number represents the tire patch length increment listed in Table 3.11.

Table 3.17. Ccontinued.

No.*	Category							
	1	2	3	4	5	6	7	8
20	0.0009	0.0025	0.0082	0.0325	0.0000	0.0251	0.0005	0.0481
21	0.0006	0.0017	0.0063	0.0255	0.0000	0.0198	0.0004	0.0372
22	0.0004	0.0012	0.0049	0.0200	0.0000	0.0156	0.0002	0.0287
23	0.0003	0.0008	0.0038	0.0157	0.0000	0.0122	0.0002	0.0221
24	0.0002	0.0005	0.0029	0.0123	0.0000	0.0096	0.0001	0.0170
25	0.0001	0.0004	0.0023	0.0096	0.0000	0.0075	0.0001	0.0131
26	0.0001	0.0003	0.0018	0.0075	0.0000	0.0059	0.0001	0.0101
27	0.0001	0.0002	0.0014	0.0059	0.0000	0.0046	0.0000	0.0077
28	0.0000	0.0001	0.0010	0.0046	0.0000	0.0036	0.0000	0.0059
29	0.0000	0.0001	0.0008	0.0036	0.0000	0.0029	0.0000	0.0046
30	0.0000	0.0001	0.0006	0.0028	0.0000	0.0022	0.0000	0.0035
31	0.0000	0.0000	0.0005	0.0022	0.0000	0.0018	0.0000	0.0027
32	0.0000	0.0000	0.0004	0.0017	0.0000	0.0014	0.0000	0.0021
33	0.0000	0.0000	0.0003	0.0013	0.0000	0.0011	0.0000	0.0016
34	0.0000	0.0000	0.0002	0.0010	0.0000	0.0008	0.0000	0.0012
35			0.0002	0.0008	0.0000	0.0007	0.0000	0.0008
36			0.0001	0.0005	0.0000	0.0004	0.0000	0.0005
37			0.0001	0.0004	0.0000	0.0000	0.0000	0.0000
38			0.0000	0.0000				

*Number represents the tire patch length increment listed in Table 3.11.

Table 3.18. Default hourly truck traffic distribution values (59).

Time Period	Distribution (%)	Time Period	Distribution (%)
12:00AM – 1:00AM	2.3	12:00PM – 1:00PM	5.9
1:00AM – 2:00AM	2.3	1:00PM – 2:00PM	5.9
2:00AM – 3:00AM	2.3	2:00PM – 3:00PM	5.9
3:00AM – 4:00AM	2.3	3:00PM – 4:00PM	5.9
4:00AM – 5:00AM	2.3	4:00PM – 5:00PM	4.6
5:00AM – 6:00AM	2.3	5:00PM – 6:00PM	4.6
6:00AM – 7:00AM	5.0	6:00PM – 7:00PM	4.6
7:00AM – 8:00AM	5.0	7:00PM – 8:00PM	4.6
8:00AM – 9:00AM	5.0	8:00PM – 9:00PM	3.1
9:00AM – 10:00AM	5.0	9:00PM – 10:00PM	3.1
10:00AM – 11:00AM	5.9	10:00PM – 11:00PM	3.1
11:00AM – 12:00PM	5.9	11:00PM – 12:00AM	3.1

Hourly number of traffic loads for each category is the final traffic input required for the analysis of reflection cracking in an asphalt overlay. To obtain the final traffic input, the daily number of axles is multiplied by the probability density factor and the hourly truck traffic distribution factors within each category for a specific axle type and vehicle class, as follows:

$$HNT_j = DNA_j \times P(L_i)_j \times HDF \quad (3.8)$$

where

HNT_j = hourly number of traffic within a category j

DNA_j = daily number of axle loads within a category j

HDF = hourly truck traffic distribution factors

The hourly number of traffic load within category 1 of LTPP section 080901 is listed in Table 3.19 as an example. It should be noted that if the traffic increases with time then the number of vehicles and tire length increments also increase with time. In addition, the number of axle applications of each traffic category for each time increment is used to predict the distress of reflective cracking related to traffic load with time.

Table 3.19. Hourly number of traffic for LTPP section in Tippecanoe, Maryland within category 1.

Tire Length (in.)	Hourly Number of Traffic																							
	12 am	1	2	3	4	5	6	7	8	9	10	11	12 pm	1	2	3	4	5	6	7	8	9	10	11
3.704	6	6	6	6	6	6	14	14	14	14	16	16	16	16	16	16	13	13	13	13	9	9	9	9
4.233	9	9	9	9	9	9	19	19	19	19	22	22	22	22	22	22	17	17	17	17	12	12	12	12
4.763	9	9	9	9	9	9	19	19	19	19	22	22	22	22	22	22	17	17	17	17	12	12	12	12
5.292	7	7	7	7	7	7	15	15	15	15	18	18	18	18	18	18	14	14	14	14	10	10	10	10
5.821	5	5	5	5	5	5	11	11	11	11	13	13	13	13	13	13	10	10	10	10	7	7	7	7
6.350	3	3	3	3	3	3	8	8	8	8	9	9	9	9	9	9	7	7	7	7	5	5	5	5
6.879	2	2	2	2	2	2	5	5	5	5	6	6	6	6	6	6	4	4	4	4	3	3	3	3
7.408	1	1	1	1	1	1	3	3	3	3	4	4	4	4	4	4	3	3	3	3	2	2	2	2
7.938	1	1	1	1	1	1	2	2	2	2	2	2	2	2	2	2	2	2	2	2	1	1	1	1
8.467	1	1	1	1	1	1	1	1	1	1	1	1	1	1	1	1	1	1	1	1	1	1	1	1
8.996	0	0	0	0	0	0	1	1	1	1	1	1	1	1	1	1	1	1	1	1	0	0	0	0
9.525	0	0	0	0	0	0	0	0	0	0	1	1	1	1	1	1	0	0	0	0	0	0	0	0
10.054	0	0	0	0	0	0	0	0	0	0	0	0	0	0	0	0	0	0	0	0	0	0	0	0
10.583	0	0	0	0	0	0	0	0	0	0	0	0	0	0	0	0	0	0	0	0	0	0	0	0

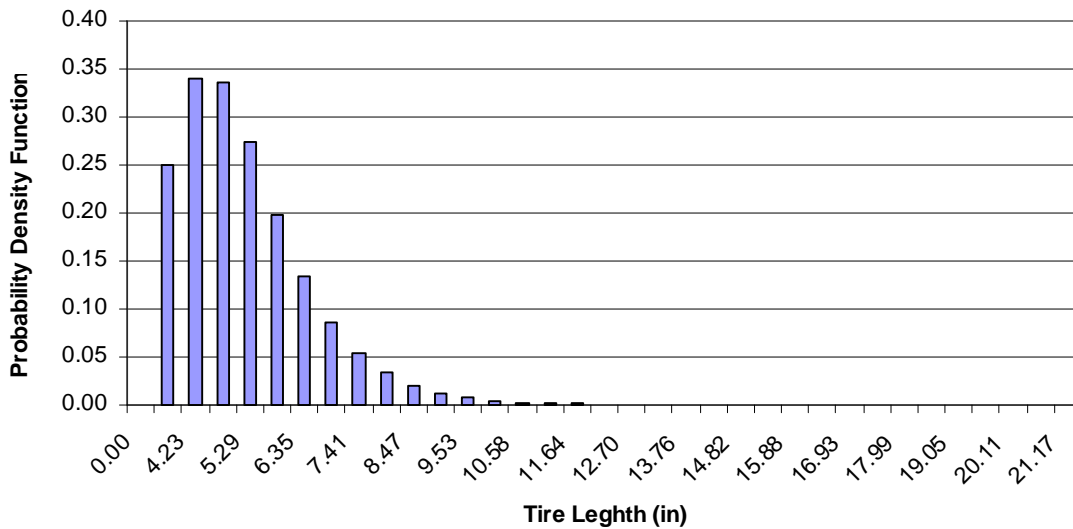
Table 3.19. Continued.

Tire Length (in.)	Hourly Number of Traffic																								
	12 am	1	2	3	4	5	6	7	8	9	10	11	12 pm	1	2	3	4	5	6	7	8	9	10	11	
11.113	0	0	0	0	0	0	0	0	0	0	0	0	0	0	0	0	0	0	0	0	0	0	0	0	0
11.642	0	0	0	0	0	0	0	0	0	0	0	0	0	0	0	0	0	0	0	0	0	0	0	0	0
12.171	0	0	0	0	0	0	0	0	0	0	0	0	0	0	0	0	0	0	0	0	0	0	0	0	0
12.700	0	0	0	0	0	0	0	0	0	0	0	0	0	0	0	0	0	0	0	0	0	0	0	0	0
13.229	0	0	0	0	0	0	0	0	0	0	0	0	0	0	0	0	0	0	0	0	0	0	0	0	0
13.758	0	0	0	0	0	0	0	0	0	0	0	0	0	0	0	0	0	0	0	0	0	0	0	0	0
14.288	0	0	0	0	0	0	0	0	0	0	0	0	0	0	0	0	0	0	0	0	0	0	0	0	0
14.817	0	0	0	0	0	0	0	0	0	0	0	0	0	0	0	0	0	0	0	0	0	0	0	0	0
15.346	0	0	0	0	0	0	0	0	0	0	0	0	0	0	0	0	0	0	0	0	0	0	0	0	0
15.875	0	0	0	0	0	0	0	0	0	0	0	0	0	0	0	0	0	0	0	0	0	0	0	0	0
16.404	0	0	0	0	0	0	0	0	0	0	0	0	0	0	0	0	0	0	0	0	0	0	0	0	0
16.933	0	0	0	0	0	0	0	0	0	0	0	0	0	0	0	0	0	0	0	0	0	0	0	0	0
17.463	0	0	0	0	0	0	0	0	0	0	0	0	0	0	0	0	0	0	0	0	0	0	0	0	0
17.992	0	0	0	0	0	0	0	0	0	0	0	0	0	0	0	0	0	0	0	0	0	0	0	0	0

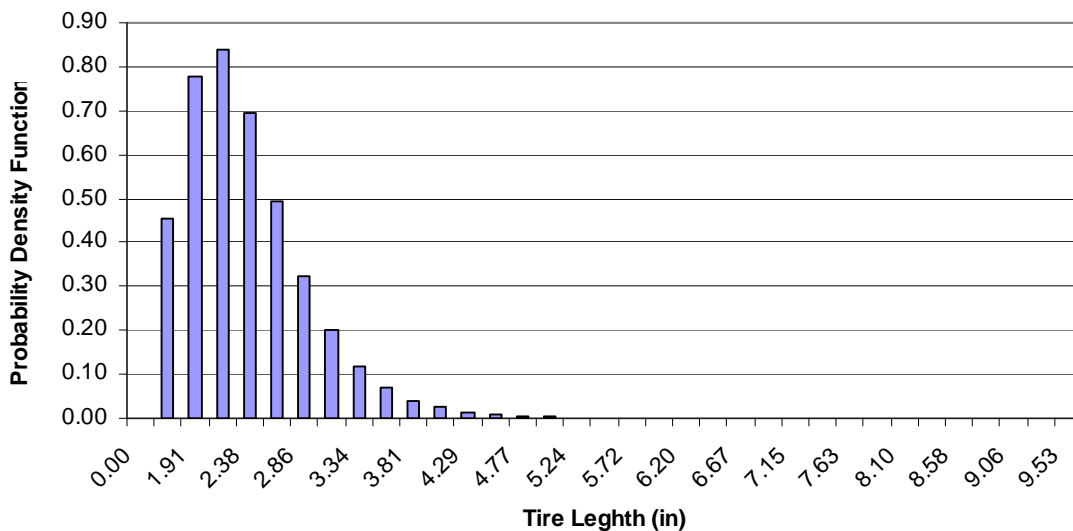
Table 3.19. Continued.

Tire Length (in.)	Hourly Number of Traffic																								
	12 am	1	2	3	4	5	6	7	8	9	10	11	12 pm	1	2	3	4	5	6	7	8	9	10	11	
18.521	0	0	0	0	0	0	0	0	0	0	0	0	0	0	0	0	0	0	0	0	0	0	0	0	0
19.050	0	0	0	0	0	0	0	0	0	0	0	0	0	0	0	0	0	0	0	0	0	0	0	0	0
19.579	0	0	0	0	0	0	0	0	0	0	0	0	0	0	0	0	0	0	0	0	0	0	0	0	0
20.108	0	0	0	0	0	0	0	0	0	0	0	0	0	0	0	0	0	0	0	0	0	0	0	0	0
20.638	0	0	0	0	0	0	0	0	0	0	0	0	0	0	0	0	0	0	0	0	0	0	0	0	0
21.167	0	0	0	0	0	0	0	0	0	0	0	0	0	0	0	0	0	0	0	0	0	0	0	0	0

The complete set of probability density functions for tire patch length for all eight traffic load categories for the LTPP Section in Tippecanoe, Maryland, are shown in Figures 3.13.

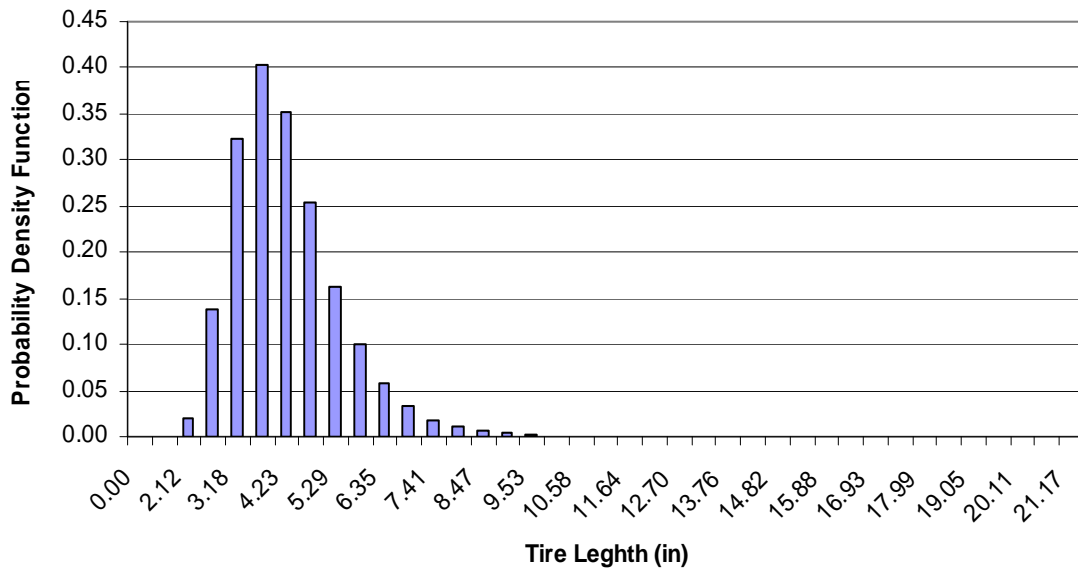


(a) Category 1 (Single axle/single tire)

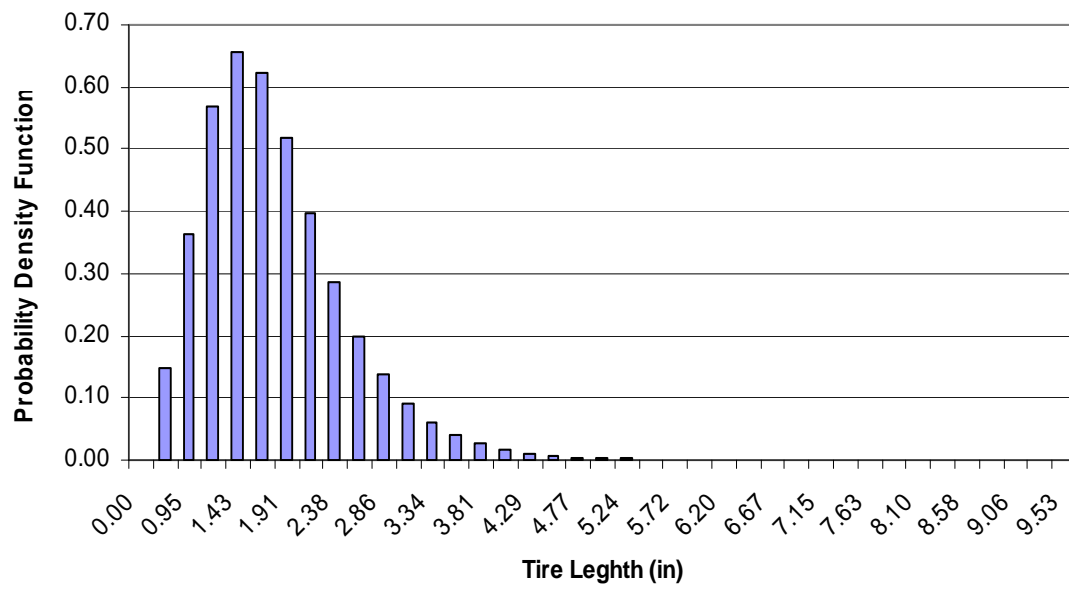


(b) Category 2 (Single axle/dual tires)

Figure 3.13. Probability density functions for LTPP section in Tippecanoe, Maryland (2004).

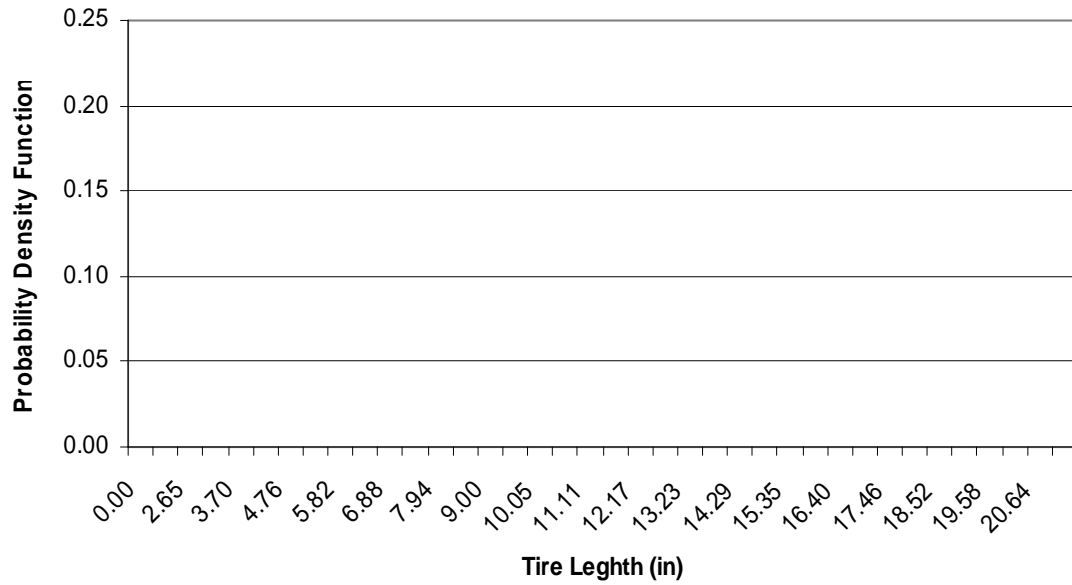


(c) Category 3 (Tandem axle/single tire)

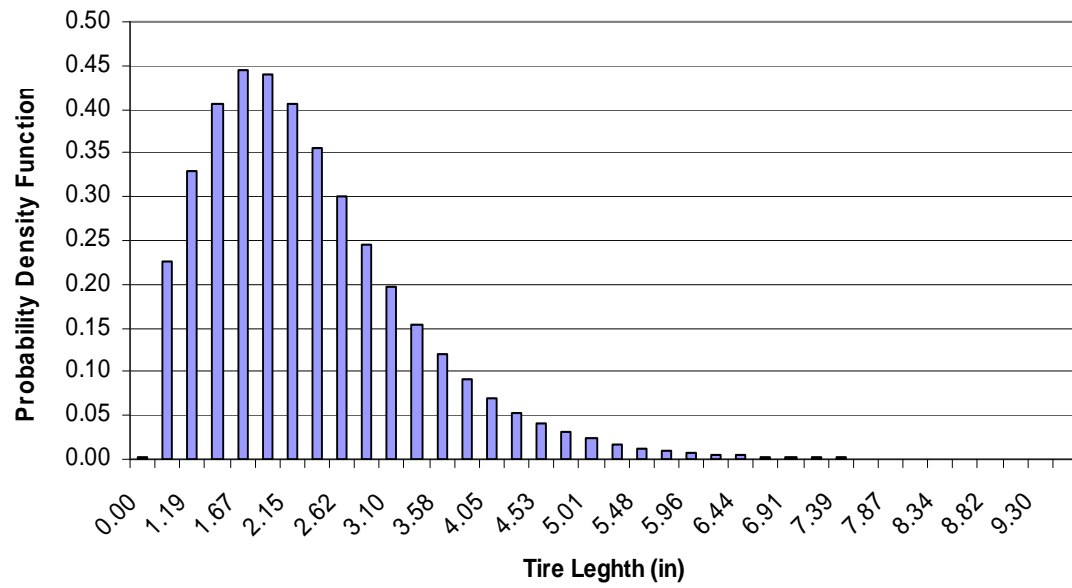


(d) Category 4 (Tandem axle/dual tires)

Figure 3.13. Continued.

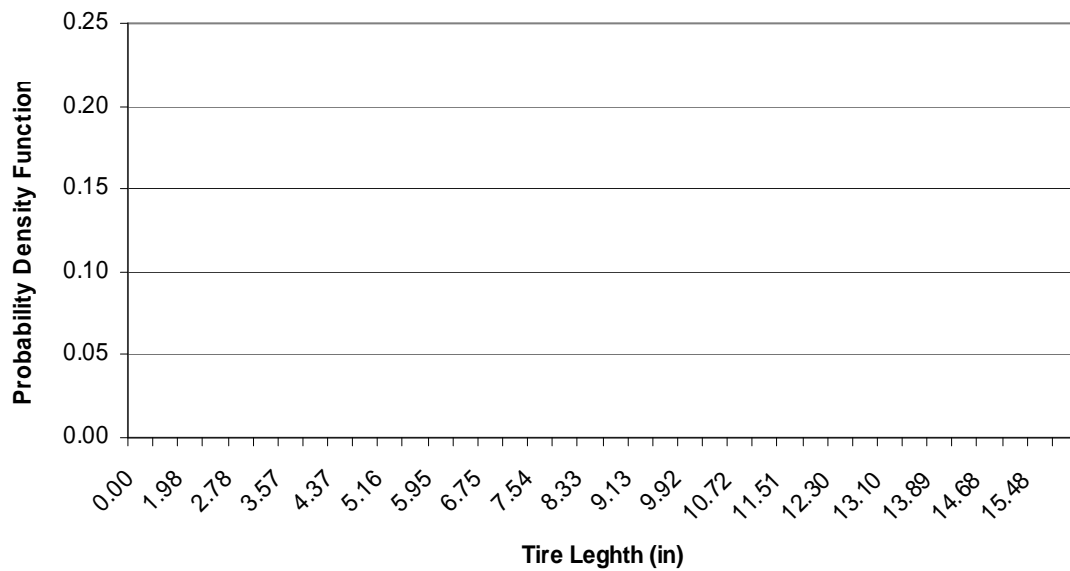


(e) Category 5 (Tridem axle/single tire)

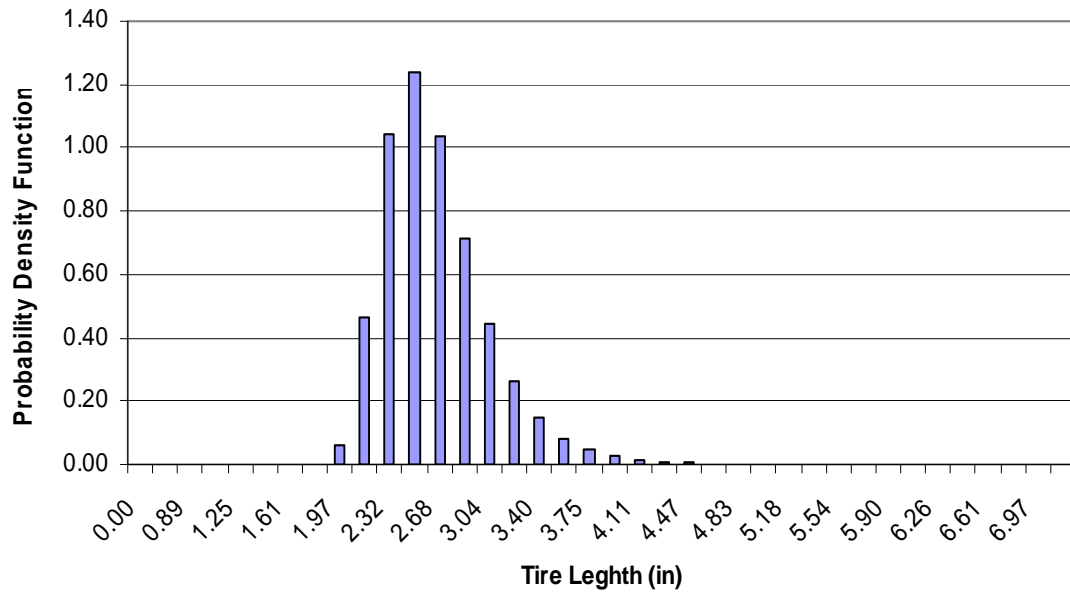


(f) Category 6 (Tridem axle/dual tires)

Figure 3.13. Continued.



(g) Category 7 (Quadrem axle/single tire)



(h) Category 8 (Quadrem axle/dual tires)

Figure 3.13. Continued.

3.7 Climatic Data Collection

The climatic data were collected from two principal sources in addition to the LTPP database (36). The hourly solar radiation and the daily air temperature and wind speed were needed to make accurate estimates of the temperature in the overlay. In addition to these data, the temperature model requires the albedo of the pavement surface and its thermal conductivity and emissivity and absorption coefficients. The solar radiation data can be obtained from the internet at METSTAT Model (Meteorological–Statistical Solar Model) and the SUNY Model for the State University of New York at Albany (http://rredc.nrel.gov/solar/old_data/nsrdb/). The daily climatic data on air temperature and wind speed can be found at <http://www.ltp-Products.com/DataPave/> (36). Although temperatures predicted with the Enhanced Integrated Climatic Model (EICM) model satisfy pavement design needs in general, there have been some large differences when compared to measured pavement temperature (66). These differences are most likely caused by the assumption that heat fluxes at the pavement surface are exactly balanced by conduction into the ground well below the surface, inaccuracy of climatic data (especially calculated solar radiation), and the assumptions of the constant temperature boundary condition and site-independent model parameter values. Therefore, it was necessary to develop a different temperature model than the one which is contained in the EICM in order to calculate the temperatures to a higher degree of accuracy.

Recently, significant improvement over the EICM model has been achieved by several groups using a similar one dimensional heat transfer model (67, 68, 69), but with

an unsteady-state surface heat flux boundary condition, measured model input data, and site-specific model parameters that were optimized based on measured pavement temperatures.

A model developed by Rongbin Han, et al. from the Artie McFerrin Department of Chemical Engineering at Texas A&M University shows that the predicted temperature correlates well to the observed data as shown in Figure 3.14 (70). This one dimensional heat transfer model employs an unsteady-state heat flux boundary condition at the pavement surface, a depth-independent heat flux 3 m below the surface, and the ability to estimate site-specific model parameters using known measured pavement temperatures. The detail of this new model is described later in Section 3.10.

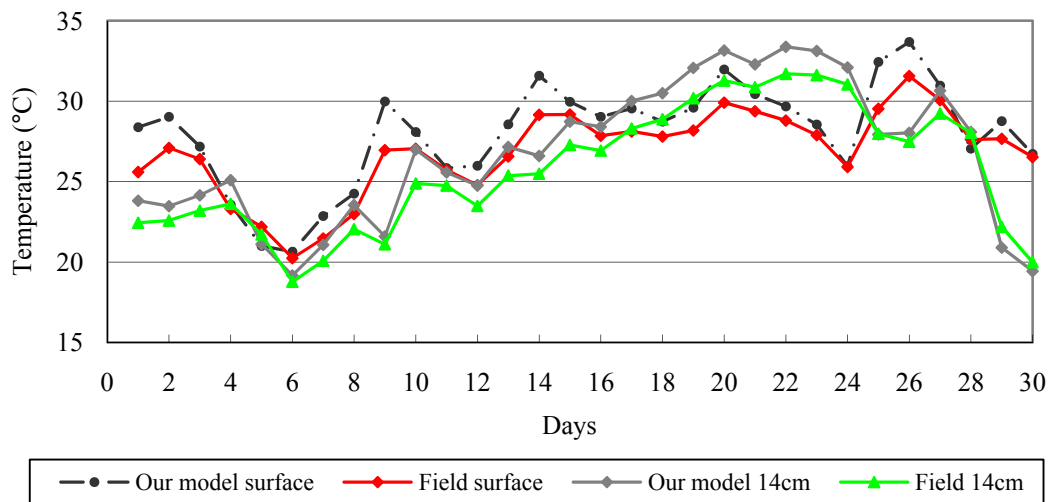


Figure 3.14. Typical daily pavement temperature prediction using improved model.

3.7.1 Hourly Climatic Input Data Collection

Climatic input data for the model includes hourly solar radiation, hourly air temperature, and daily average wind speed data in an hourly format.

Hourly solar radiation can be collected from the National Solar Radiation Database (NSRDB). Hourly solar radiation data are modeled using SUNY or METSTAT models based on satellite images, covering nearly all parts of the United States from 1961 to 2005.

Daily average wind speed can be directly collected from the Virtual Weather Station program in the LTPP database (36). Additionally, daily wind speed can be obtained directly from the National Climatic Data Center (NCDC) or the meteorological network in each state. Although hourly wind speed is preferred, site-specific hourly wind speed data are difficult to obtain and more vulnerable to environmental conditions, adding difficulty in interpolation endeavor. Fortunately, the model is not overly sensitive to wind speed and daily values work quite well.

Hourly air temperature data are not as commonly available as daily maximum and minimum air temperatures, but reasonable estimates of hourly temperatures are needed for accurate temperature calculations. In order to provide the model with hourly wind speed data, a method was developed to interpolate hourly air temperature from daily maximum and minimum air temperatures. Recorded daily maximum and minimum air temperatures can be obtained easily from the Virtual Weather Station program in the LTPP database or NCDC.

A conventional method to impute hourly air temperatures fits a sinusoidal function to daily maximum and minimum air temperatures. However, the daily profile of air temperature is not exactly sinusoidal. Typically, the time for the air temperature to rise from the daily minimum temperature to the daily maximum temperature is about 9 hours, while 15 hours are taken for the air temperature decrease from the daily maximum temperature to the daily minimum. A more accurate air temperature interpolation method should incorporate this non-sinusoidal pattern.

In order to obtain a more representative pattern of daily air temperatures, data over an entire year were obtained from the Automatic Weather Station (AWS) in the LTPP database and analyzed using a seasonal trend decomposition time series analysis (Figure 3.15). Figure 3.15 contains two sets of four rows; the top set covers an entire year while the bottom set covers five days. In each set, the first row graphs the measured hourly air temperature. The trend trace is a moving average of the measured data, which represents the daily average temperature throughout the year. The “seasonal” trace is obtained by subtracting the trend line from the measured data and finding a local polynomial which best fits the result. This trace represents the regular pattern of daily air temperature, which is used instead of a sinusoidal function. The remainder is what is left after the trend and the seasonal traces are extracted from the measured data, and shows the effect of weather on air temperature.

With a daily pattern of air temperature known, hourly air temperatures can be reconstructed from daily measured maximum and minimum data. First, the daily average air temperature data are taken from the trend trace. Then, the trend and the seasonal

traces obtained from the time series analysis are added together. Finally, the result is linearly transformed to fit the measured data, day by day. This step indirectly incorporates to some extent the remainder data into the obtained dataset.

To evaluate the time series analysis method, calculated hourly temperature data were compared to measurements over an entire year, plus a comparison was made of imputed temperatures using a sinusoidal temperature pattern. The dataset was from a Texas LTTP site. From the comparison, it is clear that the time series analysis interpolation method is significantly better than the sinusoidal method. The standard deviation of calculated versus measured errors is 1.95 °C for the pattern interpolation method and 3.07 °C for the sinusoidal method.

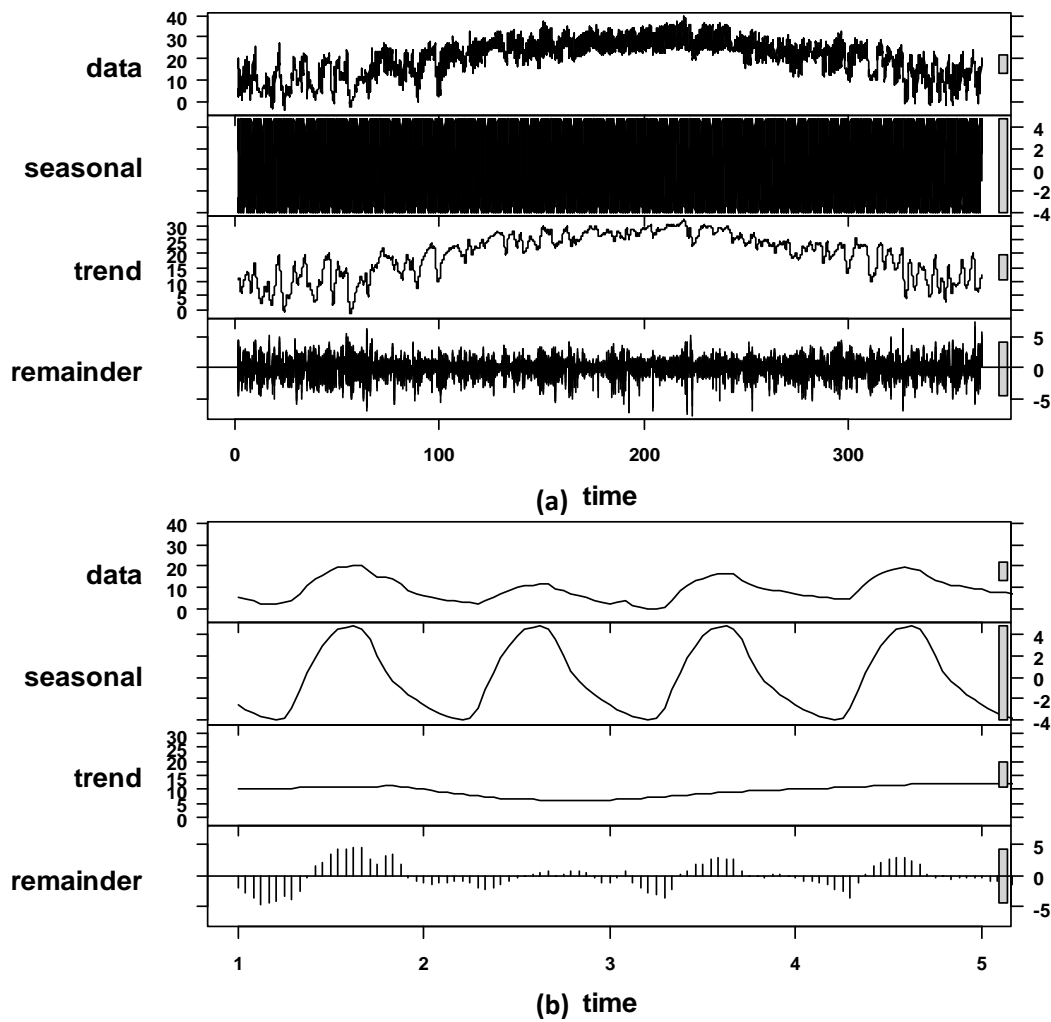


Figure 3.15. Seasonal trend decomposition of hourly air temperature. (a) For a whole year, (b) Magnified view of 5 days period.

Figure 3.16 showed several patterns were calculated for three sites in Texas, and one site each for Utah, Nevada, and South Dakota. The patterns for the sites in Texas compare quite well to each other, especially the first two sites, while the difference

between patterns from different states are quite apparent, especially Nevada and South Dakota.

Though the patterns from different states are different, the patterns share the same basic shape. When the pattern obtained from Nevada was used for interpolation of hourly pavement temperature in Texas, offsite imputed temperatures were obtained. The pattern interpolation method is better than the sinusoidal method, and the onsite pattern should be used when available. An offsite pattern produces less accurate results, but the deviation can be acceptable, especially if a close-to-site pattern is used when the onsite pattern is not available.

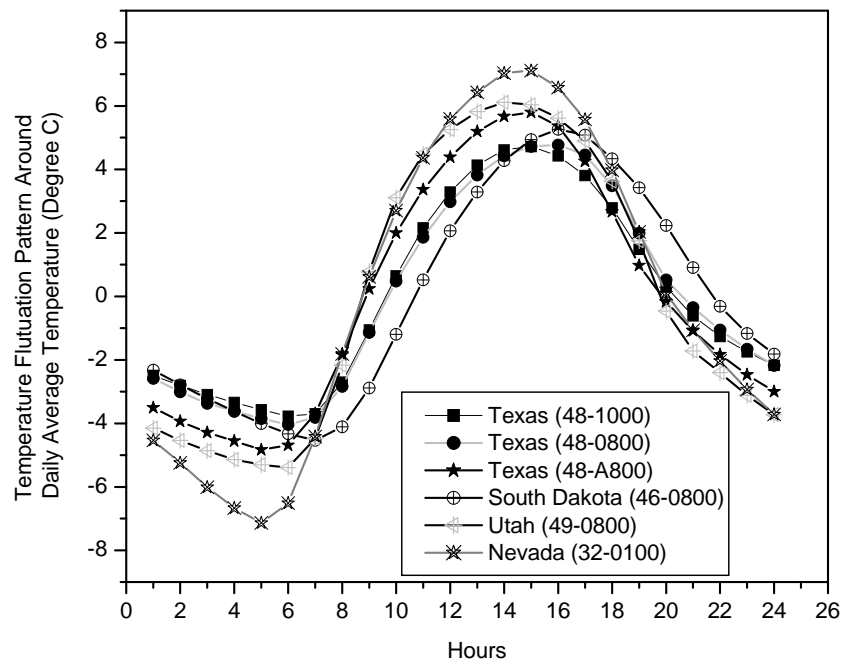


Figure 3.16. Daily air temperature patterns at 6 different pavement sites.

3.7.2 Obtaining Site-Specific Model Parameters

In order to obtain good model estimates of pavement temperatures from accurate hourly climatic input, the specific numerical values of the model parameters need to be determined. Although some parameters are fairly well known (ρ , k , C , e.g.), others require a parameter estimation process. Site specific parameters, as discussed in the model development section, include albedo, emissivity, absorption coefficient, thermal diffusivity, and the parameters a , d in the heat convection coefficient correlation.

The following discussion presents results of a parameter sensitivity analysis, optimization of the model parameters using 29 pavement sites widely distributed across the United States, an analysis of the distribution of these model parameters over a wide range of climatic regions, and interpolation strategies for each model parameter so that at any pavement site across the country reasonable values for the model parameters can be assumed.

Although albedo, emissivity, and the absorption coefficient are site specific, there is no clear understanding of how these parameters vary with climate and pavement properties. Understanding such variation is important to improving the value of the temperature prediction model. To address this issue, parameter optimization has been conducted for these model parameters at 29 pavement sites across the United States by comparing model estimates of pavement temperature to reported measurements. Previous studies revealed that albedo and emissivity values are seasonally sensitive in that their values in the winter are different from their values the rest of the year. Therefore, in this dissertation, two separate sets of model parameters were obtained, one

set for the winter and one set for the other seasons (represented by summer), to take into account this seasonal variation. Then from further analysis of the distribution and seasonal variation of those model parameters, interpolation strategies have been developed for each model parameter.

The algorithm to find values of the three parameters identified by sensitivity analysis (albedo, difference between emissivity and absorption coefficient, and the absorption coefficient) is quite straightforward. Each parameter was given a range of values and increments within the range based on literature reports. By examining the ability of each set of model parameters to give the best match between the measured and the calculated pavement temperatures, the optimum set was obtained. As a measure of the model's accuracy, the average hourly absolute difference between the measured and the calculated pavement temperatures was used. This estimation method using an average of absolute error is preferred to, for example, the least-squares error by which a section with unusual properties receives more weight than a section with more normal properties.

Twenty-nine pavement sites were identified with recorded hourly pavement temperatures from the seasonal monitoring program of the Long Term Pavement Performance database (LTPP) (36), Figure 3.17, with the pavement sites marked on a United States terrain map. Those pavement sites all have at least one month of continuous hourly temperatures measured in both the winter and summer. Model parameters were optimized by examining the ability of each set of model parameters to minimize the average absolute error in temperature. Pavement temperatures in the

middle depth of the asphalt layer, rather than the pavement surface, have been used to optimize these model parameters.

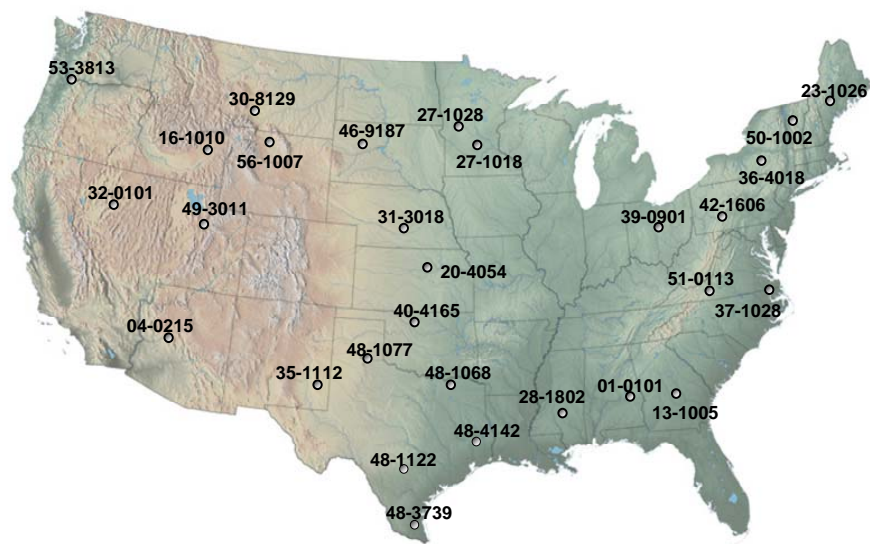


Figure 3.17. Distribution map of 29 SMP pavement sites studied.

3.8 Reflection Cracking Amount and Severity Model

The pavement distress data included the total length and severity of the cracks in the old pavement surface prior to the placement of the overlay and the length and severity of the cracks reflected through the overlay. Only transverse cracks were considered as reflection cracks in each test section. In order to have reliable ρ and β values for the S-shaped curves that were fitted to the distress data, at least three separate and sequential observations of distress were required. In some cases, no distress data were recorded on the old pavement surface prior to overlay, and a mathematical method

had to be devised to estimate the original amount of cracking which was subject to reflection. The mathematical method this dissertation used was the Systems Identification Method (SIM). The detail of SIM and modeling the reflection cracking are showing in the following subsections.

3.8.1 System Identification Process

The reflection cracking amount and severity model at a given severity level was considered to have been calibrated when the error between observed and predicted crack lengths was minimized in some sense. Since the predicted number of days is calculated by the mechanistic crack growth model at each test section, a solution method was required to determine the parameters, ρ and β , in the empirical S-shaped amount and severity model. In this chapter, the method of solving for the parameters is by use of the system identification process.

The purpose of the system identification process is to develop a mathematical model which describes the behavior of a system (real physical process) in a rationally satisfying method. The actual system and the mathematical model are identified when the error between them is minimized or satisfies the error criteria; otherwise, the model is adjusted until the error is reduced sufficiently (71). There are three different error minimization models in system identification process depending on the choice or residuals combined with the model: forward model, inverse model, and generalized model shown in Figure 3.18. The forward approach employs output error between the model and the system to minimize them using same input. In the inverse approach, the

input error is used to be minimized based on same output. The generalized model is a combination of the forward and inverse approach when the model is invertible (71).

As in the calibration process in this study, when the system output is fixed because it is observed or obtained from an actual system, the output from the model must be refined to calibrate the mathematical model by adjusting the parameters. That is, the reflection cracking amount and severity model (mathematical model) is calibrated based on observed reflection crack data (actual system output) to produce predicted crack data (model output) which is close to the observed crack data. Therefore, the forward model system identification process was used for calibrating the reflection cracking amount and severity model since it is easier to compute the model output.

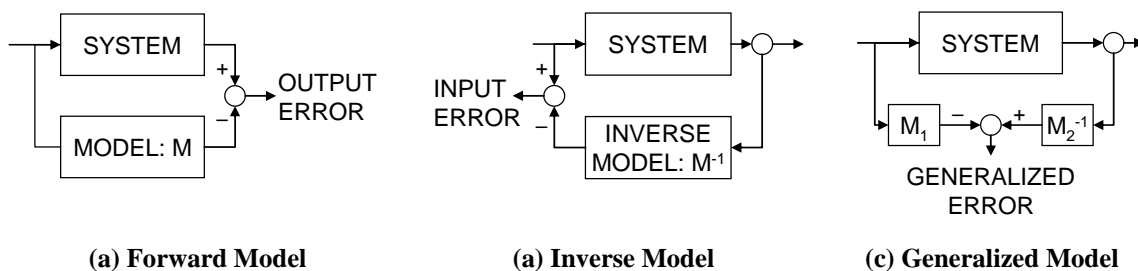


Figure 3.18. Methods for system identification process (71).

When the output error between the system and the model is small enough to meet an error criterion, it is assumed that an optimal model for the system is obtained.

However, if the error does not meet the criterion, the parameters in the mathematical model should be corrected by a parameter adjustment and adaptation algorithm. The correction process is performed iteratively until the error becomes small enough using the algorithm. Figure 3.19 depicts the scheme of a system identification process based

on the forward model and parameter adjustment and adaptation algorithm for the reflection cracking amount and severity model calibration.

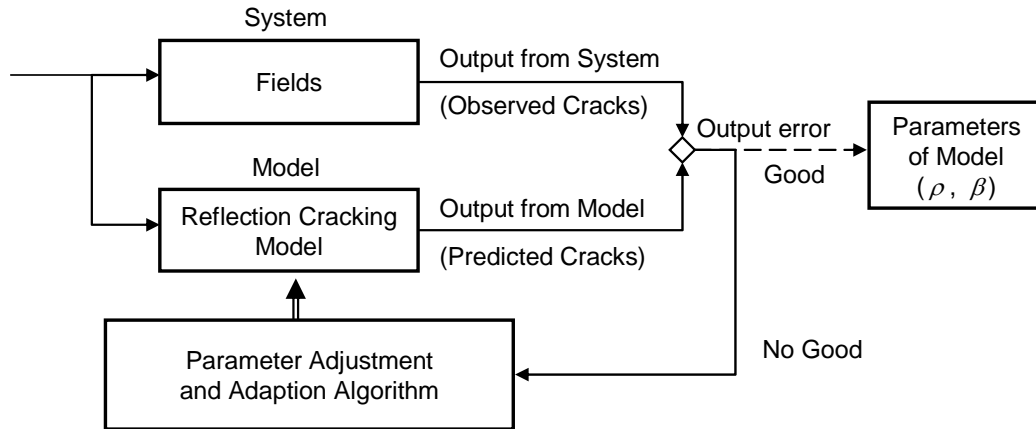


Figure 3.19. Scheme of system identification process.

3.8.2 Parameter Adjustment and Adaption Algorithm

A parameter adjustment and adaption algorithm was developed based on the Taylor series expansion as follows (72).

$$[F_{ki}]\{\alpha_i\} = \{r_k\} \quad (3.9)$$

where

$$[F_{ki}] = \text{sensitivity matrix} = \sum_{k=1}^m \sum_{i=1}^n \frac{\partial f_k}{\partial p_i} \frac{p_i}{f_k} \quad (m \times n \text{ matrix}),$$

m, n = number of output data and model parameters, respectively,

f_k = mathematical model,

p_i = model parameters,

$\{\alpha_i\}$ = change vector (relative change of parameters) = $[\alpha_1 \alpha_2 \dots \alpha_n]^T$, and

$$\{r_k\} = \text{residual vector (error between system and model outputs)} = [r_1 \ r_2 \ \dots \ r_m]^T$$

The minimization of error contained within the residual vector $\{r_k\}$ is analogous to the reduction of error employed in least squared error analysis. The squared error between the actual output and the predicted output is calculated by using a mathematical model to determine the sensitivity of the weighting parameters for allocating the squared error. It is possible to adjust the model parameters until there is no squared error remaining; however, because of the presence of random error, the values in the residual matrix $\{r_k\}$ should not be forced to zero (73). Since the elements in the residual vector $\{r_k\}$ which represents errors between the actual and model outputs are determined based on model parameters, p_i , assumed at each iteration process, they are known values. The sensitivity matrix $[F_{ki}]$ which reflects the sensitivity of the output from mathematical model, f_k , to the assumed parameters, p_i , is also a known value. Therefore, the unknown change vector $\{\alpha_i\}$ presents the relative changes of the model parameters and is the target matrix to be determined in the process. Equation 3.9 can be rewritten as:

$$\{\alpha_i\} = [F_{ki}^T F_{ki}]^{-1} [F_{ki}]^T \{r_k\} \quad (3.10)$$

As soon as change vector $\{\alpha_i\}$ is obtained using an initial assumption of parameters, a new set of parameters is determined as

$$p_i^{j+1} = p_i^j (1 + 0.6\alpha_i) \quad (3.11)$$

where

j = iteration count

By minimizing the change vector $\{\alpha_i\}$, solutions for the parameters in the model are found. In order to achieve the solution, the iteration process using Equation 3.11 was continued until there is no squared error remaining or the desired convergence was reached. In this study, the convergence criterion was set to 1.0 percent; that is, the iteration should be repeated until the elements in the change vector $\{\alpha_i\}$ are less than 0.01.

3.8.3 Calibrated Observed Reflection Cracking Length

Based on the system identification and the parameter adjustment algorithm addressed previously, the reflection cracking models were calibrated using the data obtained from LTPP, New York City, and Texas asphalt overlay test sections. The process was used to fit the predicted crack length to the measured crack length by iteration. The parameter adjustment algorithm of Equation 3.9 can be expressed for determining the parameters in the reflection cracking model as follows:

$$[F] \{\alpha\} = \{r\} \quad (3.12)$$

where

$\bar{D}(N_i)$ = crack length at N_i , calculated using ρ^j and β^j ,

$D(N_i)$ = measured crack length at N_i , and

The parameters ρ and β in the model were determined when the relative changes of adjusted parameters were minimized and so the elements in the change vector were less than 0.01.

$$\begin{bmatrix} \frac{\partial \bar{D}(N_1)}{\partial \rho^j} \frac{\rho^j}{\bar{D}(N_1)} & \frac{\partial \bar{D}(N_1)}{\partial \beta^j} \frac{\beta^j}{\bar{D}(N_1)} \\ \frac{\partial \bar{D}(N_2)}{\partial \rho^j} \frac{\rho^j}{\bar{D}(N_2)} & \frac{\partial \bar{D}(N_2)}{\partial \beta^j} \frac{\beta^j}{\bar{D}(N_2)} \\ \vdots & \vdots \\ \frac{\partial \bar{D}(N_i)}{\partial \rho^j} \frac{\rho^j}{\bar{D}(N_i)} & \frac{\partial \bar{D}(N_i)}{\partial \beta^j} \frac{\beta^j}{\bar{D}(N_i)} \end{bmatrix} \begin{bmatrix} \frac{\rho^{j+1} + \rho^j}{\rho^j} \\ \frac{\beta^{j+1} + \beta^j}{\beta^j} \end{bmatrix} = \begin{bmatrix} \frac{D(N_1) - \bar{D}(N_1)}{\bar{D}(N_1)} \\ \frac{D(N_2) - \bar{D}(N_2)}{\bar{D}(N_2)} \\ \vdots \\ \frac{D(N_i) - \bar{D}(N_i)}{\bar{D}(N_i)} \end{bmatrix} \quad (3.13)$$

The percent crack length at each of the pavement ages was used to develop the model parameters ρ and β in the reflection cracking amount and severity model along with the system identification process. Table 3.20 and Table 3.21 present an example of the predicted percent of reflective cracking development of all severity level of four LTPP sections, which were calculated based on reflection crack data. Table 3.22 shows the developed model parameters, and Figure 3.20 to 3.23 present the plots of the calibrated model corresponding to the measured data for the LTPP sections. The results presented good data fitting along with satisfying the convergence criterion. The calibrated parameters for whole asphalt overlay test sections in the LTPP, New York City and Texas databases are listed in Section 4.2.

Table 3.20. Collected reflection crack information of LTPP test sections.

Section No.	Survey Date	Days after Overlay	Observed Crack Length (meter)		
			L + M + H	M + H	H
340503	7/27/1992	0	88.20*	-	-
	11/9/1995	1,200	0.00	0.00	0.00
	8/27/1996	1,492	0.00	0.00	0.00
	10/27/1998	2,283	8.70	0.00	0.00
	10/19/1999	2,640	7.30	0.00	0.00
	10/17/2000	3,004	18.00	0.70	0.00
	10/15/2001	3,367	24.80	4.20	0.00
	11/9/2002	3,757	26.10	0.00	0.00
	11/8/2003	4,121	40.50	7.90	0.00
3/13/2004	4,247	49.20	11.90	0.00	
270506	9/15/1990	0	177.70*	-	-
	11/6/1990	52	0.00	0.00	0.00
	6/17/1992	641	51.10	3.60	0.00
	9/29/1993	1,110	54.80	40.20	0.00
	8/23/1995	1,803	82.80	46.80	10.80
	10/23/1997	2,595	114.70	95.90	37.00
	6/3/1999	3,183	119.10	111.00	29.60
	7/24/2000	3,600	118.10	114.50	84.10
8/20/2001	3,992	117.40	113.80	109.80	
240563	6/10/1992	0	40.30*	-	-
	10/19/1995	1,226	8.30	0.00	0.00
	5/14/1997	1,799	26.50	0.00	0.00
	7/14/1999	2,590	28.40	0.00	0.00
	8/17/2000	2,990	26.10	0.00	0.00
	9/6/2001	3,375	33.00	16.60	0.00
	11/7/2002	3,802	35.70	22.60	0.00
	6/5/2003	4,012	37.10	25.90	0.00
	6/22/2004	4,395	37.60	22.20	0.00
55B901	7/1/1992	0	125.40*	-	-
	10/23/1992	114	4.90	0.00	0.00
	6/24/1993	358	46.80	14.40	0.00
	11/17/1994	869	94.60	18.00	0.00
	5/5/1999	2,499	117.70	3.70	0.00
	10/17/2002	3,760	119.30	61.70	0.00

* Observed transverse crack length before asphalt overlay obtained from LTPP database

Table 3.21. Predicted reflective cracking development of L+M+H severity for LTPP test sections.

Section No.	Overlay Type	Number of Days after Overlay	% Crack Length
340503	AC/AC OL	0	0
		1,200	0
		1,492	0
		2,283	9.86
		2,640	8.28
		3,004	20.41
		3,367	28.12
		3,757	29.59
		4,121	45.92
		4,247	55.78
270506	AC/Mill/AC OL	0	0
		52	0
		641	28.76
		1,110	30.84
		1,803	46.60
		2,595	64.55
		3,183	67.02
		3,600	66.46
		3,992	66.07
240563	AC/FC/AC OL	0	0
		1226	20.60
		1799	65.76
		2590	70.47
		2990	64.76
		3375	81.89
		3802	88.59
		4012	92.06
		4395	93.30
55B901	JRC/AC OL	0	0
		114	3.91
		358	37.32
		869	75.44
		2,499	93.86
		3,760	95.14
		4,410	99.12

Table 3.22. Calibrated model parameters of LTPP sections.

LTPP Section No.	Overlay Type	Model Parameters (L+M+H)	
		β	ρ
340503	AC/AC	2.365	3,617.12
270506	AC/Mill/AC	0.702	1,004.85
240563	AC/FC/AC	2.276	1461.25
55B901	JRC/AC	1.159	329.42

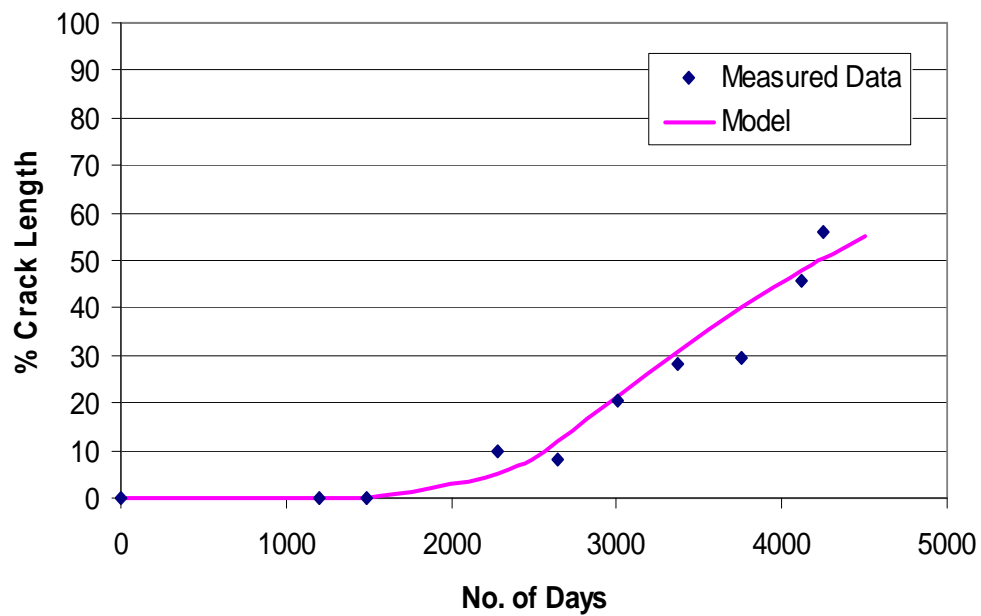


Figure 3.20. Calibrated model on measured reflective crack for LTPP section 340503.

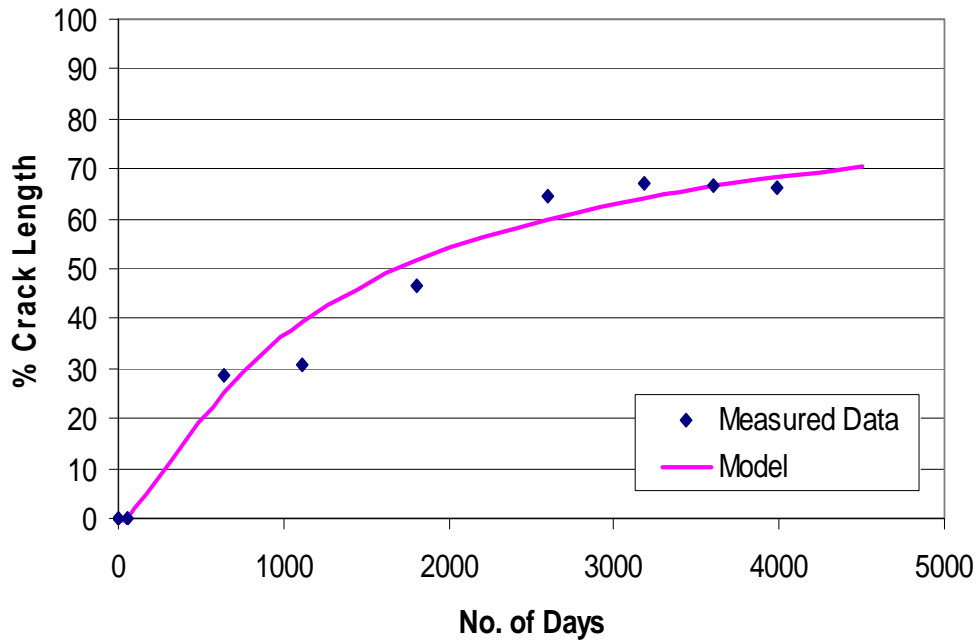


Figure 3.21. Calibrated model on measured reflective crack for LTPP section 270506.

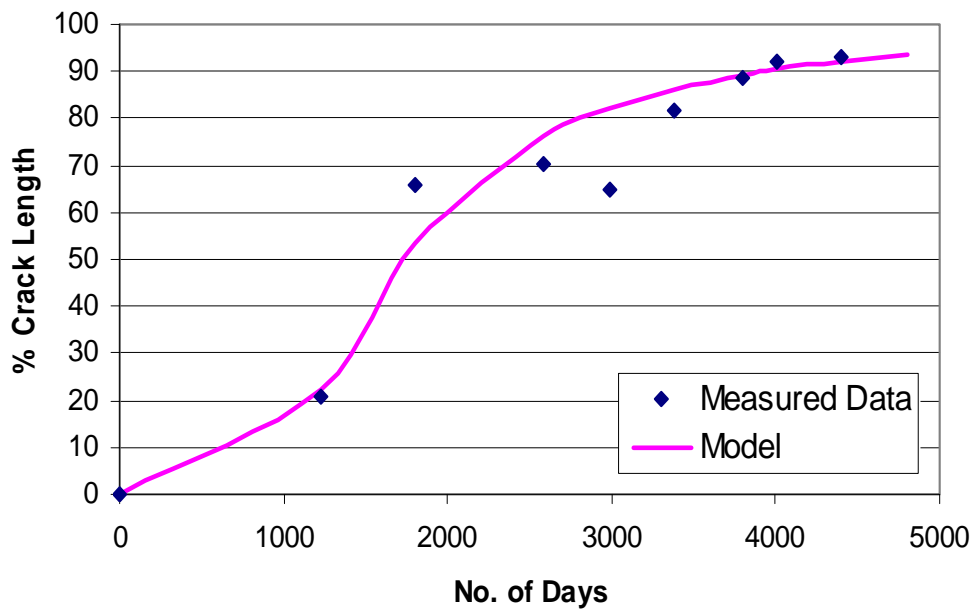


Figure 3.22. Calibrated model on measured reflective crack for LTPP section 240563.

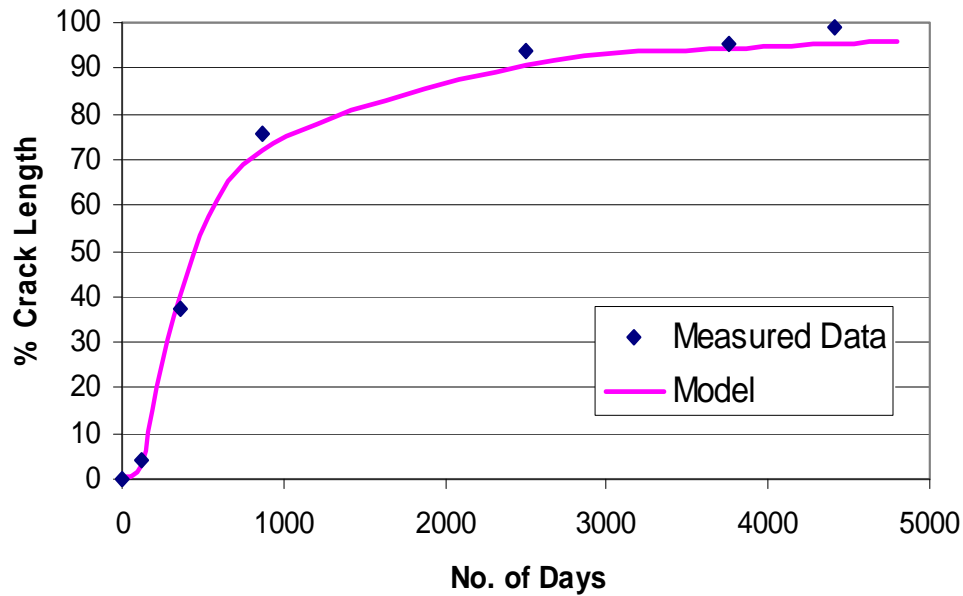


Figure 3.23. Calibrated model on measured reflective crack for LTPP section 55B901.

3.9 Viscoelastic Thermal Stress Computation

The model developed by Hiltunen and Roque (74) accounts for thermal viscoelastic material behavior through a generalized Maxwell model as illustrated in Figure 3.24. The Hiltunen and Roque model for viscoelastic thermal stress is expressed in Equation 3.14:

$$\sigma(\xi) = \int_0^{\xi} \frac{E(\xi - \xi') d\varepsilon}{d\xi'} d\xi' \quad (3.14)$$

where

$$\begin{aligned} \sigma(\xi) &= \text{stress at the reduced time } \xi; \\ E(\xi - \xi') &= \text{relaxation modulus at the reduced time } \xi - \xi'; \end{aligned}$$

ε = strain at the reduced time ξ .

This viscoelastic thermal stress equation is expressed in terms of reduced time ξ which is defined in the process of time-temperature superposition.

$$\xi = \frac{t}{a_T}$$

where

t = real time;

a_T = time-temperature shift factor.

Considering the strain is viscoelasticity. This strain can be expressed as a function of reduced time ξ' and thermal coefficient α as in Equation 3.15.

$$\varepsilon = \alpha(T(\xi') - T_0) \quad (3.15)$$

where

$T(\xi')$ = pavement temperature at the reduced time;

T_0 = pavement temperature at stress free temperature (20°C).

Therefore, Equation 3.14 can be rewritten in real time instead of reduced time (3.16).

$$\sigma(t) = \int_0^t \frac{E(\xi(t) - \xi'(t)) \left(\partial(\alpha(T(\xi') - T_0)) \right)}{\partial \xi'} \quad (3.16)$$

In order to calculate the viscoelastic thermal stress, this program uses the Collocation method to calculate the coefficients of a Prony series $(E(\xi - \xi')_i)$. The Collocation method is summarized in the next subsection. In addition, the calculation of the shift factor a_T is also shown subsequently.

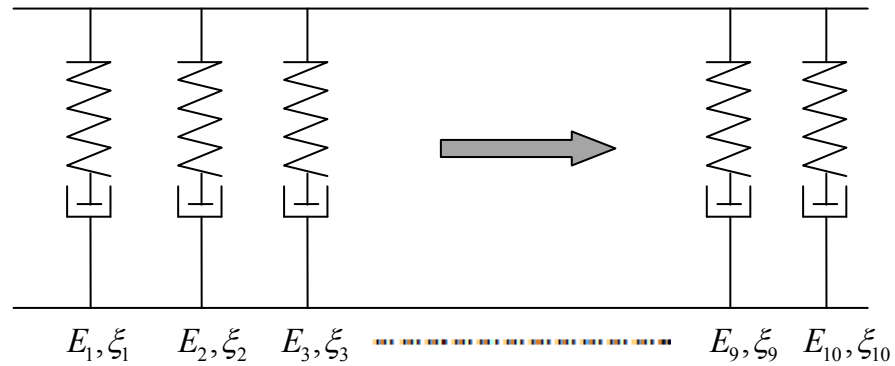


Figure 3.24. Generalized Maxwell model for relaxation.

3.9.1 Collocation Matrix

The Collocation method is a method to approximate the computed number and actual number by using predetermined loading times, t_i and corresponding retardation times, T_j . The Prony series coefficients, E_j , for the viscoelastic relaxation modulus, $(E(\xi - \xi')_i)$, are then calculated with the collocation matrix shown below.

$$\begin{bmatrix} e^{-\frac{t_1}{T_1}} & \dots & e^{-\frac{t_1}{T_{10}}} \\ \vdots & \ddots & \vdots \\ e^{-\frac{t_{11}}{T_1}} & \dots & e^{-\frac{t_{11}}{T_{10}}} \end{bmatrix} \begin{bmatrix} E_1 \\ \vdots \\ E_{10} \end{bmatrix} = \begin{bmatrix} E(t_1) + E_\infty \\ \vdots \\ E(t_{11}) + E_\infty \end{bmatrix}$$

where

t_i = 11 loading times we determined;

T_j = 10 retardation times we determined;

E_j = the coefficients of Prony series;

$E(t_i)$ = the relaxation moduli from the ANN 2006 model (3) at -10°C ;

$$E_\infty = E_{FWD}(t, T) - E_{ANN}(t_{0.06}, T_{FWD}) \quad \text{IF} \quad E_\infty \leq 0, \text{ set } E_\infty = 0$$

3.9.2 Shift Factors

Shift factors were determined at three different temperatures which are -10°C , 0°C , and 10°C . The assumed reference temperature (shift factor $a_T = 1$) is -10°C . In order to evaluate the shift factors at 0°C and 10°C , the ANN (Artificial Neural Network) relaxation modulus program is used to calculate the modulus at three different loading times which are 360 seconds, 3600 seconds (1 hour), and 36000 (10 hours) seconds. The purpose of evaluating the moduli at different temperatures is to find the log-log slope of the line (m_{mix}) of relaxation modulus versus loading time as shown in Figure 3.25. As shown in Figure 3.25, m_{mix} can be calculated at different temperatures as:

$$m_{mix(-10)} = \frac{\log E(360, -10) - \log E(36000, -10)}{\log(36000) - \log(360)}$$

$$m_{mix(0)} = \frac{\log E(360, 0) - \log E(36000, 0)}{\log(36000) - \log(360)}$$

$$m_{mix(10)} = \frac{\log E(360, 10) - \log E(36000, 10)}{\log(36000) - \log(360)}$$

Knowing the m_{mix} and relaxation modulus at different temperatures, the time-temperature shift factors for 0°C and 10°C can be determined from Equations 3.17 and 3.18.

$$\log \left(\frac{1}{a_T} \right)_{T=0} = \frac{\log E(3600, -10) - \log E(3600, 0)}{m_{mix(0)}} \quad (3.17)$$

$$\log \left(\frac{1}{a_T} \right)_{T=00} = \frac{\log E(3600, -10) - \log E(3600, 0)}{m_{mix(00)}} \quad (3.18)$$

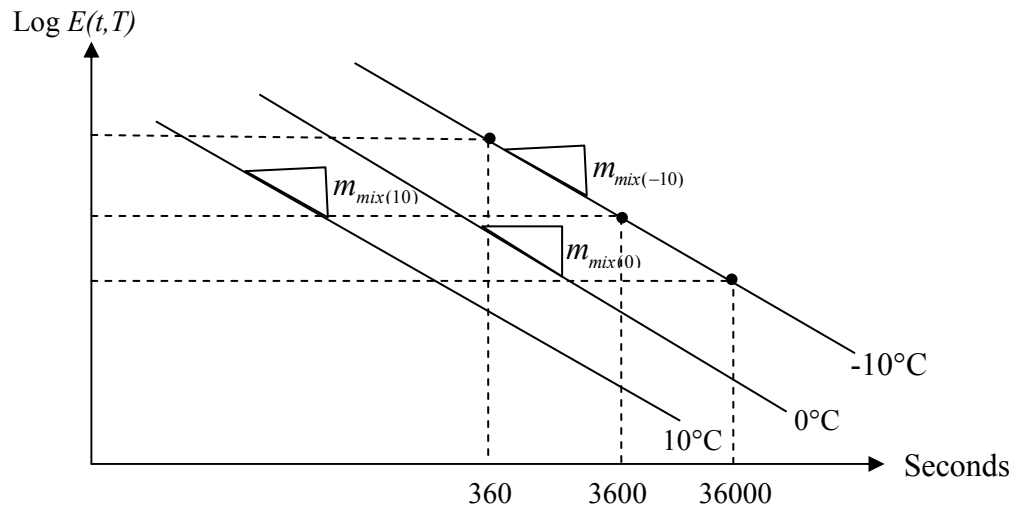


Figure 3.25. m_{mix} at different temperatures.

A numerical version of Equation 3.16 is used in a subroutine of the Calibration and Design programs to calculate the viscoelastic thermal stress at the tip of the growing crack for every hour of each day. This stress is used in turn in the ANN stress intensity factor subroutine to calculate the stress intensity factor at the tip of the crack, and the largest one that occurs each day is used to calculate the growth of the crack due to thermal stresses for that day.

3.10 Stress Intensity Factor Computation by Finite Element Method

It is well known that pavement crack propagation is influenced by traffic load, climate, material properties, pavement structure, and many other interacting variables. Many studies have been conducted to address this problem, and different models such as the fracture mechanics model (24) have been proposed to analyze and/or predict crack

propagation. After reviewing these models, it was concluded that the finite element (FE) plus fracture mechanics-based crack propagation model is conceptually sound and can be easily implemented within the current mechanistic-empirical (ME) pavement design framework (32, 33). The fundamental principle of this model is to calculate the stress intensity factor (SIF) induced by traffic loading (bending SIF and shearing SIF) and daily temperature variation (thermal SIF). Therefore, a fast and accurate SIF computational tool, capable of considering a three-dimensional (3D) pavement structure, becomes an indispensable analytical tool. A newly developed FE analysis tool “SA-CrackPro” was used in this dissertation. It has been verified that it is more accurate compared with a commercial 3D FE package ANSYS.

3.10.1 Background of the Fracture Mechanics Approach and Associated SIF

Computation Tools

Among the various laws that have been conceptualized, Paris’ law (5) is still the governing concept for modeling crack propagation, particularly for fracture-micromechanics applications. Expressed in Equation 3.19, Paris’ law has been successfully applied to HMA mix by many researchers, for the analysis of experimental test data and prediction of reflective- and low temperature-cracking (1, 75).

$$\frac{dc}{dN} = A \cdot (\Delta K)^n \quad (3.19)$$

where

- c = crack length;
- N = number of loading cycles;
- A, n = fracture properties of HMA mixture determined by lab testing;
- ΔK = SIF amplitude, depending on the geometry of pavement structure, fracture mode, and crack length.

The number of loading cycles N_f needed to propagate a crack (C_o) through the pavement thickness, h , can be estimated by numerical integration in the form of Equation 3.20.

$$N_f = \int_{C_o}^h \frac{dc}{A(\Delta K)^n} \quad (3.20)$$

SIF is one of the key parameters in Paris' law. Consequently, the rapidness and accuracy of computing SIF values becomes a critical aspect of crack propagation analysis. Currently, two categories of SIF computation tools are available.

The first category includes commercial FE packages (such as ABAQUS, ANSYS, etc) which are general- or rather multi-purpose. There are complex in nature and not user friendly, therefore it is very time consuming and often not ideal for most practicing

pavement engineers and researchers. Furthermore, these commercial FE packages are relatively costly and require licenses. The second category is those FE tools specifically developed for pavement SIF computation (such as CRACKTIP and CAPA). CRACKTIP was developed as a 2D FE program for thermal cracking by Lytton and his associates (25) at the Texas Transportation Institute (TTI) in 1976. This program has been successfully used to develop the thermal SIF model for low-temperature cracking prediction in the SHRP A-005 research project (4). However, the difference between 2D plane strain conditions and the 3D nature of a cracked pavement and traffic loading often leads to a significant overestimation of the displacements and consequently the computed SIF values under the same load. The other pavement SIF program CAPA (Computer Aided Pavement Analysis) was developed at the Delft University of Technology in the 1990s (76, 77). The CAPA-3D program has some special functions to address the reflection cracking issue; such as special elements for simulating interfaces and interlayers, automatic remeshing techniques to simulate crack propagation, etc. Unfortunately, due to its 3D characteristics, the hardware and execution time demands render it suitable primarily for research purposes. Thus there is great need to find a means to both improve the calculation speed and reduce the resource requirement without the loss of accuracy.

3.10.2 SA-CRACKPRO: A New Crack Propagation Analysis Tool

One of the methods that seems most promising for achieving the aforementioned objective is the method known as Semi-Analytical (SA) FE method. This method can

effectively transform a 3D pavement analysis problem to an equivalent 2D model pavement, at a significant saving in terms of the computational effort (78). Built on this method, a new specific pavement crack propagation analysis tool, SA-CrackPro, was developed. SA-CrackPro has a much smaller number of equations and a matrix with a narrower bandwidth than the 3D FE programs. Also, it has a much smaller amount of input and output data because of the smaller number of nodes. Consequently, it needs much shorter computing time, input data preparation time, and resulting cleaning up time. This computational efficiency makes it possible to extensively analyze crack propagation in fatigue and reflection cracking prediction analysis. The main features of this SA-CrackPro are presented in this section.

3.10.3 Isoparametric Quadratic "Quarter-Point" Element

Quarter-Point elements were developed by Henshell and Shaw (79) in 1975 and Barsoum (80) in 1976. Henshell and Shaw described a quadrilateral quarter-point element illustrated in Figure 3.26a. Barsoum proposed collapsing one edge of the element at the crack tip, where the crack-tip nodes (1, 4, 8) are constrained to move together, as shown in Figure 3.26b.

The expressions for extracting the SIF values using plane strain assumptions (81) are given in Equations 3.21 and 3.22, and the corresponding FE meshing around the crack tip is shown in Figure 3.27.

$$K_I = \frac{G\sqrt{2\pi}}{\sqrt{r_{a-b-c}}(4-4\mu)} [4(u_d - u_b) + (u_c - u_e)] \quad (3.21)$$

$$K_{II} = \frac{G\sqrt{2\pi}}{\sqrt{r_{a-b-c}}(4-4\mu)} [4(v_d - v_b) + (v_c - v_e)] \quad (3.22)$$

where

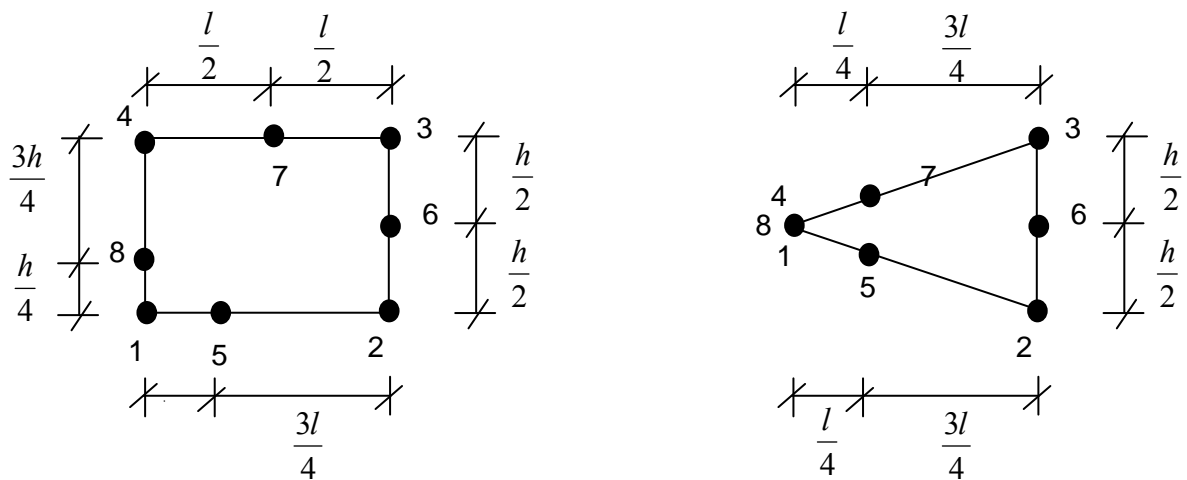
r_{a-b-c} = the distance from a crack tip point 'a' to point 'c';

K_I, K_{II} = SIF values for Mode I (opening crack mode) and Mode II (shearing crack mode), respectively;

G = shearing elastic modulus ($= E / 2(1 + \mu)$ for isotropic element);

μ = Poisson's ratio;

u_i, v_i = x, y displacements at point i .



(a) Quadrilateral quarter-point element

(b) Collapsed quadrilateral

Figure 3.26. (a) Quadrilateral and (b) Collapsed quadrilateral quarter-point element.

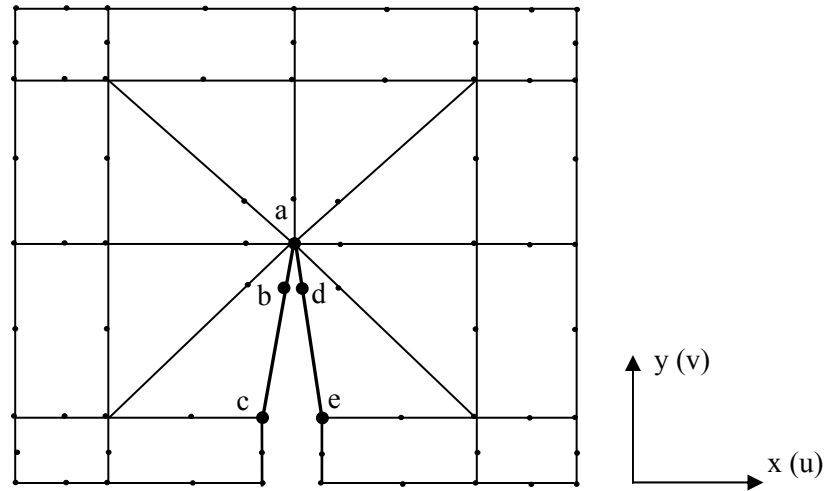


Figure 3.27. Finite elements meshing around crack tip.

These researchers found that the proper crack-tip displacement, stress, and strain fields can be modeled using isoparametric finite elements with standard quadratic order, if one simply moves the element's mid-side node to the position one quarter of the way from the crack tip to the far end of the element. Since these elements are standard and widely available, FE programs can easily be used to model the crack tip fields accurately with only minimal preprocessing required. Quarter-point elements here applied in the SA-CracPro easily and efficiently. The results of calculating SIF values are stable when adopting different meshing sizes in a reasonable range.

3.10.4 Thin-Layer Elements for Simulating Pavement Layer Contact Condition and Load Transfer Efficiency at Joints/Cracks

It is a well known fact that contact conditions between the pavement layers have significant influence on pavement response and accordingly on crack propagation. Thus, it is ideal for a crack propagation analysis tool to have the capability to simulate various pavement layer contact conditions from fully continuous to fully slipping. This is also true for the load transfer conditions at joints and/or cracks due to the aggregate interlock or the joint load transfer in PCC pavements. To simulate these conditions, the concept of thin-layer interface elements was used in SA-CrackPro. The advantages of using the thin-layer interface elements are listed below:

- The thin-layer element method can provide satisfactory solutions;
- It can be computationally more reliable than the zero thickness elements; and
- It is possible to handle various deformation modes such as fully continuous, fully slipping, or in between.

3.10.5 Automatic Meshing and Re-meshing Technique for Crack Propagation

Finite element meshing is always an uneasy work, especially for a cracked pavement structure, such as an HMA overlay over PCC pavements. For a specific crack, both quarter elements surrounding the crack tip and standard elements are required. Furthermore, these elements have to be re-meshed along each crack increment, which often makes crack propagation and the associated SIF computation tedious. To

overcome these difficulties, a series of element meshing and re-meshing algorithms were developed and implemented in SA-CrackPro. With known pavement structure thickness, material properties (modulus and Poisson ratio), and crack length, SA-CrackPro can automatically simulate the crack propagation in the vertical direction towards the pavement surface and calculate the corresponding SIF values.

3.11 Temperature Prediction Model in Hot Mix Asphalt Overlay

Many measurements of pavement temperature variations over time and depth have been reported in the literature. Also, fundamental early models of heat transfer in pavements, involving shortwave solar radiation, down-welling and upwelling long-wave radiation, and convective heat transfer at pavement surfaces and heat conduction inside the pavement have been thoroughly discussed (70, 82,83, 84, 85, 86). Following these endeavors, a one-dimensional coupled heat and moisture simulation model, the enhanced integrated climatic model (EICM), was developed and later integrated into the current mechanical-empirical pavement design guidance (MEPDG) to couple pavement design with modeled pavement temperature (64).

The EICM model uses a finite difference approximation for calculating heat conduction within the pavement and underlying layers, subject to heat fluxes at the surface (shortwave solar radiation, long-wave radiation, and convective heat transfer) and a constant-temperature boundary condition well below the pavement. Using required climatic input data including solar radiation, ambient temperature, and wind speed and

constant model parameters such as albedo, emissivity, and thermal diffusivity; the model computes numerically changes in temperature and moisture over time and with depth.

Although temperatures predicted with the EICM model satisfy pavement design needs in general, there have been some large errors when compared to measured pavement temperature (66) as shown in Figure 3.28. These errors are most likely caused by several factors: the assumption that heat fluxes at the pavement surface are exactly balanced by conduction into the ground well below the surface, inaccuracy of climatic data (especially calculated solar radiation), and the assumptions of the constant temperature boundary condition and site-independent model parameter values.

Recently, significant improvement over the EICM model has been achieved by several groups using a similar one dimensional heat transfer model, but with an unsteady-state surface heat flux boundary condition, measured model input data, and site-specific model parameters that were optimized based on measured pavement temperatures (67, 68, 69).

In this dissertation, an improved one-dimensional mathematical model, coupled with site-specific model parameters and recent improvements in the availability of required input climatic data, was used to calculate pavement temperatures nationwide. This model was developed by Rongbin Han, et al. from the Artie McFerrin Department of Chemical Engineering at Texas A&M University (70). The required input climatic data are: (in order of importance) solar radiation, air temperature, and wind speed. Hourly solar radiation and daily average wind speed can be obtained directly from existing databases. Hourly air temperatures were imputed from commonly recorded

daily maximum and minimum air temperatures. Parameter estimation identified three critical site-specific model parameters: the albedo, the difference between the emissivity and absorption coefficients, and the absorption coefficient. The national distribution of these model parameters, optimized at 29 pavement sites based on the average hourly absolute error objective function, appears to correlate with climatic patterns, suggesting interpolating those parameters based on climate. The temperature model, proposed data sources, and methods provided calculations that agreed well with experimental measurements as shown in Figure 3.29.

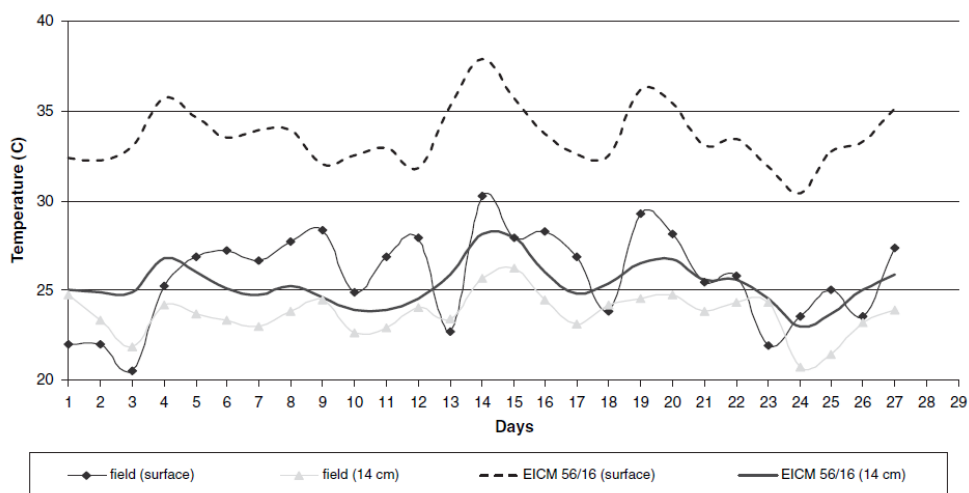


Figure 3.28. Typical daily pavement temperature prediction using EICM model (66).

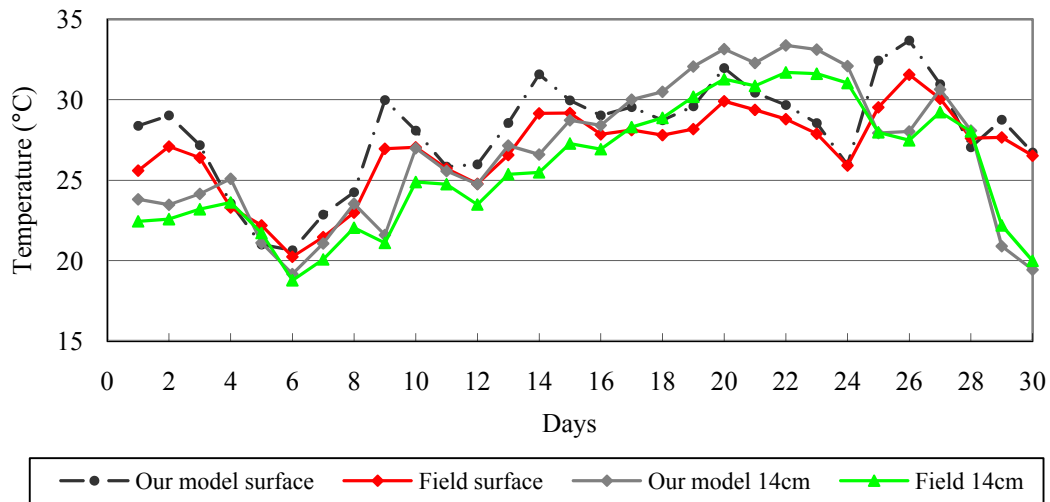


Figure 3.29. Typical daily pavement temperature prediction using improved model.

3.11.1 Heat Transfer in Pavement

The one dimensional model was developed based on radiation and conduction energy balance fundamentals. The heat transfer process is depicted in the schematic shown in Figure 3.30. There are multiple sources of heat transfer at the pavement surface: solar radiation and reflection of the solar radiation at the surface by a fraction $\tilde{\alpha}$, the albedo, absorption of atmospheric down-welling long-wave radiation by the pavement surface, emission by long-wave radiation to the atmosphere, and convective heat transfer between pavement surface and the air close to the surface, which is enhanced by wind.

Heat transfer in the pavement is governed by the classical thermal diffusion equation:

$$\frac{\partial T}{\partial t} = \alpha \frac{\partial^2 T}{\partial x^2} \quad (3.23)$$

where

T = pavement temperature as a function of time and depth below the surface (x);

α = thermal diffusivity, $\alpha = k / \rho C$;

k = thermal conductivity;

ρ = density;

C = pavement heat capacity.

Together with this equation, we consider a flux boundary condition at the pavement surface and a second flux condition at 3 m below the surface are considered.

3.11.2 The Surface Boundary Condition

Considering a differential element of the pavement surface, the thermal energy (temperature) changes to the extent the fluxes from above and below does not balance.

The various fluxes shown in Figure 3.30 lead to the following surface condition:

$$\rho C \frac{\Delta x}{2} \frac{\partial T_s}{\partial t} = Q_s - \tilde{\alpha} \cdot Q_s + Q_a - Q_r - Q_c - Q_f \quad (3.24)$$

where

ρC = volumetric heat capacity of the pavement;

T_s = pavement surface temperature;

x = the depth below the pavement surface;

$\frac{\Delta x}{2}$ = the (differential) pavement thickness for the energy balance;

Q_s = heat flux due to solar radiation;

$\tilde{\alpha}$ = albedo of pavement surface, the fraction of reflected solar radiation;

Q_a = down-welling long-wave radiation heat flux from the atmosphere;

Q_r = outgoing long-wave radiation heat flux from the pavement surface;

Q_c = the convective heat flux between the surface and the air.

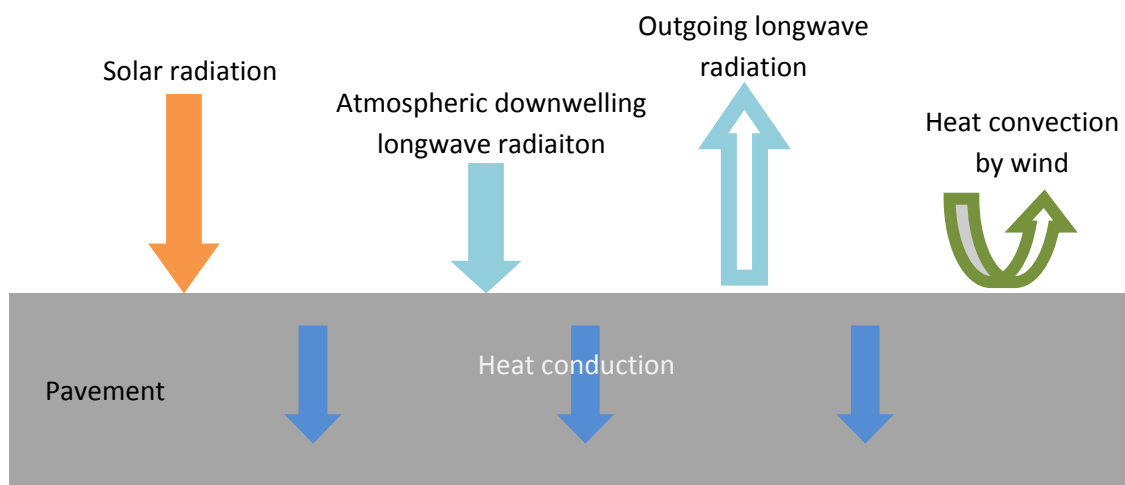


Figure 3.30. Schematic representation of heat transfer model of pavement.

The incoming and outgoing long-wave radiations are calculated by:

$$Q_a = \varepsilon_a \sigma T_a^4 \quad (3.25)$$

$$Q_r = \varepsilon \sigma T_s^4 \quad (3.26)$$

where

ε_a = absorption coefficient of pavement;

ε = emission coefficient of pavement;

T_s = pavement surface temperature;

T_a = air temperature.

$$\sigma = 5.68 \times 10^{-8} \text{ W} \cdot \text{m}^{-2} \text{ K}^{-4} \text{ (Stefan-Boltzman constant)}. \quad (3.27)$$

The convective heat flux is calculated as:

$$Q_c = h_c (T_s - T_a) \quad (3.28)$$

where

h_c = the heat transfer coefficient from the empirical equation (82);

$$h_c = 698.24 \cdot a \cdot [0.00144 (\text{abs}(\frac{T_s + T_a}{2}))^{0.3} U^d + 0.00097 (\text{abs}(T_s - T_a))^{0.3}] \quad (3.29)$$

U = the hourly wind speed;

a, d = two dimensionless empirical parameters.

The heat flux within the pavement at the surface is expressed by Fourier's equation:

$$Q_f = k \frac{\partial T_s}{\partial x} \quad (3.30)$$

where

T_s = pavement surface temperature;

k = thermal conductivity of asphalt concrete.

Combining these results, the following equation serves as the surface boundary condition:

$$\rho C \frac{\Delta x}{2} \frac{\partial T_s}{\partial t} = Q_s - \tilde{\alpha} \cdot Q_s + \varepsilon_a \sigma T_a^4 - \varepsilon \sigma T_s^4 - h_c (T_s - T_a) + k \frac{\partial T_s}{\partial x} \quad (3.31)$$

3.11.3 The Bottom Boundary Condition

Commonly, a constant-temperature boundary condition, some distance below the surface, is reported in the literature. For example, Hermansson (67) used the annual mean temperature 5 m below the surface as a bottom boundary condition. Gui (68) used a measured temperature of 33.5 °C at a depth of 3 m as the boundary condition. In the EICM model, temperatures were measured from water wells across the United States at a depth of 10 to 18 m, from which an isothermal map was constructed. Such a constant-temperature boundary condition has the advantage of simplicity.

For this dissertation, an alternate approach was used. From measured data in the LTPP database (36), it was observed that temperatures at a depth beyond 2 m tend to vary approximately linearly with depth. Using this result, an alternate boundary condition was used at a depth of 3 m.

$$\left. \frac{\partial T}{\partial x} \right|_{3m} = \text{independent of depth} \quad (3.32)$$

Such a boundary condition, which is based on field observation, has the advantage over the constant boundary condition in that it is location independent and does not require a specific value for the boundary condition. In addition, it is quite straightforward to implement this boundary condition in the finite difference calculation procedure. Of course, this linear variation with depth condition is not strictly correct as extrapolating it too great a depth will lead to significant error.

3.11.4 Optimization and Interpolation of Model Parameters

Although albedo, emissivity and the absorption coefficient are site specific, there is no clear understanding of how these parameters vary with climate and pavement properties. To address this issue, parameter optimization has been conducted for these model parameters at 29 pavement sites across the United States by comparing model estimates of pavement temperature to reported measurements. Two separate sets of model parameters have been obtained, one set for the winter and one set for the other seasons (represented by summer), to take into account this seasonal variation. Then from further analysis of the distribution and seasonal variation of those model parameters,

interpolation strategies have been developed for each model parameter and are presented below.

The algorithm to find values of the three parameters identified by sensitivity analysis (albedo, difference between emissivity and absorption coefficient, and the absorption coefficient) was straightforward. Each parameter was given a range of values and increments within the range based on literature reports. By examining the ability of each set of model parameters to give the best match between the measured and the calculated pavement temperatures, the optimum set was obtained. As a measure of the model's accuracy, the average hourly absolute difference between the measured and the calculated pavement temperatures was used. This estimation method using average of absolute error is preferred to, for example, the least-squares error by which a section with unusual properties receives more weight than a section with more normal properties.

Albedo

Figure 3.31 shows the distribution of the optimized albedo values across the United States in the 29 pavement sites for both summer and winter. As seen in Figure 3.31a, the summer optimized albedo values for most of the pavement sites is constant at 0.2, with a slight variation from 0.2 to 0.15 in several pavement sites in Texas. In the winter (Figure 3.31b), the optimal albedo values in the southern part of the United States are the same as in the summer, while the albedo values in the north increased from 0.2 to from 0.3 to 0.35. Although the exact reason for the albedo increase in the winter in the north is not clear, it seems the pavement surface property changes associated with snow

coverage and the freezing state in the winter likely is a key. Similar observations and conclusions have been reported in the literature (67, 87).

This hypothesis was validated by plotting the optimized winter albedo values on a national snowfall map from the National Climatic Data Center (NCDC) that was generated based on the average of recorded data from 1961 to 1990 (Figure 3.31c). This snowfall map also matches the NCDC freezing state distribution across the United States, recorded from 1961 to 1990. Clearly, in the southern regions the albedo values are the same in winter and in summer and range from 0.15 to 0.2, while in northern regions with heavy snowfall and freeze condition, the albedo values changed from 0.2 in summer to from 0.3 to 0.35 in the winter. There exists a distinct separating line, snowfall of 48 inches, which separates the northern and southern regions. From these results, it seems that the seasonal albedo variation of pavement is more affected by the freezing state and snowfall, and less affected by other environmental factors and material properties of the pavement.

To interpolate albedo values at other pavement sites, a reasonable approach is to use the snowfall distribution map across the United States as a reference with 48 inches snow fall to separate the northern and southern parts of the United States. As the albedo value in each region is quite stable in either the winter or summer, albedo values obtained at the nearest pavement site in the same region, based on 29 pavement sites studied in the dissertation, can simply be interpolated to give the albedo value for the specific pavement site. Alternatively, the albedo value at the nearest three pavement sites

in the same regions can be averaged to obtain the albedo value at the pavement site of interest.

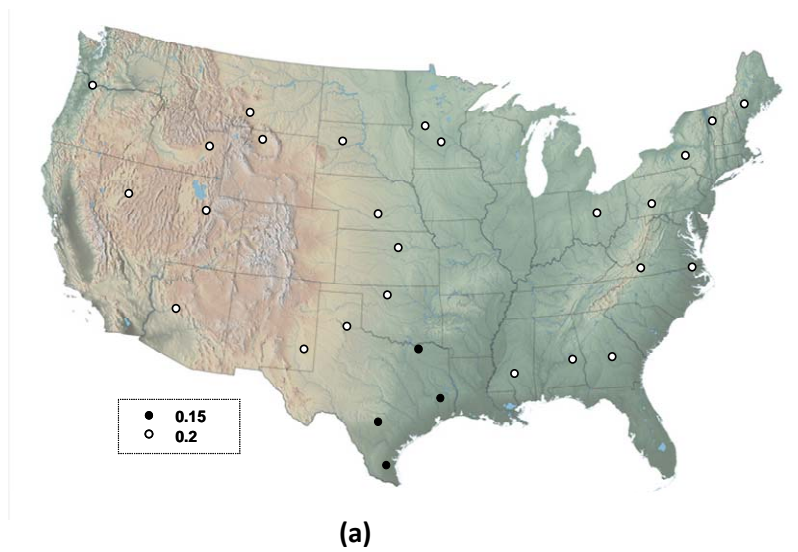


Figure 3.31. Optimized albedo values in: (a) Summer, (b) Winter, (c) Winter optimized albedo values on an annual average snowfall map.

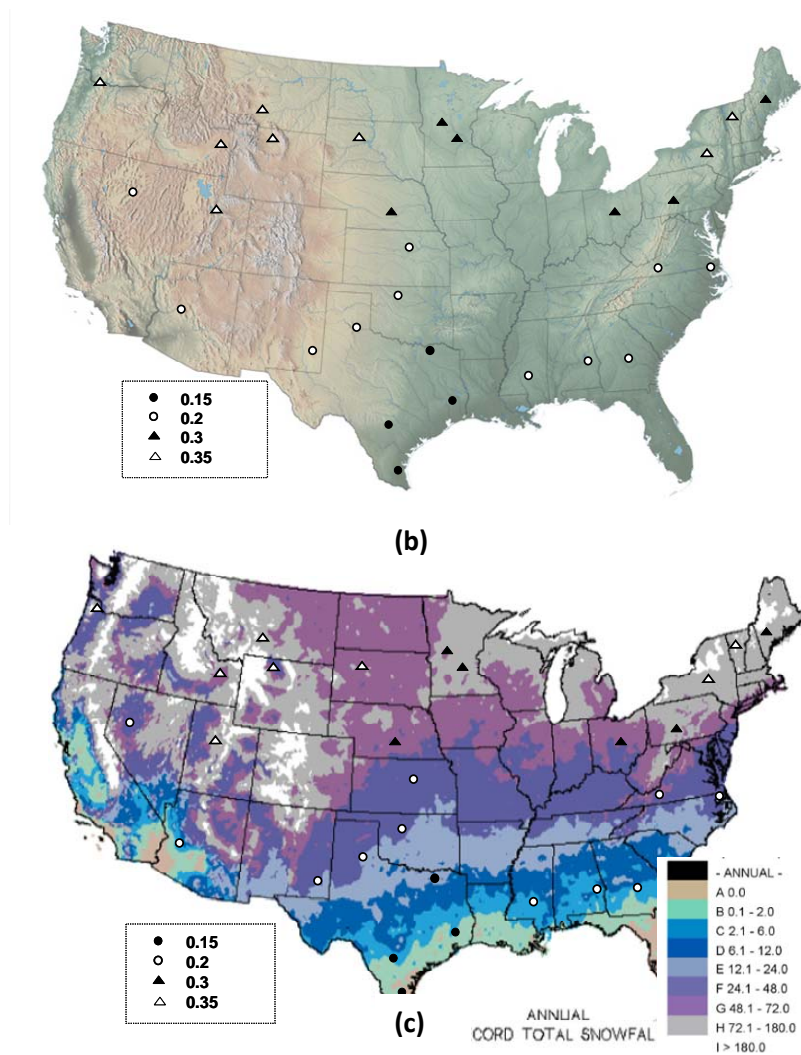


Figure 3.31. Continued.

Since snowfall and freeze conditions vary with time, ground albedo values have been recorded daily or monthly using satellite remote sensing techniques, commonly with a resolution of 10 km across the United States. These observations support the conclusion that distinctly higher values of albedo occur during winter snow coverage and freeze than during other periods. Satellite recorded albedo values have been

collected in several databases that can be easily accessed (NCDC or NSRDB). For any specific pavement site and year of interest, recorded albedo data from these databases at the nearest location can be extracted. The winter period suggested by high albedo values in those databases may then be used to define the winter period for pavement calculations.

Algebraic Difference between Emissivity and Absorption Coefficient

The second important model parameter is the algebraic difference between the pavement emissivity and absorption coefficient. Figure 3.32 shows the optimized values of the parameter for the 29 national pavement sites displayed on a national terrain map in both winter (Figure 3.32a) and summer (Figure 3.32b). Four different values were obtained (0.05, 0.1, 0.15 and 0.2) but distribution patterns that follow climatic regions can be noted. Four environmental regions that correspond generally to those four values are shown in Figure 3.32. Region A covers the northeast and east north central regions and generally experiences a humid climate with long winters. The optimized value for the algebraic difference in this region generally is 0.05. Region B, the southeast areas and part of the south is located in a mesothermal zone with humid sub-tropical climate. An optimized value of 0.1 is common for pavement sites in this region. Region D covers the western part of the United States, especially mountain regions and a dry, cold climate is dominant. Here a value of 0.2 was generally obtained in the winter while in the summer a value of 0.15 was obtained. Region C is a transition zone between Regions B and D, and a value of 0.15 was commonly obtained, both winter and summer. Despite

several slight deviations, the optimized value for the algebraic difference in most of the pavement sites followed these general trends reasonably well.

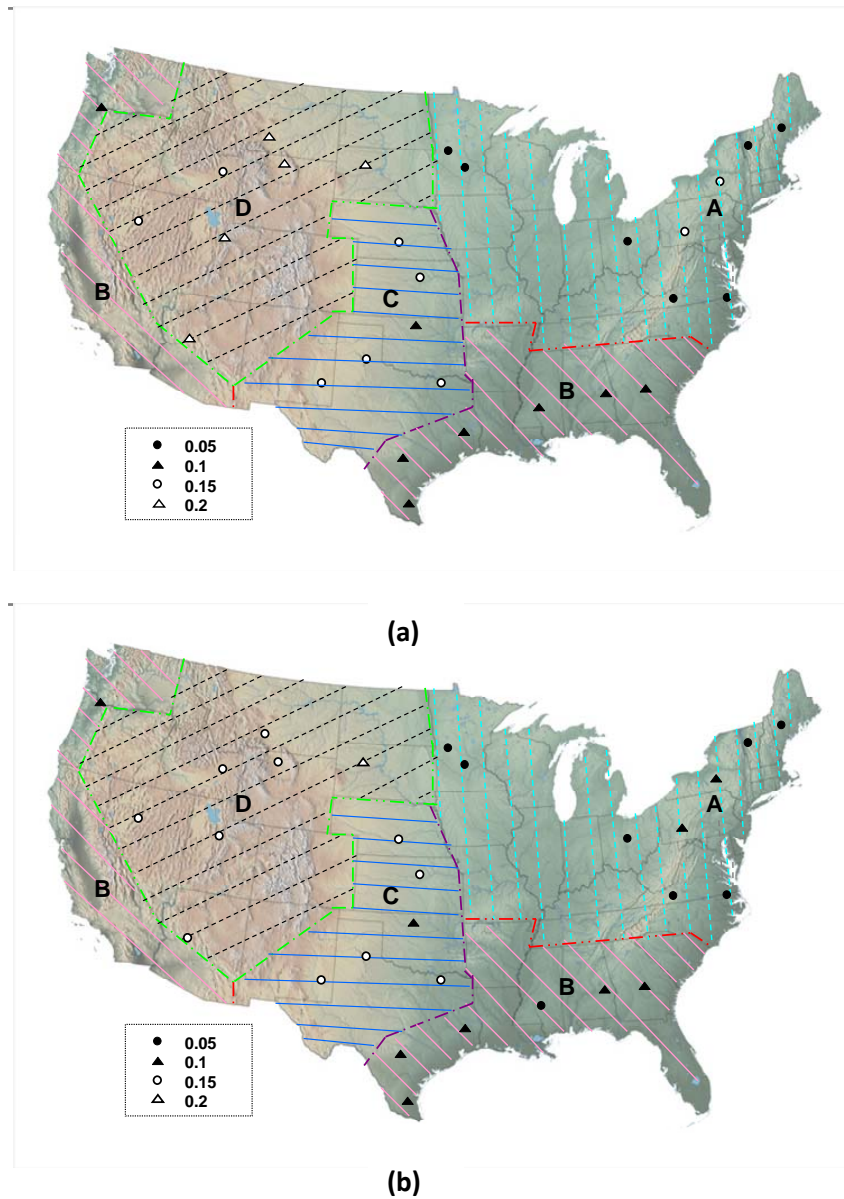


Figure 3.32. Optimized values of the algebraic difference between emissivity and absorption coefficients: (a) Summer (b) Winter.

Previous studies have suggested that the absorption coefficient is mainly affected by the water partial pressure in the air. A linear relationship between absorption coefficients with partial pressure in a clear sky condition have been further developed using linear regression techniques (88). It also has been known that the long-wave emissivity of a pavement is mainly affected by the pavement surface property and environmental conditions such as snow coverage (87). From this perspective, it is not surprising to see that the optimized values of the algebraic difference between the emissivity and absorption coefficients varies from winter to summer at pavement sites in Region D, most likely due to climatic effects. As emissivity also is affected by site-specific pavement surface properties, small deviations from the general trends of the climatic regions are reasonable.

With a known pavement location, values of the difference between the emissivity and absorption coefficient for any pavement site in each region can be obtained based on these observed trends. More realistically, and to consider possible deviations from the general trends caused by different pavement material properties, parameter values obtained from the nearest three pavement sites (of the 29 sites studied in this research) and in the same climatic region, can be averaged to obtain a value for the specific pavement site.

Absorption Coefficients

The third important parameter is the absorption coefficient for down-welling long-wave radiation from the air. Figure 3.33 shows the estimated value of the absorption coefficients for the 29 pavement sections. As the absorption coefficient is mainly affected by the water partial pressure in the air, these optimized values are shown on a national relative humidity distribution map (from NCDC) based on average recorded data from 1961 to 1990. The optimized values in both winter and summer are exactly the same, indicating the parameter is less affected by seasonal variation (data not shown). Two values of the absorption coefficient, 0.75 in the east and south (and northwest) coastal regions and 0.7 in the dryer Midwest to west regions were observed.

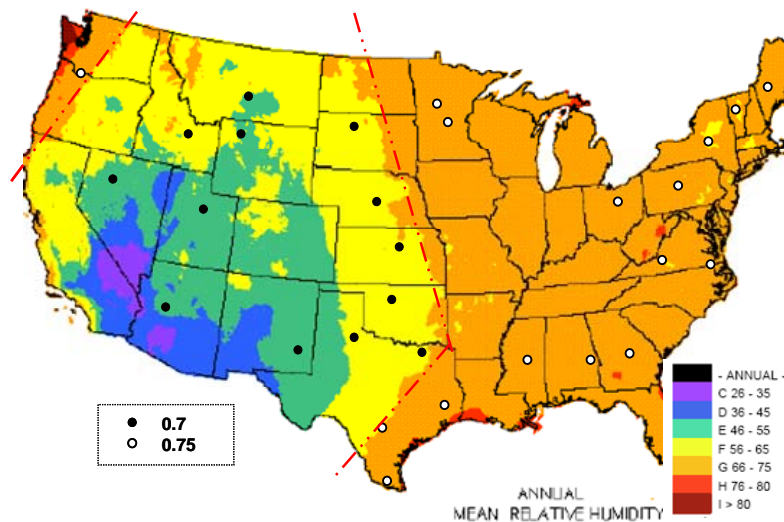


Figure. 3.33 Optimized values of absorption coefficients.

3.12 Mixture Properties Determination

The properties of a hot mix asphalt mixture in an overlay must be estimated both accurately and with computational efficiency to achieve an overlay design which is resistant to reflection cracking. The stiffness and compliance of the mixture must be calculated at widely different temperatures and loading rates (thermal and traffic). The tensile strength must also be calculated over the same wide ranges of temperature and loading rates. The fracture properties (i.e., Paris and Erdogan's Law coefficients) must be calculated. These coefficients are also sensitive to temperature and loading rates. For these reasons, ANN algorithms which reproduce Witczak's 1999 (2) and 2006 (3) Complex Modulus models were developed to form the basis for calculating the overlay stiffness under traffic loads and computing the viscoelastic thermal stress for thermal reflection cracking. The method by which ANN algorithms are constructed is described in the literature (89). The accuracy with which it reproduces the Witczak Complex Modulus models is described. The tensile strength was determined by Schapery (55, 56) to be an important variable in making realistic estimates of the Paris and Erdogan's Law fracture coefficient, A . Earlier studies presented tensile strengths obtained from field cores taken from pavement sections well distributed around the United States and Canada (4, 74) and were considered to be representative of as constructed hot asphalt mixtures. The calibration coefficients from these studies (4) could be used to predict both thermal and traffic related reflection cracking and healing between traffic loads.

3.12.1 Complex Modulus by Artificial Neural Network

This dissertation provides two ANN (Artificial Neural Network) models which developed by Dr. Halil Ceylan (89) to calculate complex modulus which are 1999 ANN complex modulus model and 2006 ANN complex modulus model. These ANN models were developed from the Wiczak 1999 (2) and 2006 (3) models. Both models are available for the thermal case, and the 2006 ANN model is designed for use in both thermal and traffic cases.

ANN 1999 Wiczak Model

The ANN 1999 Wiczak model is only available for the thermal case.

Required Input Information:

- Gradation (3/4, 3/8, #4, #200)
- Volumetric (V_a , and V_{beff})
- Dynamic Viscosity ($Log\eta$, (poise))
- Frequency ($\omega(T)$, (Hz))

The frequency $\omega(T)$ (rad/sec.) is shown in Equation 3.33. t_i is loading time.

$$\omega(T) = \frac{1}{2t_i} \left(\frac{rad.}{sec.} \right) \quad (3.33)$$

The calculations of loading times t_i for each part are shown in the below:

- 292 loading times are calculated by tire length of each axle (single, tandem, triple, and quad) and desired velocity shown in the Table 3.23. These loading times would be used to calculate ANN relaxation modulus and ANN SIF (Stress Intensity Factor).
- 18 loading times for $0.1 \times t_{category}$, $t_{category}$, $10 \times t_{category}$ are used to calculate m_{mix} for the calculation of Paris's law fracture properties A and n . The equations of loading time for each category are shown in Table 3.24:
- 3 FWD loading times : $0.1 \times \frac{t_{FWD}}{a_T}$, $\frac{t_{FWD}}{a_T}$, and $10 \times \frac{t_{FWD}}{a_T}$ are used to calculate the E_1 in the fracture properties calculation.

$$a_T = 10^{\frac{-C_1(T_{FWD}-T_D)}{C_2+T_{FWD}-T_D}}, t_{FWD} = 0.06 \text{ (sec.)}$$

The dynamic viscosity at the different temperatures is a function of the binder shear modulus, frequency of the master curve, and the slope of the $G^*(T)$ versus frequency curve.

$$\eta = \frac{|G^*(T)|}{m(T) \times [2 \times \omega_0(T)]^{1-m(T)}} \text{ (Gpa} \cdot \text{s)} \quad (3.34)$$

where

$G^*(T)$ = the binder shear modulus (Gpa);

$\omega_0(T)$ = the frequency of the master curve;

$m(T)$ = the slope of the shear modulus ($G^*(T)$) versus frequency (ω) curve.

Table 3.23. Loading times for different axles.

Axles	Loading Times (sec.)
Single Axle	$\frac{(10' + L_i)(ft)}{Velocity\left(\frac{ft}{sec.}\right)}$
Tandem Axle	$\frac{(14' + L_i)(ft)}{Velocity\left(\frac{ft}{sec.}\right)}$
Tridem Axle	$\frac{(18' + L_i)(ft)}{Velocity\left(\frac{ft}{sec.}\right)}$
Quadrem Axle	$\frac{(22' + L_i)(ft)}{Velocity\left(\frac{ft}{sec.}\right)}$

Table 3.24. Load times for different categories.

	$0.1 \times t_{category}$	$t_{category}$	$10 \times t_{category}$
Category 1	$0.1 \times \frac{(10' + 0.99)(ft)}{Velocity\left(\frac{ft}{sec.}\right)}$	$\frac{(10' + 0.99)(ft)}{Velocity\left(\frac{ft}{sec.}\right)}$	$10 \times \frac{(10' + 0.99)(ft)}{Velocity\left(\frac{ft}{sec.}\right)}$
Category 2	$0.1 \times \frac{(10' + 0.45)(ft)}{Velocity\left(\frac{ft}{sec.}\right)}$	$\frac{(10' + 0.45)(ft)}{Velocity\left(\frac{ft}{sec.}\right)}$	$10 \times \frac{(10' + 0.45)(ft)}{Velocity\left(\frac{ft}{sec.}\right)}$
Category 3	$0.1 \times \frac{(14' + 0.9)(ft)}{Velocity\left(\frac{ft}{sec.}\right)}$	$\frac{(14' + 0.9)(ft)}{Velocity\left(\frac{ft}{sec.}\right)}$	$10 \times \frac{(14' + 0.9)(ft)}{Velocity\left(\frac{ft}{sec.}\right)}$
Category 4	$0.1 \times \frac{(14' + 0.41)(ft)}{Velocity\left(\frac{ft}{sec.}\right)}$	$\frac{(14' + 0.41)(ft)}{Velocity\left(\frac{ft}{sec.}\right)}$	$10 \times \frac{(14' + 0.41)(ft)}{Velocity\left(\frac{ft}{sec.}\right)}$
Category 5	$0.1 \times \frac{(18' + 0.9)(ft)}{Velocity\left(\frac{ft}{sec.}\right)}$	$\frac{(18' + 0.9)(ft)}{Velocity\left(\frac{ft}{sec.}\right)}$	$10 \times \frac{(18' + 0.9)(ft)}{Velocity\left(\frac{ft}{sec.}\right)}$
Category 6	$0.1 \times \frac{(18' + 0.41)(ft)}{Velocity\left(\frac{ft}{sec.}\right)}$	$\frac{(18' + 0.41)(ft)}{Velocity\left(\frac{ft}{sec.}\right)}$	$10 \times \frac{(18' + 0.41)(ft)}{Velocity\left(\frac{ft}{sec.}\right)}$
Category 7	$0.1 \times \frac{(22' + 0.68)(ft)}{Velocity\left(\frac{ft}{sec.}\right)}$	$\frac{(22' + 0.68)(ft)}{Velocity\left(\frac{ft}{sec.}\right)}$	$10 \times \frac{(22' + 0.68)(ft)}{Velocity\left(\frac{ft}{sec.}\right)}$
Category 8	$0.1 \times \frac{(22' + 0.31)(ft)}{Velocity\left(\frac{ft}{sec.}\right)}$	$\frac{(22' + 0.31)(ft)}{Velocity\left(\frac{ft}{sec.}\right)}$	$10 \times \frac{(22' + 0.31)(ft)}{Velocity\left(\frac{ft}{sec.}\right)}$

The frequency of the master curve, $\omega_0(T)$ (rad/sec.) at the different temperatures is

$$\omega_0(T) = \omega(T) \times a_T = \omega(T) \times 10^{\frac{-C_1(T-T_D)}{C_2+T-T_D}} \left(\frac{rad.}{sec.} \right) \quad (3.35)$$

The slope of the $\log G^*(T)$ versus $\log \omega$ curve, $m(T)$ at the different temperatures is

$$m(T) = \frac{\left[\frac{\omega_{rm}}{\omega_0(T)} \right]^{\frac{\log 2}{R}}}{1 + \left[\frac{\omega_{rm}}{\omega_0(T)} \right]^{\frac{\log 2}{R}}} \quad (3.36)$$

The binder shear modulus $G^*(T)$ at the different temperatures is

$$|G^*(T)| = \frac{G_g}{\left[1 + \left[\frac{\omega_{rm}}{\omega_0(T)} \right]^{\frac{\log 2}{R}} \right]^{\frac{R}{\log 2}}} (Gpa) \quad (3.37)$$

where G_g , ω_{rm} , and R are coefficients that depend on the level we choose. In keeping with the MEPDG format, the binder data can be input at any of three levels. The binder data are the six properties of the CAM model, i.e., G_g , the glassy modulus in Gpa, R ,

the Rheological Index, ω_m , the cross-over frequency in rad/sec, T_d , the defining temperature in °C, and the two time-temperature shift parameters, C_1 and C_2 (90). The user may input these six properties with Level 1 input. In Level 2 input, the user may specify the Performance Grade (PG grade) of the binder and the climatic region in which the overlay is to be placed and the program internally calculates the six CAM parameters that correspond to the PG grade specified. In Level 3 input, the user only needs to specify the climatic region where the overlay was built. These simplifications can be made because the mean values of the six CAM parameters for each of the four climatic regions in North America are stored. A total of 48 sets of CAM parameters were measured on binders extracted from cores (4). The mean values for each of the climatic regions are listed in Table 2.25.

Table 2.25. Mean CAM model parameters for the four climatic regions.

Climatic Region	ω_m (rad/sec)	R	T_d (°C)	C_1	C_2	G_g (Gpa)
Wet-Freeze	0.01516	1.935	-5.8	31.57	199.2	0.861
Wet-No Freeze	7.06E-05	2.261	-6.41	42.49	259.3	0.906
Dry-Freeze	0.001397	2.286	-6.22	38.77	239.0	1.571
Dry-No Freeze	0.000845	2.032	-6.07	41.55	266.9	0.532

ANN 2006 Model – Thermal and Traffic Cases

The ANN 1999 Witczak model was available for the traffic and thermal cases.

Required Input Information:

- Gradation (3/4, 3/8, #4, #200)
- Volumetric (V_a , and V_{beff})
- Phase Angle ($\delta(T)$ (radians))
- Binder Shear Modulus ($G^*(T)$ (GPa))

The phase angle $\delta(T)$ (radians) and binder shear modulus $G^*(T)$ (GPa) at the different temperatures are shown in the Equations 3.38 and Equation 3.39.

$$\delta(T) = m(T) \times \frac{\pi}{2} (\text{radians}) \quad (3.38)$$

$$|G^*(T)| = \frac{G_g}{\left[1 + \left[\frac{\omega_{rm}}{\omega_0(T)} \right]^{\frac{\log 2}{R}} \right]^{\log 2}} (Gpa) \quad (3.39)$$

where

- $m(T)$ = the slope of the log $G^*(T)$ versus frequency curve;
- $\omega_0(T)$ = frequency of the master curve;
- G_g, ω_{rm} , and R = coefficients based on input levels.

- Level 1: User input $G_g, \omega_{rm}, C_1, C_2, T_d$, and R .
- Level 2: User input PG X-Y to find the G_g .
- Level 3: Parameters are varied by different climatic zones (Wet-Freeze, Wet-No Freeze, Dry-Freeze, and Dry-No Freeze).

The frequency of the master curve, $\omega_0(T)$ (rad/sec.) at the different temperatures is

$$\omega_0(T) = \omega(T) \times a_T = \omega(T) \times 10^{\frac{-C_1(T-T_D)}{C_2+T-T_D}} \left(\frac{\text{rad.}}{\text{sec.}} \right) \quad (3.40)$$

where

- a_T = the time-temperature shift factor;
- t_i = the loading time;
- $\omega(T)$ = frequency (rad/sec.) ($= (1/2)t_i$).

The loading times are different for traffic and thermal cases. For the thermal case, loading time was assumed to cover all the range of loading frequency (0.01 to 100,000 seconds). For the traffic case, loading times are related to the number of axles Table 3.23 and traffic categories Table 3.24.

The slope of the $\log G^*(T)$ versus $\log \omega$ curve, $m(T)$ at the different temperatures as shown in Equation 3.41.

$$m(T) = \frac{\left[\frac{\omega_{rm}}{\omega_0(T)} \right]^{\frac{\log 2}{R}}}{1 + \left[\frac{\omega_{rm}}{\omega_0(T)} \right]^{\frac{\log 2}{R}}} \quad (3.41)$$

The format of the Artificial Neural Network (ANN) relaxation modulus program is shown in the Table 3.26 and Table 3.27. The comparison of the ANN and Witzcak 1999 and 2006 models shows that the results from the ANN fit better than the Witzcak models Figure 3.34 and Figure 3.35. The R^2 of the ANN are 0.98 for 1999 model and 0.96 for 2006 model, and R^2 of Witzcak are 0.68 for 1999 model (2) and 0.77 for 2006 model (3).

Table 3.26. 1999 ANN relaxation model input format.

Gradation				Volumetric		Log $\eta(T)$	$\omega(T)$	Log $E^*(t,T)$
3/4	3/8	# 4	# 200	V_a	V_{beff}			
(%)	(%)	(%)	(%)	(%)	(%)	(Poise)	(Hz)	(psi)
4.00	20.00	56.00	6.00	6.30	8.95	9.68	25	6.45175
0	30	64.5	8.4	5.90	11.50	5.32	0.1	5.06911
0	23.4	48.9	5	8.95	9.92	11.79	25	6.63034
0	16	33	5	6.36	11.48	4.92	5	5.21269
0	16	33	5	6.36	11.48	6.48	5	5.87216
0	35	58.2	6.6	4.90	8.14	9.30	1	6.35392
10	35	51	3.5	7.17	8.91	4.56	0.1	4.42908
0.00	4.00	41.60	3.30	5.45	10.10	12.19	25	6.45609
0	13	42	6.1	7.17	11.09	4.21	0.5	4.89153
26.1	41	52.4	5.7	7.40	8.27	4.24	5	4.92430
10	35	51	3.5	10.77	8.12	7.03	0.1	5.56806
5.1	25.2	46.2	6.4	6.60	11.08	11.01	1	6.69364

Table 3.27. 2006 ANN relaxation model input format.

Gradation				Volumetric		Log $ G^* $ $\times 10^6$	$\delta(T)$	Log $E^*(t,T)$
3/4	3/8	# 4	# 200	V_a	V_{beff}			
(%)	(%)	(%)	(%)	(%)	(%)	(psi)	(deg)	(psi)
1.3	38	56	5.1	7.38	11.00	8.18	60.5	5.90
1.3	38	56	5.1	6.10	10.80	9.15	17.2	6.66
6.2	38.5	58	3.1	7.00	8.90	8.15	52.6	5.96
22.00	39.00	73.00	4.00	6.10	7.80	9.17	12.0	6.53
7.0	22.0	35.0	5.0	4.39	9.81	7.81	67.0	5.80
0.00	4.00	41.60	3.30	1.90	12.68	6.09	73.0	4.69
0	30	64.5	8.4	5.90	11.50	8.40	53.8	6.21
0	16	32	5	6.32	11.17	8.46	56.5	6.20
0	21	62	2.6	11.13	18.24	7.09	72.3	5.48
10	35	51	3.5	7.05	10.02	8.86	62.1	6.19
0	23.4	48.9	5	9.30	6.47	6.03	84.1	4.91
26.1	41	52.4	5.7	7.40	8.27	9.22	53.3	6.13
22.00	39.00	73.00	4.00	5.60	7.70	9.20	20.8	6.59

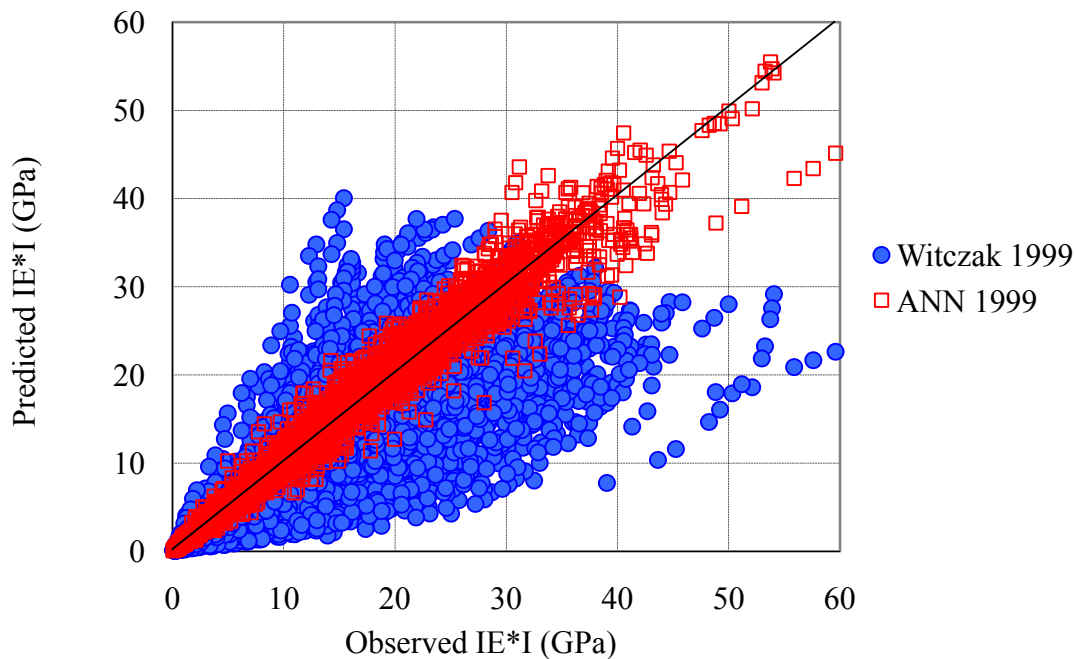


Figure 3.34. Comparison of Witczak 1999 model with artificial neural network algorithm.

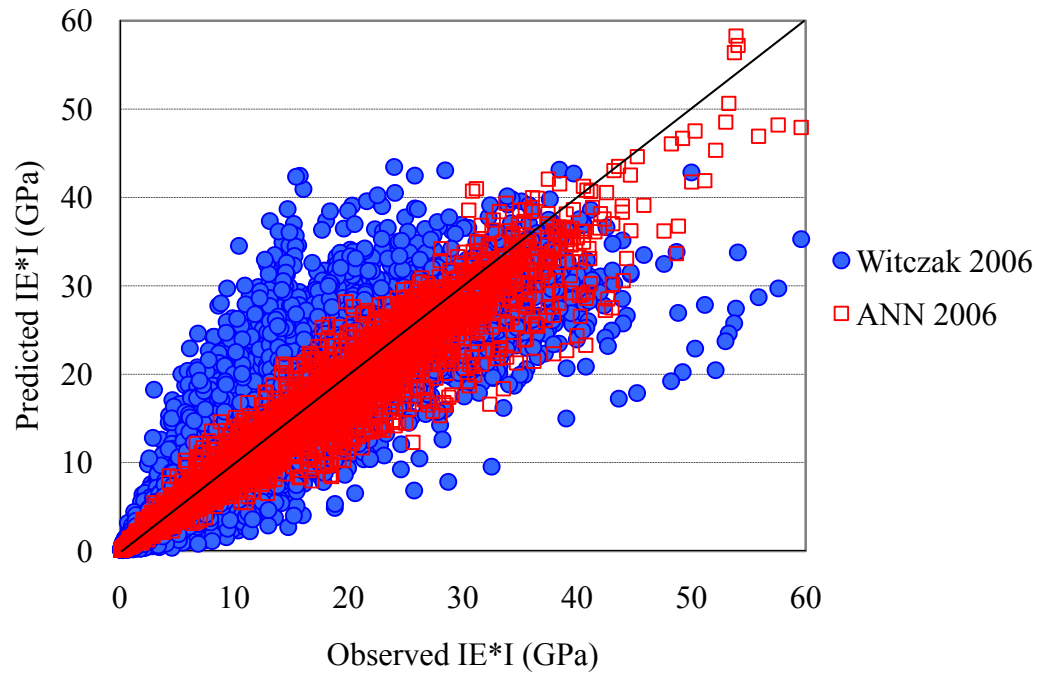


Figure 3.35. Comparison of Witczak 2006 model with artificial neural network algorithm.

3.12.2 Calculation of G_g for Level 2 Input

In the level 2 input, G_g is determined by the Superpave binder performance grading PG X-Y.

Determine G_g from X:

$$\text{Definition: } \frac{|G^*(x)|}{\sin \delta(x)} = 1.00 \text{ kPa @ } \omega(x) = 10 \frac{\text{rad.}}{\text{sec.}}$$

$$m(x) = m(\text{test temperature}) = \frac{\left[\frac{\omega_{rm}}{\omega(x) \cdot a_T} \right]^{\frac{\log 2}{R}}}{1 + \left[\frac{\omega_{rm}}{\omega(x) \cdot a_T} \right]^{\frac{\log 2}{R}}}$$

where ω_{rm} and R are the coefficient varied by different climatic zones;

$$a_T \text{ is shift factor} = 10^{\frac{-C_1(T_x - T_D)}{C_2 + T_x - T_D}}$$

$$\delta(x) = m(x) \times \frac{\pi}{2} (\text{radians})$$

$$|G^*(x)| = \frac{G_g}{\left[1 + \left[\frac{\omega_{rm}}{\omega(x) \cdot a_T} \right]^{\frac{\log 2}{R}} \right]^{\frac{R}{\log 2}}} (Kpa)$$

$$G_g = |G^*(x)| \times \left[1 + \left[\frac{\omega_{rm}}{\omega(x) \cdot a_T} \right]^{\frac{\log 2}{R}} \right]^{\frac{R}{\log 2}} (Kpa)$$

Determine G_g from Y:

Use the dynamic shear test temperature corresponding to the Y temperature.

$$\text{Definition: } \omega(y) = 10 \frac{\text{rad.}}{\text{sec.}}$$

Definition: $G^*(y) \times \sin \delta(y) \leq 5000 \text{ kPa}$

$$a_T = 10^{\frac{-C_1(T_y - T_D)}{C_2 + T_y - T_D}}$$

$$m(y) = m(\text{test temperature}) = \frac{\left[\frac{\omega_{rm}}{\omega(y) \cdot a_T} \right]^{\frac{\log 2}{R}}}{1 + \left[\frac{\omega_{rm}}{\omega(y) \cdot a_T} \right]^{\frac{\log 2}{R}}}$$

$$\delta(y) = m(y) \times \frac{\pi}{2} (\text{radians})$$

$$G^*(y) \leq \frac{5000}{\sin \delta(y)} (\text{Kpa})$$

$$G_g = |G^*(y)| \times \left[1 + \left[\frac{\omega_{rm}}{\omega(y) \cdot a_T} \right]^{\frac{\log 2}{R}} \right]^{\frac{R}{\log 2}} (\text{Kpa})$$

Comparison:

1. Compare $G_g(x)$ with $G_g(y)$, and choose the larger one
2. Compare this larger G_g with the regional G_g .

If $G_{g,\text{region}} > G_{g,\text{PGx-y}} > 0.5 * G_{g,\text{region}}$ use $G_{g,\text{PGx-y}}$

Otherwise use $G_{g,\text{region}}$

The results of G_g at different PG grading and different climatic zones are shown in the Table 3.28. This table is one of our databases. When a user chooses level 2 and inputs a PG grading, this program is able to select a G_g in the specified climatic zone.

Table 3.28. G_R database at different PG grading and climatic zones.

PG		Test temp. (°C)	Gg (Gpa)			
X (°C)	Y (°C)		WF	WNF	DF	DNF
46	-34	10	0.79428	0.90583	1.570837	0.301117
46	-40	7	0.552329	0.90583	1.570837	0.531575
46	-46	4	0.861218	0.90583	1.570837	0.531575
52	-10	25	0.861218	0.751501	1.570837	0.531575
52	-16	22	0.861218	0.533385	1.570837	0.531575
52	-22	19	0.861218	0.90583	1.103578	0.531575
52	-28	16	0.861218	0.90583	1.570837	0.531575
52	-34	13	0.861218	0.90583	1.570837	0.404961
52	-40	10	0.79428	0.90583	1.570837	0.301117
52	-46	7	0.552329	0.90583	1.570837	0.531575
58	-16	25	0.861218	0.751501	1.570837	0.531575
58	-22	22	0.861218	0.533385	1.570837	0.531575
58	-28	19	0.861218	0.90583	1.103578	0.531575
58	-34	16	0.861218	0.90583	1.570837	0.531575
58	-40	13	0.861218	0.90583	1.570837	0.404961
64	-10	31	0.861218	0.90583	1.570837	0.531575
64	-16	28	0.861218	0.90583	1.570837	0.531575
64	-22	25	0.861218	0.751501	1.570837	0.531575
64	-28	22	0.861218	0.533385	1.570837	0.531575
64	-34	19	0.861218	0.90583	1.103578	0.531575
64	-40	16	0.861218	0.90583	1.570837	0.531575

Table 3.28. Continued.

PG		Test temp. (°C)	Gg (Gpa)			
X (°C)	Y (°C)		WF	WNF	DF	DNF
70	-10	34	0.861218	0.90583	1.570837	0.531575
70	-16	31	0.861218	0.90583	1.570837	0.531575
70	-22	28	0.861218	0.90583	1.570837	0.531575
70	-28	25	0.861218	0.751501	1.570837	0.531575
70	-34	22	0.861218	0.533385	1.570837	0.531575
70	-40	19	0.861218	0.90583	1.103578	0.531575
76	-10	37	0.861218	0.90583	1.570837	0.531575
76	-16	34	0.861218	0.90583	1.570837	0.531575
76	-22	31	0.861218	0.90583	1.570837	0.531575
76	-28	28	0.861218	0.90583	1.570837	0.531575
76	-34	22	0.861218	0.533385	1.570837	0.531575
82	-10	40	0.861218	0.90583	1.570837	0.531575
82	-16	37	0.861218	0.90583	1.570837	0.531575
82	-22	34	0.861218	0.90583	1.570837	0.531575
82	-28	31	0.861218	0.90583	1.570837	0.531575
82	-34	28	0.861218	0.90583	1.570837	0.531575

3.12.3 Paris' Law - Fracture Properties A and n

Earlier studies (4, 5) provided formulas for the Paris and Erdogan's Law fracture coefficients A and n which were found to work well in predicting reflection cracking without being altered. The formulas presented in these studies had been calibrated to actual field fatigue cracking data in each of the four climatic zones. The form of the equations for both A and n were taken from viscoelastic crack growth theory by Schapery (55, 56).

$$n = g_0 + \frac{g_1}{m_{mix}} \quad (3.42)$$

$$\log A = g_2 + \frac{g_3}{m_{mix}} \log D_1 + g_4 \log \sigma_t \quad (3.43)$$

where

$g_0, g_1, g_2, g_3,$ and g_4 = the fatigue calibration coefficients;

m_{mix} = the log-log slope of the mixture modulus vs. loading time graph for the current temperature and loading rate,

$E(t, T)$ = the mixture relaxation modulus at loading time, t , (sec.) and temperature, T (in °C) (MPa),

D_1 = the coefficient of the mixture creep compliance expressed in a power law form (kPa^{-1}),

σ_t = tensile strength (kPa).

The fatigue calibration coefficients $g_0, g_1, g_2, g_3,$ and g_4 were developed in the SHRP A-003A project and reported in the SHRP Report A-357 (4). These coefficients are shown in Table 3.29 in all four climatic zones. The variable m_{mix} is the slope of the graph of the ANN relaxation modulus (E_t) versus the loading time (t_i). The three thermal loading times are based on the time during which the temperature is below the stress free temperature (20°C) as illustrated in Figure 3.36. These times are used to calculate the m_{mix} for the thermal case Figure 3.37. On the other hand, the traffic loading time was determined by the eight axle categories shown in Figure 3.38. Since the variance of pavement temperature could be significant, it was necessary to calculate the m_{mix} hourly.

Table 3.29. Fatigue calibration coefficients for four climatic zones.

	Wet-Freeze	Wet-No Freeze	Dry-Freeze	Dry-No Freeze
g_0	-2.09	-1.429	-2.121	-2.024
g_1	1.952	1.971	1.677	1.952
g_2	-6.108	-6.174	-5.937	-6.107
g_3	0.154	0.19	0.192	1.53
g_4	-2.111	-2.079	-2.048	-2.113
g_5	0.037	0.128	0.071	0.057
g_6	0.261	1.075	0.762	0.492
T_d (°C)	-5.8	-6.4125	-6.22	-6.07142857
C_1	31.57	42.49	38.77	41.55
C_2	199.21	259.28	239.04	266.89

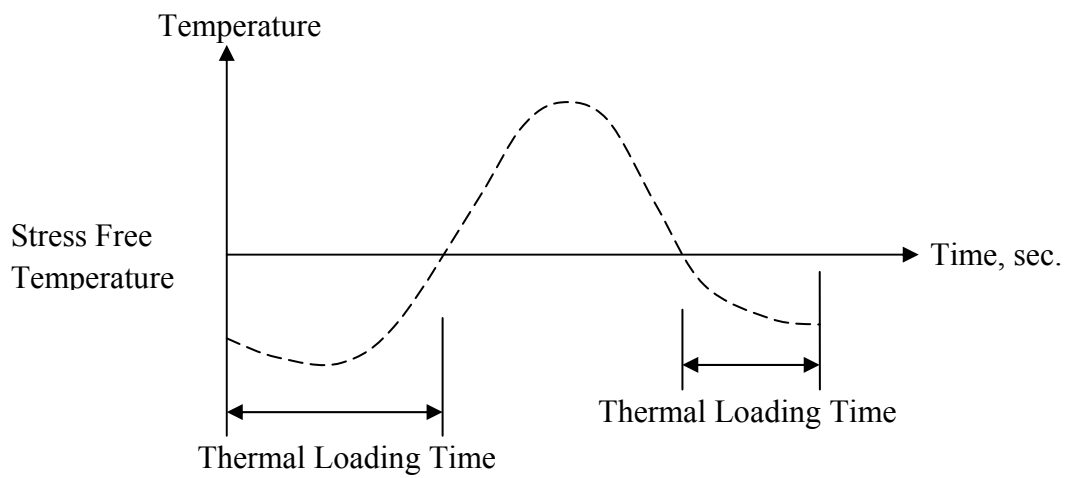


Figure 3.36. Loading time under stress free temperature.

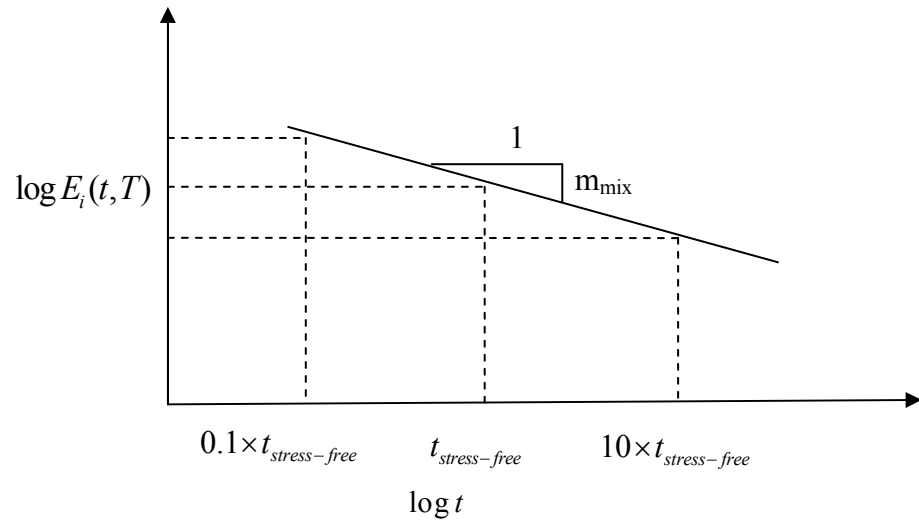


Figure 3.37. Method to evaluate the m_{mix} of fracture properties for thermal case.

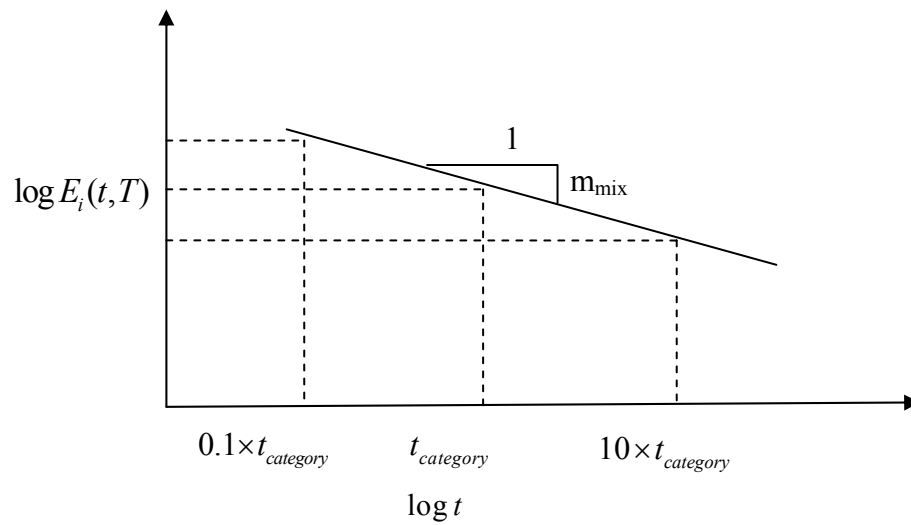


Figure 3.38. Method to evaluate the m_{mix} of fracture properties for traffic case.

The other unknown term is tensile strength σ_t . The equations of tensile strength σ_t are different in thermal and traffic cases shown in Table 3.30.

The coefficient D_1 is the coefficient in the master creep compliance power law equation which is shown in Equation 3.44. In the Calibration program, E_1 is calculated by Equation 3.45. For the Design Program, the equation for E_1 is Equation 3.46 which is not a function of the FWD modulus.

$$D_1 = \frac{\sin(m_{mix} \times \pi)}{E_1 \times m_{mix} \times \pi} (psi) \quad (3.44)$$

$$\log E_1(t, T) = \log E_{ANN}\left(\frac{t_{FWD}}{a_T}, T\right) - m_{mix-FWD} \times \log\left(\frac{t_{FWD}}{a_T}\right) \quad (3.45)$$

$$\log E_1(t, T) = \log E(t, T) - m_{mix} \times \log\left(\frac{t}{a_T}\right) \quad (3.46)$$

where $m_{mix-FWD}$ is the slope of the graph of the ANN relaxation moduli versus loading time; a_T is the shift factor based on the FWD temperature (T_{FWD}) as shown in Equation 3.47, C_1 , C_2 , and T_d are the parameters of the Time- Temperature shift function in Table 3.29;

$$a_T = 10^{\frac{-C_1(T_{FWD}-T_d)}{C_2+T_{FWD}-T_d}} \quad (3.47)$$

The method to obtain the $m_{mix-FWD}$ is basically the same as m_{mix} that we introduced earlier in Figure 3.39. Assuming the FWD loading time is 0.06 second, consider three loading times which are FWD loading time divided by shift factor, 10 times the FWD loading time divided by the shift factor, and 0.1 times the FWD loading time divided by the shift factor. Use these loading times and the FWD testing temperature to evaluate the relaxation moduli, and find the $m_{mix-FWD}$.

Table 3.30. Tensile strength of asphalt mixtures.

	Tensile Strength (psi)	Temperature (°F)	r (in/m in)
Thermal	$\sigma_t = \left[\frac{E(t,T)(MPa)}{21.3} \right]^{\frac{1}{1.95}}$	77	0.005
Traffic	$\sigma_t = \left[\frac{E(t,T)(MPa)}{45.5} \right]^{\frac{1}{1.56}}$	77	0.5

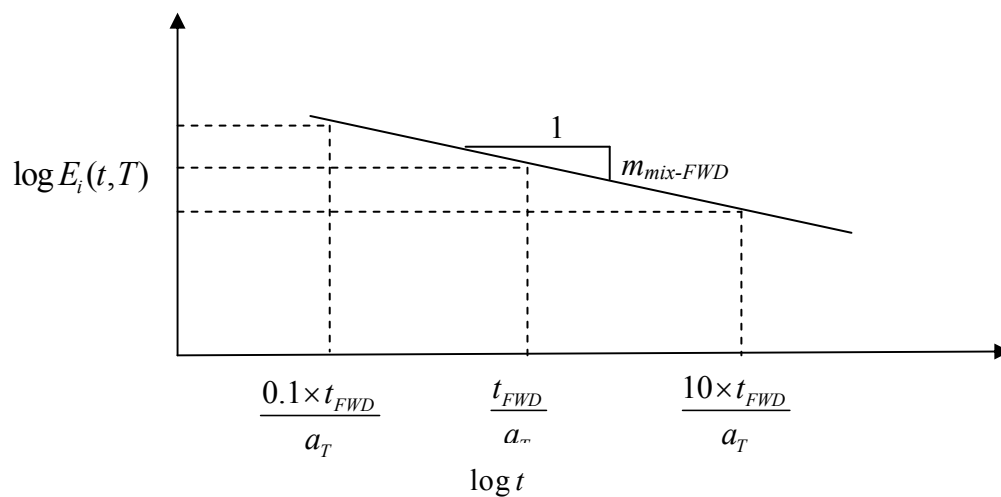


Figure 3.39. Method to evaluate the $m_{mix-FWD}$.

3.12.4 Healing Coefficients

In addition to the fracture coefficients, the healing coefficients obtained in earlier studies (4) are used to account for the healing shift function that occurs between the traffic loads on the overlay. The healing shift function is

$$SF_{healing} = 1 + g_5 (\Delta t_{rest})^{g_6} \quad (3.48)$$

The rest period in seconds between load applications is calculated as the number of seconds in a day (86,400) divided by the average daily traffic in vehicles per day. Values for the coefficients g_0 through g_6 were determined for each of the four climatic zones; these are listed in Table 3.29 (4). These coefficients were used without alteration and the fracture coefficients g_0 through g_4 were applied without modification to determine both the thermal and traffic fracture properties. The healing coefficients were used only with the traffic crack growth equations.

3.12.5 Stress Wave Pattern Correction

Schapery's theory of crack growth in viscoelastic materials takes into account the loading time and the shape of the stress pulse during the time that the material is being loaded (55, 56). The correction term for viscoelastic crack growth a_k is given by Equation 3.49. The normalized wave shape, $w(t)$, has a peak value of 1.0. The exponent, n , is the Paris and Erdogan's Law exponent which is given in Equation 3.42 and is

typically between 2 and 6. The wave shape rises to 1.0 and falls back to zero in a length of time, Δt . The equations of Δt for different axles are shown in Table 3.31. L_j is the length of the tire footprint, V is the speed of travel as Equation 3.50.

$$a_k = \int_0^{\Delta t} w(t)^n dt \quad (3.49)$$

$$\text{Speed of Travel, } V = V \frac{\text{miles}}{\text{hour}} \times \frac{22 \frac{\text{ft}}{\text{sec.}}}{15 \frac{\text{miles}}{\text{hour}}} \quad (3.50)$$

Table 3.31. Upper limit of integration of a_k in different axles.

	Δt (second)
Single Axle	$\frac{L_j + 10 \text{ ft}}{V}$
Tandem Axle	$\frac{L_j + 14 \text{ ft}}{V}$
Tridem Axle	$\frac{L_j + 18 \text{ ft}}{V}$
Quadrem Axle	$\frac{L_j + 22 \text{ ft}}{V}$

If the applied load is a square wave, the integral is equal to 1.0. If the stress wave is a rising and falling shape as is commonly the case with traffic and thermal stresses, the value of a_k is usually considerably less than 1.0. The patterns of the stress

waves were used in determining the effect during each day of each set of axle groupings on the growth of reflection cracks.

Although the stress intensity factors for bending and shear occur at the same time under traffic loads, the crack growth technique adopted in this project calculates the growth of cracks due to each of the two stresses separately. Thus, Paris and Erdogan's Law for the incremental crack growth each day is calculated from the accumulated effects of all of the traffic that have passed over the reflection crack during that day as Equations 3.51 and 3.52, respectively. The $SF_{healing}$ is the healing shift factor as shown in Equation 3.48.

$$dc = \sum_{i=1}^{i=n} A (K_{IIi})^n (a_{ki}) dN_i \left(\frac{1}{SF_{healing}} \right) \rightarrow Bending \quad (3.51)$$

$$dc = \sum_{i=1}^{i=n} A (2K_{IIIi})^n (a_{ki}) dN_i \left(\frac{1}{SF_{healing}} \right) \rightarrow Shearing \quad (3.52)$$

The wave patterns for the viscoelastic a_k -factor are shown in Figure 3.40 to Figure 3.47 for each of the types of traffic loading: bending and shearing and each of the four axle groupings. With shearing stresses, there is a peak shearing stress as the leading edge of the tire approaches the reflection crack and then another peak shearing stress of a different sign as the trailing edge of the tire leaves the location of the reflection crack. Thus there are two peak shearing stress intensity factors with the passage of a single tire.

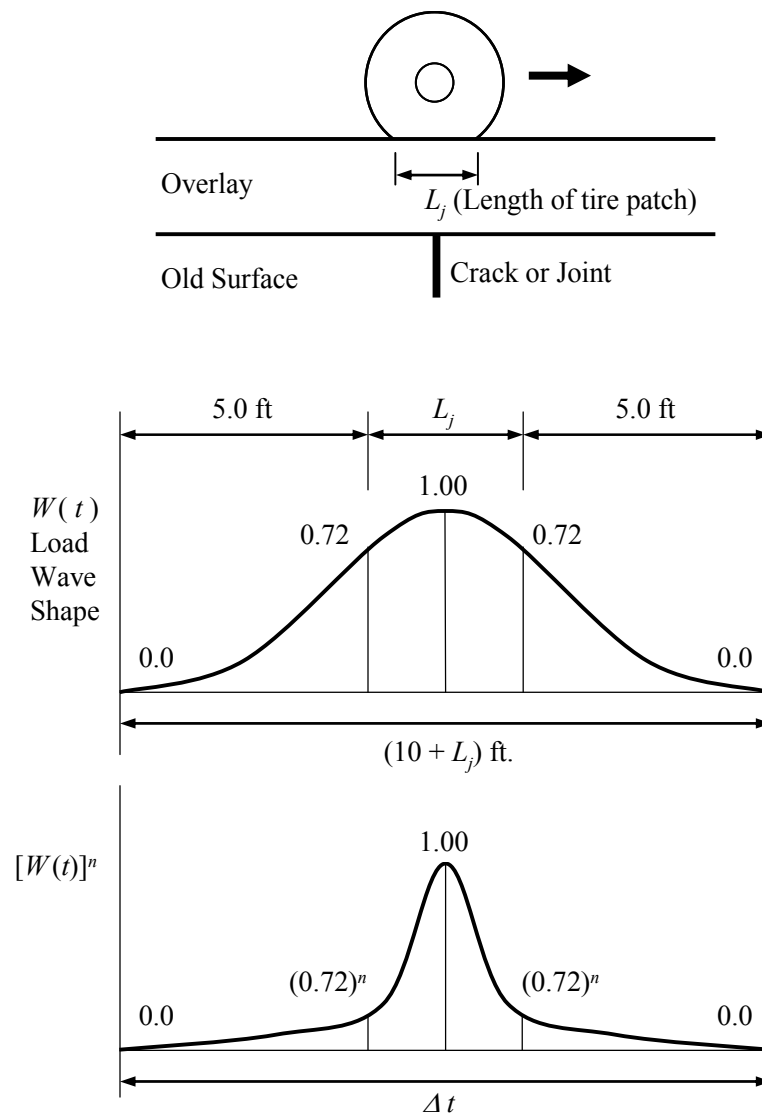


Figure 3.40. Load wave shape for single axle in bending crack propagation.

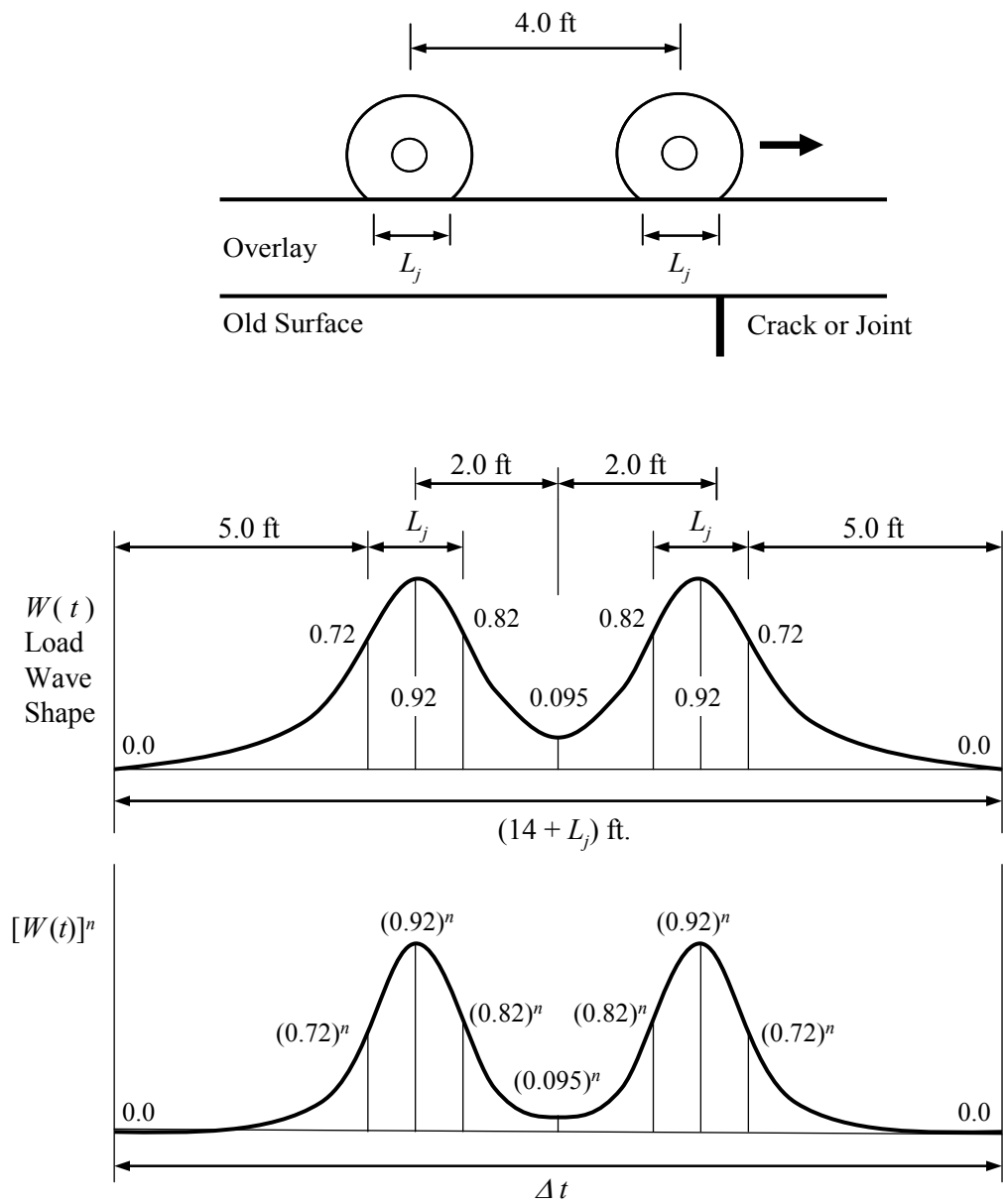


Figure 3.41. Load wave shape for tandem axle in bending crack propagation.

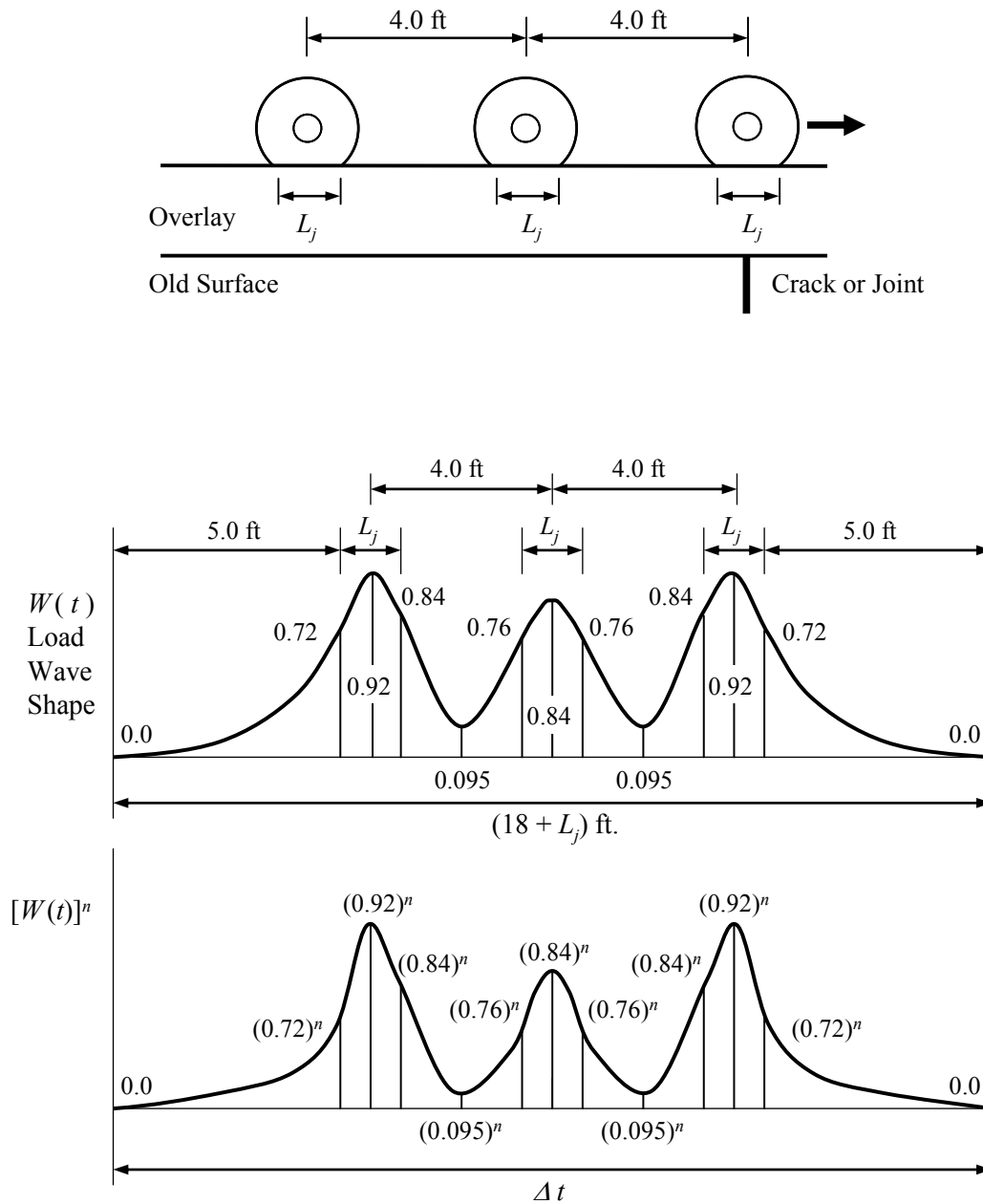


Figure 3.42. Load wave shape for triple axle in bending crack propagation.

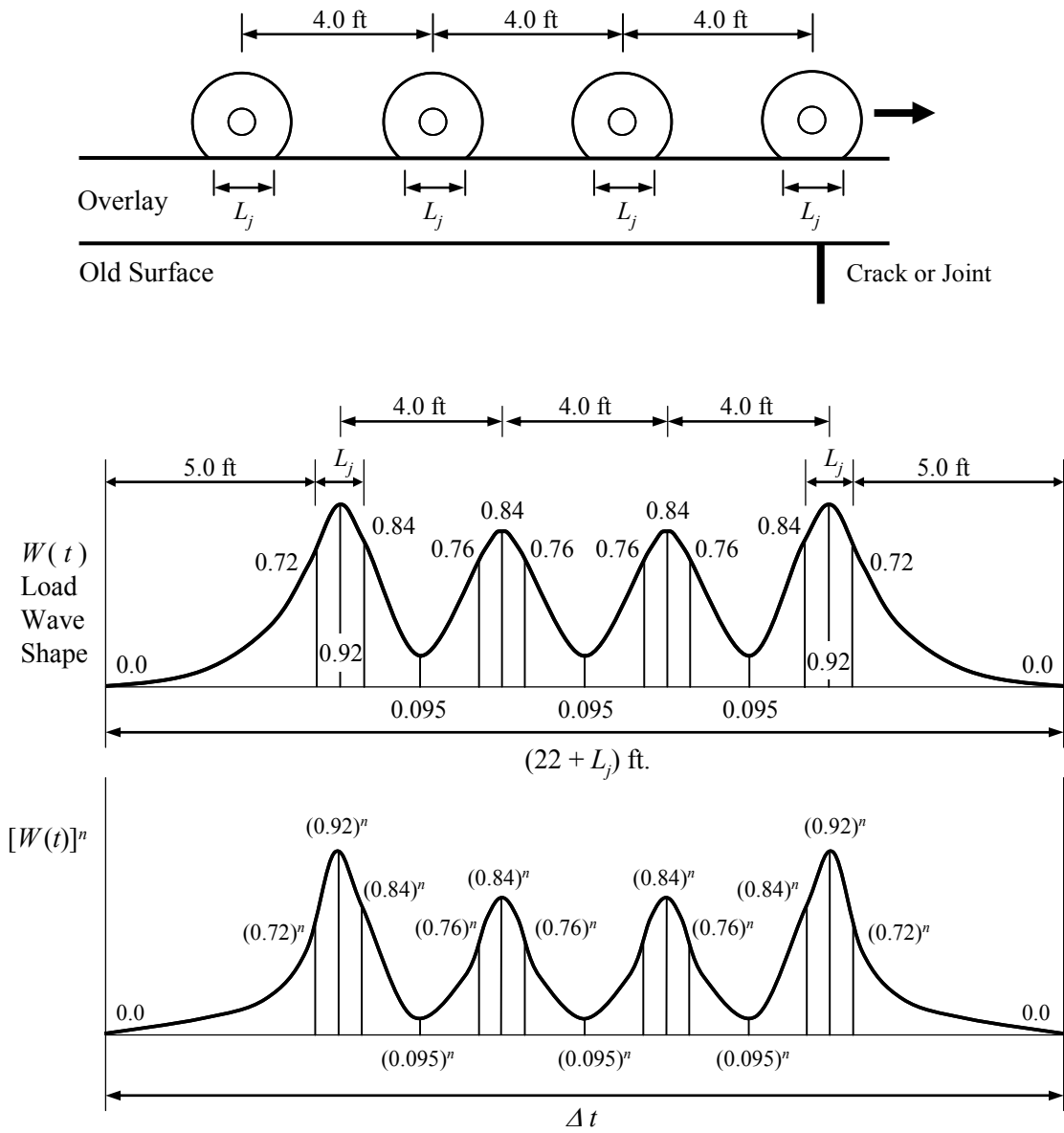


Figure 3.43. Load wave shape for quad axle in bending crack propagation.

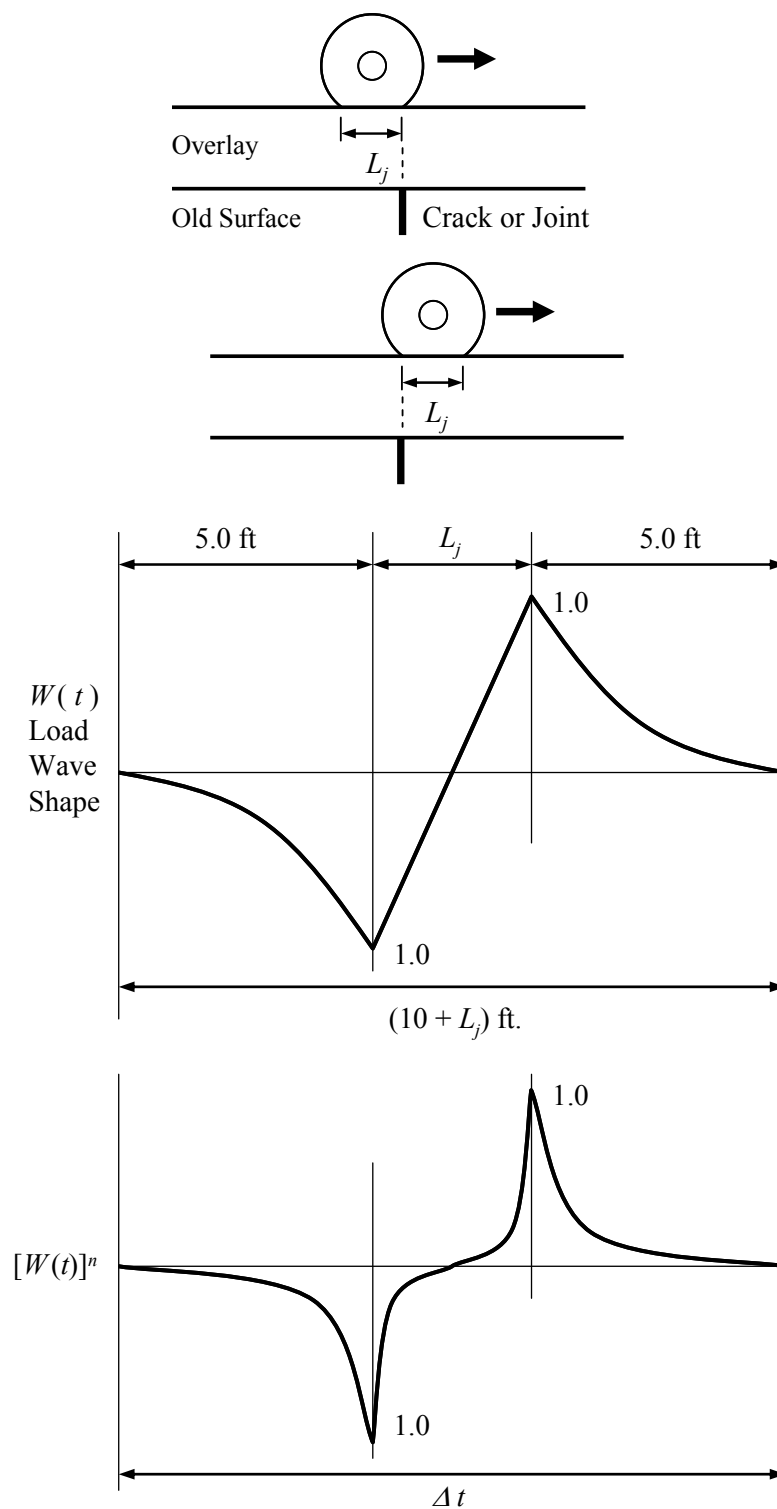


Figure 3.44. Load wave shape for single axle in shearing crack propagation.

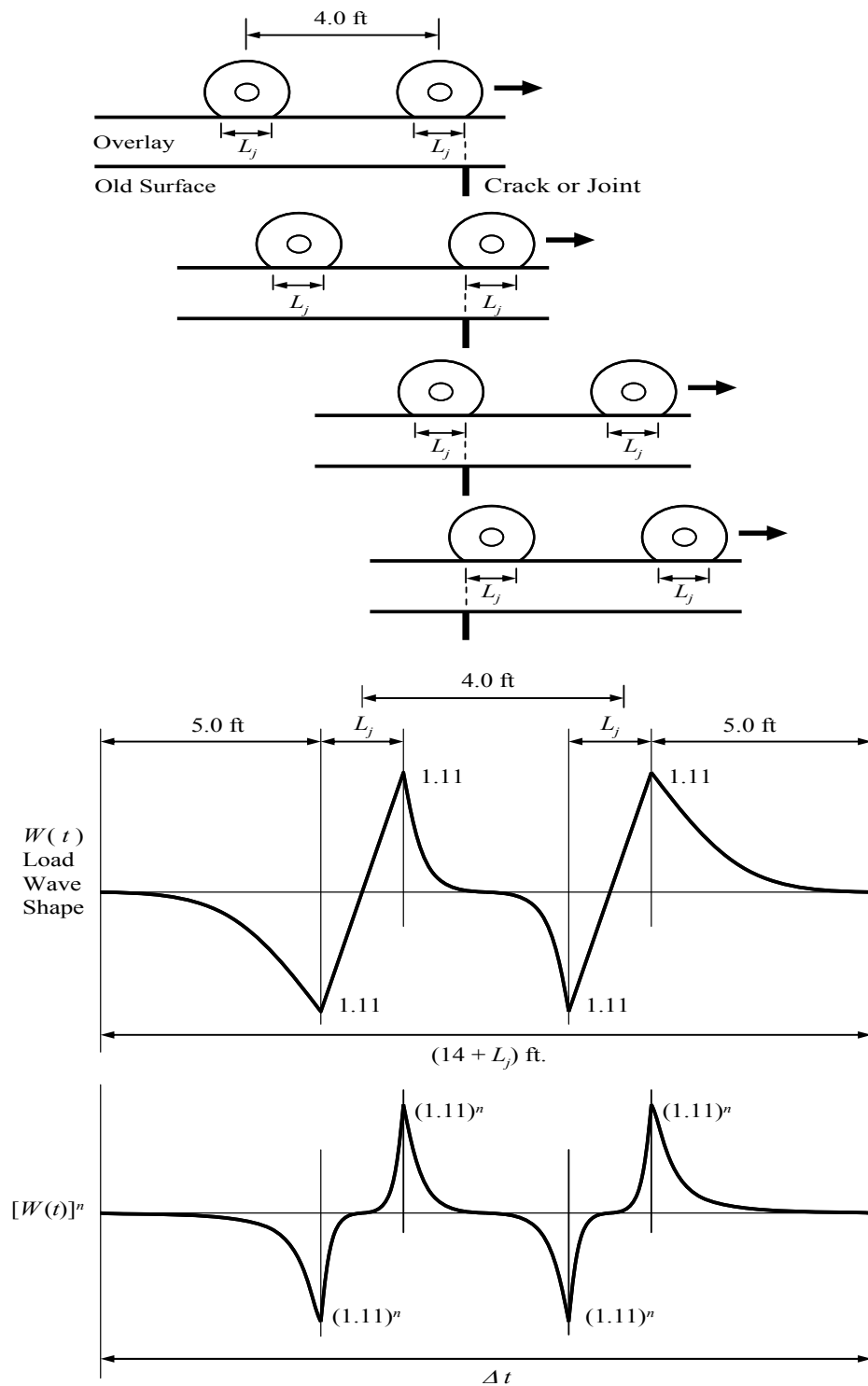


Figure 3.45. Load wave shape for tandem axle in shearing crack propagation.

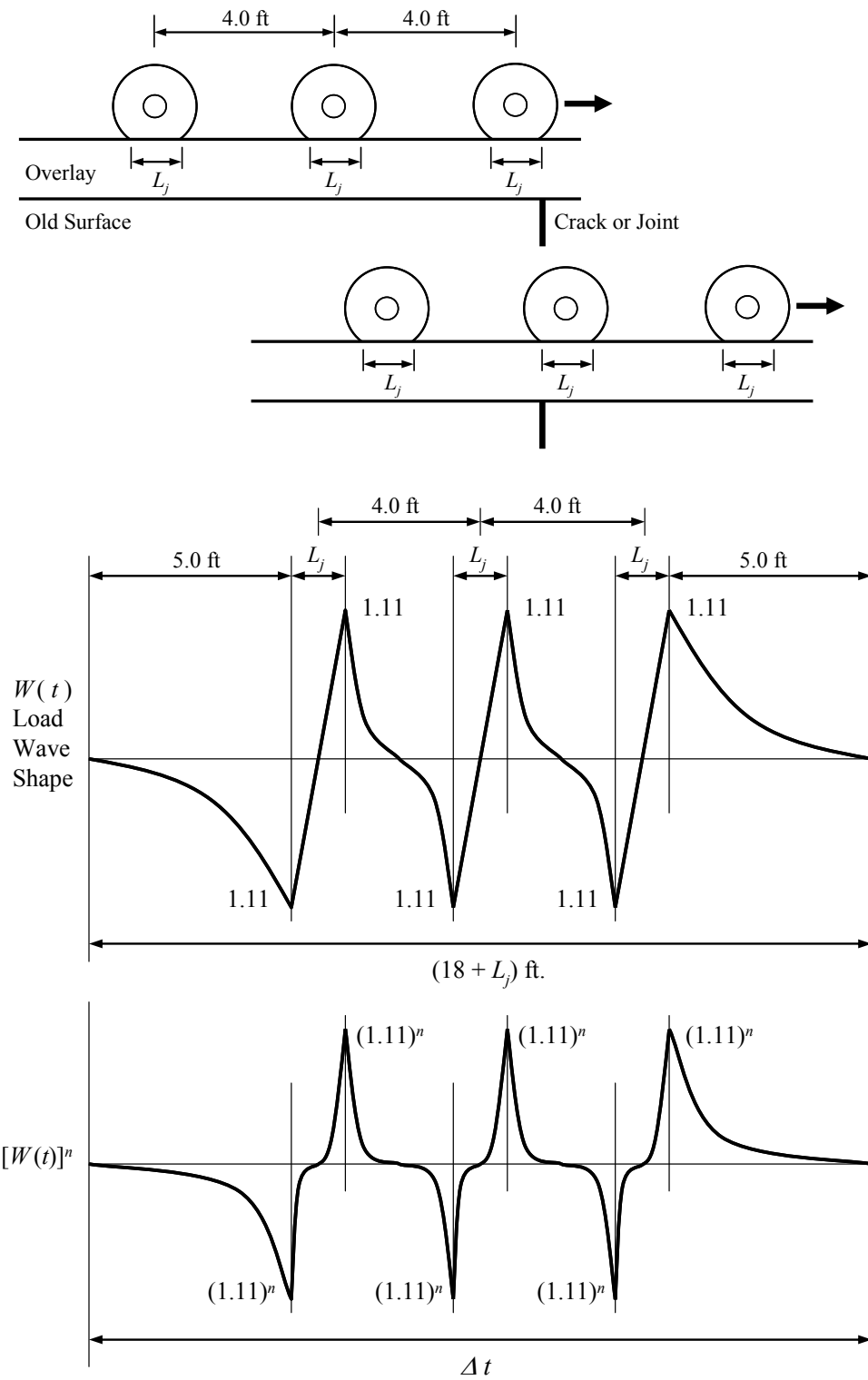


Figure 3.46. Load wave shape for triple axle in shearing crack propagation.

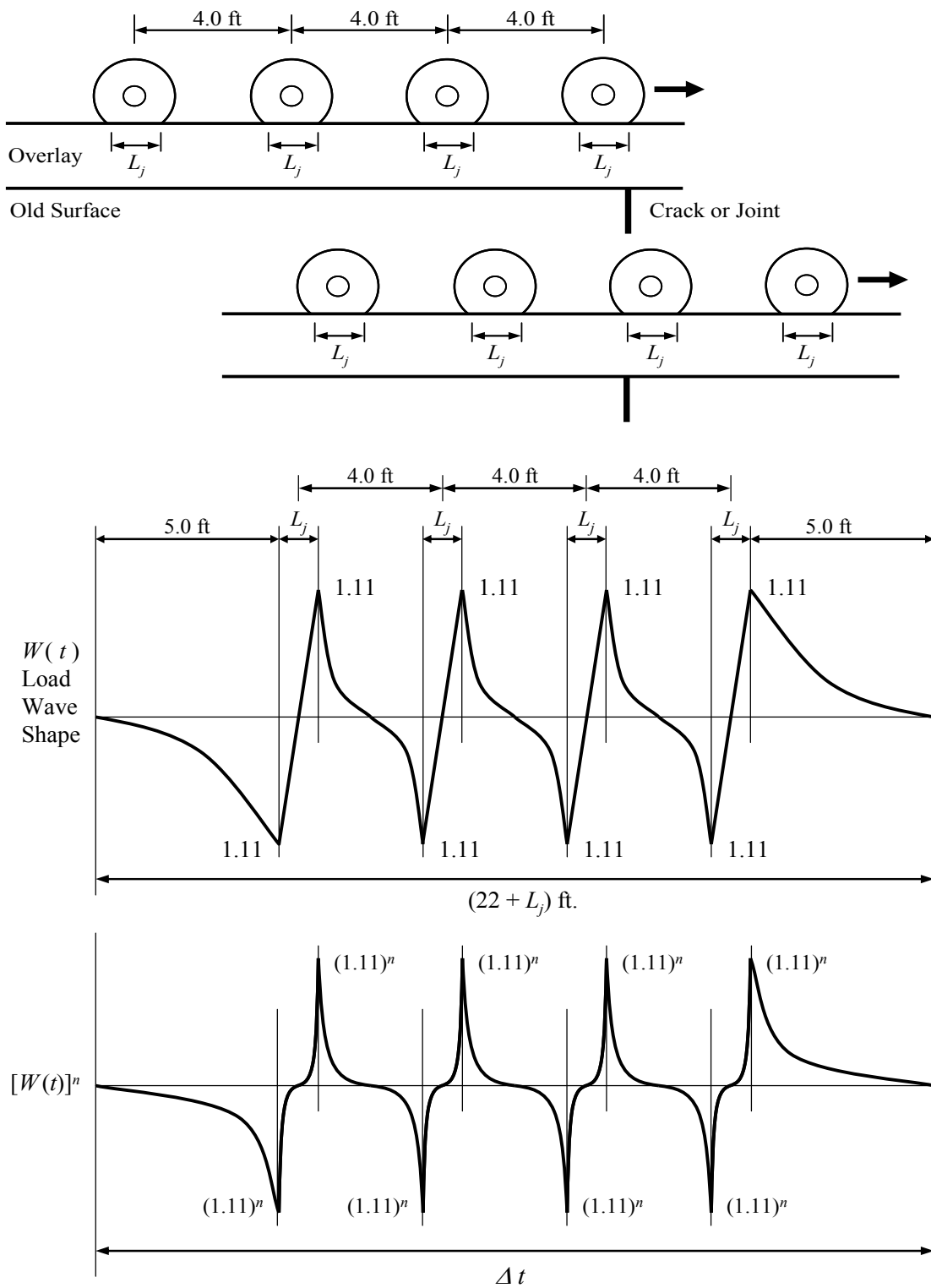


Figure 3.47. Load wave shape for quad axle in shearing crack propagation.

3.13 Stress Intensity Factor Models by Artificial Neural Network

The SIF is the driving engine in fracture mechanics. In this dissertation, it was found that the computational time to calculate new stress intensity factors using the finite element method at the daily location of the tip of the crack was too long. Therefore, a method was adopted to calculate the SIF for a wide variety of conditions, pavement structures, and crack lengths using a finite element method and then to model the computed results with the ANN which is a very computationally efficient algorithm.

Artificial Neural Network (ANN) algorithms, while being computationally powerful, have limitations just as do regression models. One of the limitations that the two methods have in common is that they are not expected to extrapolate well beyond their inference space. Consequently, it is important for the user to be conversant with the ranges of variables upon which each of the 18 ANN algorithms used in the reflection cracking program is based.

Table 3.32 lists the pavement structures and the number of computer runs performed for developing the SIF. The total number of computer runs was 94,500. The number of bending stress intensity factor computations was reduced because the bending stresses become compressive only a short distance into the overlay.

Table 3.32. Number of computer runs of SIF.

Pavement Structures	Number of Test Sections	Computer Runs of Stress Intensity Factors with Varying Crack Lengths		
		Thermal	Shear	Bending
AC/AC OL	233	1,620	25,920	4,320
JCP/AC OL	69	14,580	25,920	4,320
AC/SAMI/AC OL	38	6,480	-	-
AC/GRID/AC OL	50	9,720	-	-
CRC/AC OL	21	1,620	-	-

Three types of ANN algorithms were assembled: thermal, shear, and bending. Two types of pavement overlay structure were considered: asphalt overlays over a cracked asphalt surface layer and over jointed concrete. Some special cases were included such as asphalt overlays over continuous reinforced concrete, asphalt overlays over seal coats or open graded friction courses, and asphalt overlays with reinforcing interlayers.

In the discussion that follows, the thermal cases will be presented first and then the traffic loading cases of shearing and bending. A schematic diagram of the 18 ANN algorithms is shown in Figure 3.48.

The variables that were included in each of the sets of finite element computational runs were the layer thickness modulus of overlay, surface layer, and base course and the crack or joint spacing.

In the thermal stress cases, different levels of thermal expansion coefficient were used. With the jointed concrete pavement structures, different levels of load transfer efficiency were used. For those cases where a compliant interlayer (SAMI) was used, the thickness and modulus of that layer were also varied. In those pavement structures in which reinforcing geosynthetics were used, the thickness and the grid stiffness were used. Because there are no uniform industry standards for specifying the properties of these commercially available products, three levels of geosynthetic stiffness: high, medium, and low were used in the computer runs. The appropriate level can be chosen by the user by referring to the graph in Figure 3.49. The user will plot the interlayer stiffness and thickness of the selected material on the above graph and input the stiffness description that is closest to the plotted point.

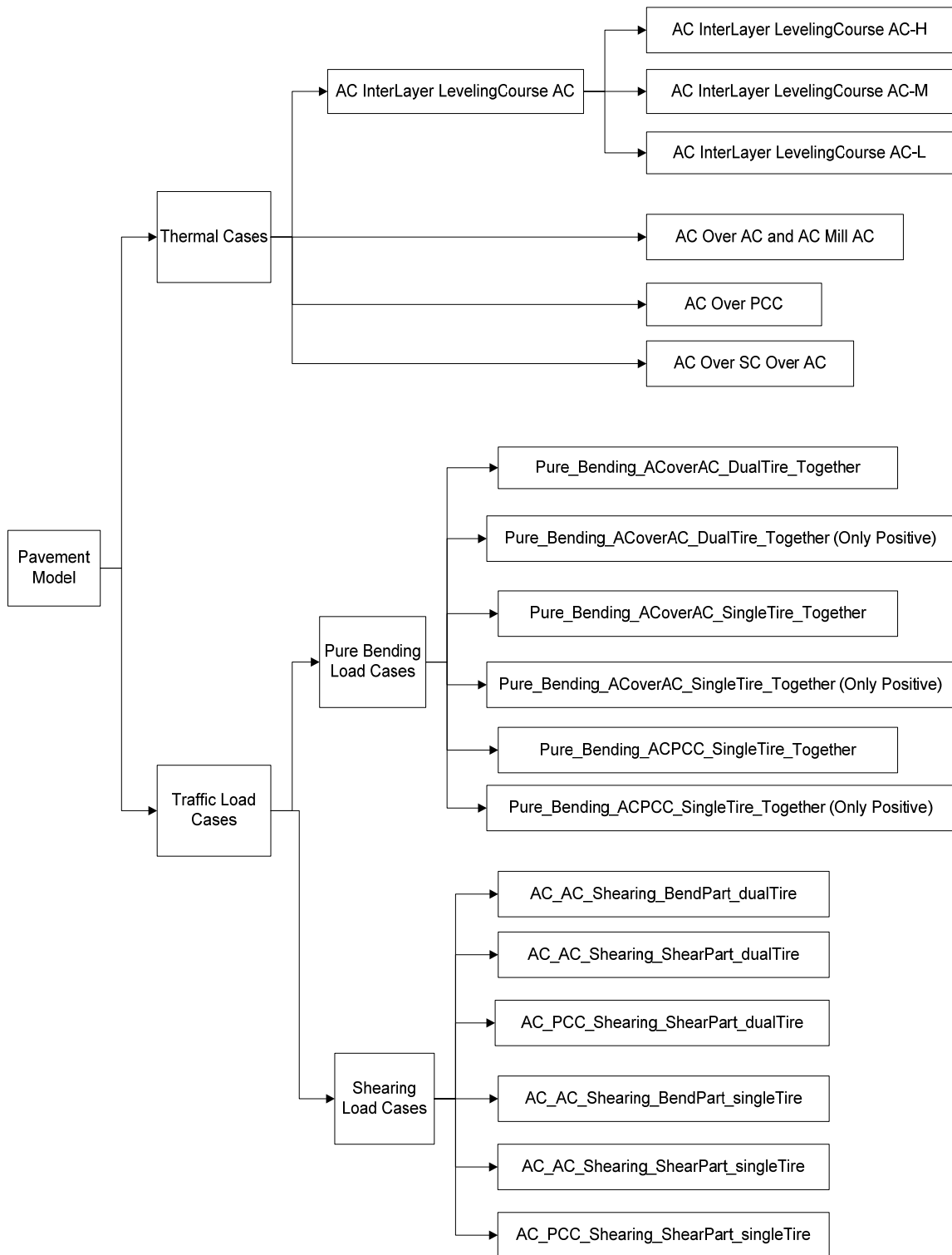


Figure 3.48. Artificial neural network models for stress intensity factors.

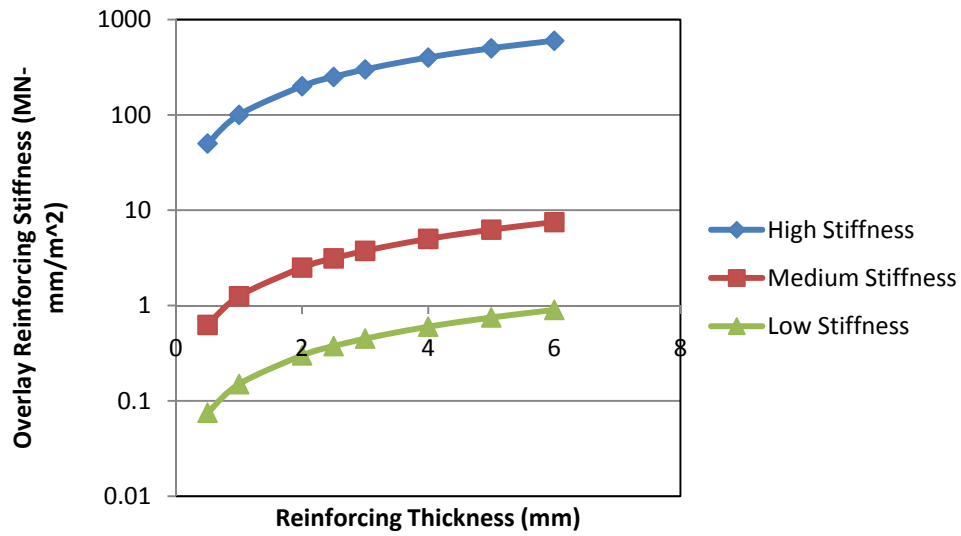


Figure 3.49. Interlayer reinforcing stiffness (MN-mm/m²) versus reinforcing thickness (mm).

With the grid-type, the reinforcing stiffness, S , is given by

$$S = \frac{Ea}{s} \quad (3.53)$$

where

- S = the interlayer stiffness, MN-mm/m²
- E = the secant modulus of the grid material in the longitudinal direction, MN/m²
- a = the cross-sectional area of a rib of the grid, mm²
- s = the spacing of the ribs, mm

With a sheet-type of reinforcing interlayer, the reinforcing stiffness is given by

$$S = Et \quad (3.54)$$

where, as before,

$$\begin{aligned} E &= \text{the secant modulus of the sheet material, MN/m}^2 \\ t &= \text{the thickness of the sheet, mm} \end{aligned}$$

The reinforcing interlayer must be locked in to the overlay in order to reinforce it. With a grid-type of interlayer, this means that there is a sufficiently large grid opening that the largest aggregate from both above and below the interlayer can interpenetrate and lock the grid in place. An interlayer that is not locked into the mixture both above and below it does not reinforce. There are three bending stress intensity factor models that are described as “Only Positive” and these are the only ones that are used in calculating the bending stress intensity factors in the reflection cracking program. The “Only Positive” description refers to the fact that bending causes a reflection crack to grow only when the bending stress at the tip of the crack is tensile (or “positive”). Many of the runs of the finite element program found that the calculated bending stress at the tip of the crack was compressive and therefore, according to the sign convention, “negative.” The bending stress is positive only when the crack is in the bottom of the overlay. The other three bending stress intensity factor models predict the complete set of both tensile and compressive stress intensity factors.

The thermal reflection cracking cases are illustrated in Figures 3.50 through 3.59. Each of these includes a sketch of the pavement structure with a list of the variables in the companion Tables 3.33 through 3.36 that were included in the full factorial set of finite element runs. These finite element runs generated the set of stress intensity factors that are predicted by the Artificial Neural Network algorithm.

3.13.1 Thermal Reflection Cracking Cases

1. HMA Overlay on Asphalt Concrete Pavement

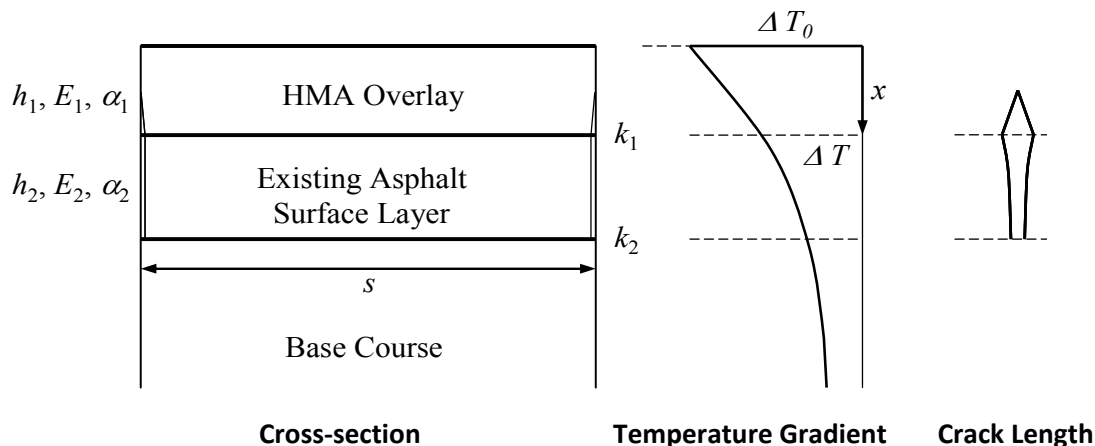


Figure 3.50. Diagrams of HMA overlay on asphalt concrete pavement-thermal.

Table 3.33. Thermal stress variables in HMA overlay on asphalt concrete pavement system.

Variable		Unit	Value
Overlay Layer	Thickness (h_1)	mm	38, 75, 150
	Modulus (E_1)	MPa	70, 300, 700
	Coefficient of Thermal Expansion (α_1)	strain/ $^{\circ}$ C	2×10^{-5} , 4×10^{-5}
Interface Condition (k_1)*		-	1.0
Existing Surface	Thickness (h_2)	mm	100, 200, 300
	Modulus (E_2)	MPa	70, 300, 700
	Coefficient of Thermal Expansion (α_2)	strain/ $^{\circ}$ C	2×10^{-5} , 4×10^{-5}

* 0 (fully slipped) $< k_i < 1.0$ (fully bonded)

Table 3.33. Continued.

Variable	Unit	Value
Half Crack Spacing ($s/2$)	mm	4500
Ratio of Crack Length to Layer Thickness (c / h_1)	-	0.1, 0.3, 0.5, 0.7, 0.9
Interface Condition (k_2)*	-	1.0
Temperature Differential (ΔT_0)	°C	30

* 0 (fully slipped) $< k_i < 1.0$ (fully bonded)

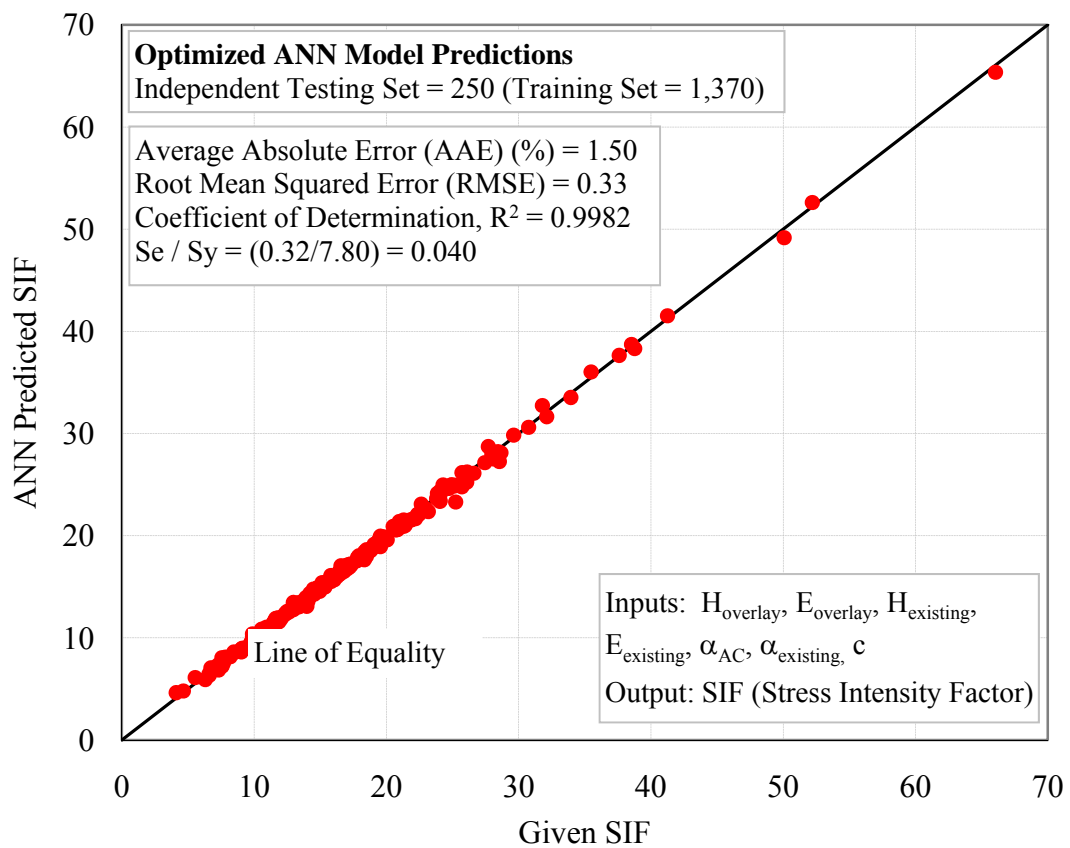


Figure 3.51. ANN Model of thermal stress intensity factors for asphalt overlays over cracked asphalt surface layer.

2. HMA Overlay on Jointed Concrete Pavement

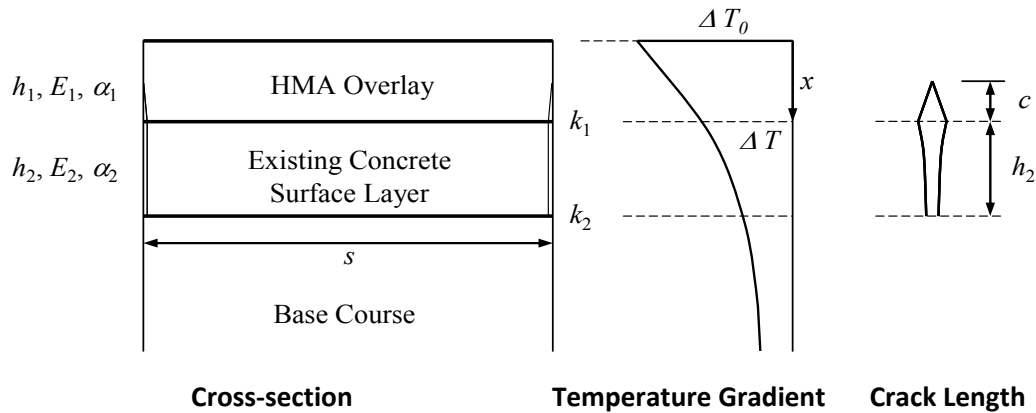


Figure 3.52. Diagrams of HMA overlay on jointed concrete pavement-thermal.

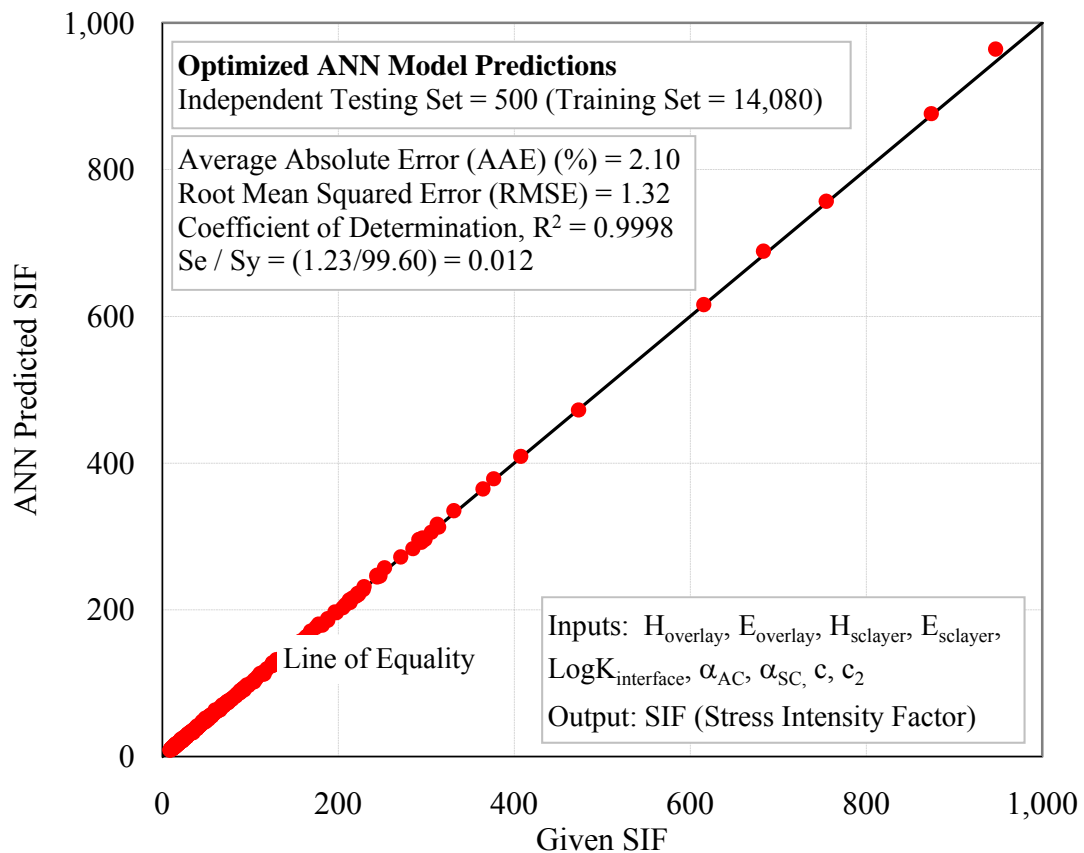


Figure 3.53. ANN model of stress intensity factors of asphalt overlay on jointed concrete pavement.

Table 3.34. Thermal stress variables in HMA overlay on jointed concrete pavement system.

Variable		Unit	Value
Overlay Layer	Thickness (h_1)	mm	38, 75, 150
	Modulus (E_1)	MPa	70, 300, 700
	Coefficient of Thermal Expansion (α_1)	strain/°C	2×10^{-5} , 4×10^{-5}
Interface Condition (k_1)		-	1.0
Existing Surface	Thickness (h_2)	mm	200, 300, 350
	Modulus (E_2)	MPa	20,000, 30,000, 40,000
	Coefficient of Thermal Expansion (α_2)	strain/°C	1×10^{-5} , 2×10^{-5}
Interface Condition (k_2)		-	0, 0.5, 1.0
Temperature Differential (ΔT_0)		°C	30
Half Slab Length between Joints ($s/2$)		mm	2250, 4500, 7500
Ratio of Crack Length to Layer Thickness (c / h_1)		-	0.1, 0.3, 0.5, 0.7, 0.9

3. HMA Overlay on Asphalt Concrete Pavement with Seal Coat or Friction Course-Thermal

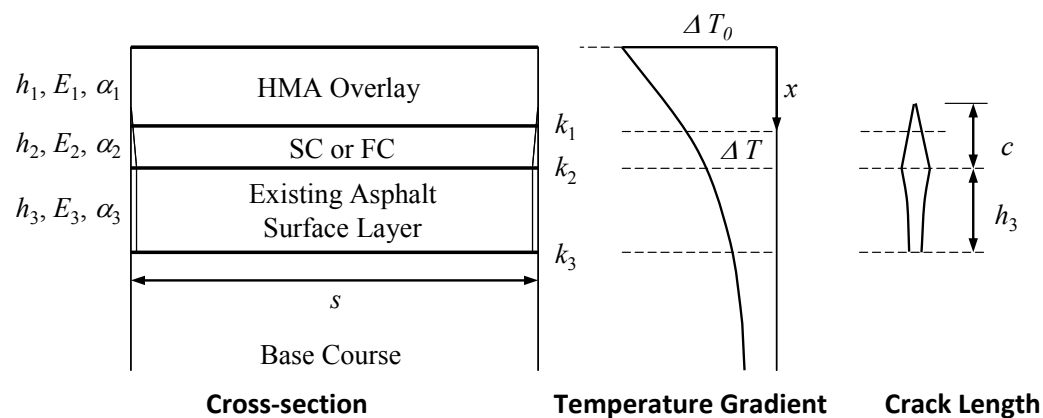


Figure 3.54. Diagram of HMA overlay on asphalt concrete pavement with SC or FC-thermal.

Table 3.35. Thermal stress-variables in HMA overlay on asphalt concrete pavement with SC or FC system.

Variable		Unit	Value
Overlay Layer	Thickness (h_1)	mm	38, 75, 150
	Modulus (E_1)	MPa	70, 300, 700
	Coefficient of Thermal Expansion (α_1)	strain/ $^{\circ}$ C	2×10^{-5} , 4×10^{-5}
Interface Condition (k_1)		-	1.0
SC or FC	Thickness (h_2)	mm	15, 60
	Modulus (E_2)	MPa	50, 300
	Coefficient of Thermal Expansion (α_2)	strain/ $^{\circ}$ C	2×10^{-5} , 4×10^{-5}
Interface Condition (k_2)		-	1.0
Existing Surface	Thickness (h_3)	mm	100, 200, 300
	Modulus (E_3)	MPa	70, 300, 700

Table 3.35. Continued.

Variable		Unit	Value
Existing Surface	Coefficient of Thermal Expansion (α_3)	strain/°C	2×10^{-5} , 4×10^{-5}
Interface Condition (k_3)		-	1.0
Temperature Differential (ΔT_0)		°C	30
Half Crack Spacing ($s/2$)		mm	4500
Ratio of Crack Length to Layer Thickness ($c/[h_1+h_2]$)		-	0.1, 0.3, 0.5, 0.7, 0.9

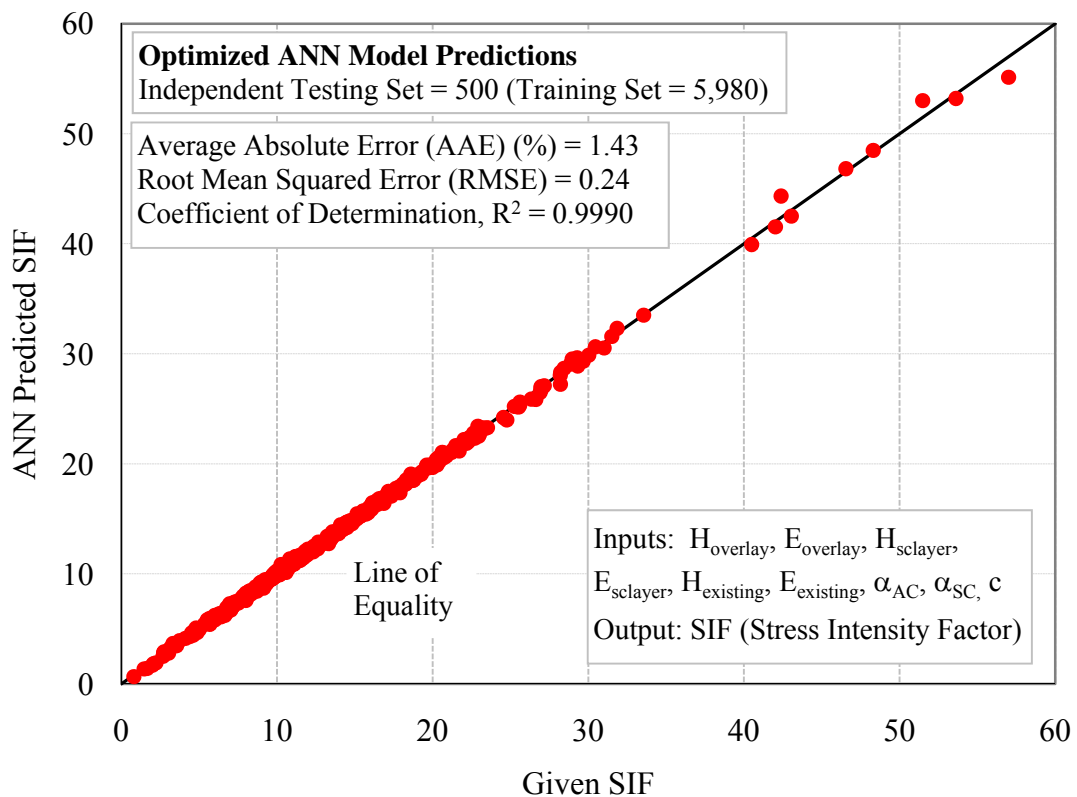


Figure 3.55. ANN model of stress intensity factor for asphalt overlay over seal coat or open graded friction course over cracked asphalt surface layer.

4. HMA Overlay on Asphalt Concrete Pavement with Reinforcing Interlayer on Level-up and Beneath Overlay

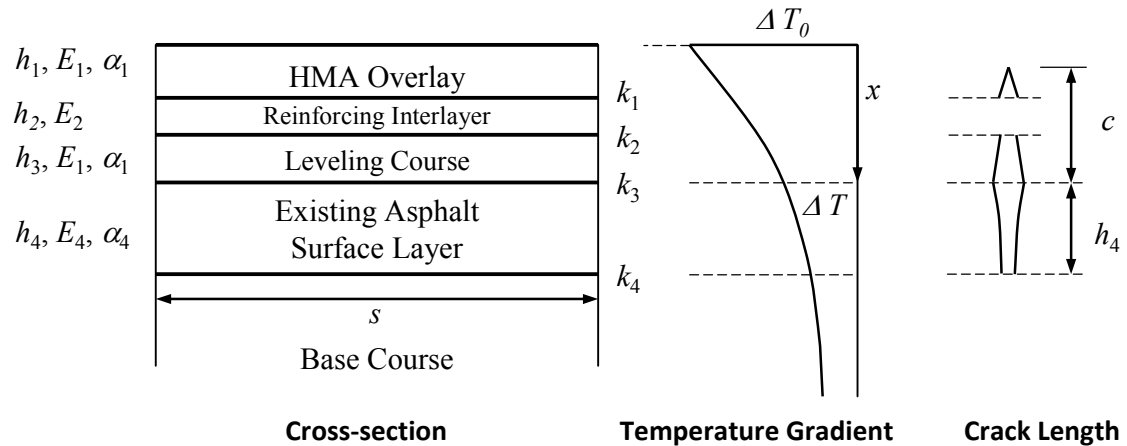


Figure 3.56. Diagram of HMA overlay on asphalt concrete pavement with reinforcing interlayer beneath overlay-thermal.

As noted in Table 3.36, three levels of interlayer reinforcing were modeled using three different ANN models. In the following three figures, the fit that was achieved with each of the three levels of reinforcing are illustrated.

Table 3.36. Thermal stress variables in HMA overlay on asphalt concrete pavement with reinforcing interlayer on level-up and beneath overlay system.

Variable		Unit	Value
Overlay Layer	Thickness (h_1)	mm	38, 75, 150
	Modulus (E_1)	MPa	70, 300, 700
	Coefficient of Thermal Expansion (α_1)	strain/°C	2×10^{-5} , 4×10^{-5}
Interface Condition (k_1)		-	1.0
Reinf. Interlayer	[Thickness (h_2), Modulus (E_2)]	[mm, MPa]	[2.5, 10000], [1, 1250], [2, 150]
Interface Condition (k_2)		-	0
Leveling Course	Thickness (h_3)	mm	25, 50
Interface Condition (k_3)		-	1.0
Existing Surface	Thickness (h_4)	mm	100, 200, 300
	Modulus (E_4)	MPa	70, 300, 700
	Coefficient of Thermal Expansion (α_4)	strain/°C	2×10^{-5} , 4×10^{-5}
Interface Condition (k_4)		-	1.0
Temperature Differential (ΔT_0)		°C	30
Half Crack Spacing ($s/2$)		mm	4500
Ratio of Crack Length to Layer Thickness ($c / [h_1+h_3]$)		-	0.1, 0.3, 0.5, 0.7, 0.9

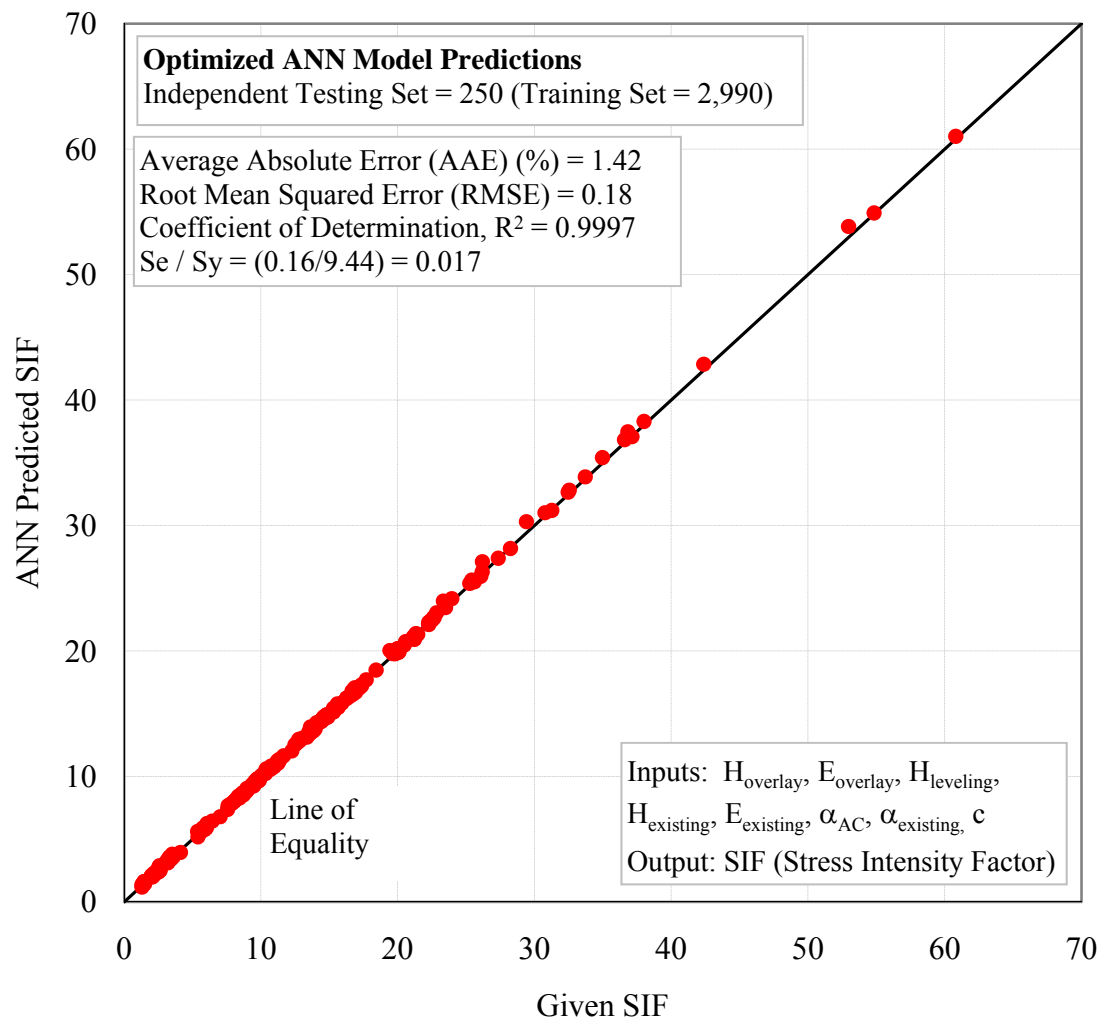


Figure 3.57. ANN models for stress intensity factors for overlays over cracked asphalt surface layer–low interlayer reinforcing stiffness level-thermal.

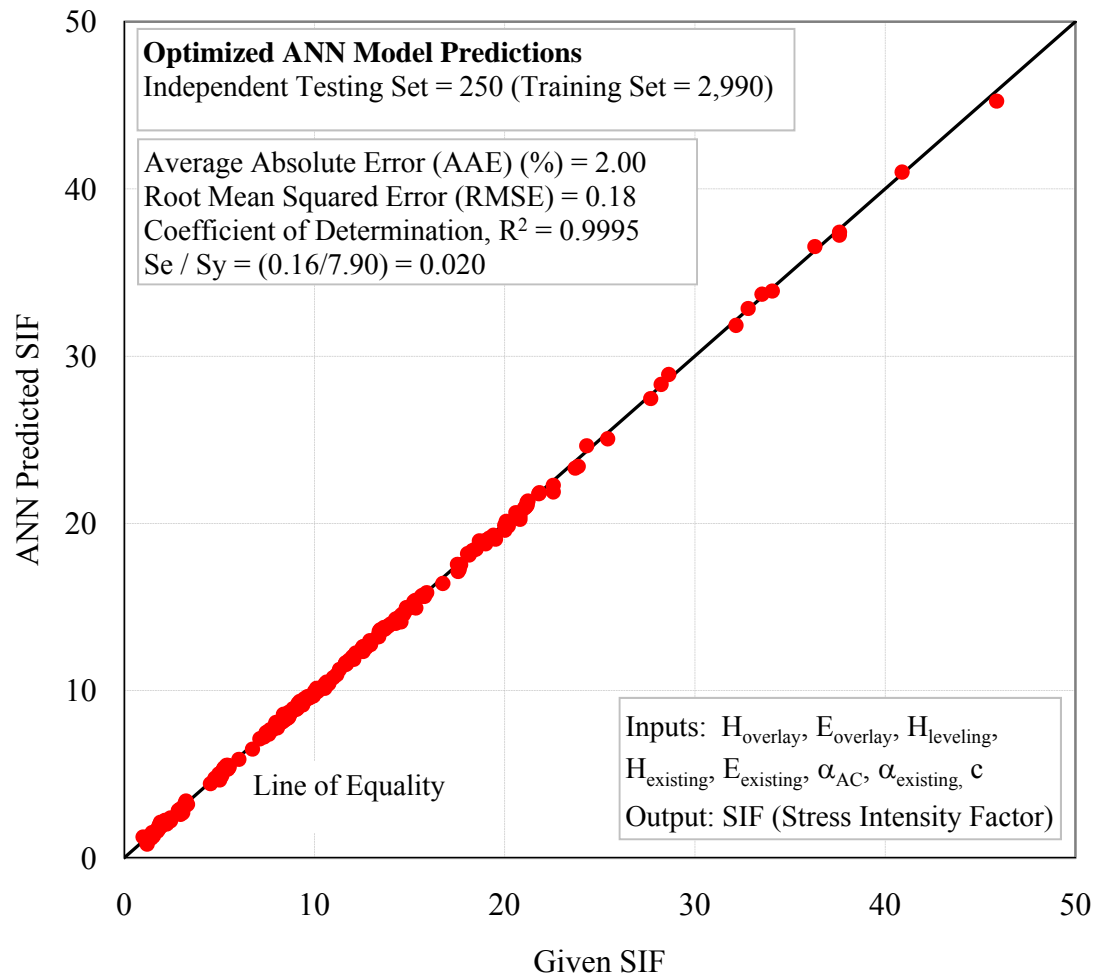


Figure 3.58. ANN models for stress intensity factors for asphalt overlays over cracked asphalt surface layer–medium interlayer reinforcing stiffness level–thermal.

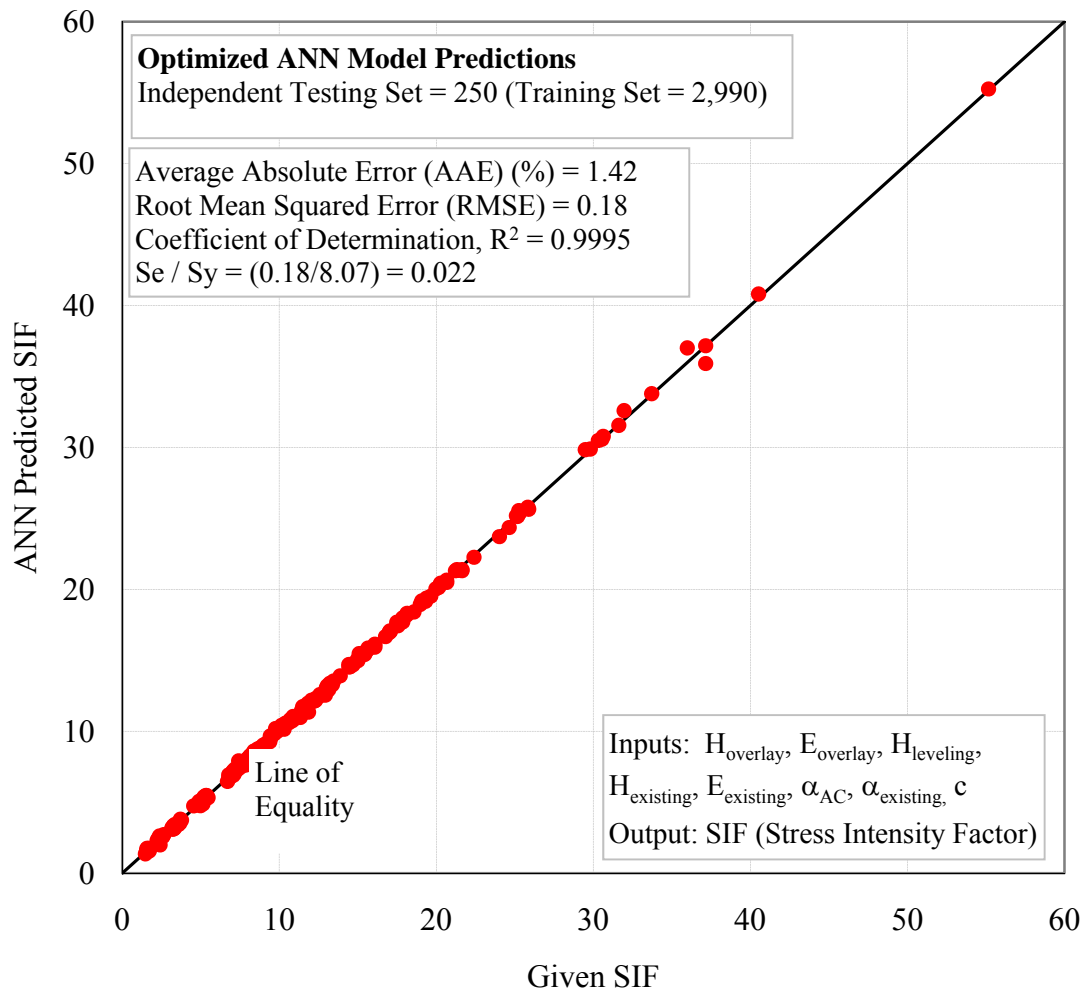


Figure 3.59. ANN Models for stress intensity factors for asphalt overlays over cracked asphalt surface layer–high interlayer reinforcing stiffness level–thermal.

The four shearing reflection cracking cases are shown in Figures 3.60 through 3.67 and the companion tables of variables, Tables 3.37 through 3.40. When the shearing stress intensity factor reaches a peak as the tire both approaches and leaves the vicinity of the reflection crack, there is always a bending stress intensity factor also present at the tip of the crack. This explains why there is a “Shearing Part” and a

“Bending Part” of the shearing stress intensity factor models and graphs. Having analyzed the bending stress intensity factors as the tire approaches, travels over, and leaves the vicinity of the reflection crack has allowed the use of the stress intensity factor wave form which is called for in Schapery’s theory of crack growth in viscoelastic media.

3.13.2 Shearing Reflection Cracking Cases

a) HMA Overlay on Asphalt Concrete Pavement (Single Axle – Single Tire)

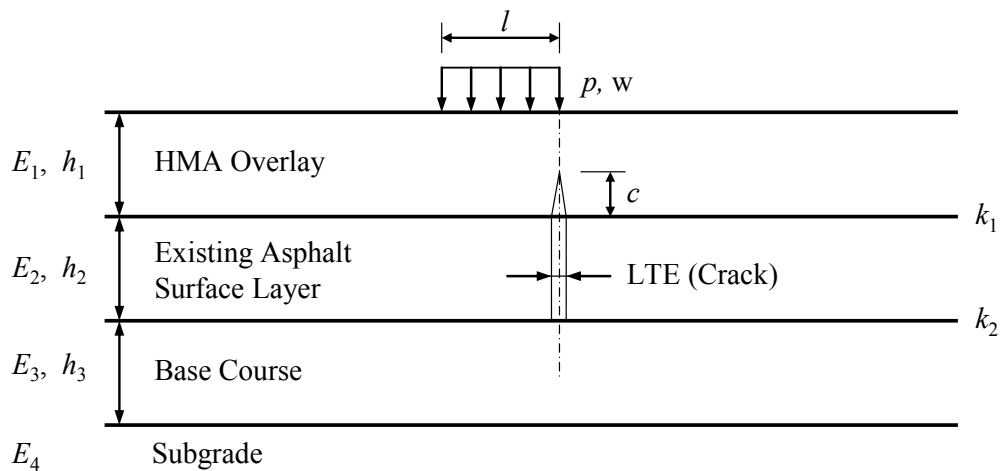


Figure 3.60. Diagram of HMA overlay on asphalt concrete pavement-shearing.

Table 3.37. Shearing stress variables in HMA overlay on asphalt concrete pavement system.

Variable		Unit	Value
Overlay Layer	Thickness (h_1)	mm	38, 75, 150
	Modulus (E_1)	MPa	1,000, 10,000
Interface Condition (k_1)		-	1.0
Existing Surface	Thickness (h_2)	mm	100, 200, 300
	Modulus (E_2)	MPa	500, 5,000
Interface Condition (k_2)		-	1.0
Base Course	Thickness (h_3)	mm	100, 1,000
	Modulus (E_3)	MPa	150, 600
Subgrade	Modulus (E_4)	MPa	30, 150
Traffic Load	Length of Tire Patch (l)	mm	64, 305, 406
	Tire Pressure (p)	psi	96
	Tire Width (w)	mm	200
Load Transfer Efficiency (LTE)		-	0.3, 0.7, 1.0
Ratio of Crack Length to Layer Thickness (c / h_1)		-	0.1, 0.3, 0.5, 0.7, 0.9

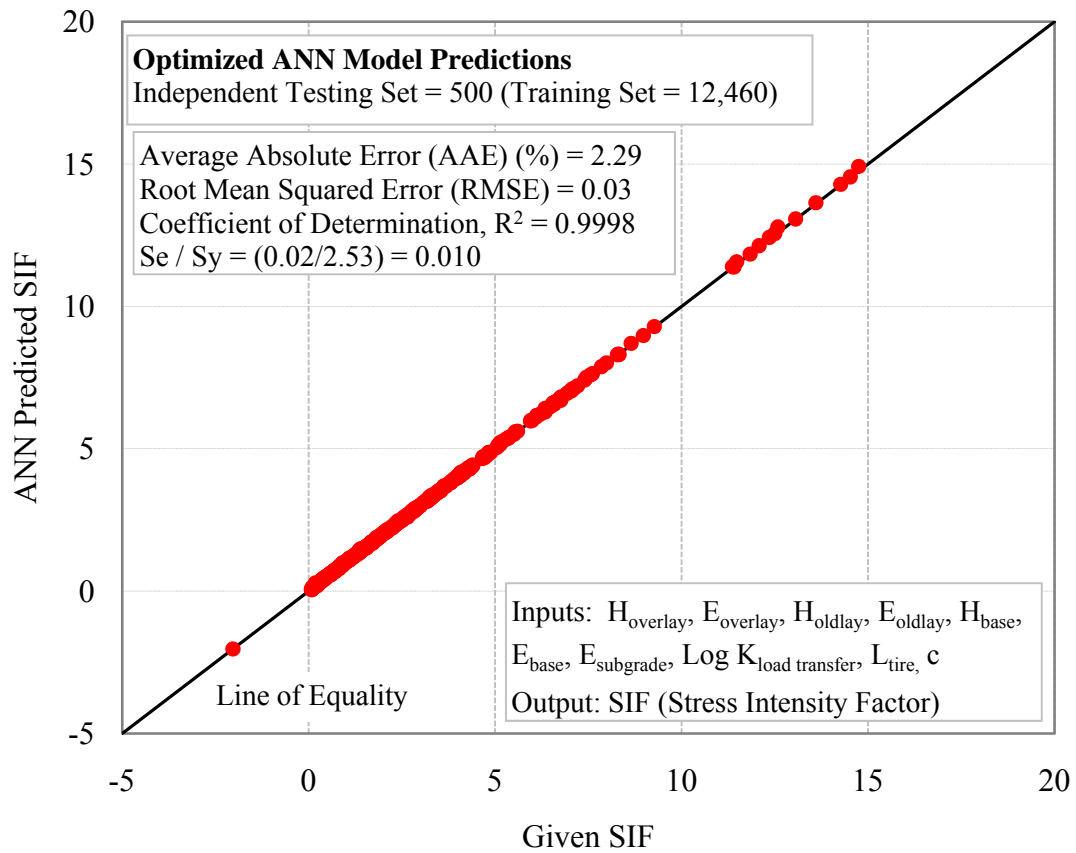


Figure 3.61. ANN model of the shearing part of the shearing stress intensity factors for asphalt overlays over cracked asphalt surface layer (single axle-single tire).

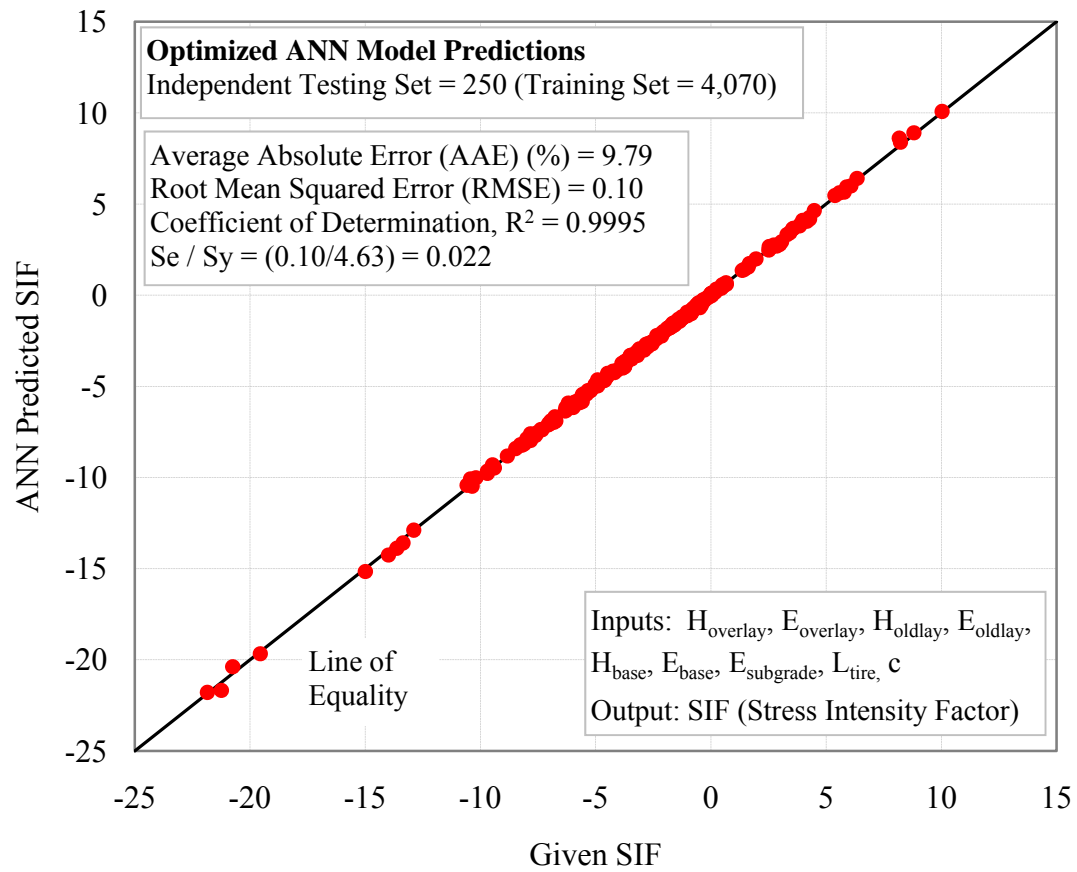


Figure 3.62. ANN model of the bending part of the shearing stress intensity factors for asphalt overlays over cracked asphalt surface layer (single axle–single tire).

b) HMA Overlay on Asphalt Concrete Pavement (Single Axle – Dual Tires)

Table 3.38. Shearing stress variables in HMA overlay on asphalt concrete pavement system.

Variable		Unit	Value
Overlay Layer	Thickness (h_1)	mm	38, 75, 150
	Modulus (E_1)	MPa	1,000, 10,000
Interface Condition (k_1)		-	1.0
Existing Surface	Thickness (h_2)	mm	100, 200, 300
	Modulus (E_2)	MPa	500, 5,000
Interface Condition (k_2)		-	1.0
Base Course	Thickness (h_3)	mm	100, 1,000
	Modulus (E_3)	MPa	150, 600
Subgrade	Modulus (E_4)	MPa	30, 150
Traffic Load	Length of Tire Patch (l)	mm	64, 127, 229
	Tire Pressure (p)	psi	96
	Tire Width (w)	mm	222
Load Transfer Efficiency (LTE)		-	0.3, 0.7, 1.0
Ratio of Crack Length to Layer Thickness (c / h_1)		-	0.1, 0.3, 0.5, 0.7, 0.9

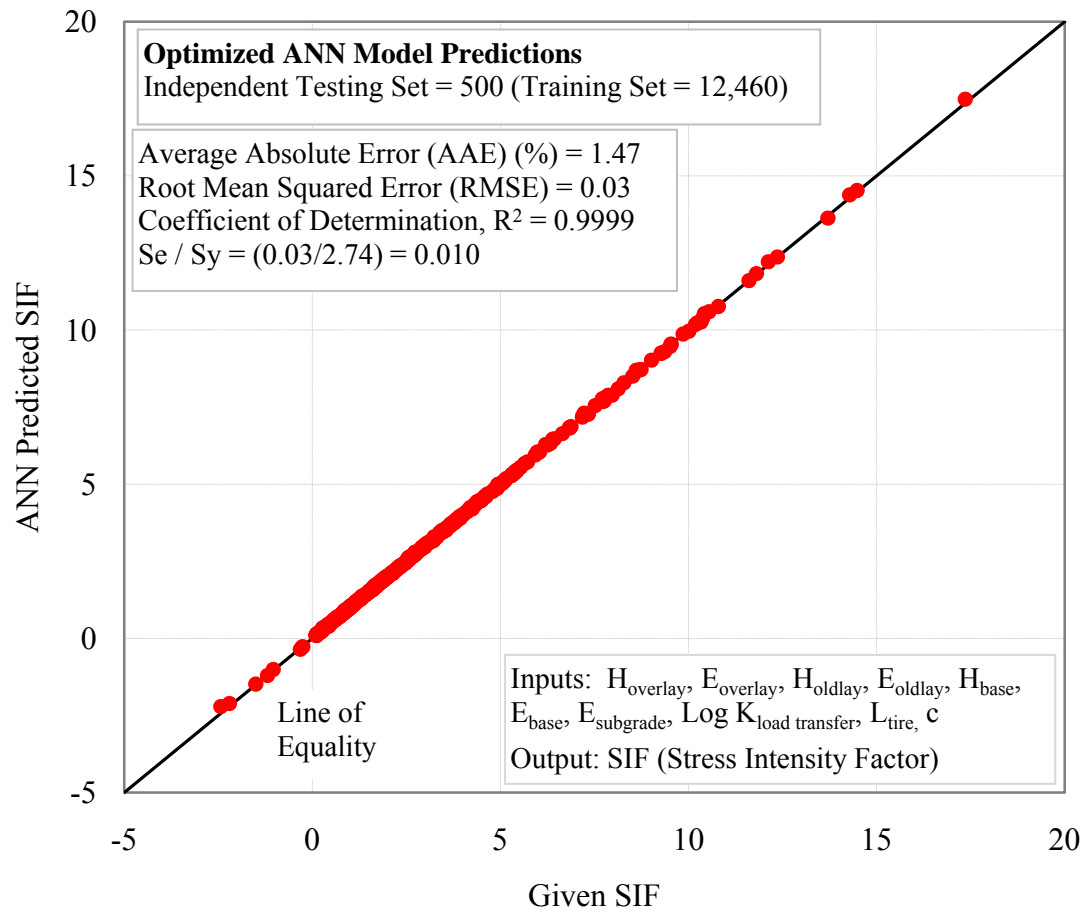


Figure 3.63. ANN model of the shearing part of the shearing stress intensity factors for asphalt overlays over cracked asphalt surface layer (single axle–dual tire).

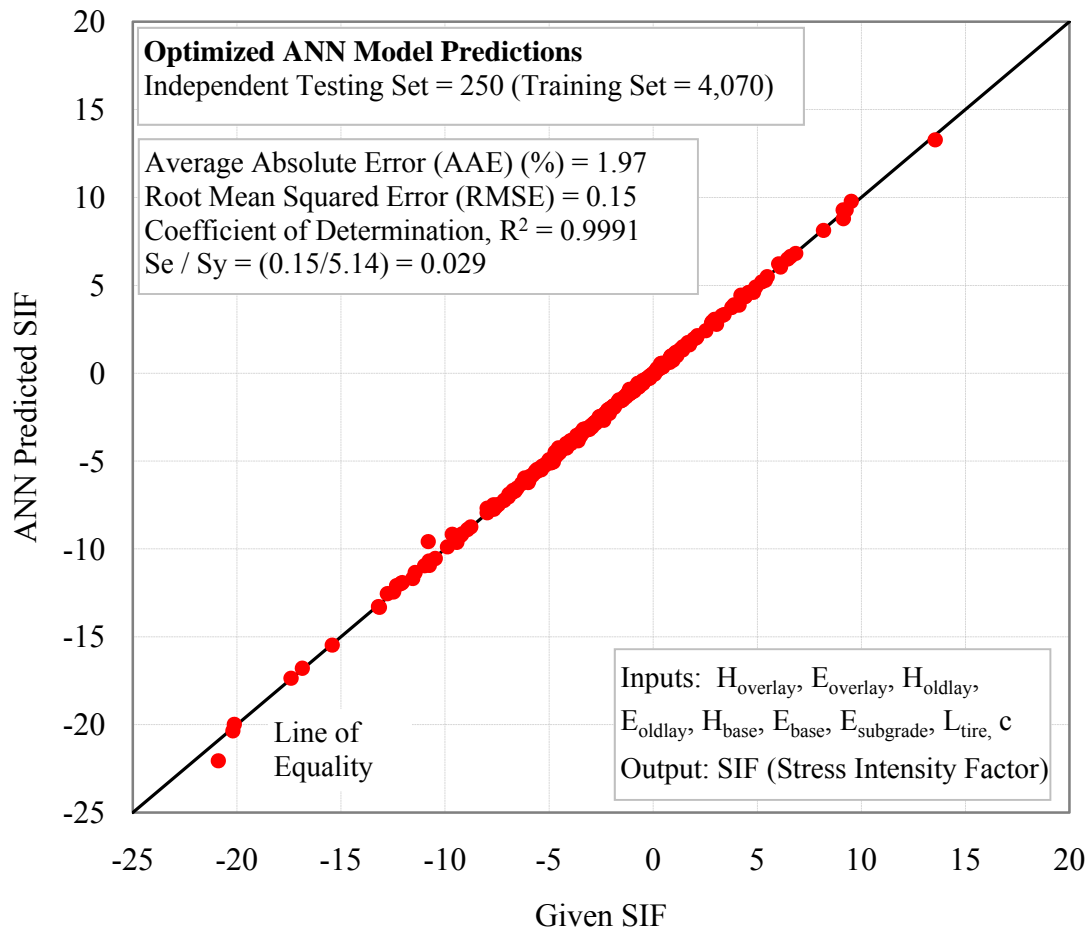


Figure 3.64. ANN model of the bending part of the shearing stress intensity factors for asphalt overlays over crack asphalt surface layer (single axle–dual tire).

c) HMA Overlay on Jointed Concrete Pavement (Single Axle – Single Tire)

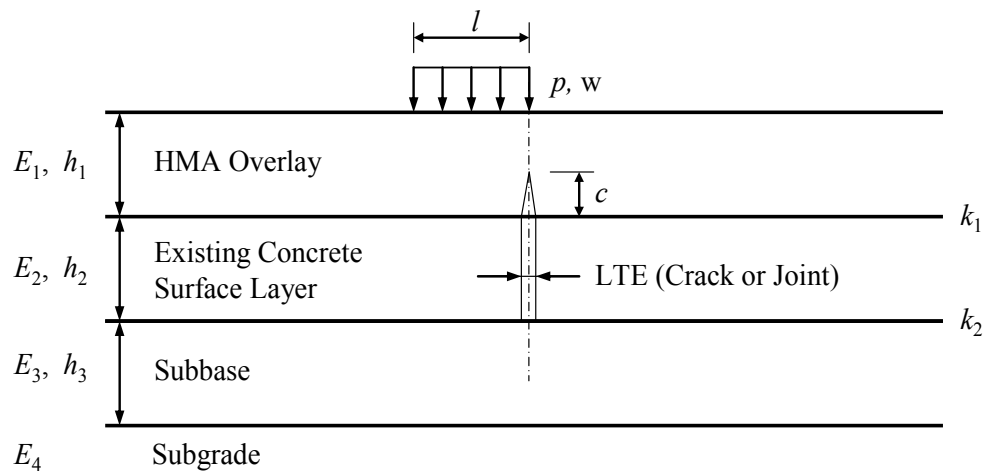


Figure 3.65. Diagram of HMA overlay on jointed concrete pavement-shearing.

Table 3.39. Shearing stress variables in HMA overlay on jointed concrete pavement system.

Variable		Unit	Value
Overlay Layer	Thickness (h_1)	mm	38, 75, 150
	Modulus (E_1)	MPa	1,000, 10,000
Interface Condition (k_1)		-	1.0
Existing Surface	Thickness (h_2)	mm	200, 300, 350
	Modulus (E_2)	MPa	20,000, 30,000, 40,000
Interface Condition (k_2)		-	0.5
Subbase	Thickness (h_3)	mm	100, 1,000
	Modulus (E_3)	MPa	150, 600
Subgrade	Modulus (E_4)	MPa	30, 150

Table 3.39. Continued.

Variable		Unit	Value
Traffic Load	Length of Tire Patch (l)	mm	64, 305, 406
	Tire Pressure (p)	psi	96
	Tire Width (w)	mm	200
Load Transfer Efficiency (LTE)		-	0.3, 0.7, 1.0
Ratio of Crack Length to Layer Thickness (c / h_1)		-	0.1, 0.3, 0.5, 0.7, 0.9

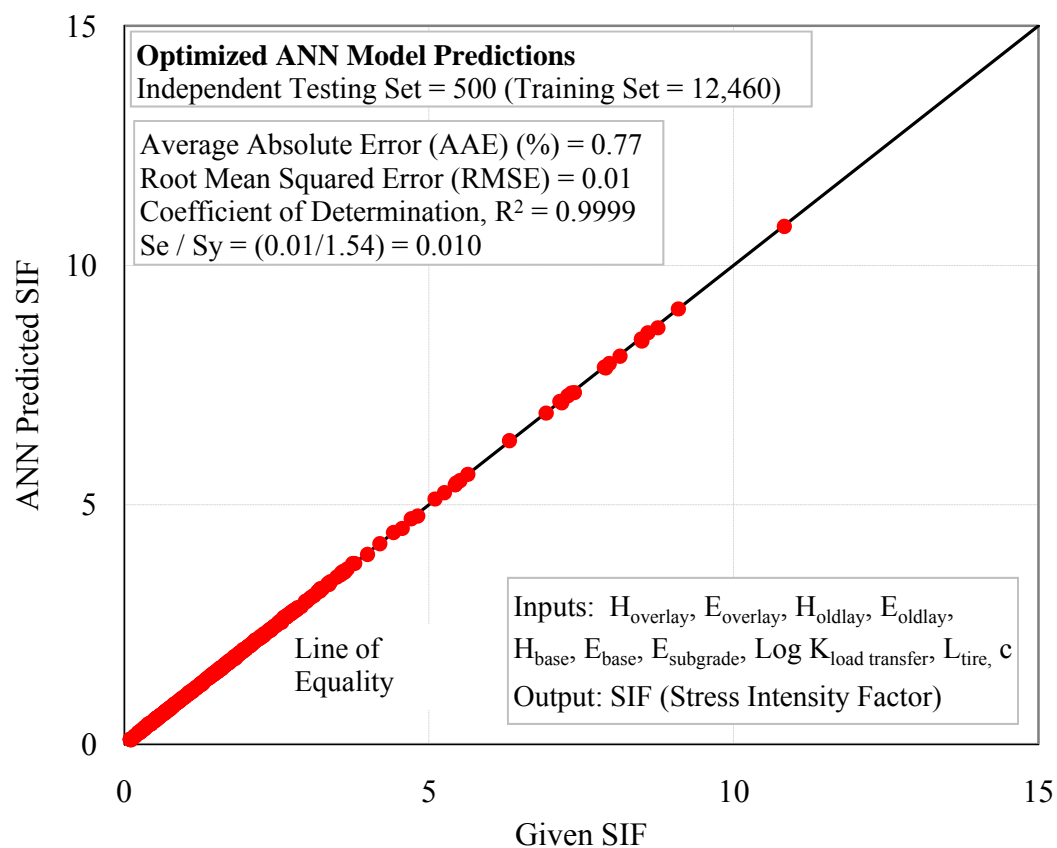


Figure 3.66. ANN model of the shearing stress intensity factors for asphalt overlays over jointed concrete surface layer (single axle–single tire).

d) HMA Overlay on Jointed Concrete Pavement (Single Axle – Dual Tires)

Table 3.40. Shearing stress variables in HMA overlay on jointed concrete pavement system.

Variable		Unit	Value
Overlay Layer	Thickness (h_1)	mm	38, 75, 150
	Modulus (E_1)	MPa	1,000, 10,000
Interface Condition (k_1)		-	1.0
Existing Surface	Thickness (h_2)	mm	200, 300, 350
	Modulus (E_2)	MPa	20,000, 30,000, 40,000
Interface Condition (k_2)		-	0.5
Subbase	Thickness (h_3)	mm	100, 1,000
	Modulus (E_3)	MPa	150, 600
Subgrade	Modulus (E_4)	MPa	30, 150
Traffic Load	Length of Tire Patch (l)	mm	64, 127, 229
	Tire Pressure (p)	psi	96
	Tire Width (w)	mm	222
Load Transfer Efficiency (LTE)		-	0.3, 0.7, 1.0
Ratio of Crack Length to Layer Thickness (c / h_1)		-	0.1, 0.3, 0.5, 0.7, 0.9

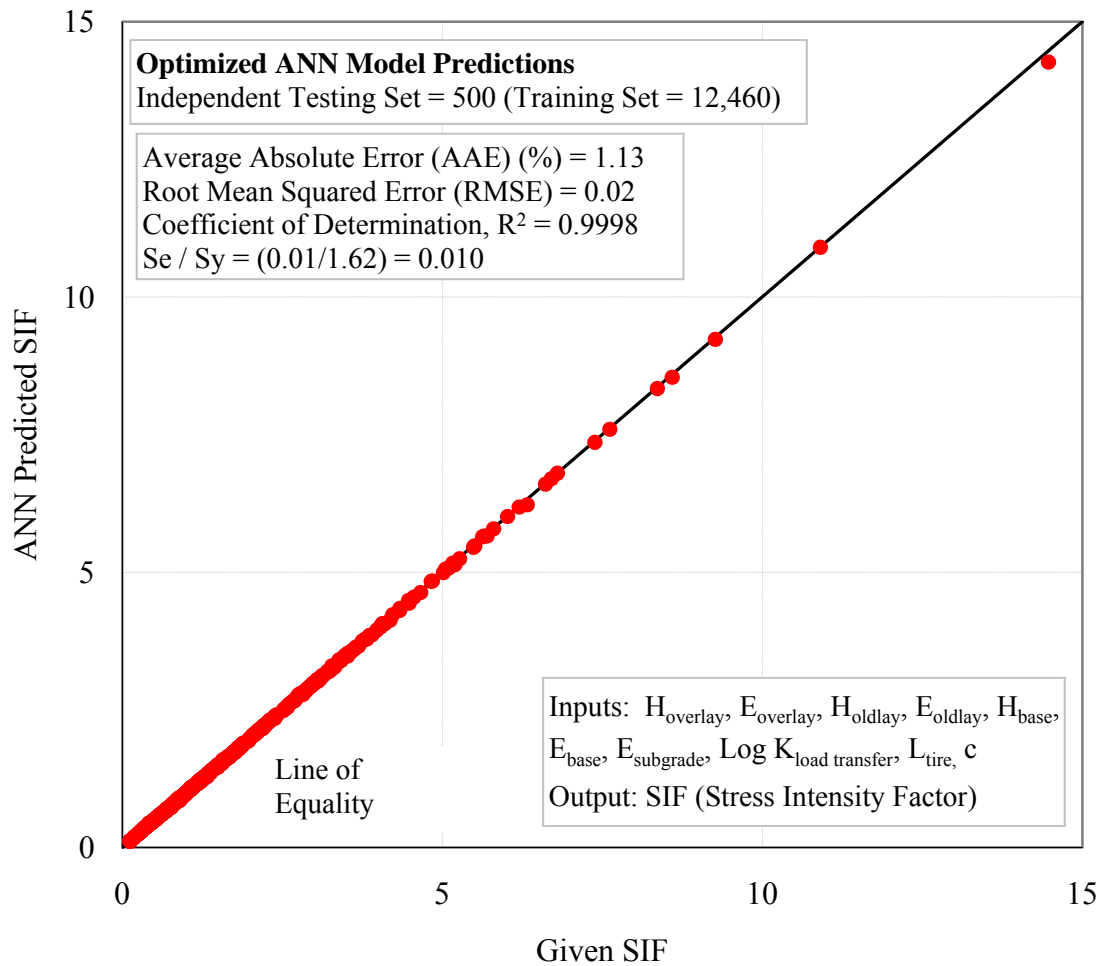


Figure 3.67. ANN model of the shearing stress intensity factors for asphalt overlays over jointed concrete surface layer (single axle – dual tire).

The four bending reflection cracking stress intensity factor cases are shown in Figures 3.68 through 3.75 and the companion tables of variables shown in Tables 3.41 through 3.44.

3.12.3 Bending Reflection Cracking Cases

a) HMA Overlay on Asphalt Concrete Pavement (Single Axle – Single Tire)

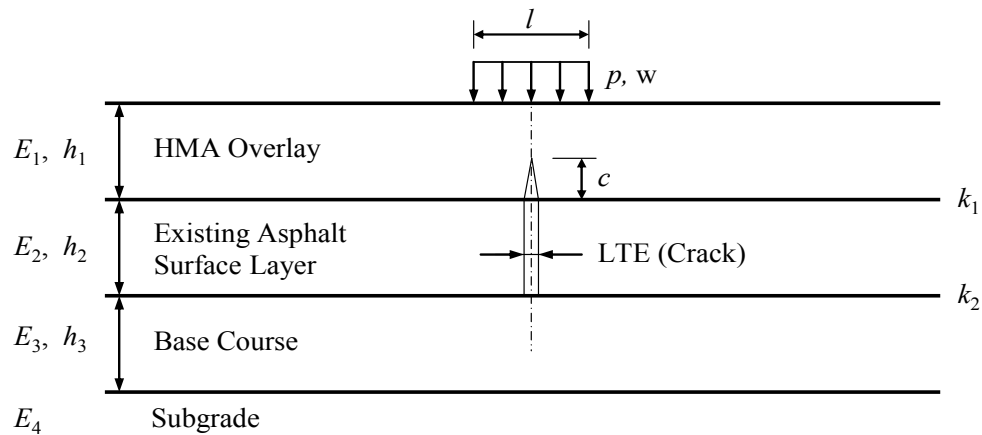


Figure 3.68. Diagram of HMA overlay on asphalt concrete pavement-bending.

Table 3.41. Bending stress variables in HMA overlay on asphalt concrete pavement system.

Variable		Unit	Value
Overlay Layer	Thickness (h_1)	mm	38, 75, 150
	Modulus (E_1)	MPa	1000, 10,000
Interface Condition (k_1)		-	1.0
Existing Surface	Thickness (h_2)	mm	100, 200, 300
	Modulus (E_2)	MPa	500, 5,000
Interface Condition (k_2)		-	0.5
Base Course	Thickness (h_3)	mm	150, 600
	Modulus (E_3)	MPa	100, 1,000
Subgrade	Modulus (E_4)	MPa	30, 150

Table 3.41. Continued.

Variable		Unit	Value
Traffic Load	Length of Tire Patch (l)	mm	64, 305, 406
	Tire Pressure (p)	psi	96
	Tire Width (w)	mm	200
Load Transfer Efficiency (LTE)		-	0.3, 0.7, 1.0
Ratio of Crack Length to Layer Thickness (c / h_1)		-	0.1, 0.3, 0.5, 0.7, 0.9

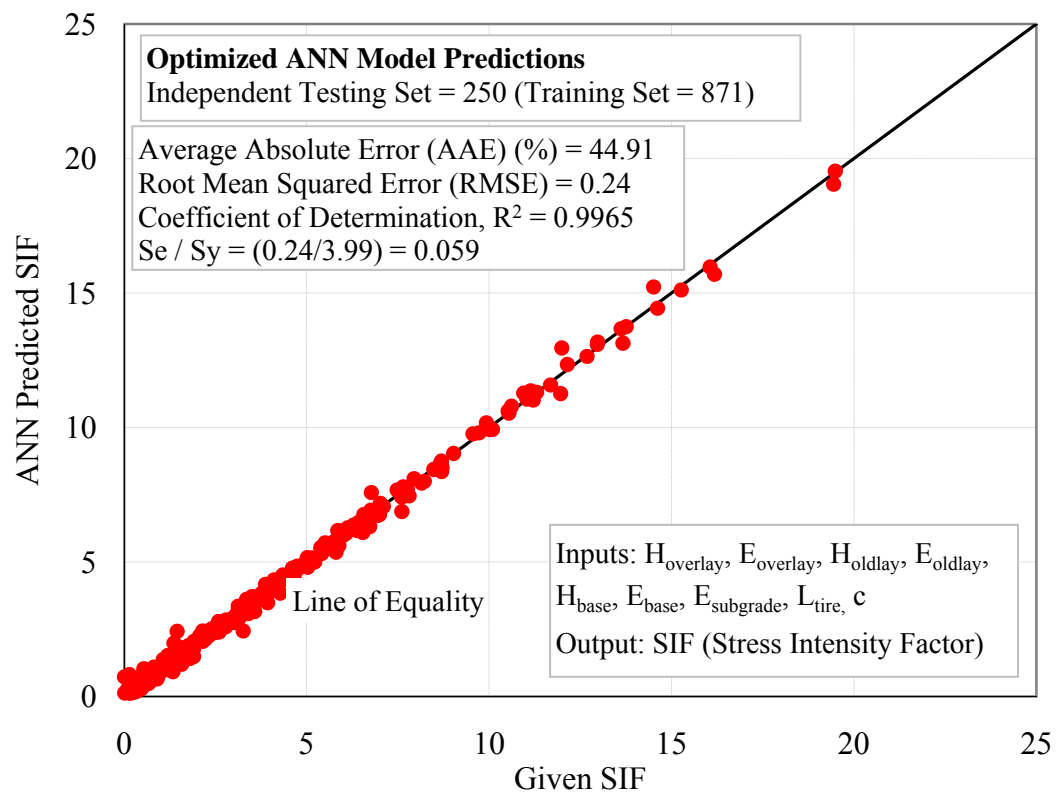


Figure 3.69. ANN model of the positive part of the bending stress intensity factors for asphalt overlays over cracked asphalt surface layer (single axle–single tire).

As a matter of possible interest, the graph in Figure 3.70 shows the results of an ANN model of both the positive and negative stress intensity factors for the single axle, single tire loading case.

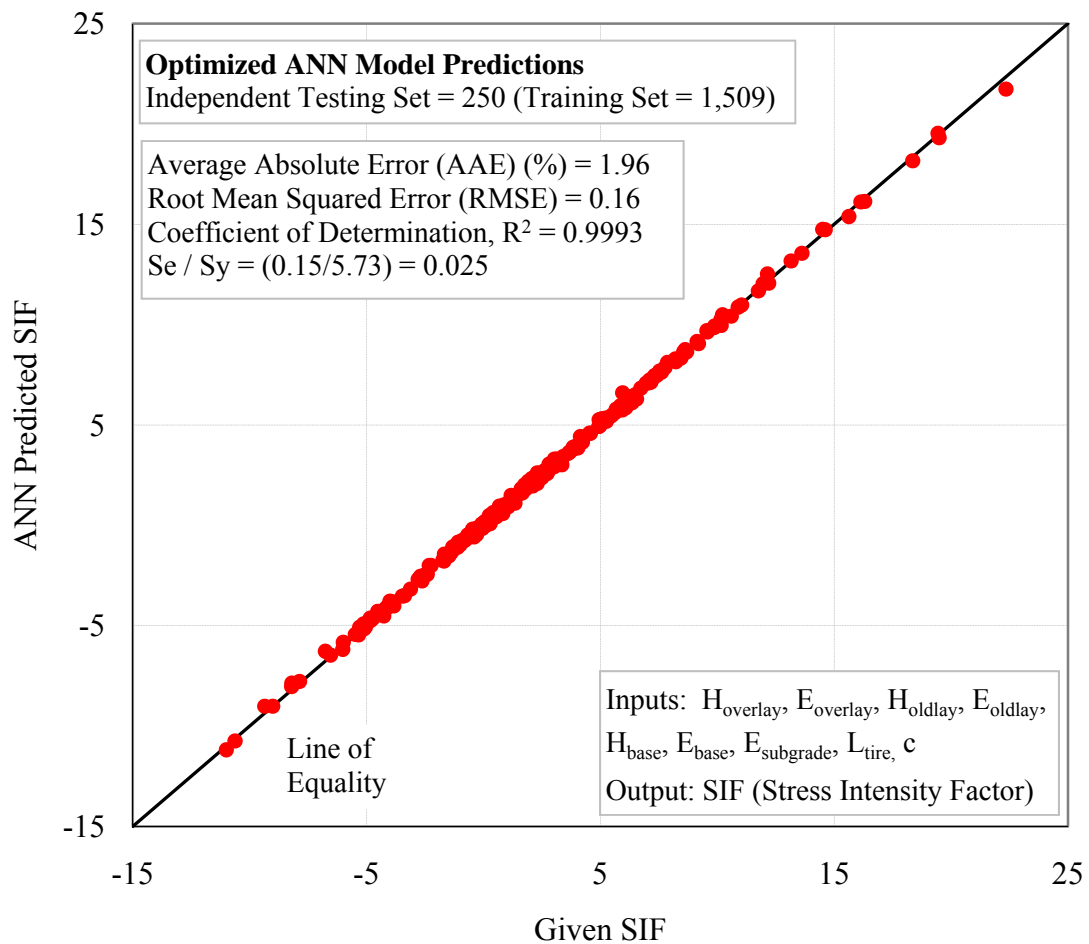


Figure 3.70. ANN model of the positive and negative parts of the bending stress intensity factors for asphalt overlays over cracked asphalt surface layer (single axle–single tire).

b) HMA Overlay on Asphalt Concrete Pavement (Single Axle – Dual Tires)

Table 3.42. Bending stress variables in HMA overlay on asphalt concrete pavement system.

Variable		Unit	Value
Overlay Layer	Thickness (h_1)	mm	38, 75, 150
	Modulus (E_1)	MPa	1,000, 10,000
Interface Condition (k_1)		-	1.0
Existing Surface	Thickness (h_2)	mm	100, 200, 300
	Modulus (E_2)	MPa	500, 5000
Interface Condition (k_2)		-	0.5
Base Course	Thickness (h_3)	mm	150, 600
	Modulus (E_3)	MPa	100, 1,000
Subgrade	Modulus (E_4)	MPa	30, 150
Traffic Load	Length of Tire Patch (l)	mm	64, 127, 229
	Tire Pressure (p)	psi	96
	Tire Width (w)	mm	222
Load Transfer Efficiency (LTE)		-	0.3, 0.7, 1.0
Ratio of Crack Length to Layer Thickness (c / h_1)		-	0.1, 0.3, 0.5, 0.7, 0.9

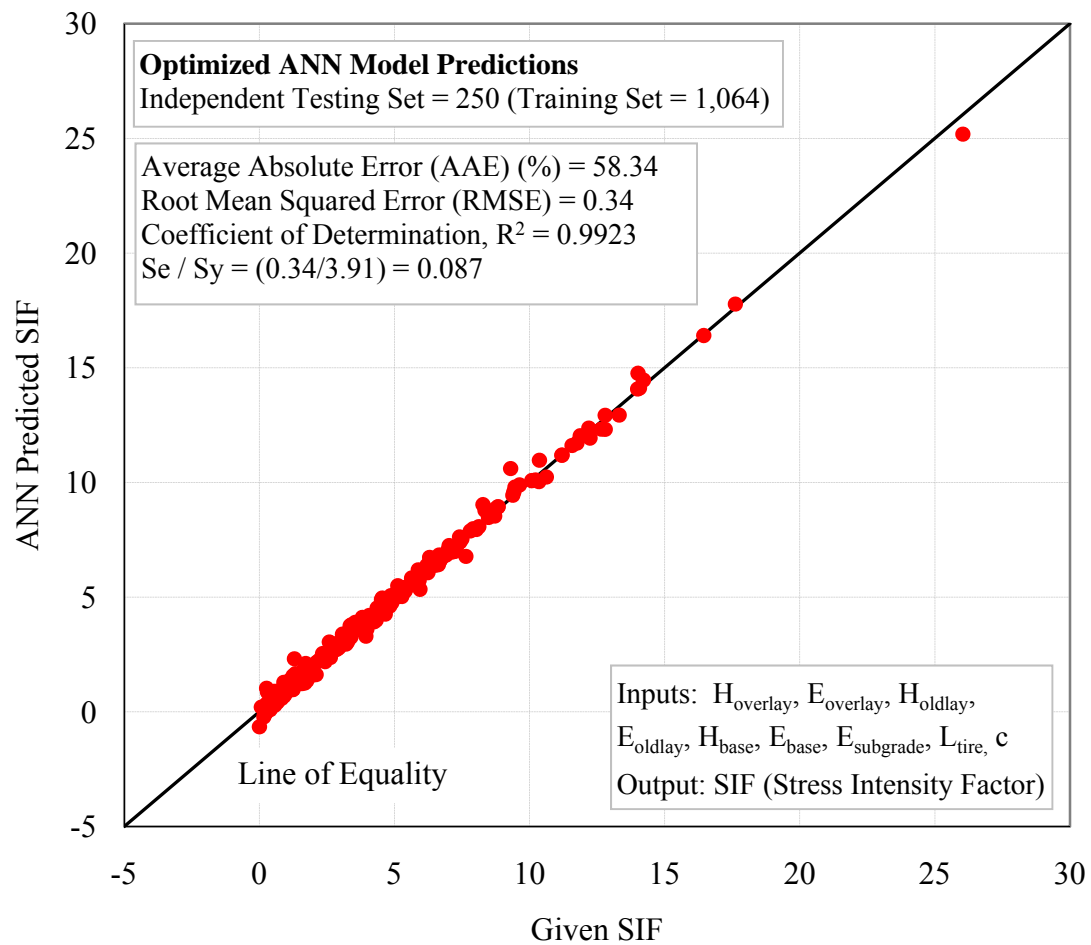


Figure 3.71. ANN model of the positive part of the bending stress intensity factors for asphalt overlays over cracked asphalt surface layer (single axle–dual tire).

As with the single axle, single tire case, Figure 3.72 presents the ANN model for both the positive and negative stress intensity factors for the single axle, dual tire case.

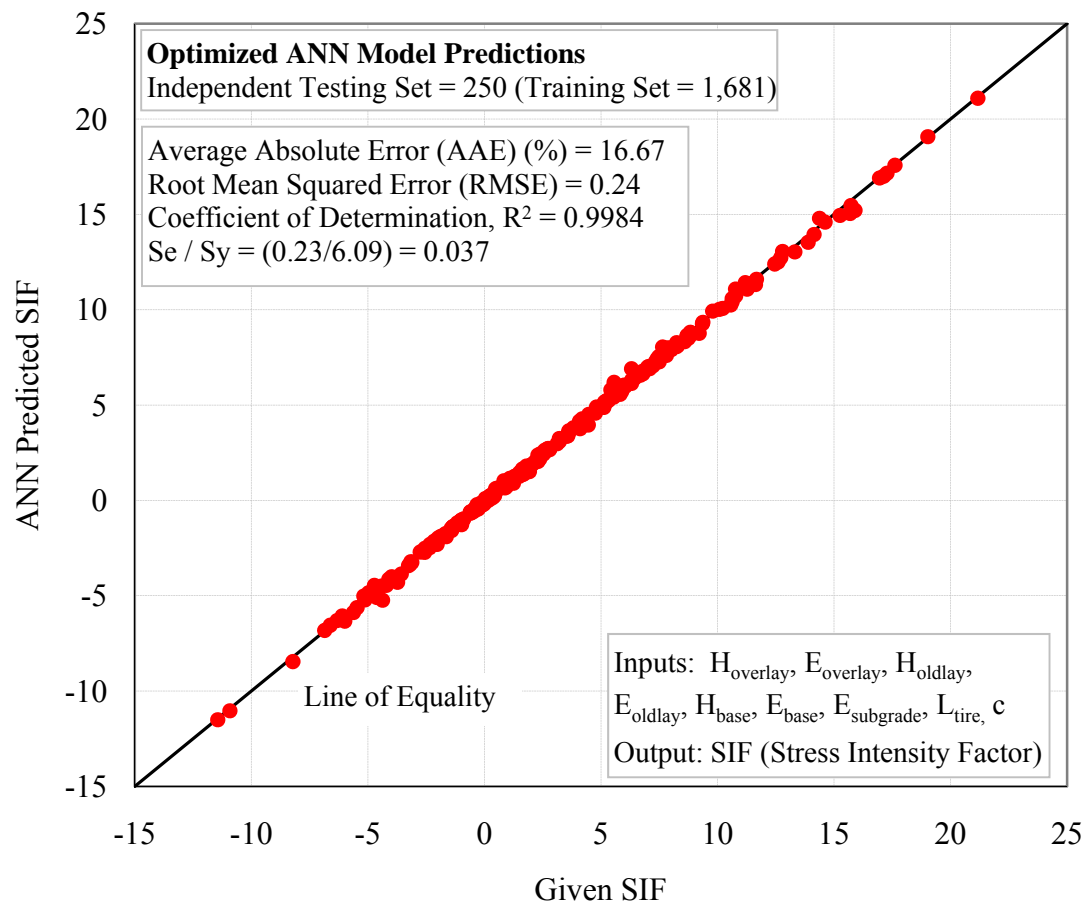


Figure 3.72. ANN model of the positive and negative parts of the bending stress intensity factors for asphalt overlays over cracked asphalt surface layer (single axle–dual tire).

c) HMA Overlay on Jointed Concrete Pavement (Single Axle – Single Tire)

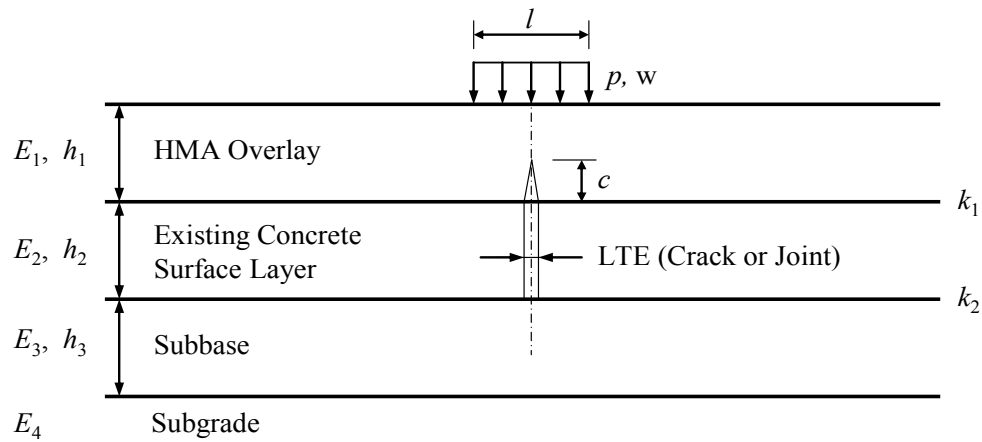


Figure 3.73. Diagram of HMA overlay on jointed concrete pavement-bending.

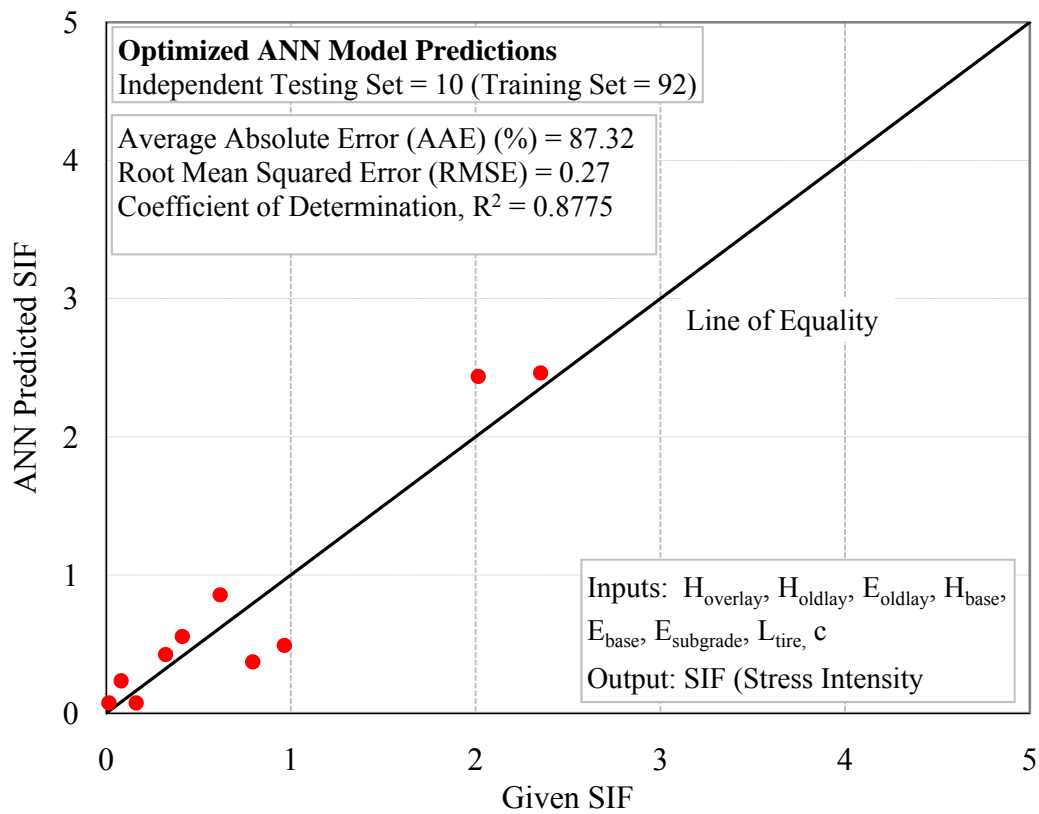


Figure 3.74. ANN model of positive part of the bending stress intensity factors for asphalt overlays over jointed concrete surface layer (single axle–single tire).

Table 3.43. Bending stress variables in HMA overlay on jointed concrete pavement system.

Variable		Unit	Value
Overlay Layer	Thickness (h_1)	mm	38, 75, 150
	Modulus (E_1)	MPa	1,000, 10,000
Interface Condition (k_1)		-	1.0
Existing Surface	Thickness (h_2)	mm	200, 300, 350
	Modulus (E_2)	MPa	20,000, 40,000
Interface Condition (k_2)		-	0.5
Subbase	Thickness (h_3)	mm	150, 600
	Modulus (E_3)	MPa	100, 1,000
Subgrade	Modulus (E_4)	MPa	30, 150
Traffic Load	Length of Tire Patch (l)	mm	64, 305, 406
	Tire Pressure (p)	psi	96
	Tire Width (w)	mm	200
Load Transfer Efficiency (LTE)		-	0.3, 0.7, 1.0
Ratio of Crack Length to Layer Thickness (c / h_1)		-	0.1, 0.3, 0.5, 0.7, 0.9

As is seen in Figure 3.74, there is more scatter and fewer points than with any of the other models. This is because there were so few positive bending stress intensity factors when an asphalt overlay is placed over a jointed concrete pavement. As a matter of possible interest, Figure 3.75 shows the ANN model for both positive and negative Stress Intensity Factors for single axle, single tires on asphalt overlays over jointed

concrete pavements. The positive model only was used in the reflection cracking program.

Although numerous runs were made with this dual tire case of an asphalt overlay over jointed concrete pavement, the number of positive stress intensity factors caused by bending were even fewer than in the case of the single tires. As a consequence of this, the decision was reached not to develop an ANN model of this case.

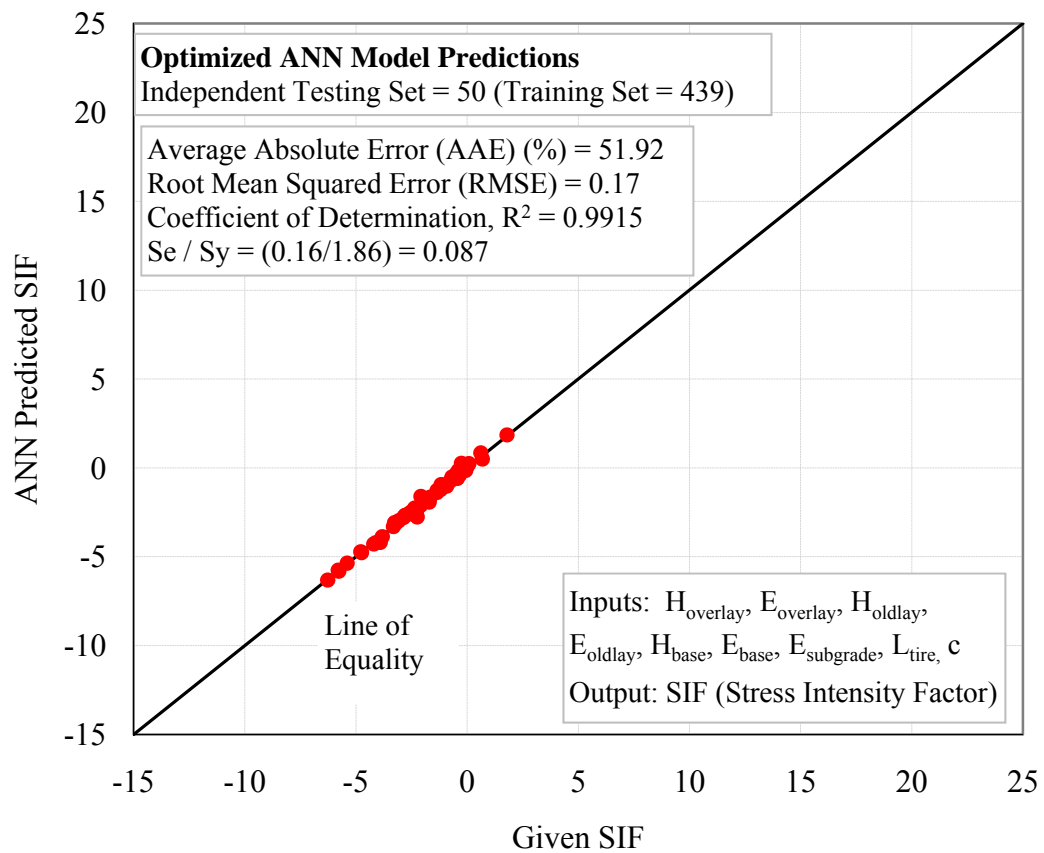


Figure 3.75. ANN model of positive and negative parts of the bending stress intensity factors for asphalt overlays over jointed concrete surface layer (single axle–single tire).

d) HMA Overlay on Jointed Concrete Pavement (Single Axle – Dual Tires)

Table 3.44. Bending stress variables in HMA overlay on jointed concrete pavement system.

Variables		Unit	Value
Overlay Layer	Thickness (h_1)	mm	38, 75, 150
	Modulus (E_1)	MPa	1,000, 10,000
Interface Condition (k_1)		-	1.0
Existing Surface	Thickness (h_2)	mm	200, 300, 350
	Modulus (E_2)	MPa	20,000, 40,000
Interface Condition (k_2)		-	0.5
Subbase	Thickness (h_3)	mm	150, 600
	Modulus (E_3)	MPa	100, 1,000
Subgrade	Modulus (E_4)	MPa	30, 150
Traffic Load	Length of Tire Patch (l)	mm	64, 127, 229
	Tire Pressure (p)	psi	96
	Tire Width (w)	mm	222
Load Transfer Efficiency (LTE)		-	0.3, 0.7, 1.0
Ratio of Crack Length to Layer Thickness (c / h_1)		-	0.1, 0.3, 0.5, 0.7, 0.9

CHAPTER IV

FIELD OBSERVED DISTRESS CALIBRATION AND CALIBRATED COEFFICIENTS DETERMINATION

4.1 Introduction

The models and methods introduced in the Chapter III were combined and perform to be a reflection cracking program. Three curves are adopted here to represent the extent and severity of reflection cracks as they are observed in the field (Figure 4.1). Each curve is plotted against the percent of the original length of transverse cracks in the old pavement surface.

The curves show the growth of the high severity reflection cracks; the sum of the percentages of the high and medium severity cracks; and the sum of the percentages of the high, medium, and low severity cracks. The difference between the curves represents the percentages of the individual levels of distress severity. This S-shaped curve is defined by two parameters: ρ , the scale parameter and β , the shape parameter. The scale parameter (ρ) is the number of days required for the percentage of reflected cracks to reach 36.8 percent, $1/e$, of the original length of the transverse cracks or joints in the old pavement surface. The shape parameter (β) determines how steep the growth of the curve is as it reaches the 36.8 percent mark. This model allows a simple, consistent, and comprehensive description of the distress history of an overlay. It also made the task of calibrating the calculated reflection cracking lives due to traffic and

thermal stresses to the field observations possible. More detail of this model will be introduced in this chapter.

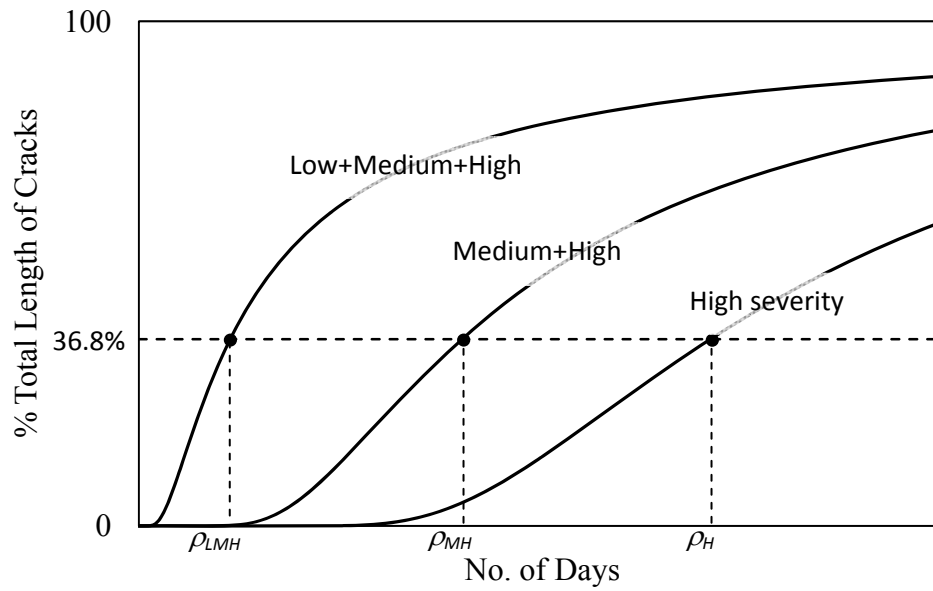


Figure 4.1. Illustration of amount and severity of reflection cracking distress curves.

4.2 Calibration of Calculated Overlay Life to the Observed Distress

Based on the system identification and the parameter adjustment algorithm that described Section 3.8, model parameters ρ and β in the reflection cracking model can be obtained from LTPP (Long Term Pavement Performance) (36), New York City, and Texas asphalt overlay test sections.

The observed model parameters (ρ and β) of 155 sites are shown in Table 4.1. The model parameters ρ and β for the three levels of distress (high, high+medium, and high+medium+low severities) are the field data which was calibrated to the number of days for a crack to propagate through the overlay computed with the reflection cracking model. The coefficients by which the different modes of crack propagation relate to these field derived model parameters are the calibration coefficients which defined a particular application (pavement structure, climatic zone, region) of the reflection cracking model developed in this dissertation.

Table 4.1 Observed coefficients ρ and β for each calibration section.

LTPP ID	State	County	Climatic Zone	H+M+L		H+M		H	
				β	ρ	β	ρ	β	ρ
014129	Alabama	COOSA	WNF	2.400	1266.20				
010563	Alabama	HOUSTON	WNF	5.393	4290.66				
011001	Alabama	LEE	WNF	8.131	2681.98				
010503	Alabama	HOUSTON	WNF	2.753	4409.68				
010505	Alabama	HOUSTON	WNF	3.999	2696.95				
021004	Alaska	ANCHORAGE	WF	0.265	2493.43	0.517	4696.20	3.207	5191.29
021002	Alaska	KENAI PENINSULA	WF	0.965	259.11	1.391	317.99	1.333	671.05
041007	Arizona	MARICOPA	DNF	1.863	2592.64	5.976	3231.69		
040504	Arizona	PINAL	DNF	3.567	4876.01	9.530	5099.01		
040505	Arizona	PINAL	DNF	1.858	3901.33	3.200	4112.13	1.653	6478.76
040506	Arizona	PINAL	DNF	6.718	4260.71	8.279	4736.42	21.845	5086.69
040559	Arizona	PINAL	DNF	3.409	3593.92	2.852	4916.43		
040560	Arizona	PINAL	DNF	3.534	3663.92	3.978	4844.05		
040502	Arizona	PINAL	DNF	4.163	4271.87	2.950	5891.55		
040503	Arizona	PINAL	DNF	2.122	2940.47	3.106	4165.53		
052042	Arkansas	ASHLEY	WNF	2.250	2979.32	3.082	4649.33		
053058	Arkansas	CRAIGHEAD	WNF	0.881	1829.40	3.759	3519.13		
060563	California	SAN BERNARDINO	DNF	1.034	8677.29				
068149	California	SAN BERNARDINO	DNF	5.716	4490.91	9.271	4564.57		
060504	California	SAN BERNARDINO	DNF	3.878	3239.27	8.877	3920.00		
060507	California	SAN BERNARDINO	DNF	4.999	3618.72	7.189	4193.35		
060568	California	SAN BERNARDINO	DNF	2.334	4207.03				
080503	Colorado	LINCOLN	DF	7.565	2561.66	6.857	2810.08	5.751	3030.00
080501	Colorado	LINCOLN	DF	1.095	2191.48	4.346	3077.12	2.333	4108.79

Table 4.1 Continued.

LTPP ID	State	County	Climatic zone	H+M+L		H+M		H	
				β	ρ	β	ρ	β	ρ
080502	Colorado	LINCOLN	DF	0.908	2551.02	1.990	2931.90	11.140	3014.69
080504	Colorado	LINCOLN	DF	4.501	2061.10	21.241	2576.50	20.323	2910.96
080505	Colorado	LINCOLN	DF	2.325	1970.86	2.073	2814.74		
080559	Colorado	LINCOLN	DF	3.328	1406.19	6.678	2503.62	31.976	2906.12
080560	Colorado	LINCOLN	DF	5.368	2432.08	6.983	2721.08	5.680	3333.01
091803	Connecticut	NEW LONDON	WF	0.756	640.37	2.298	1255.32		
134420	Georgia	BRYAN	WNF	1.595	2584.91				
170603	Illinois	CHAMPAIGN	WF	0.424	751.68	1.249	4843.29	2.699	6386.50
170604	Illinois	CHAMPAIGN	WF	0.486	1038.80	1.255	6915.75		
175217	Illinois	MC LEAN	WF	1.171	1393.61	0.722	1686.47		
179327	Illinois	MC LEAN	WF	2.322	1088.89	1.207	2913.93	2.369	3599.00
18A902	Indiana	HANCOCK	WF	0.951	2858.82	2.286	2972.68		
183003	Indiana	MARSHALL	WF	1.777	1482.73	1.490	2126.02		
180901	Indiana	TIPPECANOE	WF	1.031	9483.01				
180905	Indiana	TIPPECANOE	WF	1.171	6537.4	1.216	8319.26		
180904	Indiana	TIPPECANOE	WF	1.898	4974.22	3.102	5061.18		
18A901	Indiana	HANCOCK	WF	4.765	1254.58	4.628	1317.18	6.982	2011.14
190601	Iowa	POLK	WF	1.562	3489.90	0.920	6126.68	1.100	6849.38
199126	Iowa	SCOTT	WF	1.554	717.10	1.761	3454.83		
199116	Iowa	WORTH	WF	0.606	7766.99				
190602	Iowa	POLK	WF	1.902	2911.81	1.472	3507.14		
204067	Kansas	HARVEY	WF	0.608	5512.32				
200106	Kansas	KIOWA	WF	3.941	1014.22				
201009	Kansas	STAFFORD	WF	3.348	2595.59				

Table 4.1 Continued.

LTPP ID	State	County	Climatic zone	H+M+L		H+M		H	
				β	ρ	β	ρ	β	ρ
230502	Maine	PENOBSCOT	WF	13.889	3511.78				
240504	Maryland	FREDERICK	WF	1.009	3041.47	1.607	4308.59		
240505	Maryland	FREDERICK	WF	0.523	679.28	1.157	1952.56	4.953	4261.28
240559	Maryland	FREDERICK	WF	0.835	768.99	3.290	3565.63		
240560	Maryland	FREDERICK	WF	1.018	2009.67	13.339	4654.15		
240561	Maryland	FREDERICK	WF	0.886	1542.61	5.523	3963.47		
240562	Maryland	FREDERICK	WF	1.076	2820.29	2.988	4998.90		
240563	Maryland	FREDERICK	WF	2.276	1461.25	5.618	3695.47		
270507	Minnesota	BELTRAMI	WF	0.247	4912.94	0.589	4796.83		
270561	Minnesota	BELTRAMI	WF	0.891	562.72	1.064	1038.24	1.651	3497.14
270902	Minnesota	SCOTT	WF	0.249	18902.46	0.326	23698.11		
275076	Minnesota	WASHINGTON	WF	1.009	4971.47	1.493	6915.26		
270559	Minnesota	BELTRAMI	WF	0.196	2493.43	0.445	3956.79	1.287	4984.75
270903	Minnesota	SCOTT	WF	0.281	15072.46	0.234	24557.28		
270909	Minnesota	SCOTT	WF	0.689	691.96	0.198	22998.11		
282807	Mississippi	LAFAYETTE	WNF	0.489	1027.64				
283091	Mississippi	LAUDERDALE	WNF	0.588	559.99	1.010	3500		
280504	Mississippi	YAZOO	WNF	2.710	2828.65				
280502	Mississippi	YAZOO	WNF	7.217	2512.12				
280503	Mississippi	YAZOO	WNF	3.266	1671.77				
295483	Missouri	CLAY	WF	0.806	1757.13	0.768	2210.07	1.380	5460.17
295403	Missouri	DUNKLIN	WF	1.083	2068.20	6.159	3861.86	2.841	5441.40
295413	Missouri	DUNKLIN	WF	3.624	3879.37	3.700	4463.56	2.160	7417.96
294069	Missouri	PLATTE	WF	2.590	2072.02	1.275	3173.28		

Table 4.1 Continued.

LTPP ID	State	County	Climatic zone	H+M+L		H+M		H	
				β	ρ	β	ρ	β	ρ
295393	Missouri	ST CHARLES	WF	5.567	2355.11	4.258	2780.28	2.990	3905.46
290507	Missouri	TANEY	WF	3.908	2700.58				
341033	New Jersey	HUNTERDON	WF	2.535	1614.23	2.560	1835.50		
340560	New Jersey	MONMOUTH	WF	2.009	5369.19				
341003	New Jersey	SUSSEX	WF	2.535	1614.23	2.560	1835.50		
340504	New Jersey	MONMOUTH	WF	1.470	4177.91	5.392	4701.23		
361008	New York	ONEIDA	WF	1.789	2282.40	1.083	3709.18		
361644	New York	ST LAWRENCE	WF	0.607	5552.37				
361643	New York	WASHINGTON	WF	0.736	4278.16	1.090	3923.40	2.664	3410.05
371801	North Carolina	BUNCOMBE	WF	4.714	2537.93	4.784	2683.37		
371814	North Carolina	MACON	WNF	1.875	1896.21				
393013	Ohio	BROWN	WF	0.603	183.25	3.377	2449.63		
421691	Pennsylvania	BEAVER	WF	0.367	2058.82	0.960	3436.64	7.502	4136.91
421614	Pennsylvania	CENTRE	WF	0.382	418.20				
421613	Pennsylvania	DELAWARE	WF	0.441	586.60				
421617	Pennsylvania	MONTGOMERY	WF	2.864	2523.45				
421605	Pennsylvania	NORTHUMBERLAND	WF	0.884	1197.66				
421618	Pennsylvania	SOMERSET	WF	4.561	3031.34	7.862	3958.55		
460601	South Dakota	BROWN	WF	1.883	3760.66				
460605	South Dakota	BROWN	WF	4.065	3707.32	2.393	4510.51	3.186	4572.37
473108	Tennessee	ANDERSON	WF	3.218	2751.85				
472008	Tennessee	GIBSON	WF	5.868	2955.60				
471029	Tennessee	MARION	WNF	4.137	1704.25				
473110	Tennessee	MC MINN	WNF	0.854	3017.57				

Table 4.1 Continued.

LTPP ID	State	County	Climatic zone	H+M+L		H+M		H	
				β	ρ	β	ρ	β	ρ
481119	Texas	CHEROKEE	WNF	3.267	3512.14				
486079	Texas	DEAF SMITH	DF	0.742	75.49	0.695	70.89	0.600	73.04
483855	Texas	FAYETTE	WNF	1.068	3011.34				
483865	Texas	MILLS	WNF	2.909	716.98				
483875	Texas	SHERMAN	DF	1.074	2299.40	1.383	4951.88		
501682	Vermont	CHITTENDEN	WF	0.535	23.75	0.599	2497.00		
501683	Vermont	CHITTENDEN	WF	2.096	7998.09				
501681	Vermont	CHITTENDEN	WF	1.120	6155.32				
512021	Virginia	CARROLL	WF	6.603	3770.20	2.931	4395.25		
512004	Virginia	PITTSYLVANIA	WNF	3.444	1922.09	9.443	2008.55		
511023	Virginia	PRINCE GEORGE	WNF	4.868	2361.23				
511464	Virginia	YORK	WNF	6.425	2289.81	6.425	2289.81		
531008	Washington	SPOKANE	DF	0.681	978.41	0.675	1298.94	3.553	3151.42
55B900	Wisconsin	ASHLAND	WF	1.061	968.90	1.072	1671.61	5.923	4598.87
550902	Wisconsin	MONROE	WF	0.778	2188.13	0.919	3563.78	1.613	5920.96
55A900	Wisconsin	WAUKESHA	WF	0.892	2055.53	0.719	4706.15		
550901	Wisconsin	MONROE	WF	0.308	2130.56	0.581	4583.75	1.510	7799.83
	Texas	Waco	WNF	0.36	906.71				
	Texas	Waco	WNF	0.8	1881.81				
	Texas	Waco	WNF	0.427	308.27				
	Texas	Waco	WNF	1.043	1427.13				
	Texas	Waco	WNF	0.606	1873.72				
	Texas	Waco	WNF	0.447	729.85				

Table 4.1 Continued.

LTPP ID	State	County	Climatic zone	H+M+L		H+M		H	
				β	ρ	β	ρ	β	ρ
	Texas	Waco	WNF	1.074	2379.75				
	Texas	Amarillo	DF	1.266	1664.9				
	Texas	Amarillo	DF	1.355	1758.09				
	Texas	Amarillo	DF	1.49	1819.89				
	Texas	Amarillo	DF	0.667	1619.74				
	Texas	Amarillo	DF	2.383	2036.85				
	Texas	Amarillo	DF	1.494	1766.2				
	Texas	Amarillo	DF	1.436	2015.39				
	Texas	Amarillo	DF	6.784	1762.73				
	Texas	Amarillo	DF	1.345	1633.91				
	Texas	Amarillo	DF	0.896	1929.89				
	Texas	Amarillo	DF	2.806	1997.73				
	New York	New York	WF	0.867	322.42	0.805	473.25		
	New York	New York	WF	0.991	2197.32	0.676	4753.42		
	New York	New York	WF	0.766	1123.27	0.985	2237.87		
	New York	New York	WF	0.731	1402.14	0.711	2799.96		
	New York	New York	WF	0.955	1403.55	1.171	2034.02		
	New York	New York	WF	0.539	2260.60	1.092	2660.89		
	New York	New York	WF	0.162	550.14	0.835	2618.90		
	New York	New York	WF	0.554	1622.74	0.923	3385.46		
	New York	New York	WF	0.715	484.53	2.158	1510.52		
	New York	New York	WF	1.728	1299.36	0.881	3037.79		
	New York	New York	WF	1.165	1458.92	1.659	2014.79		

Table 4.1 Continued.

LTPP ID	State	County	Climatic zone	H+M+L		H+M		H	
				β	ρ	β	ρ	β	ρ
	New York	New York	WF	1.367	1184.70	2.026	2308.27		
	New York	New York	WF	2.684	991.36	2.084	1611.83		
	New York	New York	WF	1.050	2578.42	1.212	5019.59		
	New York	New York	WF	2.485	1192.14	1.817	2358.40		
	New York	New York	WF	1.627	1607.16	0.819	4612.83		
	New York	New York	WF	2.625	1037.27	1.003	2258.14		
	New York	New York	WF	2.117	1194.36	1.160	3517.76		
	New York	New York	WF	2.872	906.24	2.487	1346.83		
	New York	New York	WF	23.709	856.86	2.781	1098.01		
	New York	New York	WF	1.761	1388.10	0.757	6103.60		
	New York	New York	WF	1.010	1622.78	0.773	3318.02		
	New York	New York	WF	1.686	558.64	2.783	996.77		
	New York	New York	WF	0.499	351.29	1.451	1029.74		

4.3 Calibrated Model and Calibrated Coefficients Determination

At the end of the computations, there are five calculated numbers of days for a crack to reach a designated point within an overlay, (Position I) at which the bending stresses become compressive and no longer cause crack growth and (Position II) the surface of the overlay. These five numbers of days are illustrated in Figure 4.2.

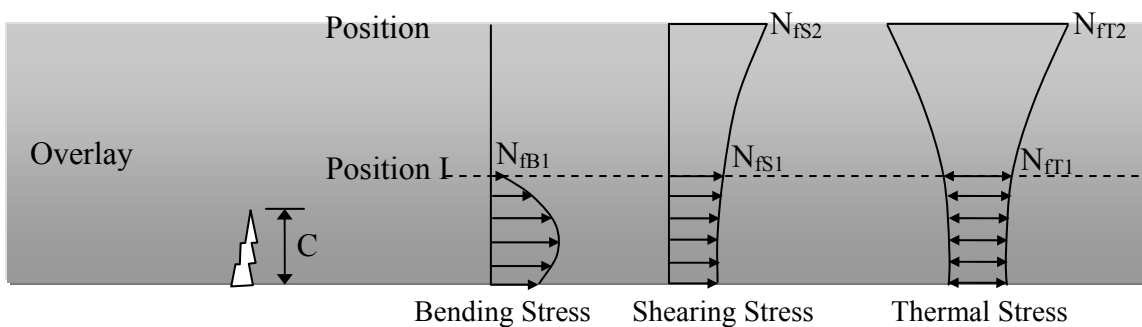


Figure 4.2. Definition of the number of days of crack growth.

- N_{FB1} = Number of days for crack growth due to bending to reach Position I.
- N_{FT1} = Number of days for thermal crack growth to reach Position I.
- N_{FS1} = Number of days for crack growth due to shearing stress to reach Position I.
- N_{FT2} = Number of days for thermal crack growth to go from Position I to Position II.
- N_{FS2} = Number of days for crack growth due to shearing stress to go from Position I to Position II.

These five numbers of days can be combined in several ways to model the value of ρ , the scale parameter of the amount and severity of the observed reflection cracking distress. One of these ways of modeling the ρ -value is to assume that the principal cause of reflection cracking is bending stress and another way is to assume that shearing stress is the principal cause of reflection cracking. In both cases, it becomes necessary to find how many days of each of the other types of cracking are the equivalent of the number of days of the principal cause of the distress. This concept is illustrated in Figure 4.1 which shows ρ -values of three severities, i.e., ρ_{LMH} , ρ_{MH} , and ρ_H . The linear regression form of the model for the ρ_{LMH} -value assuming that bending stress is the principal cause of the reflection cracking up to Position I and shearing is the principal cracking mechanism from Position I up to the surface of the overlay, is presented in Equations 40 through Equation 42.

The thermal calibration model for the low+medium+high distress curve is in Equation 4.1.

$$\rho_{LMH} = N_{fB1} \left(\alpha_0 - \alpha_1 \frac{N_{fB1}}{N_{fT1}} - \alpha_2 \frac{N_{fB1}}{N_{fS1}} \right) + N_{fT2} \left(\alpha_3 - \alpha_4 \frac{N_{fT2}}{N_{fS2}} \right) \quad (4.1)$$

Calibration Coefficients : $\alpha_0, \alpha_1, \alpha_2, \alpha_3, \alpha_4, \beta_{LMH}$

The thermal calibration models for the High and Medium + High distress curves are shown below.

$$\rho_{MH} = N_{fB1} \left(\alpha_5 - \alpha_6 \frac{N_{fB1}}{N_{fT1}} - \alpha_7 \frac{N_{fB1}}{N_{fS1}} \right) + N_{fT2} \left(\alpha_8 - \alpha_9 \frac{N_{fT2}}{N_{fS2}} \right) \quad (4.2)$$

Calibration Coefficients : $\alpha_5, \alpha_6, \alpha_7, \alpha_8, \alpha_9, \beta_{MH}$

$$\rho_H = N_{fB1} \left(\alpha_{10} - \alpha_{11} \frac{N_{fB1}}{N_{fT1}} - \alpha_{12} \frac{N_{fB1}}{N_{fS1}} \right) + N_{fT2} \left(\alpha_{13} - \alpha_{14} \frac{N_{fT2}}{N_{fS2}} \right) \quad (4.3)$$

Calibration Coefficients : $\alpha_{10}, \alpha_{11}, \alpha_{12}, \alpha_{13}, \alpha_{14}, \beta_H$

A similar set of coefficients can be derived by linear regression analysis assuming that bending is the principal mode of reflection cracking until it reaches Position I and then shearing stress is the principal mode of reflection cracking from Position I to the surface of the overlay. An example of this assumed calibration form is shown in Equation 4.4.

$$\rho_{LMH} = N_{fB1} \left(\alpha_0 - \alpha_1 \frac{N_{fB1}}{N_{fT1}} - \alpha_2 \frac{N_{fB1}}{N_{fS1}} \right) + N_{fS2} \left(\alpha_3 - \alpha_4 \frac{N_{fS2}}{N_{fT2}} \right) \quad (4.4)$$

The calibration coefficients are, as in the first form of this model, $\alpha_0, \alpha_1, \alpha_2, \alpha_3$ and α_4 . Similar models are assumed for the scale parameters ρ_{MH} and ρ_H . Similar linear regression models were also used to model the shape parameter, β .

In performing the calibration analysis, the thermal, bending, and shearing forms of equation were tried and the one which proved to have the highest coefficient of determination, R^2 , was selected. In general, the model with bending as the principal cracking mechanism up to Position I and thermal stress as the principal cracking mechanism from there to the surface of the overlay had the highest R^2 -value with all

overlay types except for one category of pavement. The exception was the AC overlay with reinforcing interlayer pavement structures. In this case, bending was the principal crack growth mode up to Position I in this model. Shearing was the principal cracking mode from Position I to the surface of the overlay as Equation 4.4.

The method used to develop calibration coefficients is linear regression analysis and observation of the patterns of the predicted versus the observed values of both ρ and β . If the coefficient of determination (R^2) was acceptable and the scatter of the data was clustered around the line of equality, the calibration coefficients were considered acceptable. This approach had to be taken because only 131 of the sections were unique; the rest were similar in pavement features (structure, materials), traffic, and weather, such that there were not enough sections to separate the sections into two categories (calibration sections and validation sections).

There are total of 131 sections used in the calibration evaluation. The regression coefficients ρ and β are calibrated to the observed values of field data which contained high severity (ρ_H, β_H), medium + high severity (ρ_{MH}, β_{MH}), and low + medium + high severity (ρ_{LMH}, β_{LMH}) data. Based on these observed values of ρ and β as shown in Table 4.1, linear regression can be used to calibrate the coefficients of the mechanistic crack growth model for different types of pavement structures and climatic zones.

The summary of the results for different climatic zones and pavement structures are shown in Table 4.2. Figures 4.3 to Figure 4.26 show the results of the linear regression method.

Table 4.2. Summary of modeling coefficients for different pavement structures and climatic zones.

			α_0	α_1	α_2	α_3	α_4	$R^2_{w/o\ outlier}$	$R^2_{w/ outlier}$
ρ_{LMH}	WF	AC/AC	1.36E+02	-9.53E-01	5.85E+01	8.22E+01	-1.99E-01	0.488215	0.37662
		JRC/JPC	-6.35E+08	-6.35E+08	4.03E+03	-3.06E+01	5.90E+00	0.524717	0.45657
		FC/AC	1.72E+10	1.72E+10	5.38E+02	1.73E+01	-1.81E+02	0.760757	0.26949
		CRC/AC	-6.50E+08	-6.36E+08	-1.47E+07	-3.81E+02	-1.63E+04	0.775576	0.77558
		AC/Reinforcing/PCC	-1.72E+10	-8.59E+09	-8.59E+09	1.97E+01	-6.01E+00	0.35734	0.31101
	WNF	AC/AC	2.29E+03	1.78E+03	-9.49E+02	8.58E+00	-1.16E-01	0.784504	0.53332
		FC/AC	-1.30E+05	-1.28E+04	-1.18E+05	-8.58E+00	-8.80E+01	0.768855	0.4567
		AC/Reinforcing/PCC	-1.64E+03	1.44E+03	1.41E+03	2.10E+03	1.59E+02	0.583384	0.37016
	DF	AC/Reinforcing/AC	2.04E+03	-2.99E+04	3.01E+04	-9.92E-01	-5.75E+00	0.134864	0.13486
		AC/AC	8.35E+01	8.49E+00	-2.62E+00	5.08E+01	1.56E+01	0.71824	0.64161
	DNF	AC/AC	4.57E+02	1.09E+01	4.47E+01	3.41E+01	1.27E+01	0.885011	0.66384
			β_0	β_1	β_2	β_3	β_4	$R^2_{w/o\ outlier}$	$R^2_{w/ outlier}$
β_{LMH}	WF	AC/AC	7.13E-01	1.12E-01	-6.35E-02	1.41E-02	-2.74E-03	0.681528	0.5702
		JRC/JPC	6.21E-01	-1.21E+00	-7.86E-01	-4.25E-02	-1.41E-02	0.502271	0.466
		FC/AC	3.26E+10	1.63E+10	1.63E+10	1.26E-02	1.22E-02	0.668079	0.31107
		CRC/AC	3.61E+03	-2.21E+00	3.61E+03	1.36E-01	4.01E+00	0.86974	0.86974
		AC/Reinforcing/PCC	1.12E+09	5.60E+08	5.60E+08	4.81E-02	-1.19E-02	0.443029	0.43709
	WNF	AC/AC	4.45E+00	5.06E+00	-2.85E+00	2.27E-02	1.86E-06	0.643317	0.59368
		FC/AC	-1.72E+10	-8.59E+09	-8.59E+09	-5.73E-03	-1.50E-01	0.813614	0.66452
		AC/Reinforcing/PCC	1.38E+00	-5.68E+00	4.30E+00	-4.99E-01	-3.65E-02	0.572104	0.35183
	DF	AC/Reinforcing/AC	1.03E+00	-3.12E+01	3.28E+01	3.66E-02	-1.20E-02	0.731422	0.58526
		AC/AC	-1.09E-01	-5.38E-02	4.60E-02	9.70E-02	2.65E-02	0.719001	0.54557
	DNF	AC/AC	2.06E-01	5.04E-03	2.13E-02	3.54E-02	1.68E-03	0.700608	0.58154

Table 4.2. Continued.

			α_0	α_1	α_2	α_3	α_4	$R^2_{w/o\ outlier}$	$R^2_{w/ outlier}$
ρ_{MH}	WF	AC/AC	4.52E+03	8.49E+02	-2.52E+02	1.84E+01	1.40E+01	0.714736	0.2102
		JRC/JPC	1.82E+07	1.82E+07	1.40E+04	2.86E+01	6.02E+01	0.501718	0.49972
		FC/AC	1.63E+10	1.63E+10	-3.39E+02	3.61E+01	-1.90E+01	0.480755	0.41402
		CRC/AC	-1.54E+07	1.10E+07	-2.64E+07	4.19E+02	3.07E+04	0.999995	0.99999
		AC/Reinforcing/PCC	2.32E+03	-9.38E+02	-2.18E+03	-2.30E+01	-2.52E+01	0.452683	0.32298
	WNF	AC/AC	2.32E+03	9.38E+02	-2.18E+03	-2.30E+01	-1.19E+00	0.929697	0.9297
		FC/AC	N/A	N/A	N/A	N/A	N/A	N/A	N/A
		AC/Reinforcing/PCC	N/A	N/A	N/A	N/A	N/A	N/A	N/A
	DF	AC/Reinforcing/AC	N/A	N/A	N/A	N/A	N/A	N/A	N/A
		AC/AC	9.98E+01	1.12E+01	-1.81E+01	6.33E+01	1.35E+01	0.767309	0.59148
DNF	AC/AC	5.47E+02	-3.13E+00	8.56E+01	2.41E+01	-6.77E+00	0.482832	0.44129	
			β_0	β_1	β_2	β_3	β_4	$R^2_{w/o\ outlier}$	$R^2_{w/ outlier}$
β_{MH}	WF	AC/AC	6.62E+08	9.31E+07	5.69E+08	1.31E-01	4.56E-01	0.806066	0.40459
		JRC/JPC	9.51E+00	9.38E+00	-2.82E+00	-3.90E-02	-1.83E-02	0.564571	0.49286
		FC/AC	-4.12E+09	-2.06E+09	-2.06E+09	7.46E-02	1.34E-01	0.771652	0.77165
		CRC/AC	-2.42E+02	-1.51E+02	-9.25E+01	-9.59E-02	-1.17E+01	1	1
		AC/Reinforcing/PCC	1.08E+07	5.41E+06	5.41E+06	4.66E-02	-9.22E-03	0.364102	0.28908
	WNF	AC/AC	6.37E+00	7.66E+00	-4.94E+00	1.11E-01	1.27E-03	1	0.52431
		FC/AC	N/A	N/A	N/A	N/A	N/A	N/A	N/A
		AC/Reinforcing/PCC	N/A	N/A	N/A	N/A	N/A	N/A	N/A
	DF	AC/Reinforcing/AC	N/A	N/A	N/A	N/A	N/A	N/A	N/A
		AC/AC	-4.50E-01	-1.44E-01	8.61E-02	4.15E-01	1.25E-01	0.944937	0.74096
DNF	AC/AC	3.52E-01	-1.89E-02	8.46E-02	7.11E-02	1.13E-02	0.864728	0.47192	

Table 4.2. Continued.

			α_0	α_1	α_2	α_3	α_4	$R^2_{w/o\ outlier}$	$R^2_{w/ outlier}$
ρ_H	WF	AC/AC	9.32E+09	4.66E+09	4.66E+09	1.79E+02	5.07E+02	0.452578	0.45258
		JRC/JPC	-7.63E+09	-7.63E+09	-5.75E+03	5.11E+01	-5.37E+00	0.599614	0.59961
		FC/AC	-5.84E+05	-1.60E+05	-1.63E+05	-6.79E+04	-9.50E+04	0.5	0.5
		CRC/AC	N/A	N/A	N/A	N/A	N/A	N/A	N/A
		AC/Reinforcing/PCC	N/A	N/A	N/A	N/A	N/A	N/A	N/A
	WNF	AC/AC	N/A	N/A	N/A	N/A	N/A	N/A	N/A
		FC/AC	N/A	N/A	N/A	N/A	N/A	N/A	N/A
		AC/Reinforcing/PCC	N/A	N/A	N/A	N/A	N/A	N/A	N/A
	DF	AC/Reinforcing/AC	N/A	N/A	N/A	N/A	N/A	N/A	N/A
		AC/AC	2.18E+03	4.91E+02	2.55E+03	1.11E+02	2.00E+01	0.476257	0.40535
	DNF	AC/AC	7.23E+02	-1.51E+00	2.13E+02	3.68E+01	7.22E+02	1	1
				β_0	β_1	β_2	β_3	β_4	$R^2_{w/o\ outlier}$
β_H	WF	AC/AC	1.67E+00	1.08E-01	1.52E-01	6.66E-02	1.17E-01	0.549172	0.54917
		JRC/JPC	1.11E+09	1.11E+09	7.00E+00	6.99E-05	1.06E-02	0.809196	0.66975
		FC/AC	-8.62E+02	-3.01E+02	-4.22E+02	-1.10E+02	-1.30E+02	0.5	0.5
		CRC/AC	N/A	N/A	N/A	N/A	N/A	N/A	N/A
		AC/Reinforcing/PCC	N/A	N/A	N/A	N/A	N/A	N/A	N/A
	WNF	AC/AC	N/A	N/A	N/A	N/A	N/A	N/A	N/A
		FC/AC	N/A	N/A	N/A	N/A	N/A	N/A	N/A
		AC/Reinforcing/PCC	N/A	N/A	N/A	N/A	N/A	N/A	N/A
	DF	AC/Reinforcing/AC	N/A	N/A	N/A	N/A	N/A	N/A	N/A
		AC/AC	3.12E+01	7.19E+00	3.75E+01	7.57E-01	1.47E-01	0.960595	0.96059
	DNF	AC/AC	-5.32E-01	-4.91E-01	-3.99E-02	7.35E-01	-2.01E-01	1	1

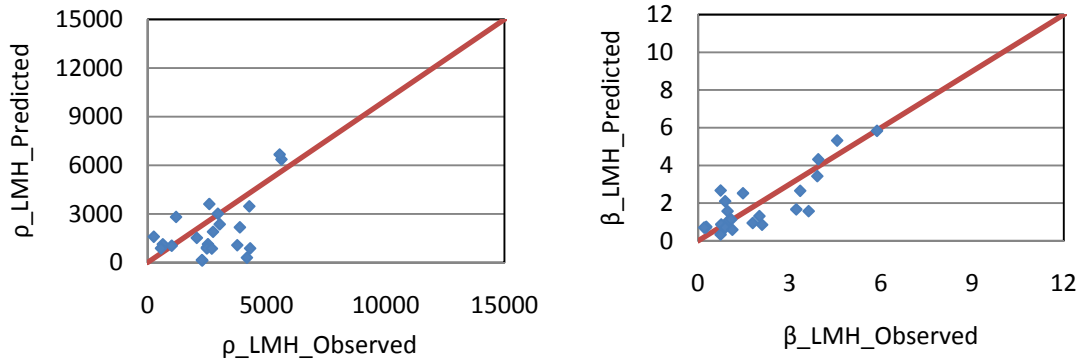


Figure 4.3. LMH Regression results of ρ and β for AC over AC pavement and Wet-Freeze climatic zone.

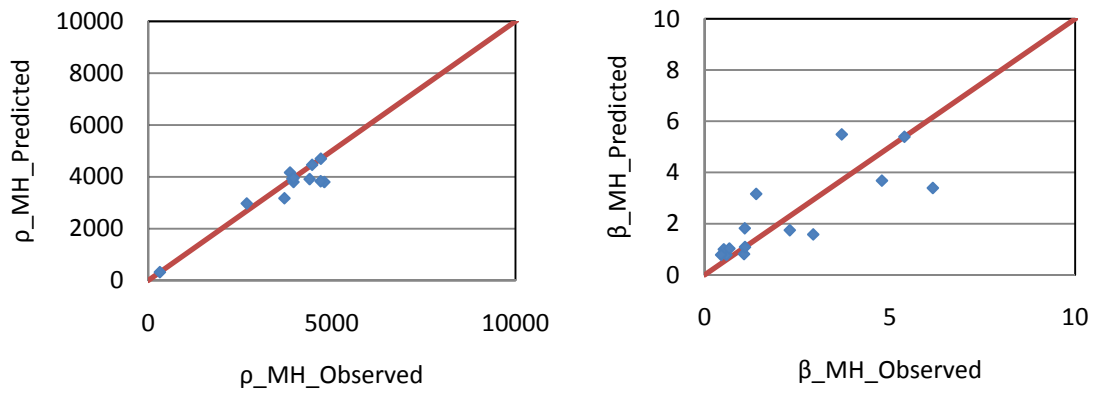


Figure 4.4. MH Regression results of ρ and β for AC over AC pavement and Wet-Freeze climatic zone.

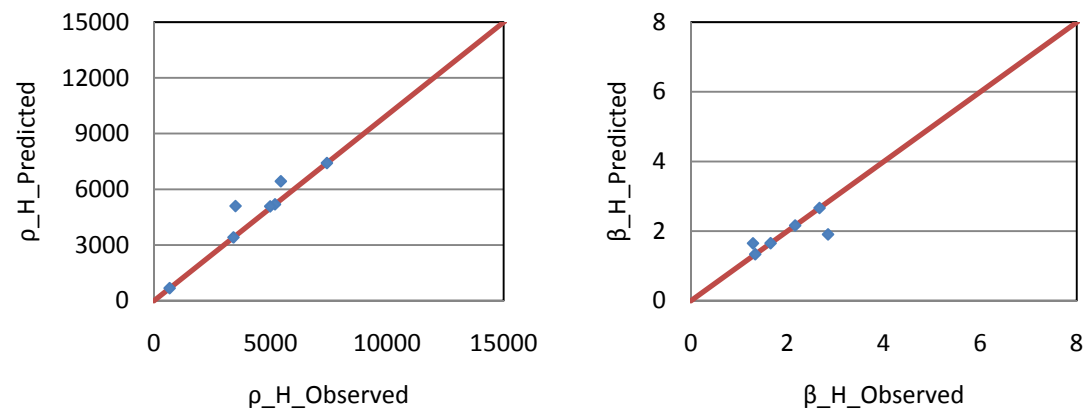


Figure 4.5. H Regression results of ρ and β for AC over AC pavement and Wet-Freeze climatic zone.

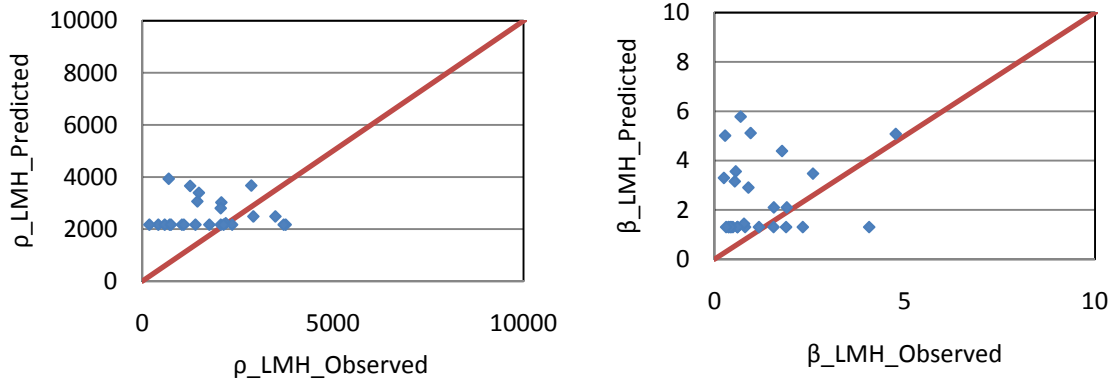


Figure 4.6. LMH Regression results of ρ and β for AC over JPC/JRC pavement and Wet-Freeze climatic zone.

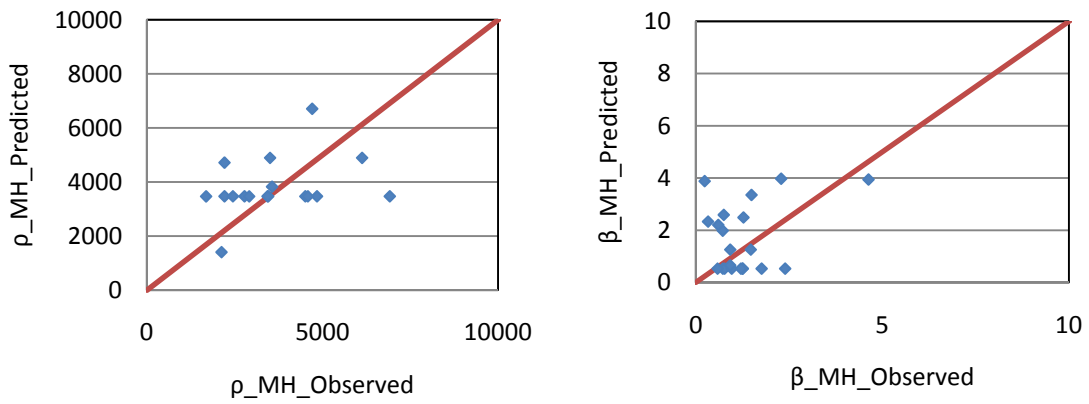


Figure 4.7. MH Regression results of ρ and β for AC over JPC/JRC pavement and Wet-Freeze climatic zone.

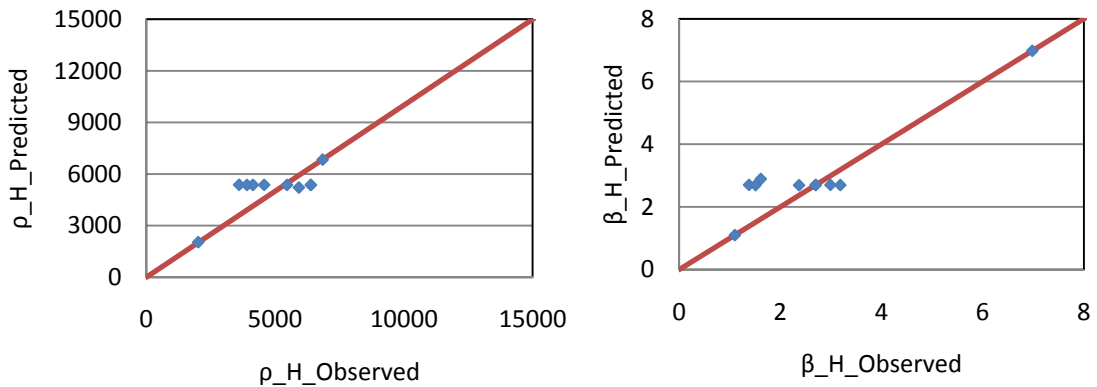


Figure 4.8. H Regression results of ρ and β for AC over JPC/JRC pavement and Wet-Freeze climatic zone.

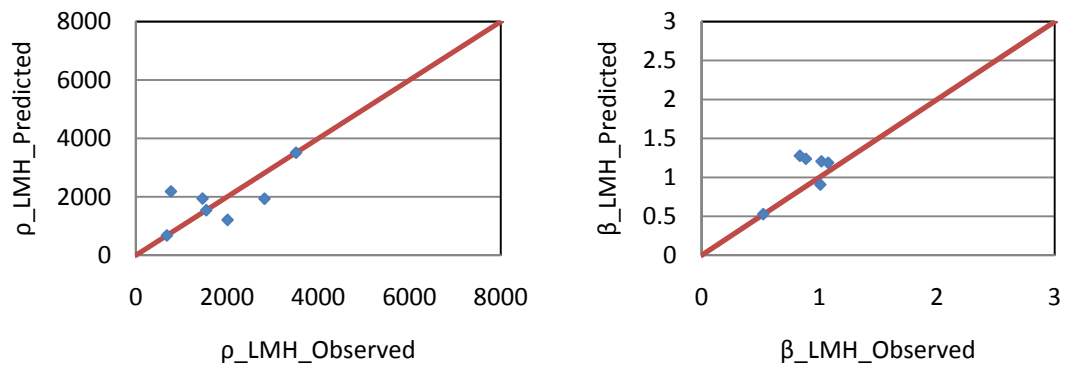


Figure 4.9. LMH Regression results of ρ and β for AC over FC/SC pavement and Wet-Freeze climatic zone.

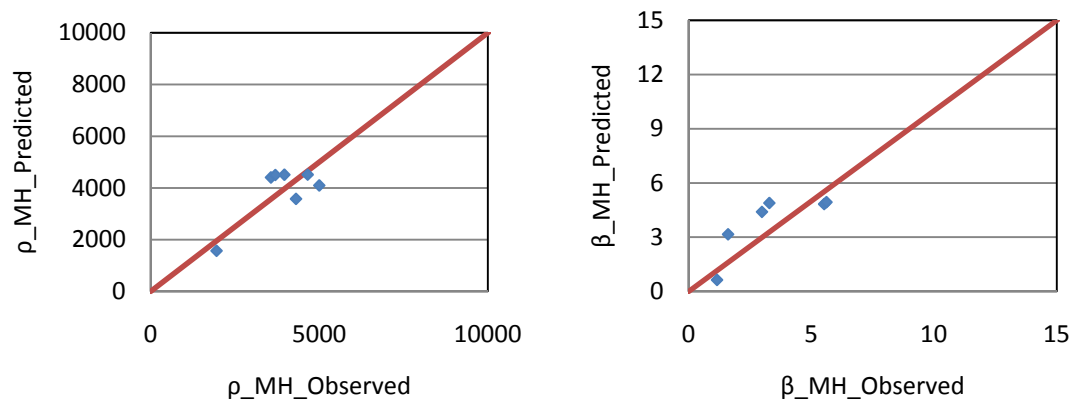


Figure 4.10. MH Regression results of ρ and β for AC over FC/SC pavement and Wet-Freeze climatic zone.

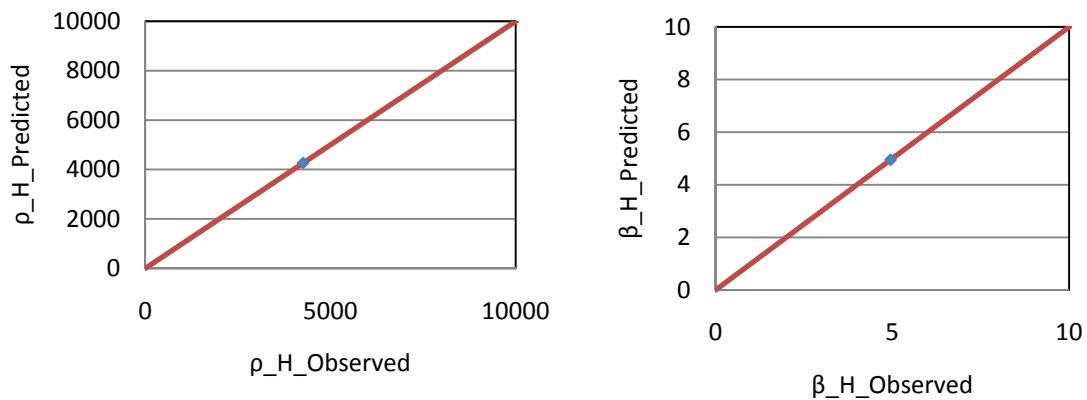


Figure 4.11. H Regression results of ρ and β for AC over FC/SC pavement and Wet-Freeze climatic zone.

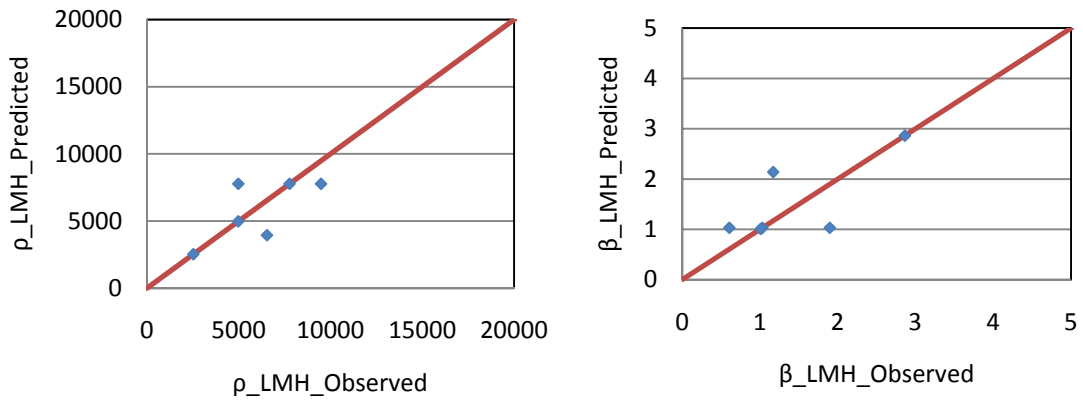


Figure 4.12. LMH Regression results of ρ and β for AC over CRC pavement and Wet-Freeze climatic zone.

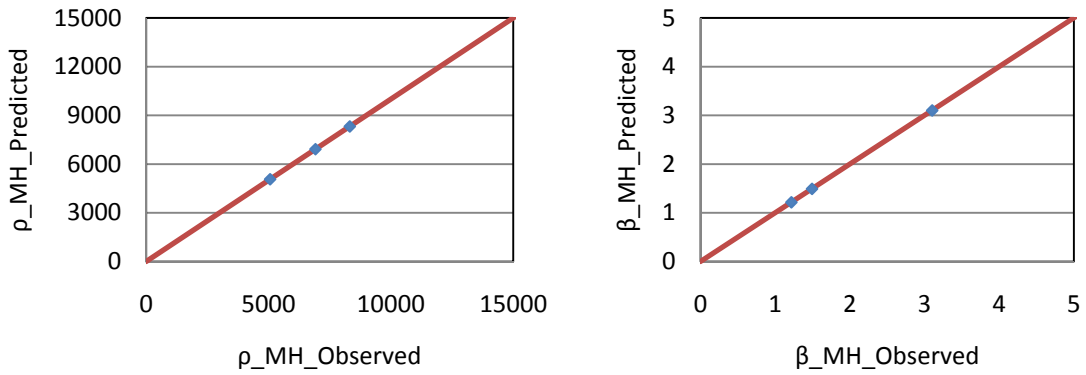


Figure 4.13. MH Regression results of ρ and β for AC over CRC pavement and Wet-Freeze climatic zone.

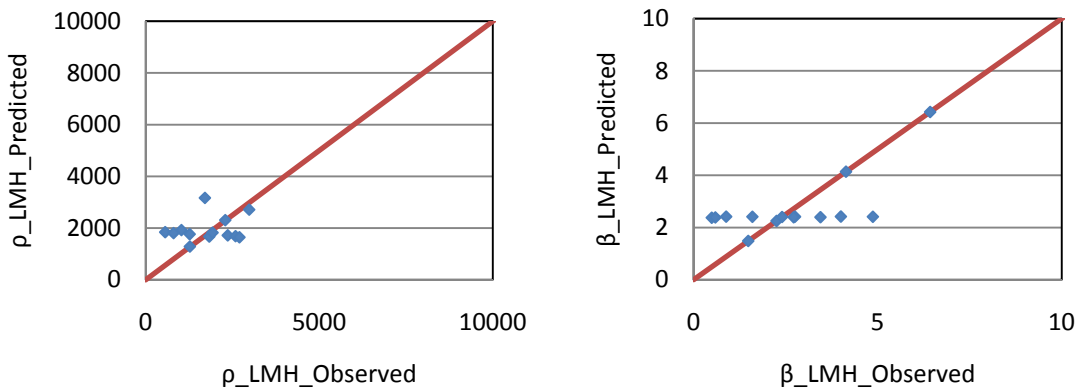


Figure 4.14. LMH Regression results of ρ and β for AC over AC pavement and Wet-No Freeze climatic zone.

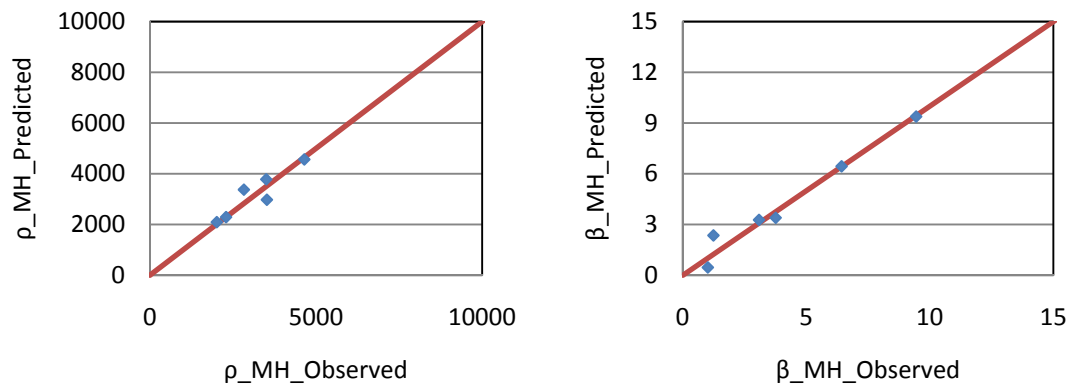


Figure 4.15. MH Regression results of ρ and β for AC over AC pavement and Wet-No Freeze climatic zone.

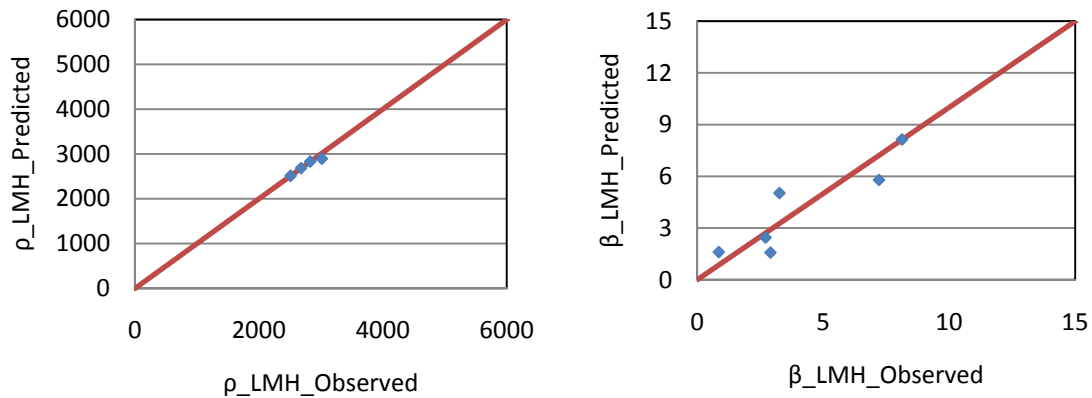


Figure 4.16. LMH Regression results of ρ and β for AC over FC/SC pavement and Wet-No Freeze climatic zone.

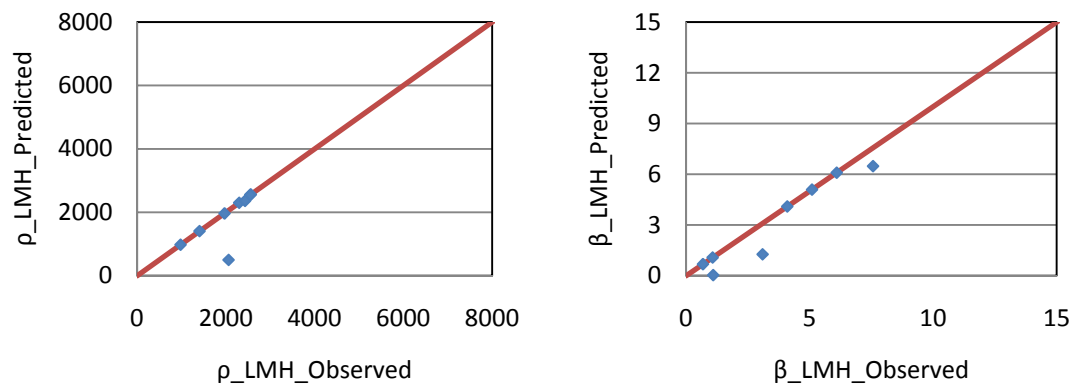


Figure 4.17. LMH Regression results of ρ and β for AC over AC pavement and Dry-Freeze climatic zone.

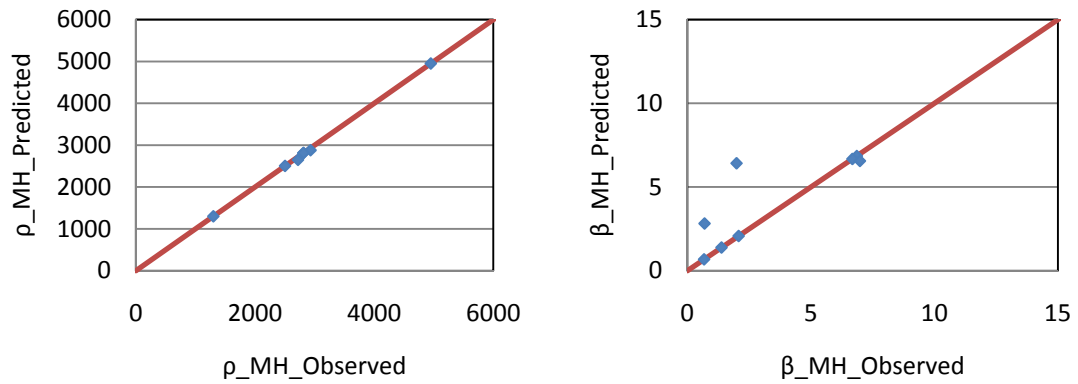


Figure 4.18. MH Regression results of ρ and β for AC over AC pavement and Dry-Freeze climatic zone.

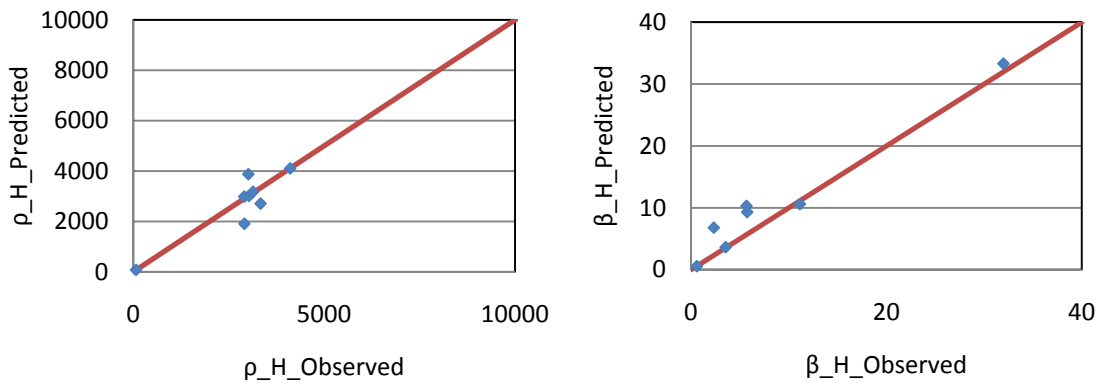


Figure 4.19. H Regression results of ρ and β for AC over AC pavement and Dry-Freeze climatic zone.

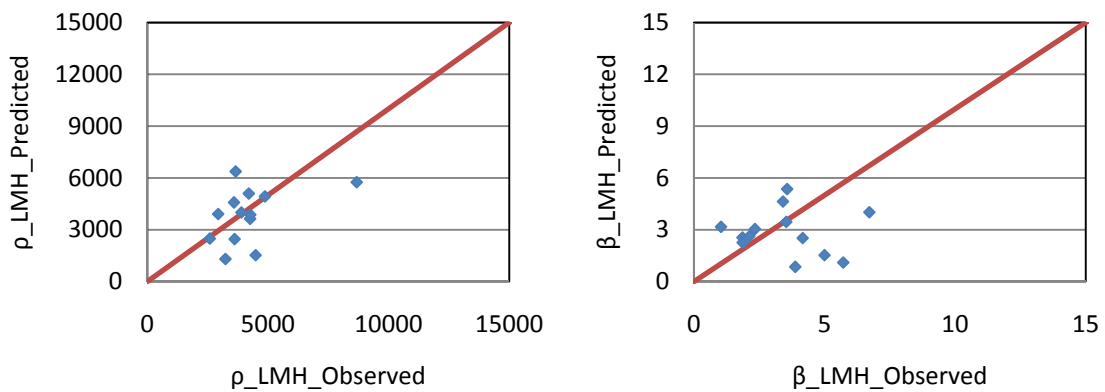


Figure 4.20. LMH Regression results of ρ and β for AC over AC pavement and Dry-No Freeze climatic zone.

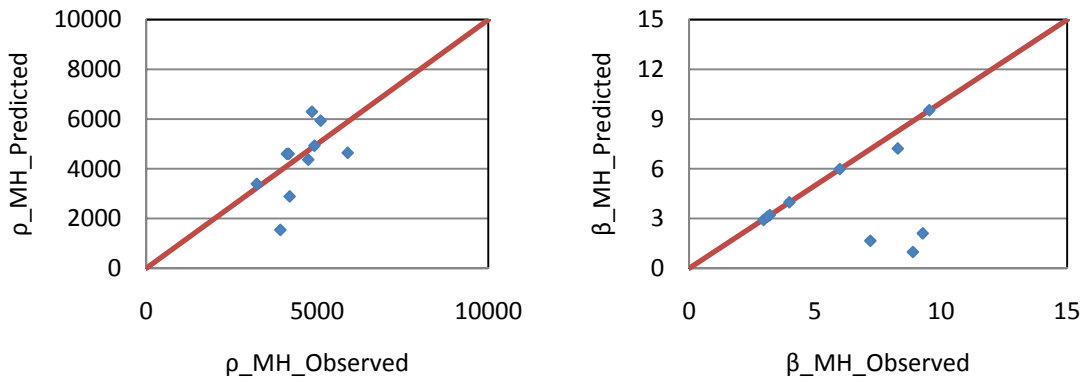


Figure 4.21. MH Regression results of ρ and β for AC over AC pavement and Dry-No Freeze climatic zone.

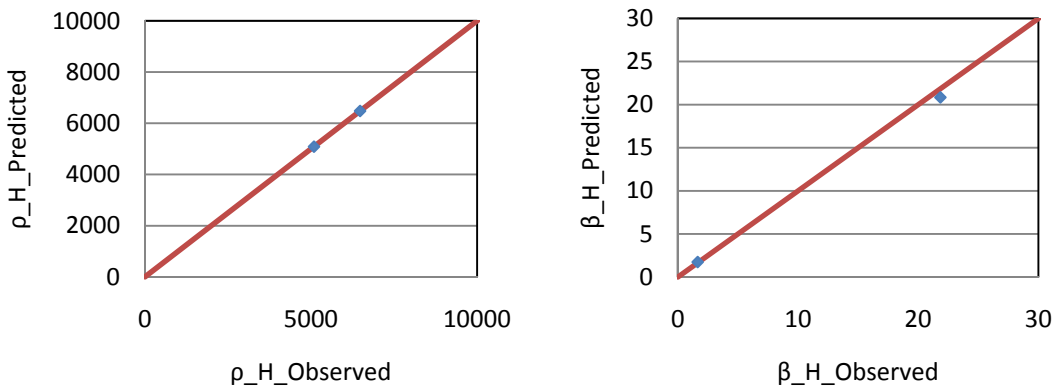


Figure 4.22. H Regression results of ρ and β for AC over AC pavement and Dry-No Freeze climatic zone.

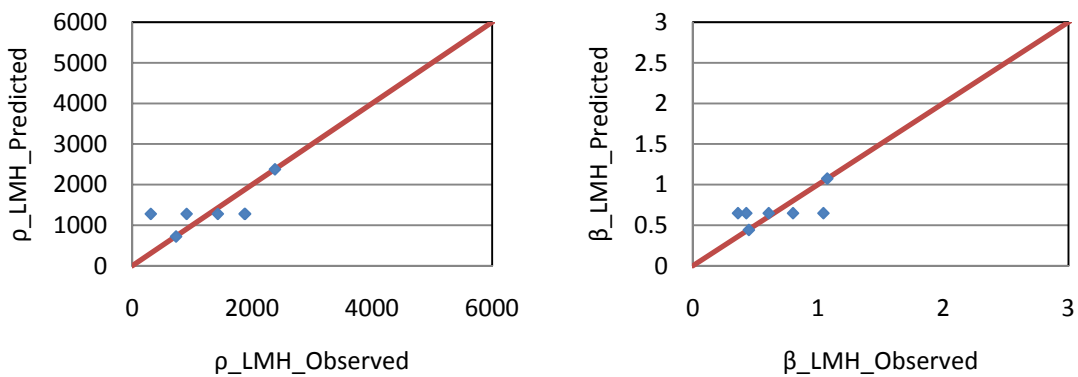


Figure 4.23. LMH Regression results of ρ and β for AC with reinforcing over PCC pavement and Wet-No Freeze climatic zone.

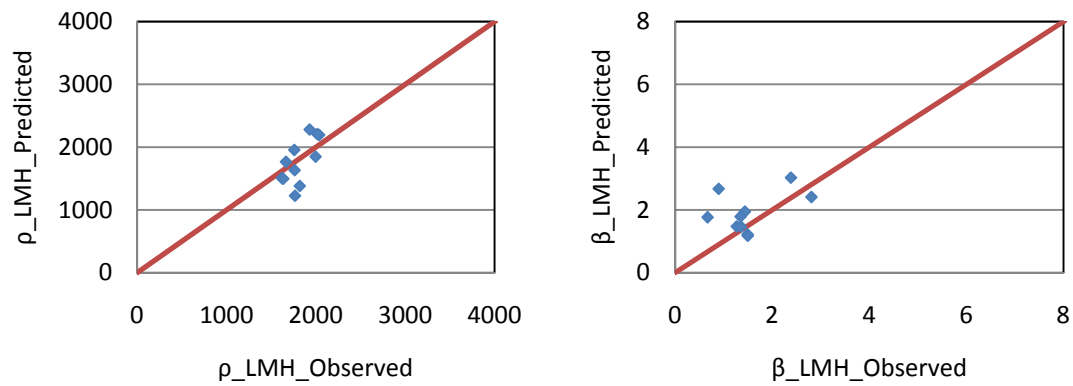


Figure 4.24. LMH Regression results of ρ and β for AC with reinforcing over AC pavement and Dry-Freeze climatic zone.

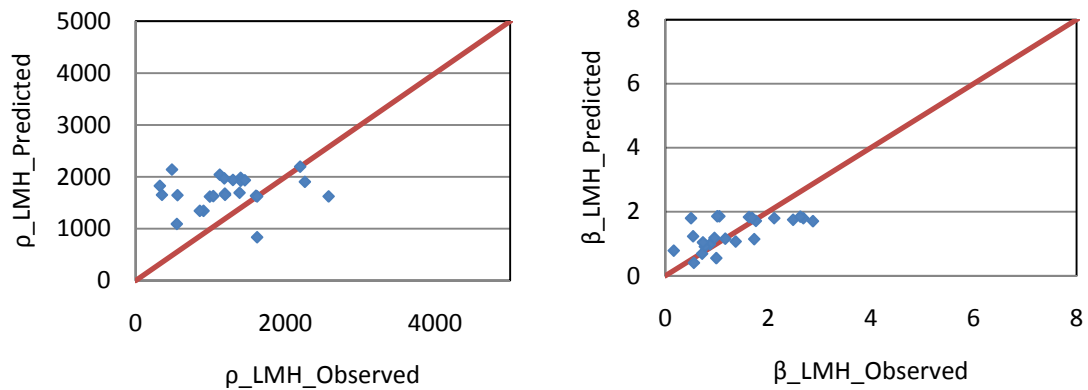


Figure 4.25. LMH Regression results of ρ and β for AC with Reinforcing over PCC pavement and Wet-Freeze climatic zone.

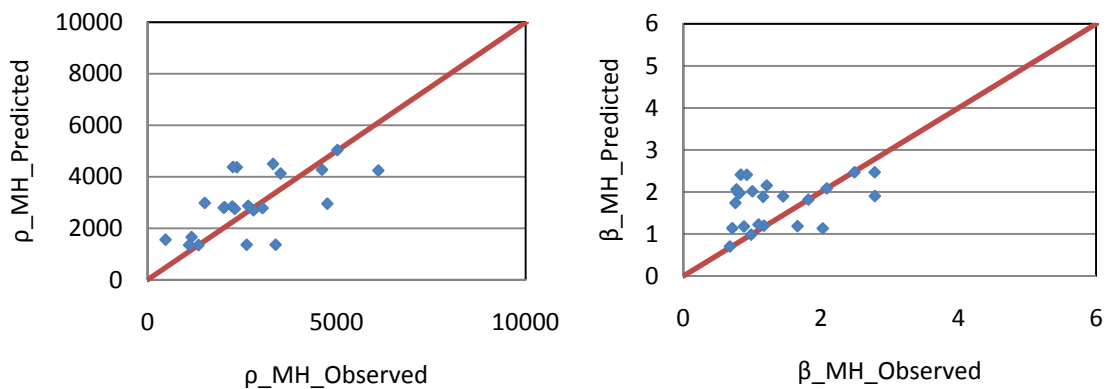


Figure 4.26. MH Regression results of ρ and β for AC with Reinforcing over PCC pavement and Wet-Freeze climatic zone.

CHAPTER V

REFLECTION CRACKING PREDICTION AND SENSITIVITY ANALYSIS

5.1 Introduction

Once the final sets of calibration coefficients (Chapter IV) were obtained, a further quality control step was taken by graphically plotting the distress patterns for all of the test sections to make certain that the predicted patterns of distress accumulation were both reasonable and realistic. The next step was building a Design Program to predict reflection cracking. In the Design Program, the sets of calibration coefficients that developed in Chapter IV were adopted. Inputting the calibration coefficients manually would be another option in this Design Program.

In the Design Program, logical tests were programmed into the Design Program to make certain that the predicted distress patterns will be correctly ordered from Low to Medium to High levels of distress. In this chapter, the predictions of reflection cracking in three severity levels were shown for eleven models. All the predicting results were compared with field measured data. In additions, sensitivity analyses for scale parameter (ρ) were also shown in this chapter.

5.2 Predictions of Overlay Reflection Cracking

Eleven sets of calibration coefficients were developed, one set for each combination of pavement structure and climatic zone for which sufficient data were available. Each set of model calibration coefficients have a maximum of three pairs of ρ and β values corresponding to the three levels of distress severity. In some cases, there were no observed high or medium severity distress levels. Thus data were available for 24 out of a total of 33 possible sets of model calibration coefficients. Figures 5.1 through 5.11 present 11 sample sets of calculated distress curves, one for each of the pavement structure and climatic zone combinations. Table 5.1 lists each of these figures.

Figure 5.1 shows the predicted distress for an HMA Overlay over a cracked asphalt pavement surface in a Wet-Freeze climatic zone (Lincoln, Maine) for the progressive development of transverse reflection cracking at the LMH (low+medium+high), MH (medium+high), and H (high) levels of severity. The High Level of Severity begins to appear at around 100 days of service life.

Figure 5.2 shows the predicted development of transverse reflection cracking extent and severity for an HMA Overlay over a Jointed Reinforced Concrete pavement in a Wet-Freeze climatic zone (Beaver, Pennsylvania). The high level of severity remains low for a long time before beginning its sharp rise. The difference between the rates of distress development shown in Figures 5.1 and 5.2 is due mainly to the difference in thermal stresses. Figure 5.3 shows the predicted development of transverse reflection cracking extent and severity of an HMA Overlay over an open graded friction course which was used as a strain relieving interlayer over a cracked asphalt pavement

surface in a Wet-Freeze climatic zone (Frederick, Maryland). Figure 5.4 shows the predicted development of transverse reflection cracking extent and severity of an HMA Overlay over a continuously reinforced concrete pavement surface in a Wet-Freeze climatic zone (Minnesota, Washington). Figure 5.4 indicates no observed high severity reflection cracks.

Table 5.1. Figures showing calculated reflection cracking distress curves.

Figure Number	Overlaid Pavement Type	Climatic Zone	Distress Severity Levels
5.1	Asphalt	WF	L, M, H
5.2	Jointed Reinforced Concrete	WF	L, M, H
5.3	Friction Course over Asphalt	WF	L, M, H
5.4	Continuously Reinforced Concrete	WF	L, M
5.5	Reinforcing Geosynthetic over Jointed Concrete	W-NF	L
5.6	Reinforcing Geosynthetic Over Asphalt	DF	L
5.7	Asphalt	W-NF	L, M
5.8	Friction Course Over Asphalt	W-NF	L
5.9	Asphalt	DF	L, M, H
5.10	Asphalt	D-NF	L, M, H
5.11	Reinforcing Geosynthetic Over Jointed Concrete	WF	L, M

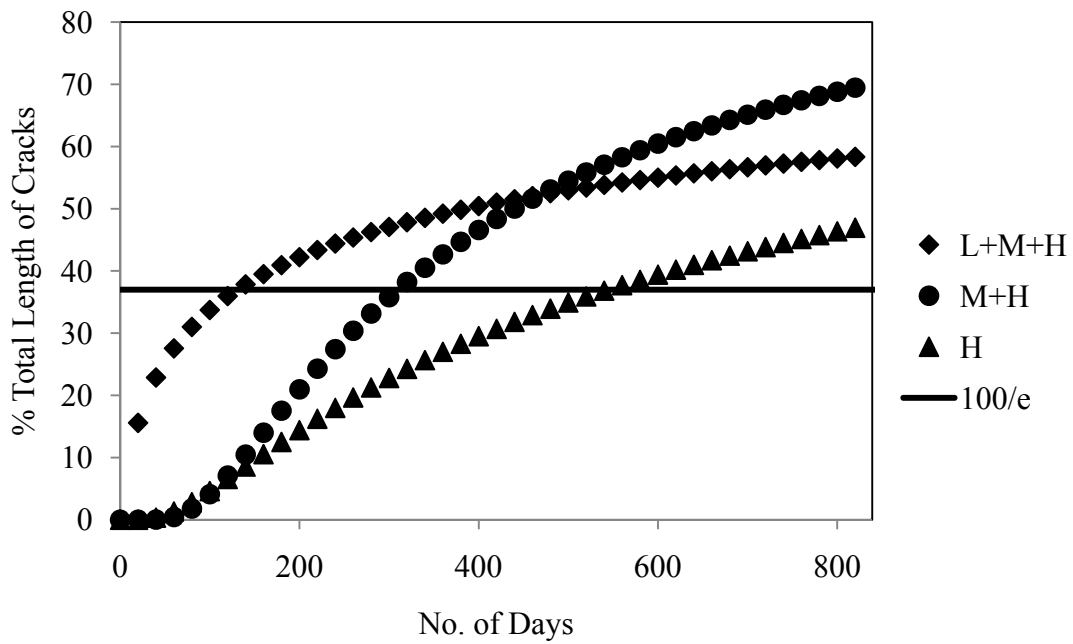


Figure 5.1. Development of transverse reflection cracking distress extent and severity for HMA overlay over asphalt surface in Wet-Freeze climatic zone (Lincoln, Maine).

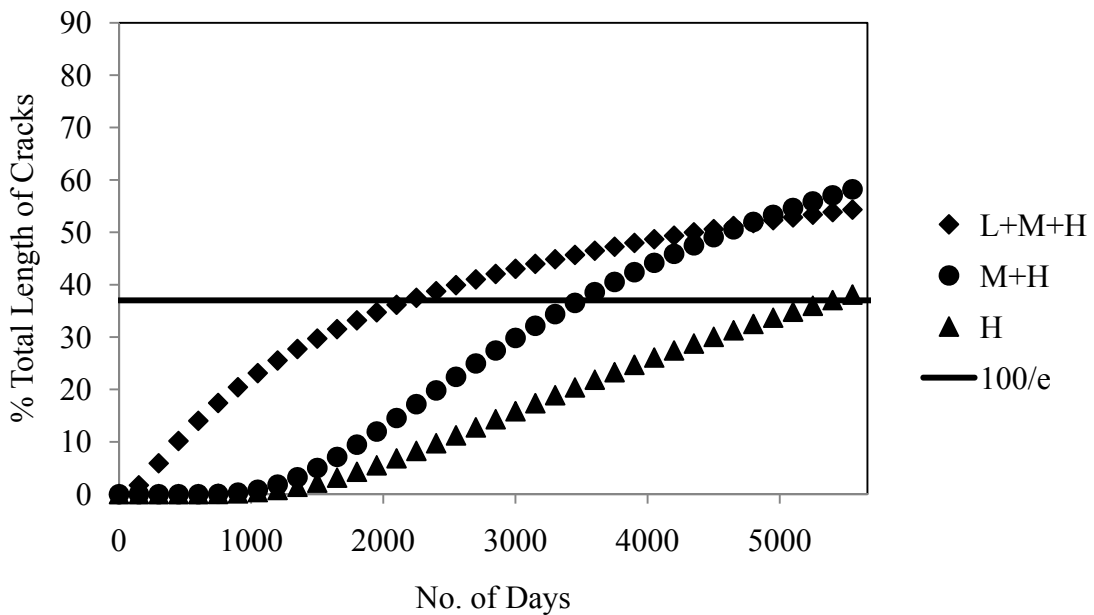


Figure 5.2. Development of transverse reflection cracking distress extent and severity for HMA overlay over jointed reinforced concrete in Wet-Freeze climatic zone (Beaver, Pennsylvania).

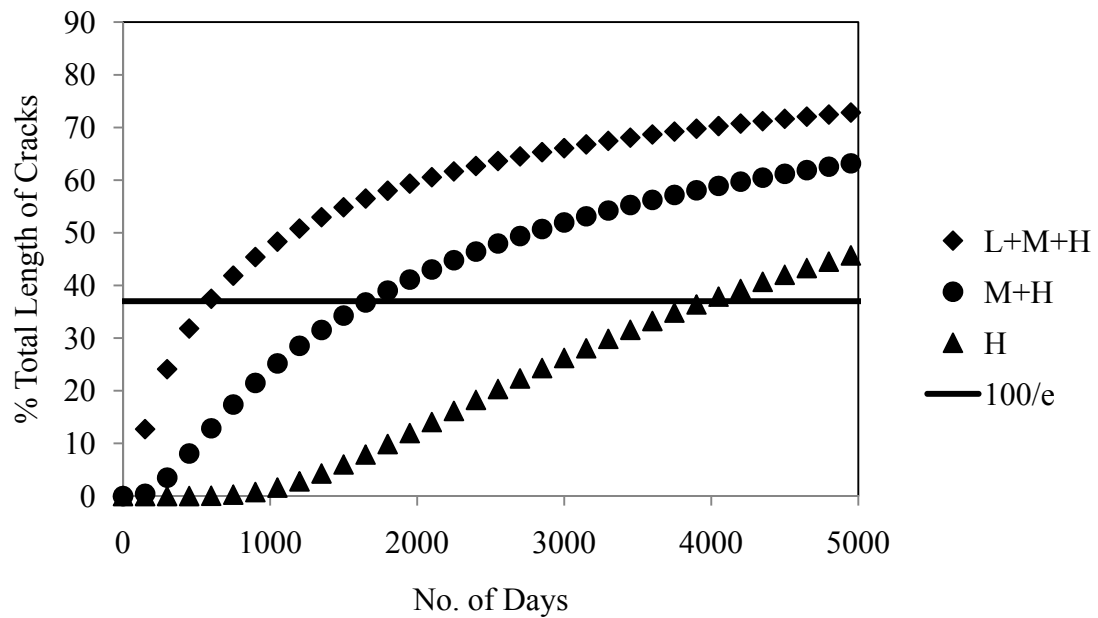


Figure 5.3. Development of transverse reflection cracking distress extent and severity for HMA overlay over friction course over asphalt surface in Wet-Freeze zone (Frederick, Maryland).

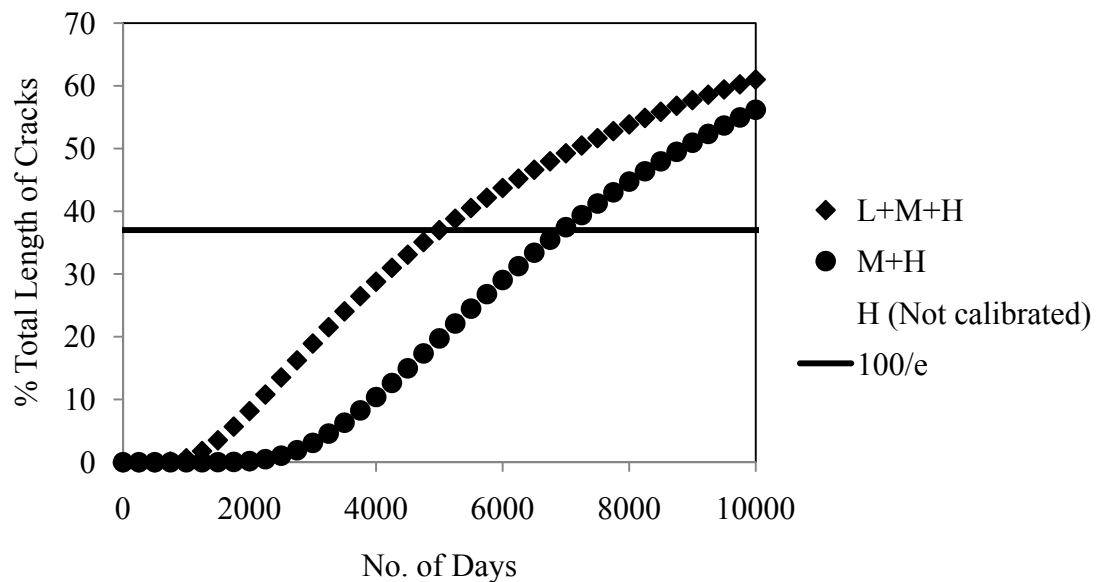


Figure 5.4. Development of transverse reflection cracking distress extent and severity for HMA overlay over continuously reinforced concrete pavement in Wet-Freeze zone (Minnesota, Washington).

Figure 5.5 shows the predicted development of transverse reflection cracking extent and severity of an HMA Overlay reinforced with a geosynthetic material and placed over a jointed concrete pavement in a Wet-No Freeze climatic zone (Waco, Texas). In this case, medium or high levels of severity were not observed during the monitoring period and only the low level of severity could be modeled. Figure 5.6 shows the predicted development of transverse reflection cracking extent and severity of an HMA Overlay reinforced with a geosynthetic material and placed on a cracked asphalt pavement surface in a Dry-Freeze climatic zone (Amarillo, Texas). No medium or high level severity distress was observed on any of the test sections during the monitoring period.

Figure 5.7 shows the predicted development of transverse reflection cracking extent and severity of an HMA Overlay over a cracked asphalt pavement surface in a Wet-No Freeze climatic zone (Pittsylvania, Virginia). The Low Severity distress appeared around 900 days and Medium Level Severity began to appear after around six years; no High Level Severity distress was observed.

Figure 5.8 shows the predicted development of transverse reflection cracking extent and severity of an HMA Overlay over an open graded friction course which was used as a strain relieving interlayer over a cracked asphalt pavement surface in a Wet-No Freeze climatic zone (Yazoo, Mississippi). Only the low level severity of distress was observed.

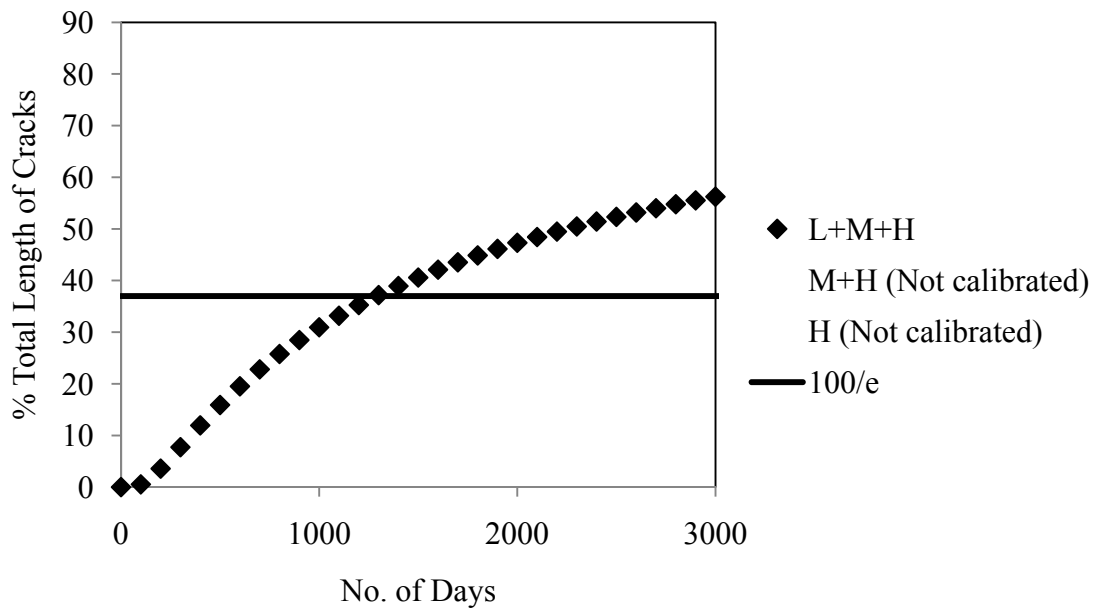


Figure 5.5. Development of transverse reflection cracking distress extent and severity for HMA overlay with reinforcing geosynthetic over jointed concrete in Wet-No Freeze zone (Waco, Texas).

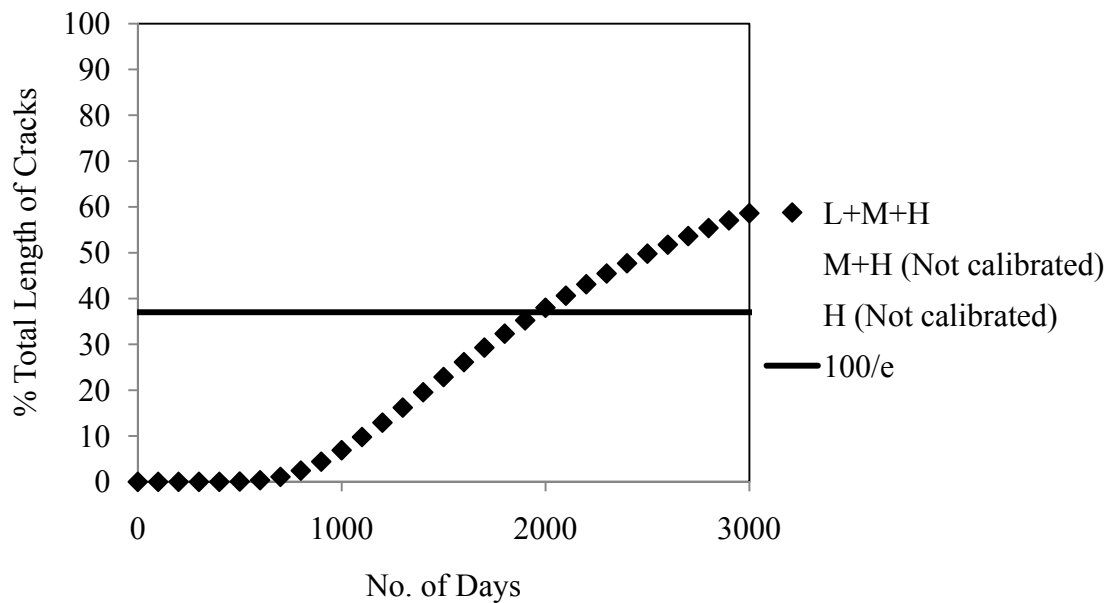


Figure 5.6. Development of transverse reflection cracking distress extent and severity for HMA overlay with reinforcing geosynthetic over asphalt surface in Dry-Freeze zone (Amarillo, Texas).

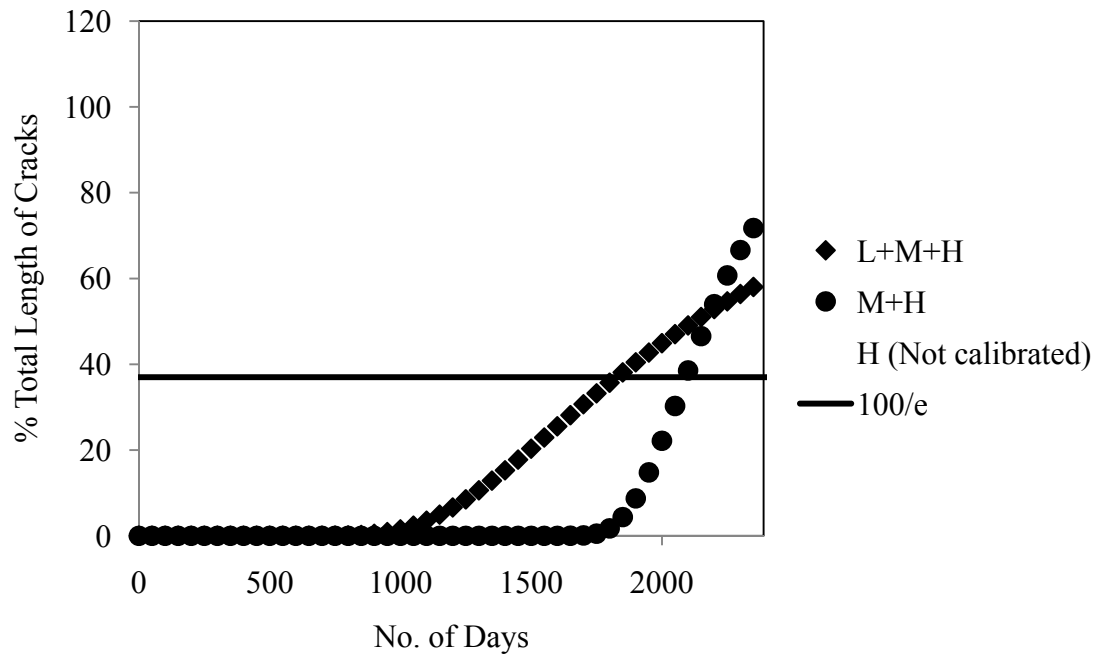


Figure 5.7. Development of transverse reflection cracking distress extent and severity for HMA overlay over asphalt surface in Wet-No Freeze zone (Pittsylvania, Virginia).

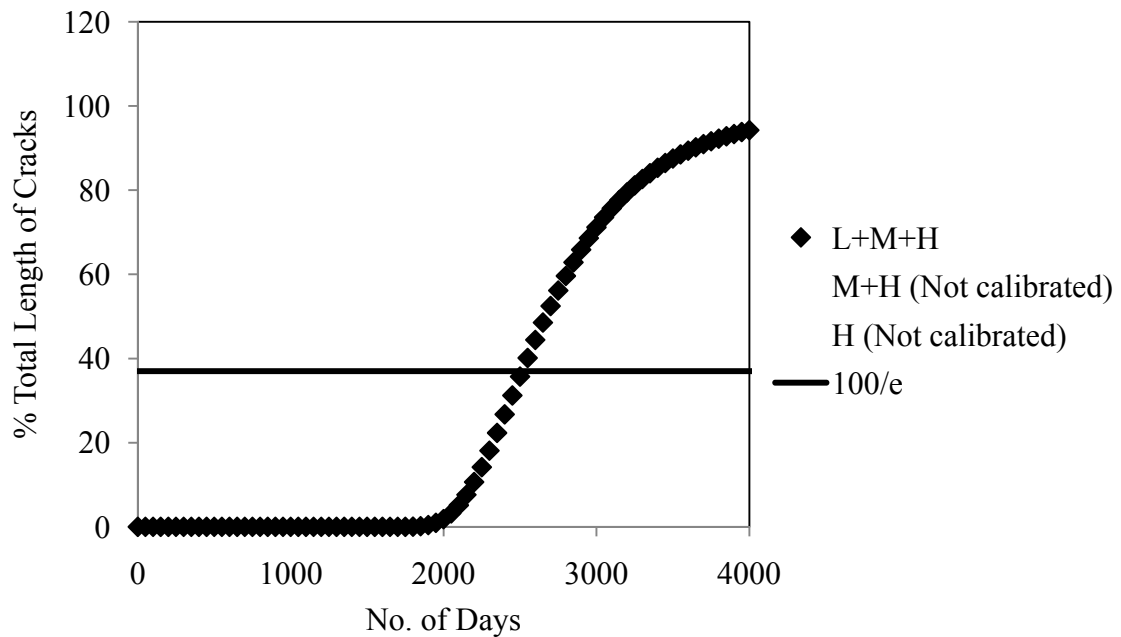


Figure 5.8. Development of transverse reflection cracking distress extent and severity for HMA overlay over friction course over asphalt surface in Wet-No Freeze zone (Yazoo, Mississippi).

Figure 5.9 shows the predicted development of transverse reflection cracking extent and severity of an HMA Overlay over a cracked asphalt pavement surface in a Dry- Freeze climatic zone (Deaf Smith County, Texas). The high, medium, and low levels of distress severity appeared within the first year.

Figure 5.10 shows the predicted development of transverse reflection cracking extent and severity of an HMA Overlay over a cracked asphalt pavement surface in a Dry-No Freeze climatic zone (Pinal, Arizona). In this overlay, the medium level severity of distress appeared around the six year and began its sharp rise.

Figure 5.11 shows the predicted development of transverse reflection cracking extent and severity of an HMA Overlay with geosynthetic reinforcing over a jointed concrete pavement surface in a Wet-Freeze climatic zone (New York, New York). No high level severity distress was observed.

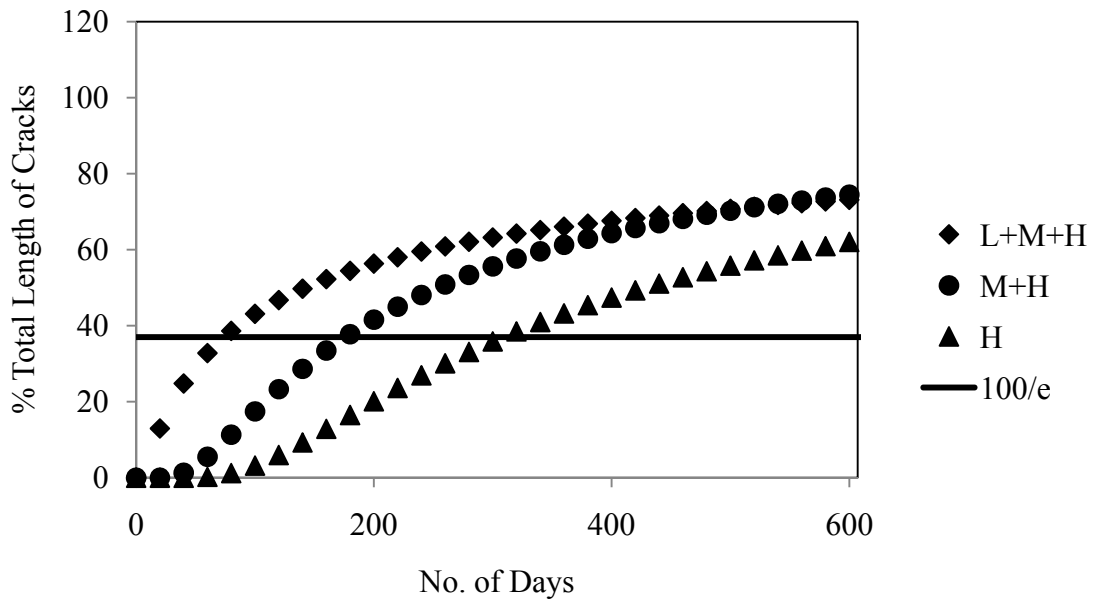


Figure 5.9. Development of transverse reflection cracking extent and severity for HMA overlay over asphalt pavement surface in Dry-Freeze zone (Deaf Smith County, Texas).

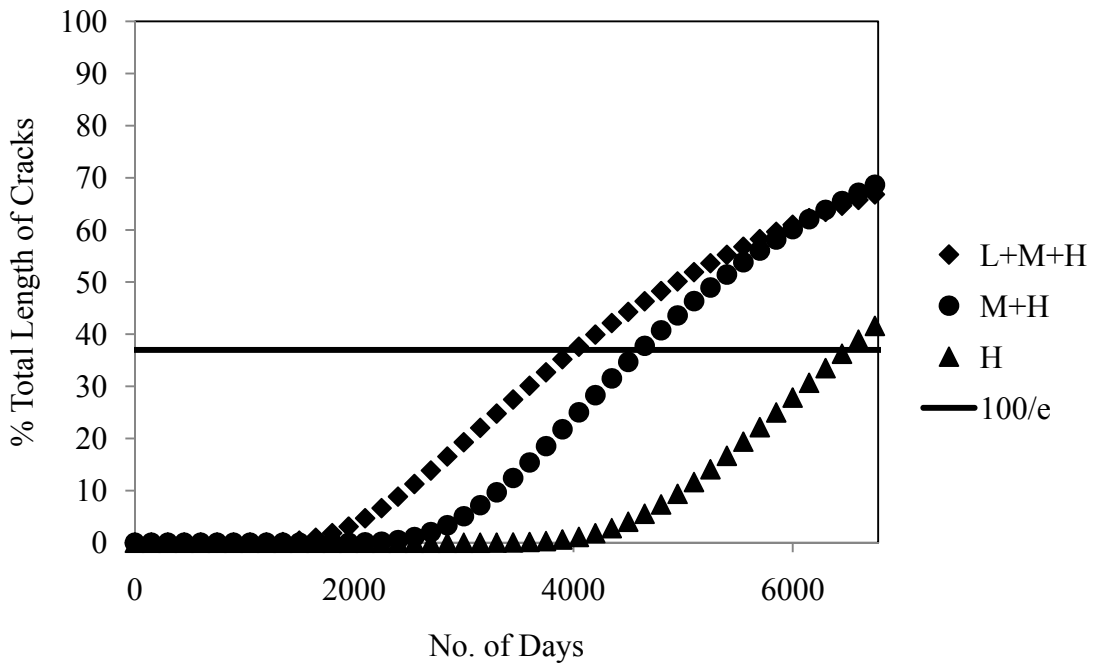


Figure 5.10. Development of transverse reflection cracking extent and severity for HMA overlay over asphalt pavement surface in Dry-No Freeze zone (Pinal, Arizona).

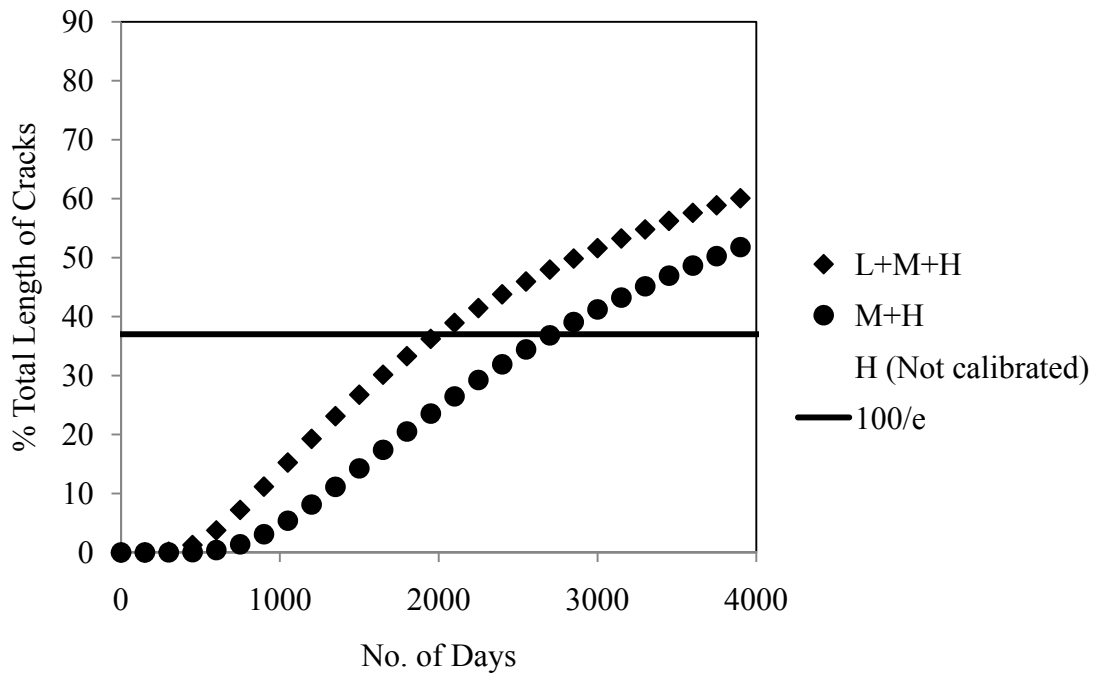


Figure 5.11. Development of transverse reflection cracking distress extent and severity for HMA overlay with reinforcing geosynthetic over jointed concrete pavement in Wet-Freeze zone (New York, New York).

Figures 5.1 through 5.11 illustrate the predictions for each of the sets of reflection cracking model calibration coefficients. Each of the four major climatic zones are represented but not all of the pavement structure-overlay types. Although eleven sets of calibration coefficients were developed, a total of forty combinations are possible (four climatic zones and ten pavement structure-overlay types). All of these additional sets of calibration coefficients can be entered into this Design Program and can be used in the design of hot mix asphalt overlays to represent each unique combination of climatic zone and pavement structure-overlay type.

5.3 Comparison of Predicted Overlay Life and Observed Data

This section shows comparison examples between the observed reflection crack extent and severity for all the different types of overlay-pavement structure-climatic zone combinations that were developed in this project from the field survey and the predicted result from the reflection cracking prediction program. The field information used to determine the crack growth condition was mainly collected from the LTPP (Long Term Pavement Performance) database (36).

The first set of cases illustrates different AC (Asphalt Concrete) overlays over different existing pavement structures in a Wet-Freeze climatic zone. An AC overlay over an existing AC pavement structure is illustrated in Figure 5.12. The result of comparing the observed and predicted LMH severity distress shows that the predicting program predicts the crack growth behavior for the early stage very well. After 7 years, it shows a slight difference between the field and the predicted result. Figures 5.13 and 5.14 show the LMH and MH severity distresses, respectively, for an AC overlay over an existing JCP (Jointed Concrete Pavement) structure in a Wet-Freeze climatic zone. For the field data in the LMH case, the crack growth appeared in the 3rd year and the rate of the crack growth was lower than the predicted results. However, the predicted results show that the crack growth increases slightly in the 3rd year, followed by a sharp increase in the rate of the crack growth after that. The MH case in Figure 5.14 shows good correlation between the field and predicted rates of crack growth.

The results of the LMH and MH severity distresses for an AC overlay over an either FC (Friction Course) or SC (Seal Coat) pavement structure in a Wet-Freeze

climatic zone are shown in Figures 5.15 and 5.16, respectively. Figure 5.15 illustrates how the prediction program simulates the early stage of crack growth; however, the predicted results have a higher rate of crack growth than the field data. Conversely, the results in the case of MH severity distress, Figure 5.16, show that the predicted results have a lower rate of crack growth than the field data; however, the predicted and observed rates of crack growth are close.

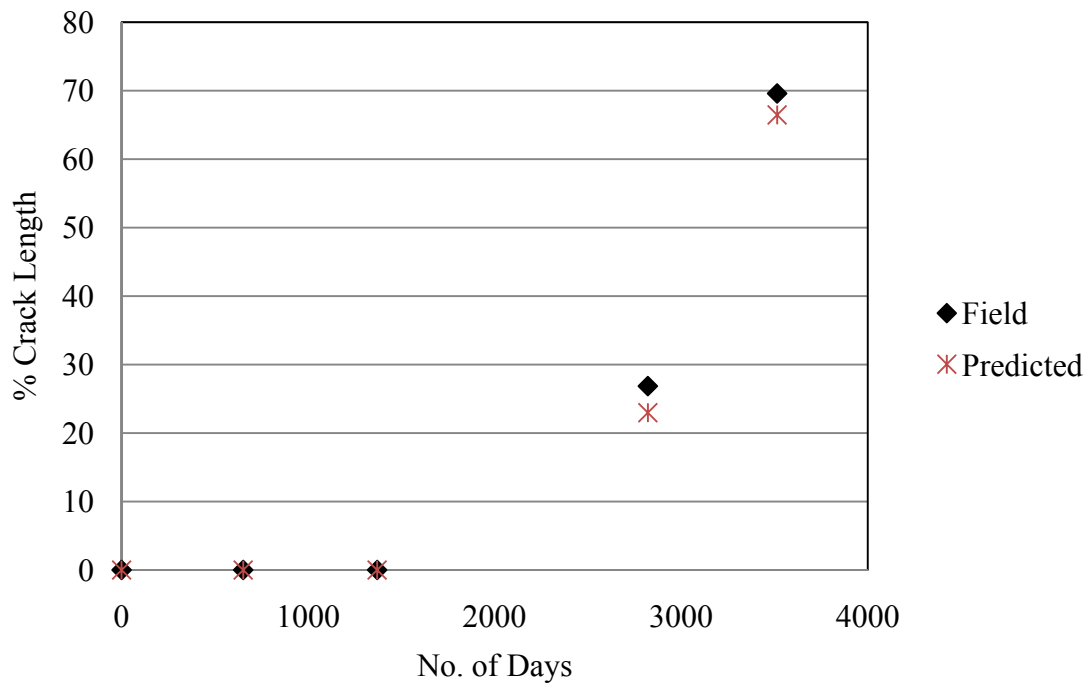


Figure 5.12. The comparison between field and predicted results for LMH severity distress (AC over AC pavement structure, Wet-Freeze climatic zone).

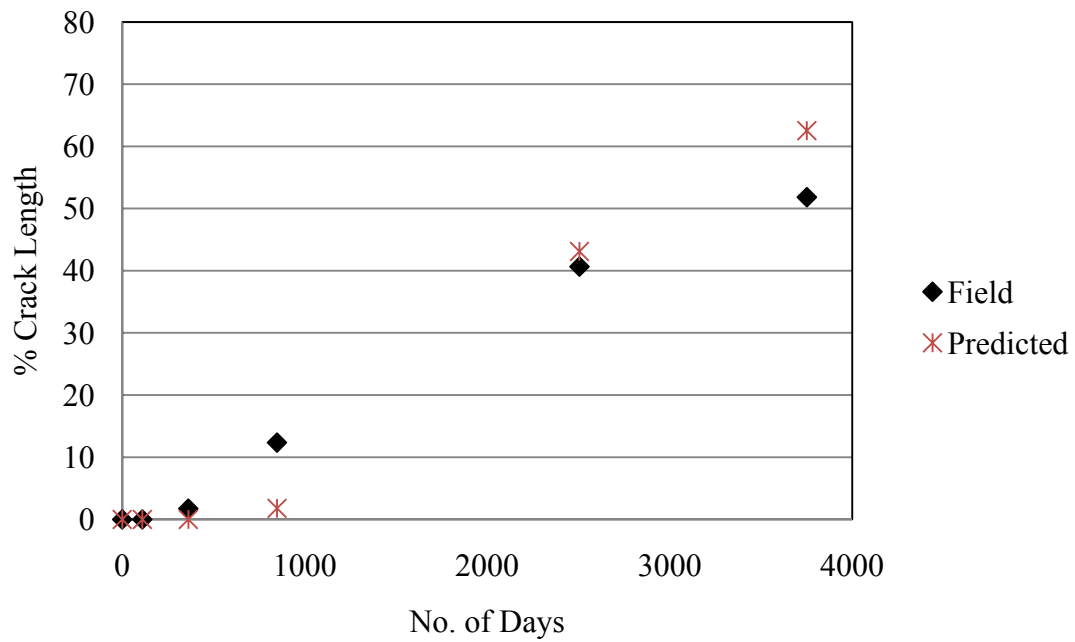


Figure 5.13. The comparison between field and predicted results for LMH severity distress (AC over JPC pavement structure, Wet-Freeze climatic zone).

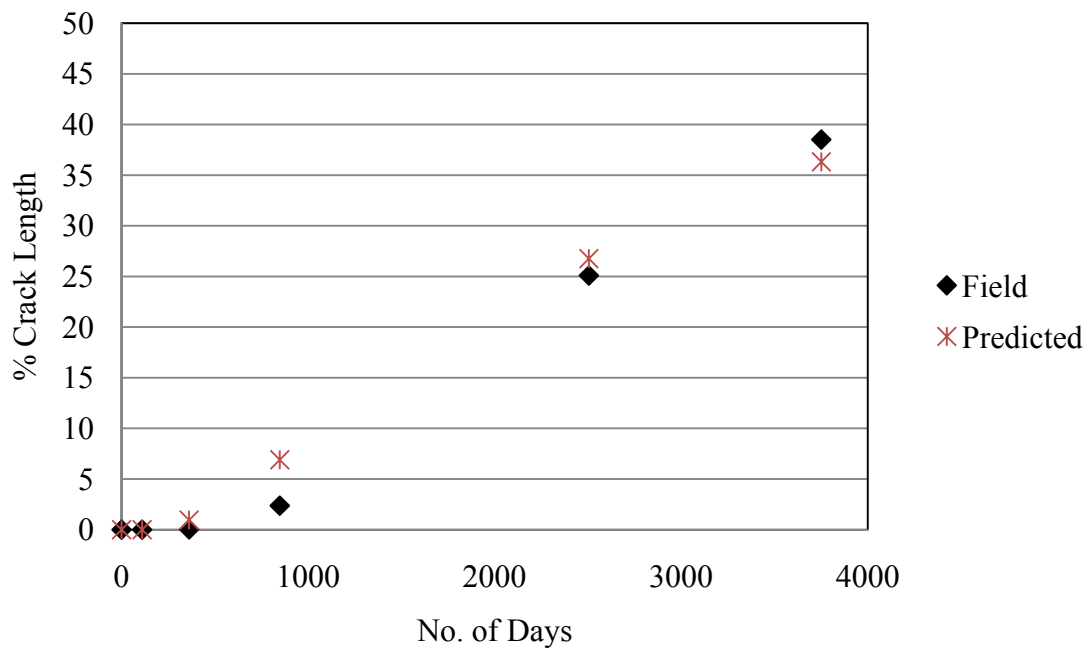


Figure 5.14. The comparison between field and predicted results for MH severity distress (AC over JPC pavement structure, Wet-Freeze climatic zone).

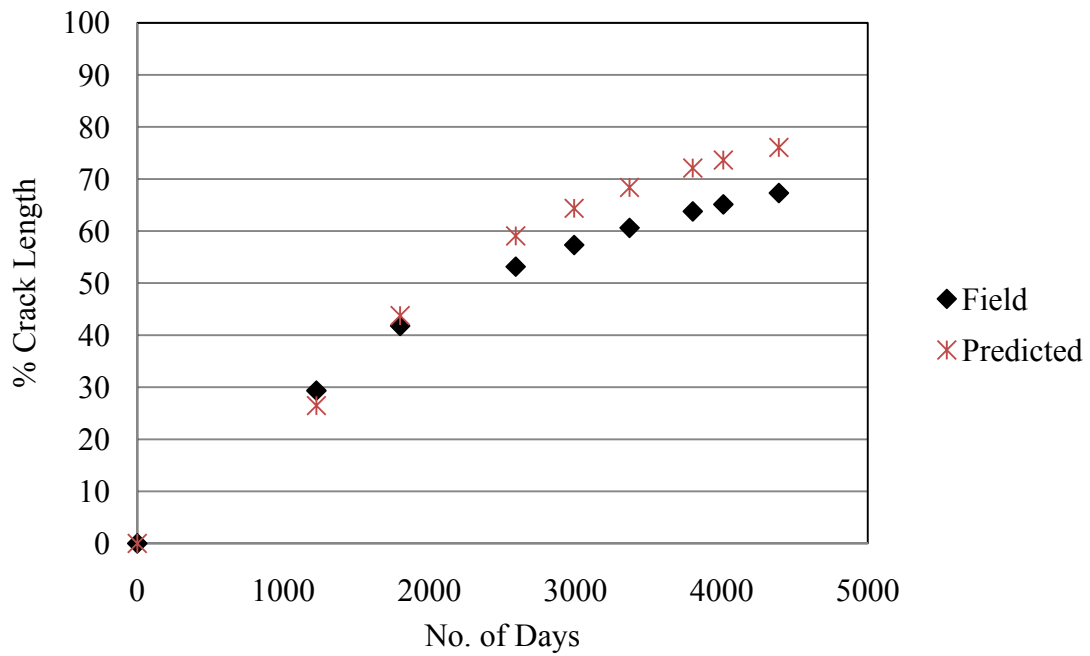


Figure 5.15. The comparison between field and predicted results for LMH severity distress (AC over FC pavement structure, Wet-Freeze climatic zone).

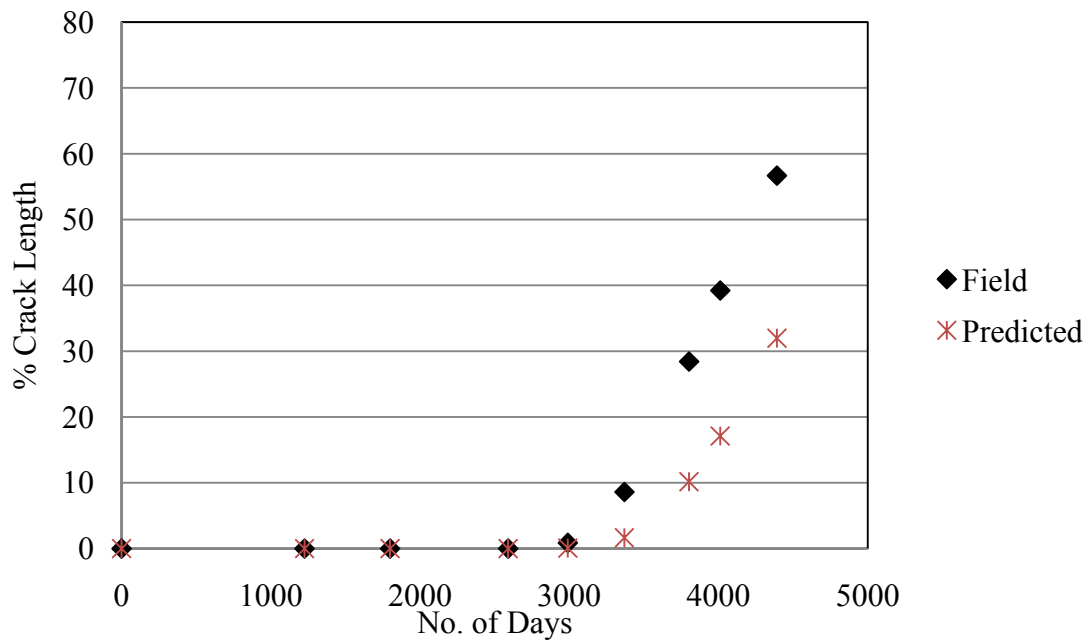


Figure 5.16. The comparison between field and predicted results for MH severity distress (AC over FC pavement structure, Wet-Freeze climatic zone).

Figures 5.17 and 5.18 show the comparison of LMH and MH severity levels, respectively, for an AC overlay over an existing CRCP (Continuously Reinforced Concrete Pavement) structure in a Wet-Freeze climatic zone. In this case, the predicted and field survey results for both the LMH and MH severity levels are very close. The next case is located in New York City and is an AC overlay over a reinforcing interlayer over a PCC pavement structure in a wet-freeze climatic zone. The results for the LMH and MH severity distresses are shown in Figures 5.19 and 5.20, respectively. The prediction program accurately simulated the field crack growth behavior for the LMH severity level as shown in Figure 5.19. For the MH severity level, in Figure 5.20, the prediction program predicts a higher rate of crack growth than those observed in the field.

The second set of cases illustrates different AC overlays over different existing pavement structures in a Wet-No Freeze climatic zone. The LMH and MH severity distresses for an AC overlay over an existing AC pavement structure in a Wet-No Freeze climatic zone are shown in Figures 5.21 and 5.22. The prediction program predicted LMH severity distress around 6 percent greater than the field survey data. The MH severity distress prediction shown in Figure 5.22 is close to the field survey data. The next two cases, displayed in Figures 5.23 and 5.24, are an AC overlay over an existing FC pavement structure and an AC overlay over a reinforcing interlayer over an existing PCC pavement structure in a Wet-No Freeze climatic zone. These two cases show good predictions compared with the field data.

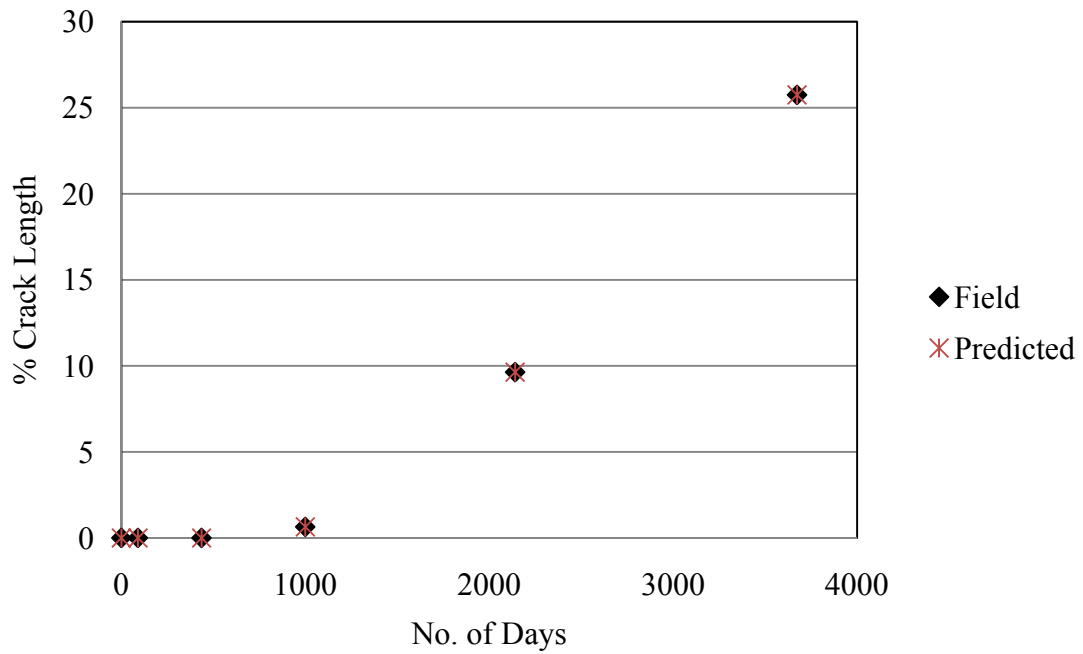


Figure 5.17. The comparison between field and predicted results for LMH severity distress (AC over CRC pavement structure, Wet-Freeze climatic zone).

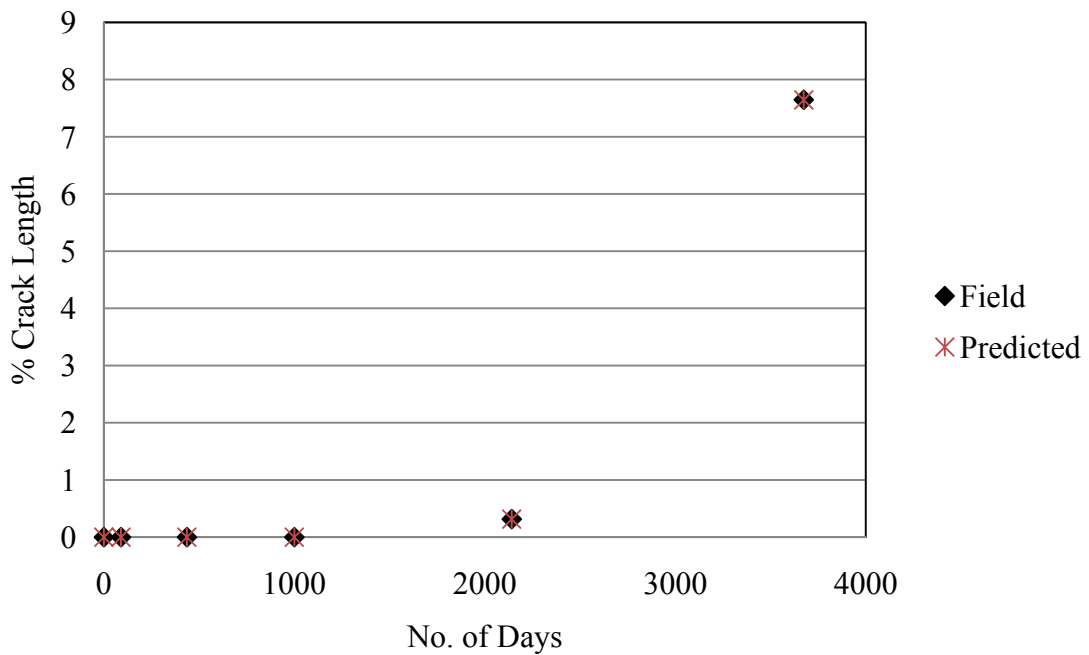


Figure 5.18. The comparison between field and predicted results for MH severity distress (AC over CRC pavement structure, Wet-Freeze climatic zone).

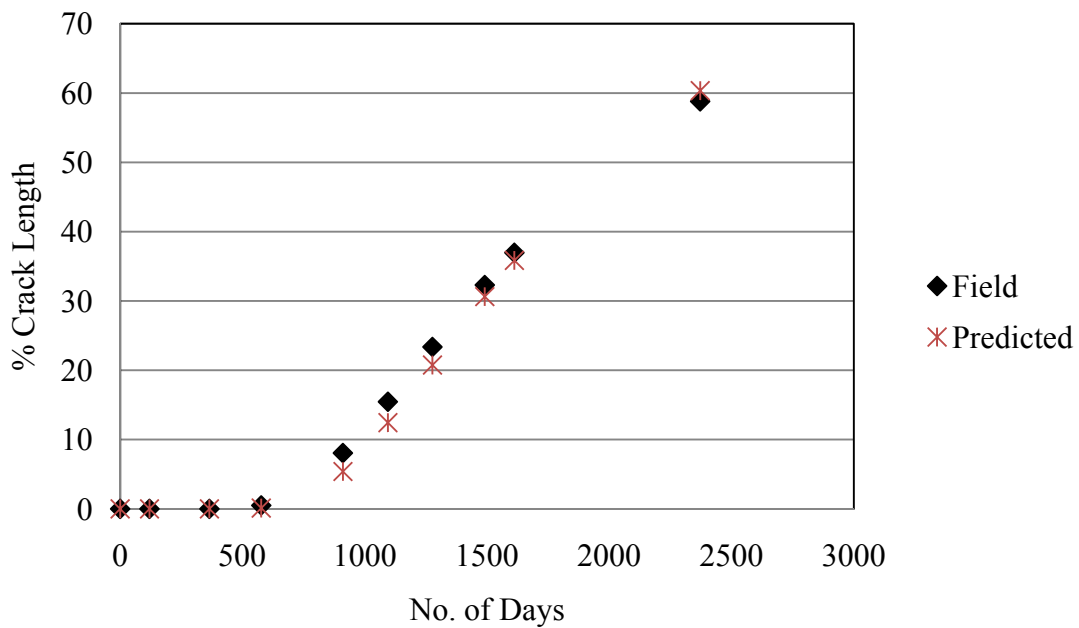


Figure 5.19. The comparison between field and predicted results for LMH severity distress (AC over reinforcing interlayer over PCC pavement structure, Wet-Freeze climatic zone).

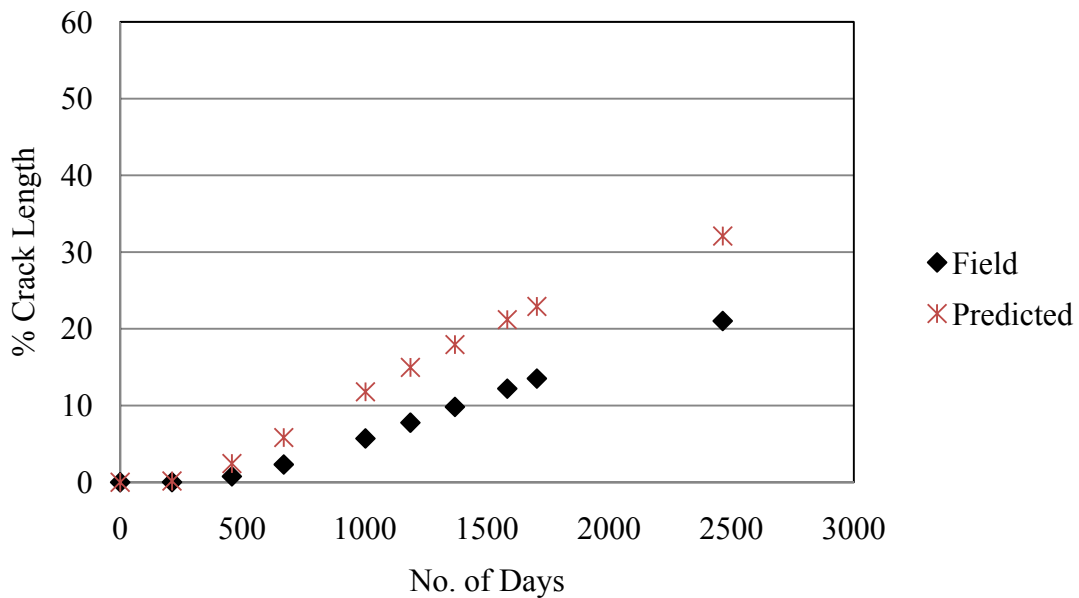


Figure 5.20. The comparison between field and predicted results for MH severity distress (AC over reinforcing interlayer over PCC pavement structure, Wet-Freeze climatic zone).

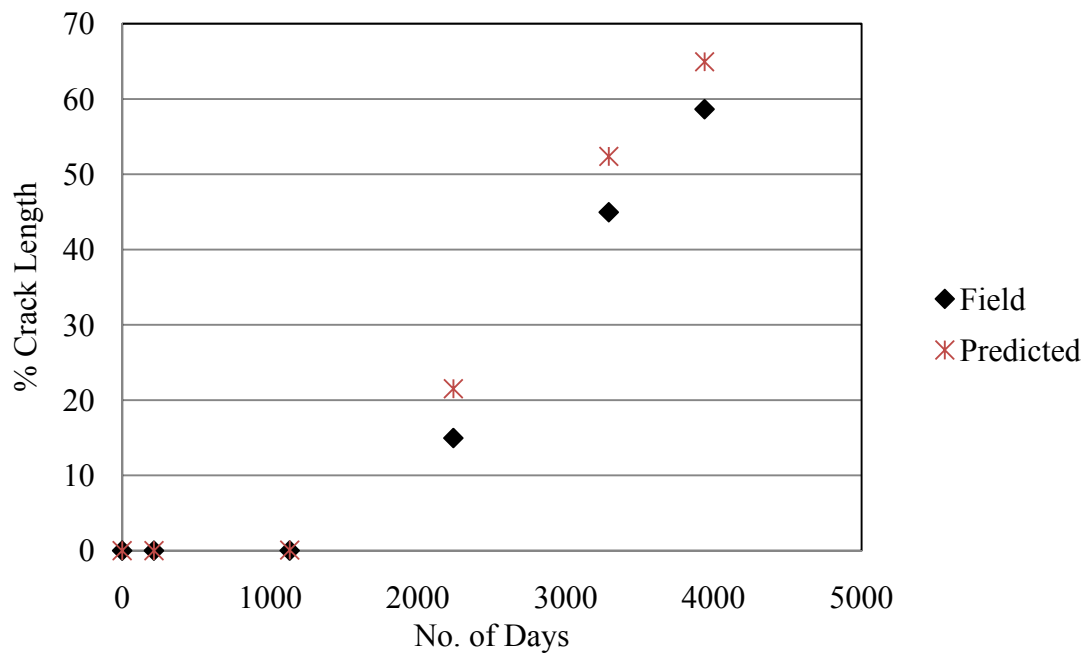


Figure 5.21. The comparison between field and predicted results for LMH severity distress (AC over AC pavement structure, Wet-No Freeze climatic zone).

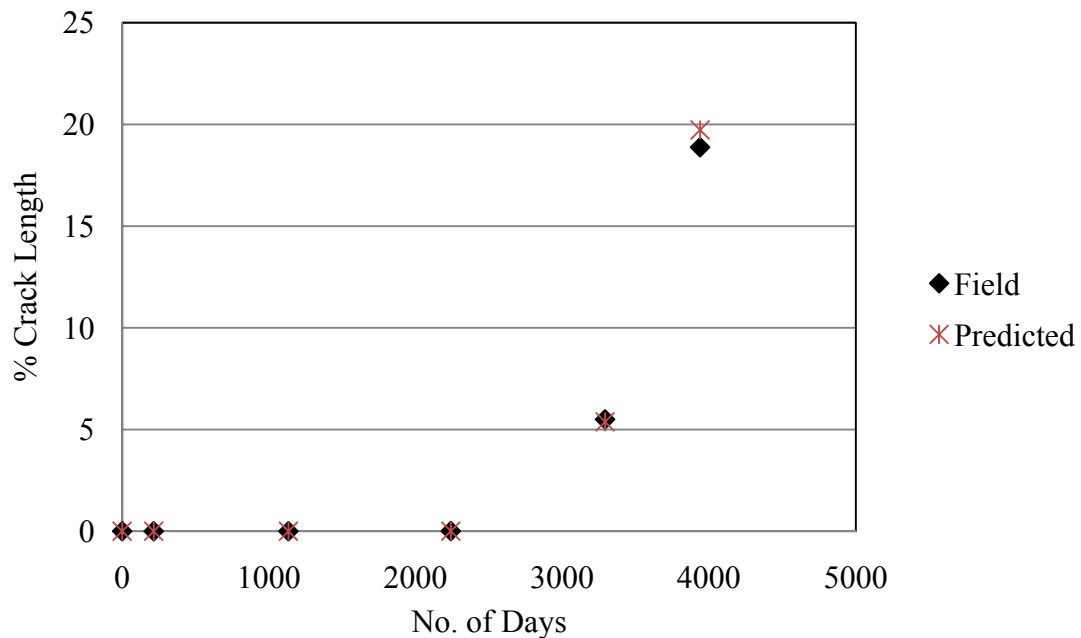


Figure 5.22. The comparison between field and predicted results for MH severity distress (AC over AC pavement structure, Wet-No Freeze climatic zone).

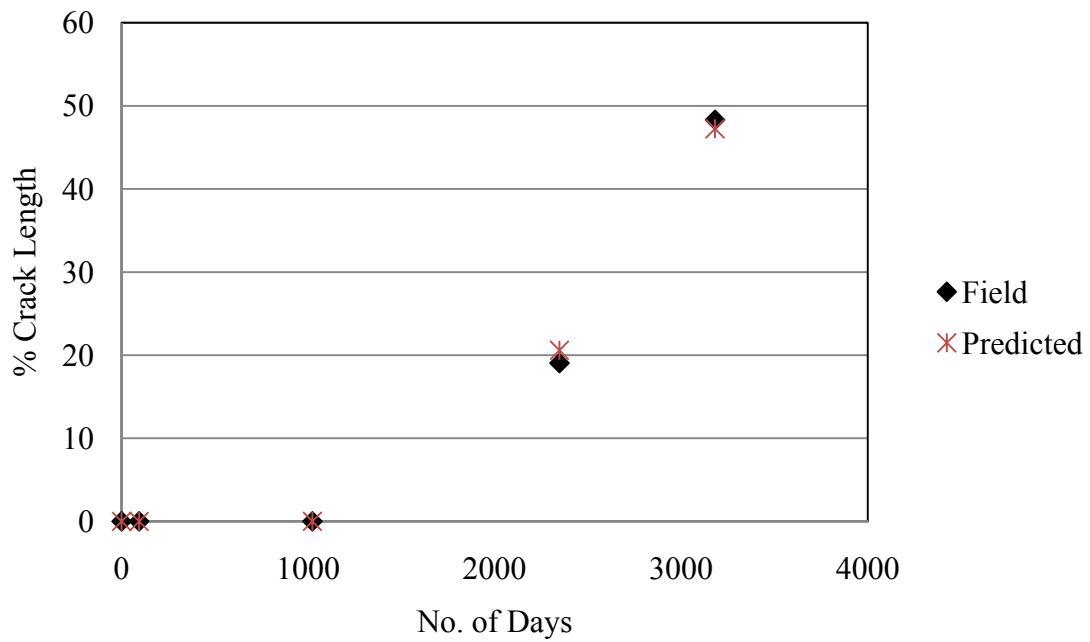


Figure 5.23. The comparison between field and predicted results for LMH severity distress(AC over FC pavement structure, Wet-No Freeze climatic zone).

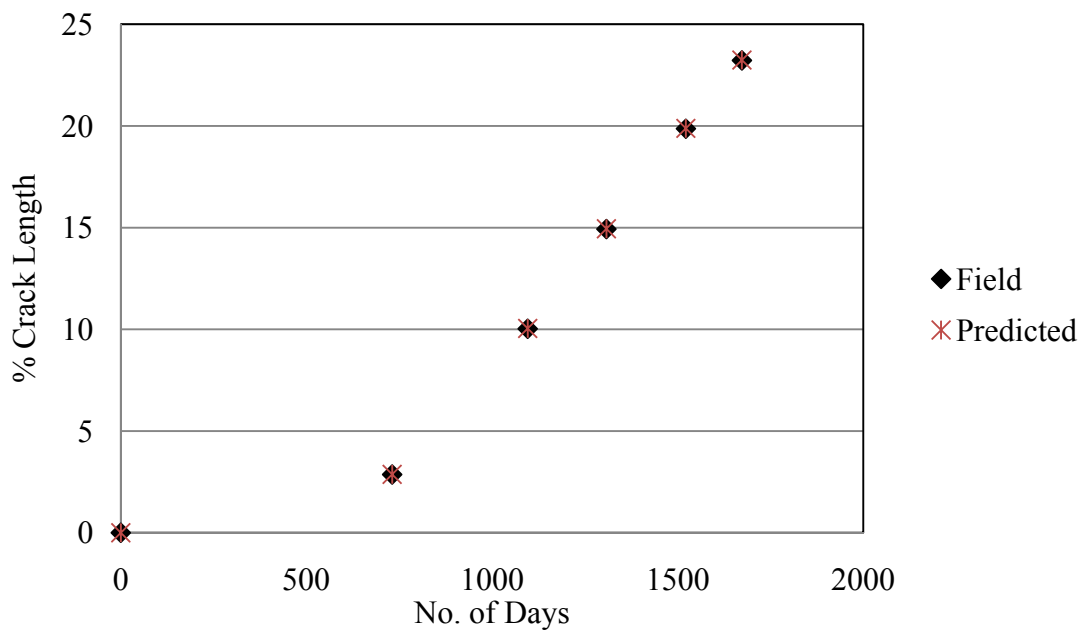


Figure 5.24. The comparison between field and predicted results for LMH severity distress(AC over reinforcing interlayer over PCC pavement structure, Wet-No Freeze climatic zone).

The third set of cases illustrates different AC overlays over different existing pavement structures in a Dry-Freeze climatic zone. Figures 5.25, 5.26, and 5.27 display the results of LMH, MH, and H severity distresses, respectively, for an AC overlay over an existing AC pavement structure in a Dry-Freeze climatic zone. There is good correlation between the predicted and observed field survey data in both the LMH and MH severity levels in Figure 5.25 and Figure 5.26. In the H severity distress prediction in Figure 5.27, the field survey recorded that there was no high severity cracking observed within the first seven years, and then a 33 percent crack length occurred in the eight year. The prediction program predicted no crack growth for the first seven years, but in the eight year, the percentage of crack growth was predicted to increase only to 6 percent. An AC overlay over a reinforcing interlayer over an existing AC pavement structure in a Dry-Freeze climatic zone is shown in Figure 5.28. The slope of the crack growth is the same for both the field and the predicted results; however, the percentage of the predicted crack length is smaller than the field data by around 3 percent.

The final set of cases illustrates different AC overlays over different existing pavement structures in a Dry-No Freeze climatic zone. Figures 5.29 and 5.30 show the LMH and MH severity distresses, respectively. In both Figures 5.29 and 5.30, after seven years, there are some differences between the field and the predicted results, but the differences are less than 5 percent.

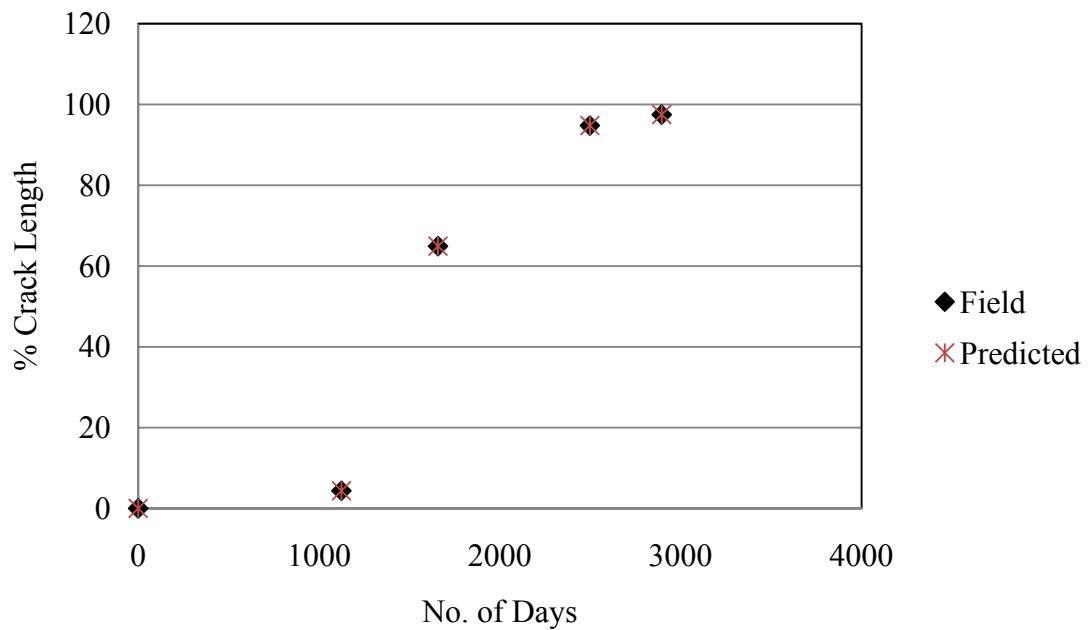


Figure 5.25. The comparison between field and predicted results for LMH severity distress (AC over AC pavement structure, Dry-Freeze climatic zone).

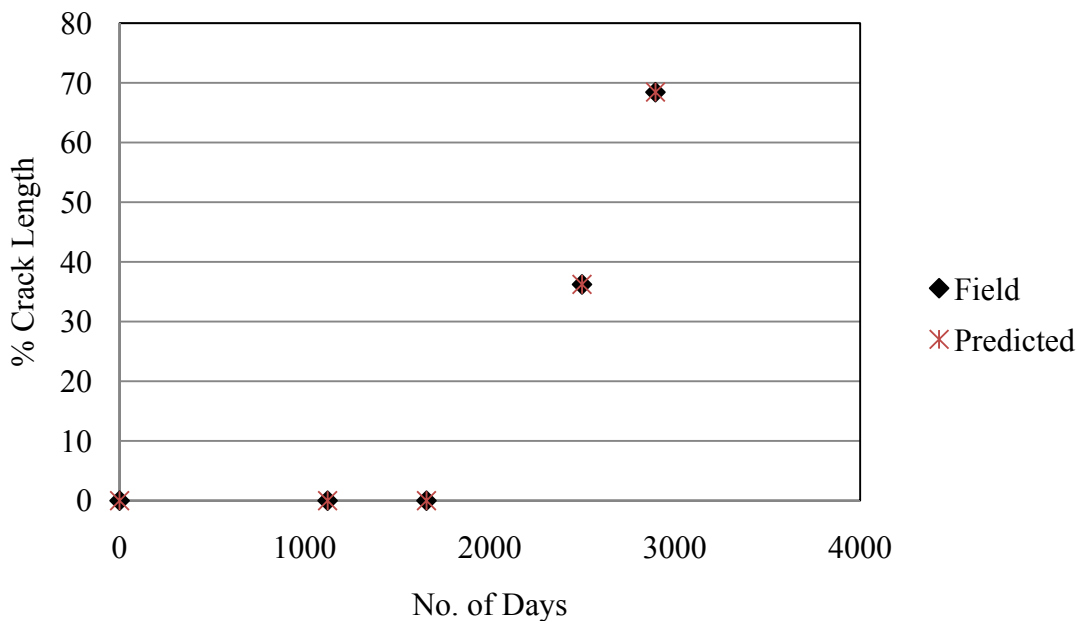


Figure 5.26. The comparison between field and predicted results for MH severity distress (AC over AC pavement structure, Dry-Freeze climatic zone).

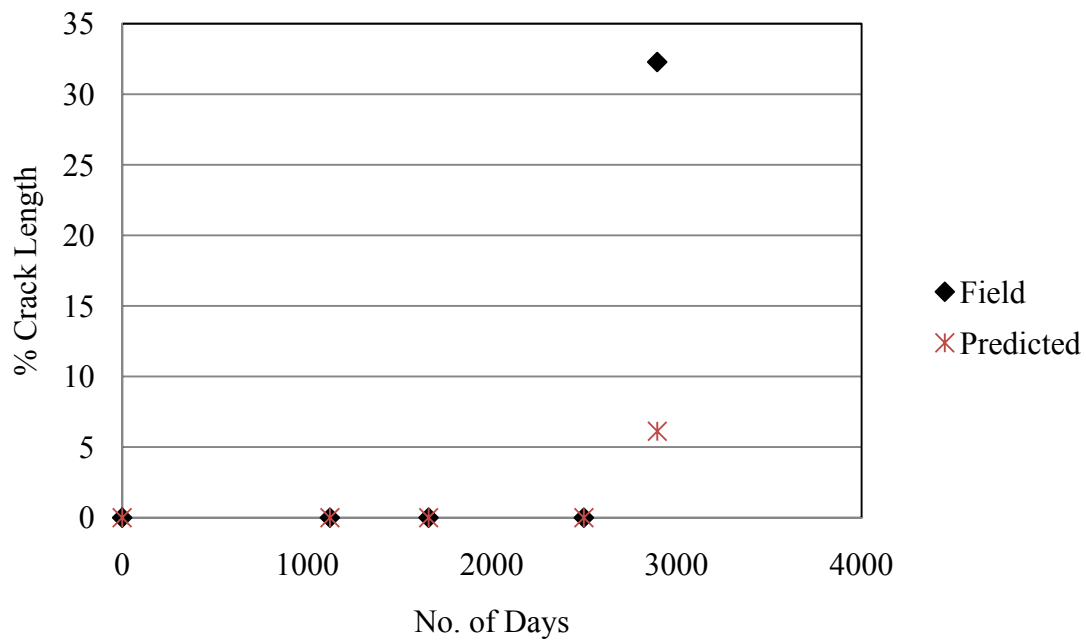


Figure 5.27. The comparison between field and predicted results for H severity distress (AC over AC pavement structure, Dry-Freeze climatic zone).

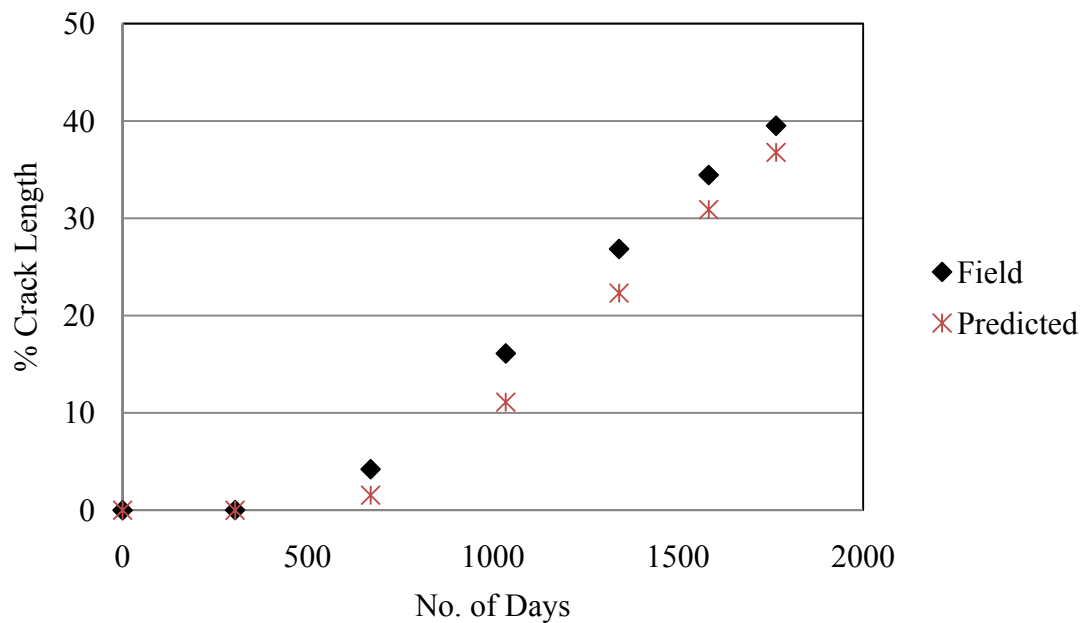


Figure 5.28. The comparison between field and predicted results for LMH severity distress (AC over reinforcing interlayer over AC pavement structure, Dry-Freeze climatic zone).

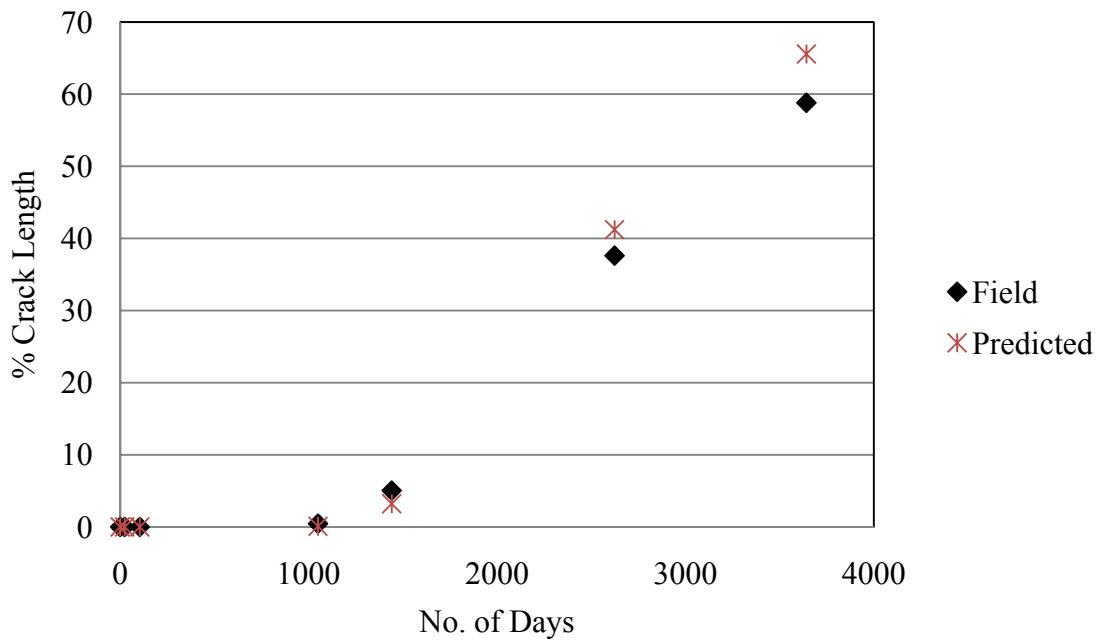


Figure 5.29. The comparison between field and predicted results for LMH severity distress (AC over AC pavement structure, Dry-No Freeze climatic zone).

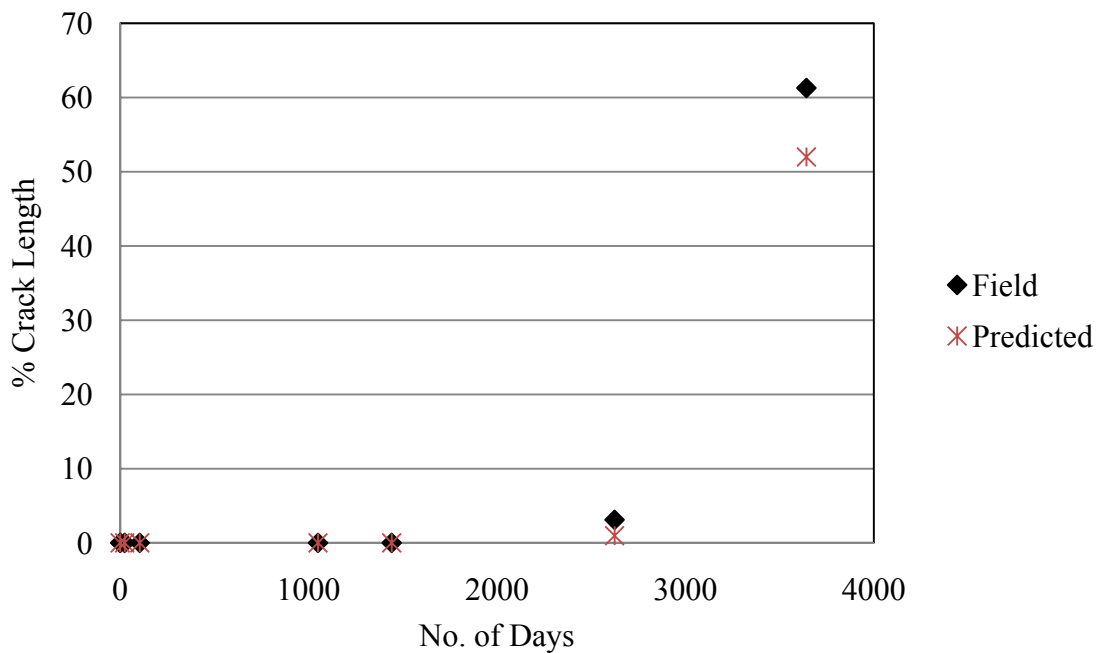


Figure 5.30. The comparison between field and predicted results for MH severity distress (AC over AC pavement structure, Dry-No Freeze climatic zone).

5.4 Sensitivity Analysis Scale Parameter, ρ

The scale coefficient, ρ , is the number of days for reflection cracks to reach 36.8 percent ($=1/e$) of their total length in the overlaid pavement prior to overlay. In the sensitivity analysis, the overlay is varied between 0.5 inch and 10 inches thickness in six or seven increments. The results of predicted scale coefficients, ρ , for different climatic zones and pavement structures is presented. Table 5.2 summarizes the number of sections to run the sensitivity analysis in each different pavement structures and climatic zones.

Table 5.2. Summary of sensitivity analytic sections in different climatic zones and pavement structures.

Climatic Zones	Pavement Structures Overlay/Existing Layer	ρ_{LMH}	ρ_{MH}	ρ_H
Wet-Freeze	AC/AC	25	25	25
	AC/JPC (JRC)	27	27	27
	AC/FC(SC)	8	8	8
	AC/CRC	6	6	N/A
	AC/Reinforcing/PCC	24	24	N/A
Wet-No Freeze	AC/AC	16	16	N/A
	AC/FC(SC)	6	N/A	N/A
	AC/Reinforcing/PCC	7	N/A	N/A
Dry-Freeze	AC/AC	9	9	9
	AC/Reinforcing/AC	10	N/A	N/A
Dry-No Freeze	AC/AC	13	13	13

Figure 5.31 shows the sensitivity of ρ_{LMH} for an AC overlay over an AC pavement in a Wet-Freeze climatic zone. The model for this sensitivity analysis includes 25 LTPP (Long Term Pavement Performance) sections (36). It shows the upper bound and the lower bound of this model. According to the trend of both bounds, the scale coefficients (ρ_{LMH}) become more variable when the overlay thickness increases. When the overlay thickness is thin, the mean value of ρ_{LMH} is around 1450 days. The upper bound of thin overlay is 1.38 times the mean value, and the lower bound is 0.62 times the mean value. When overlay thickness increases to 6 inches, the mean value increases to 3200 days, the ratios of upper bound and lower bound to the mean value are 1.87 and 0.13, respectively. A similar trend exists in the same model for ρ_{MH} in Figure 5.32. A thin overlay thickness shows a smaller mean value of ρ (4000 days), and the ratio of upper bound and lower bound to the mean value are 1.5 and 0.5, respectively. The mean value of the ρ -value increases with the overlay thickness (4850 days), and the ratio of upper bound and lower bound to the mean are 1.86 and 0.14, respectively. However, the high severity level (ρ_H) model shows a different trend in Figure 5.33. The trend of the upper bound and lower bound of the ρ_H -values is slightly decreased with the overlay thickness. In addition, the lower bound shows a more significant decrease because of the two outlier sections.

A total of 27 LTPP sections were used in the sensitivity analysis of an AC overlay over a JPC pavement structure in a Wet-Freeze climatic zone. Figures 5.34, 5.35, and 5.36 show the results of ρ_{LMH} , ρ_{MH} , and ρ_H severity levels, respectively, with the range of ρ -values increasing with overlay thickness. The upper bound of the three

severity levels shows a direct relationship to overlay thickness, but the lower bound shows an inverse relationship to overlay thickness. Figures 5.37, 5.38, and 5.39 show the results of the sensitivity analyses of an AC overlay over an FC(SC) pavement structure in a Wet-Freeze climatic zone. This model shows the same trend in the ρ -values. The thin overlay pavement has a greater range of ρ -values than the thick overlay pavement, and the scale coefficient, ρ , for each severity level increases with overlay thickness.

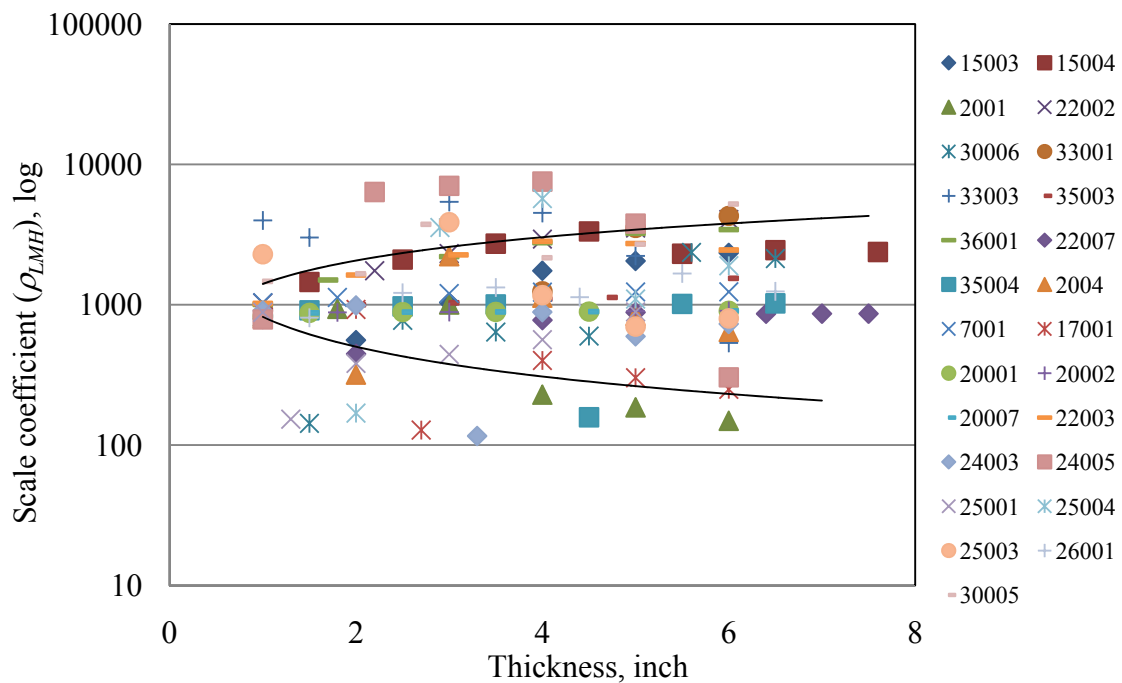


Figure 5.31. Sensitivity analysis of ρ_{LMH} for AC over AC pavement structure in a Wet-Freeze climatic zone.

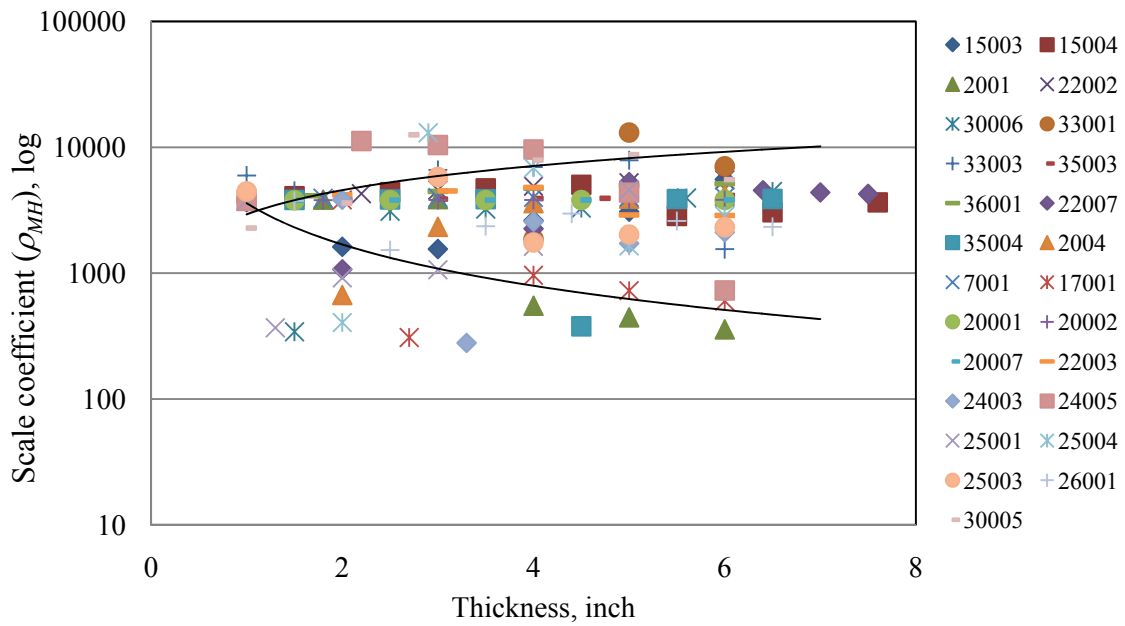


Figure 5.32. Sensitivity analysis of ρ_{MH} for AC over AC pavement structure in a Wet-Freeze climatic zone.

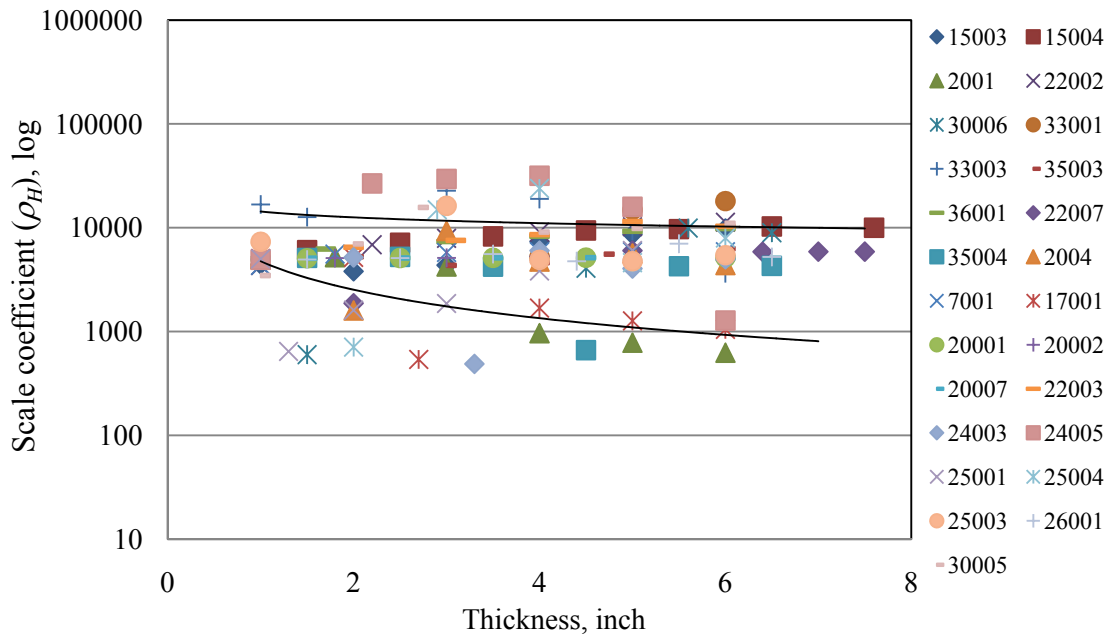


Figure 5.33. Sensitivity analysis of ρ_H for AC over AC pavement structure in a Wet-Freeze climatic zone.

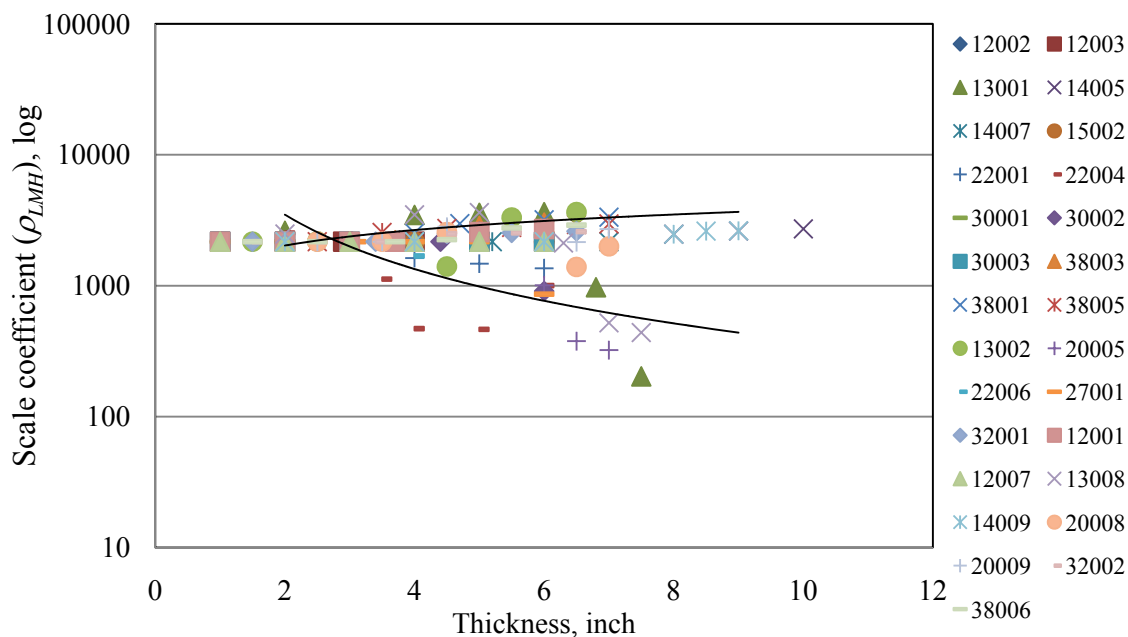


Figure 5.34. Sensitivity analysis of ρ_{LMH} for AC over JPC pavement structure in a Wet-Freeze climatic zone.

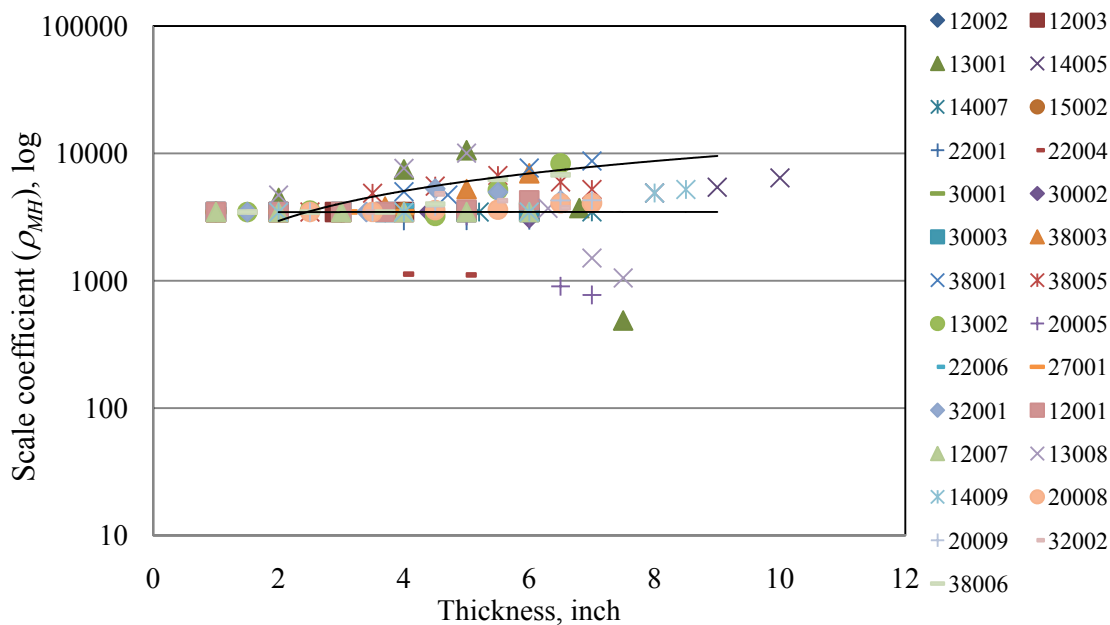


Figure 5.35. Sensitivity analysis of ρ_{MH} for AC over JPC pavement structure in a Wet-Freeze climatic zone.

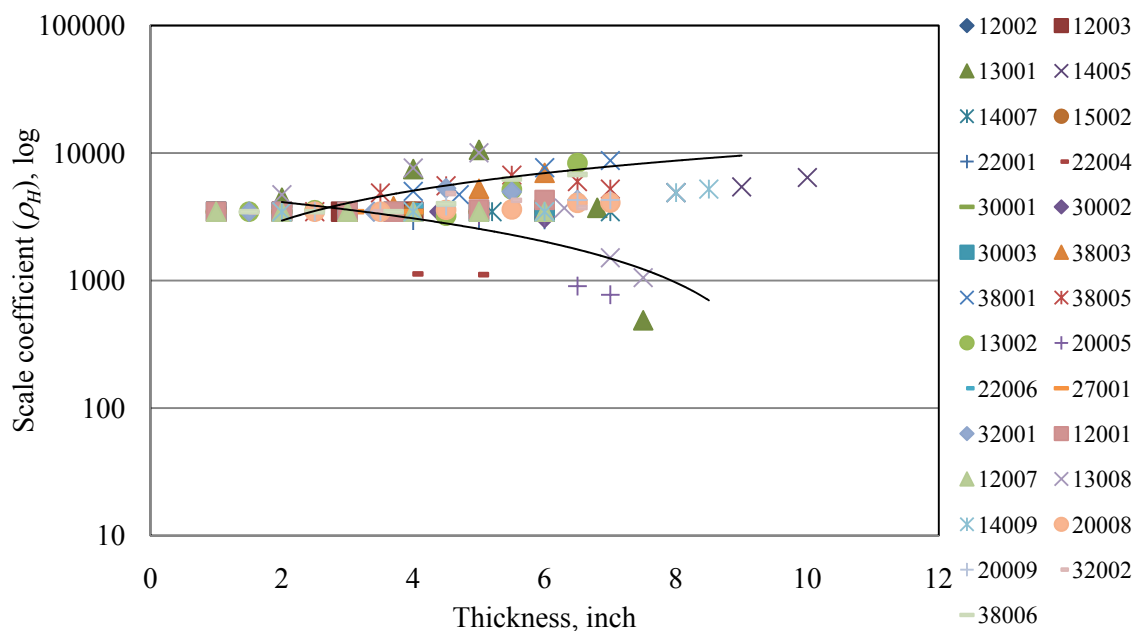


Figure 5.36. Sensitivity analysis of ρ_H for AC over JPC pavement structure in a Wet-Freeze climatic zone.

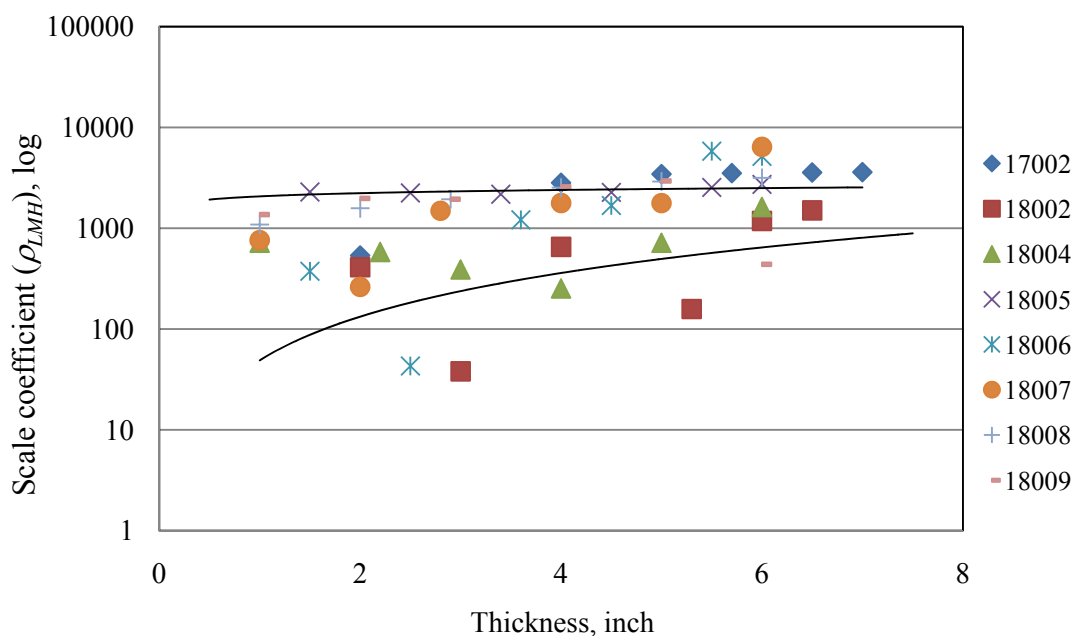


Figure 5.37. Sensitivity analysis of ρ_{LMH} for AC over FC (SC) pavement structure in a Wet-Freeze climatic zone.

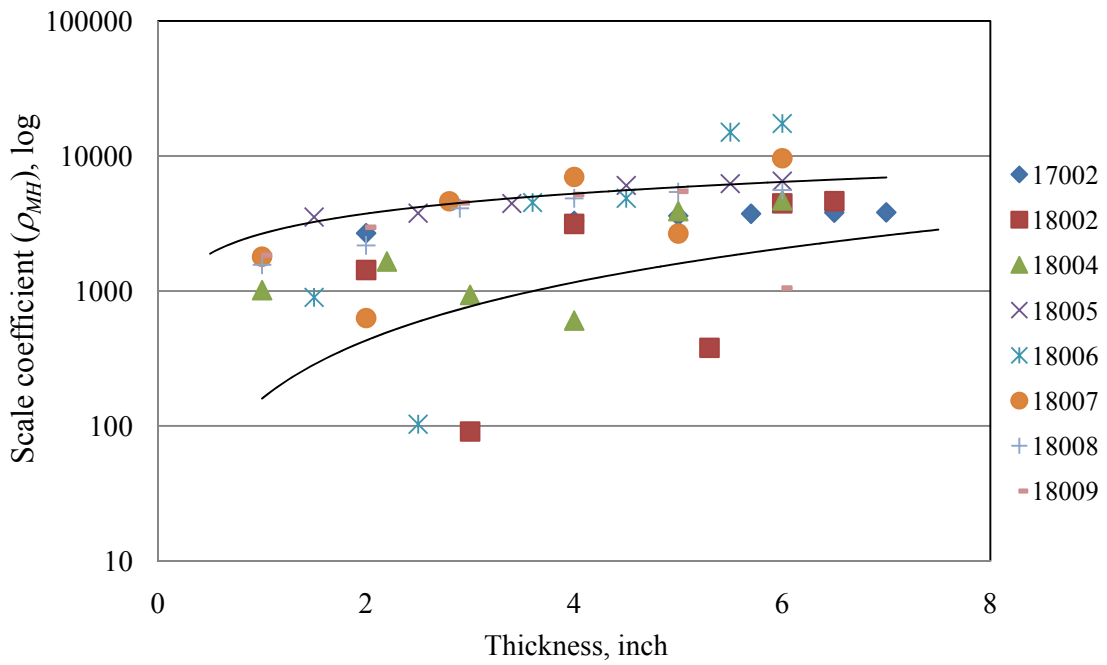


Figure 5.38. Sensitivity analysis of ρ_{MH} for AC over FC (SC) pavement structure in a Wet-Freeze climatic zone.

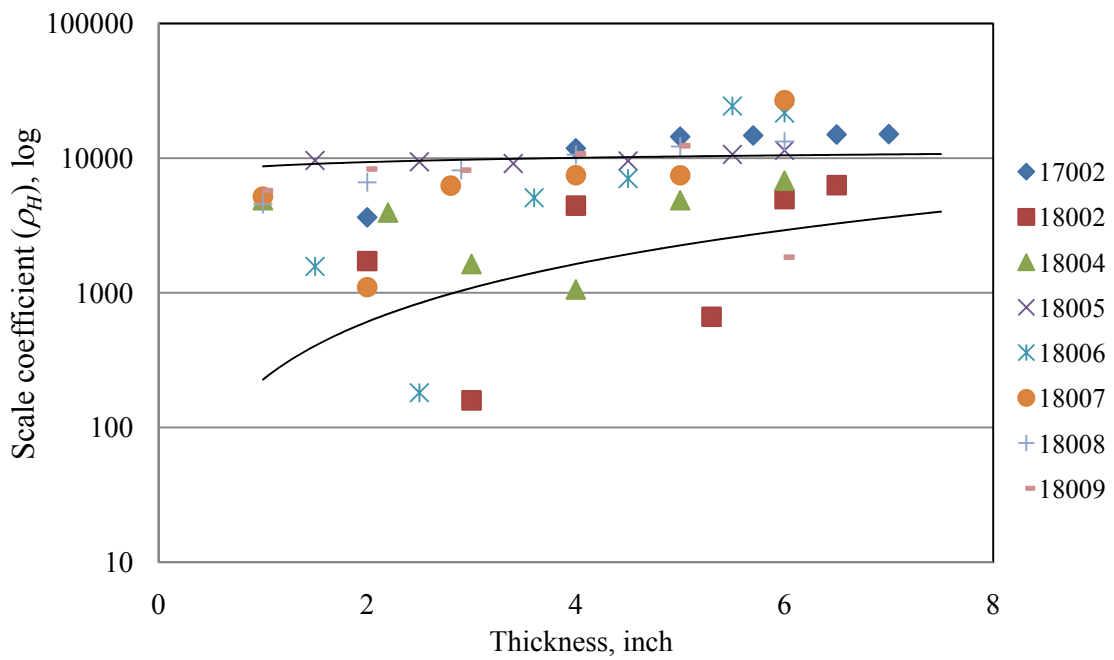


Figure 5.39. Sensitivity analysis of ρ_H for AC over FC (SC) pavement structure in a Wet-Freeze climatic zone.

The sensitivity analyses of an AC overlay over a CRC pavement structure in a Wet-Freeze climatic zone for ρ_{LMH} and ρ_{MH} are shown in Figures 5.40 and 5.41, respectively. This model shows a smaller range of ρ -values. In the low+medium+high severity level (Figure 5.40), the upper bound shows no change with different thicknesses, and the lower bound shows a steeply decreasing trend because of the one outlier section. The medium+high severity level in Figure 5.41 shows no significant ρ -value range with changing overlay thickness. Figures 5.42 and 5.43 present an AC overlay over AC pavement structures in a Wet-No Freeze climatic zone for ρ_{LMH} and ρ_{MH} severity levels. This model shows that the ρ -value range increases with overlay thickness. Increasing the overlay thickness to 6-inches, the mean value of ρ_{LMH} increases to around 3500 days, and 5500 days for ρ_{MH} . The sensitivity analysis of ρ_{LMH} for an AC overlay over an FC(SC) pavement structure in a Wet-No Freeze climatic zone (Figure 5.44) exhibits the same pattern as the previous AC overlay over an AC pavement structure model, but the ρ -value range in a thick overlay is much smaller relative to the mean value (4250 days). These are 0.82 times the mean value for lower bound and 1.18 times for the upper bound.

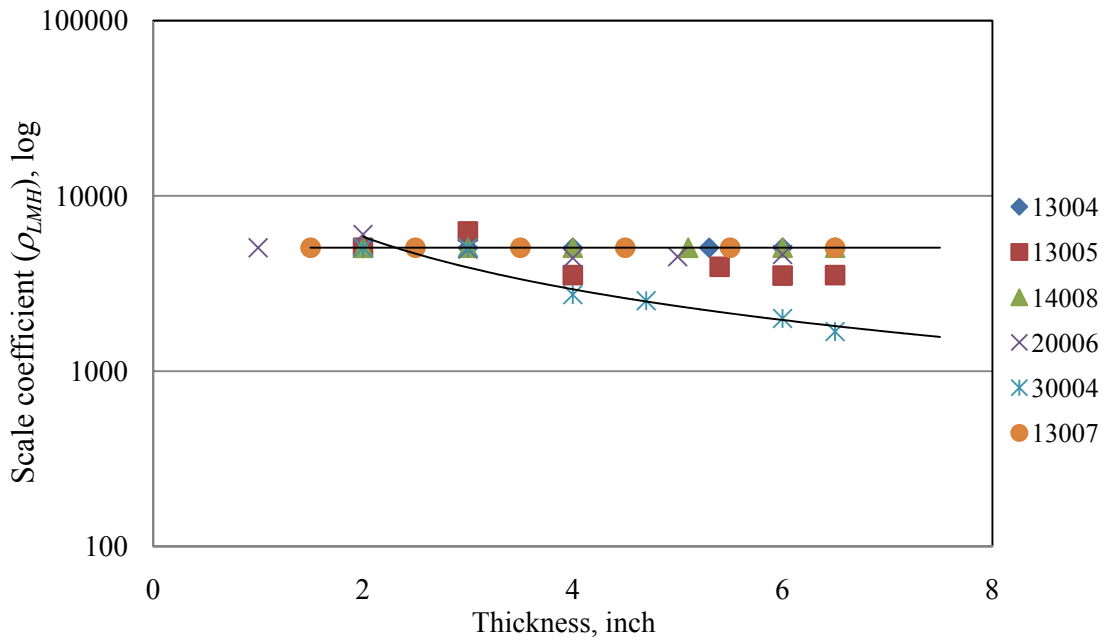


Figure 5.40. Sensitivity analysis of ρ_{LMH} for AC over CRC pavement structure in a Wet-Freeze climatic zone.

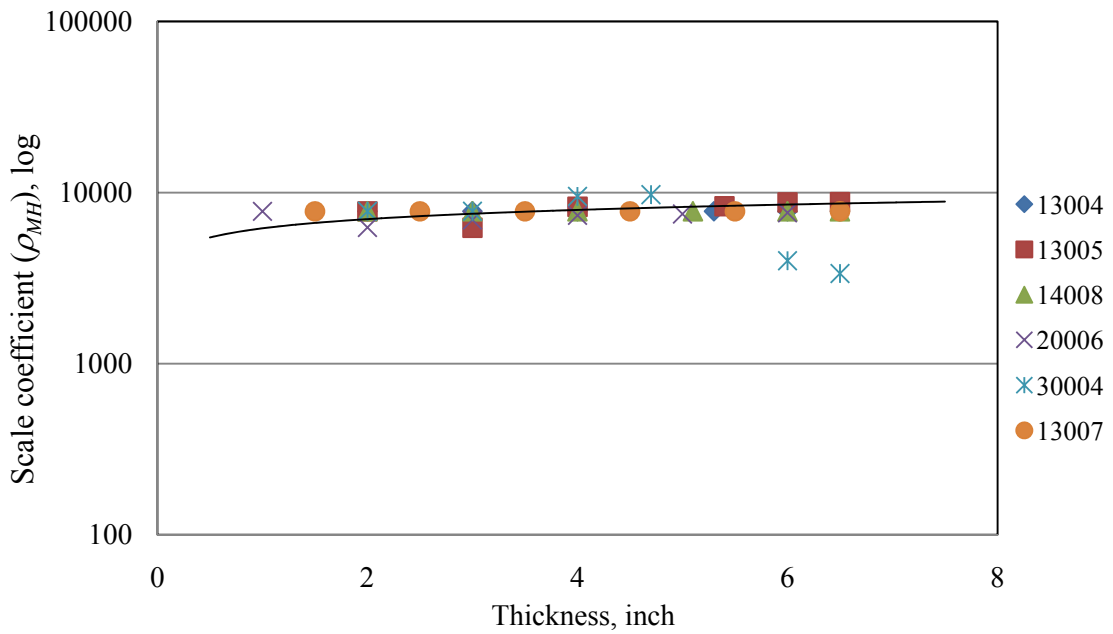


Figure 5.41. Sensitivity analysis of ρ_{MH} for AC over CRC pavement structure in a Wet-Freeze climatic zone.

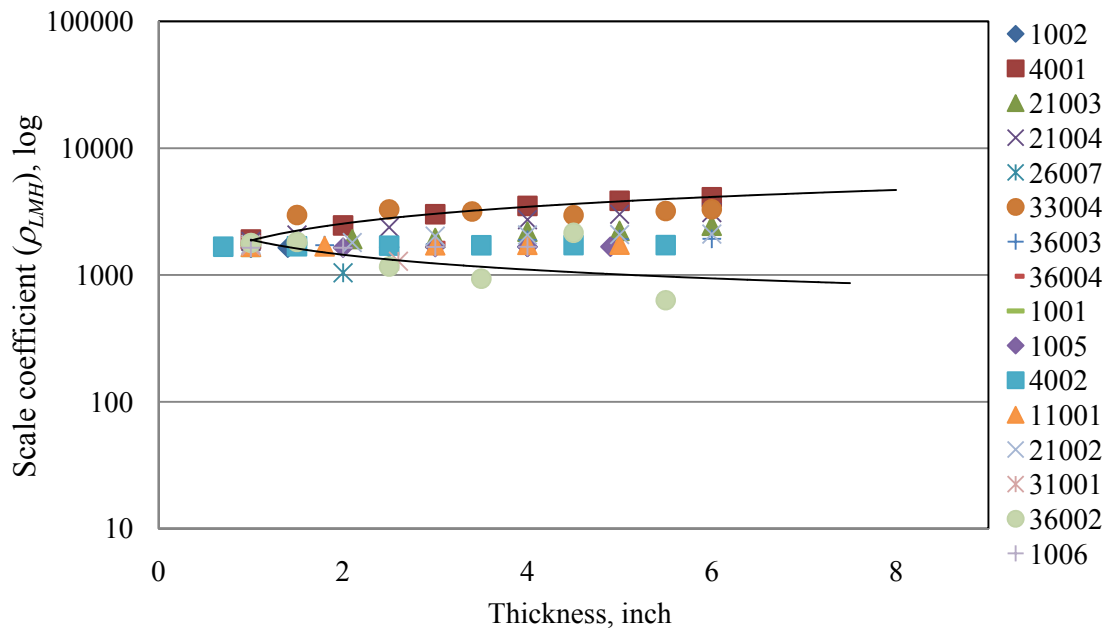


Figure 5.42. Sensitivity analysis of ρ_{LMH} for AC over AC pavement structure in a Wet-No Freeze climatic zone.

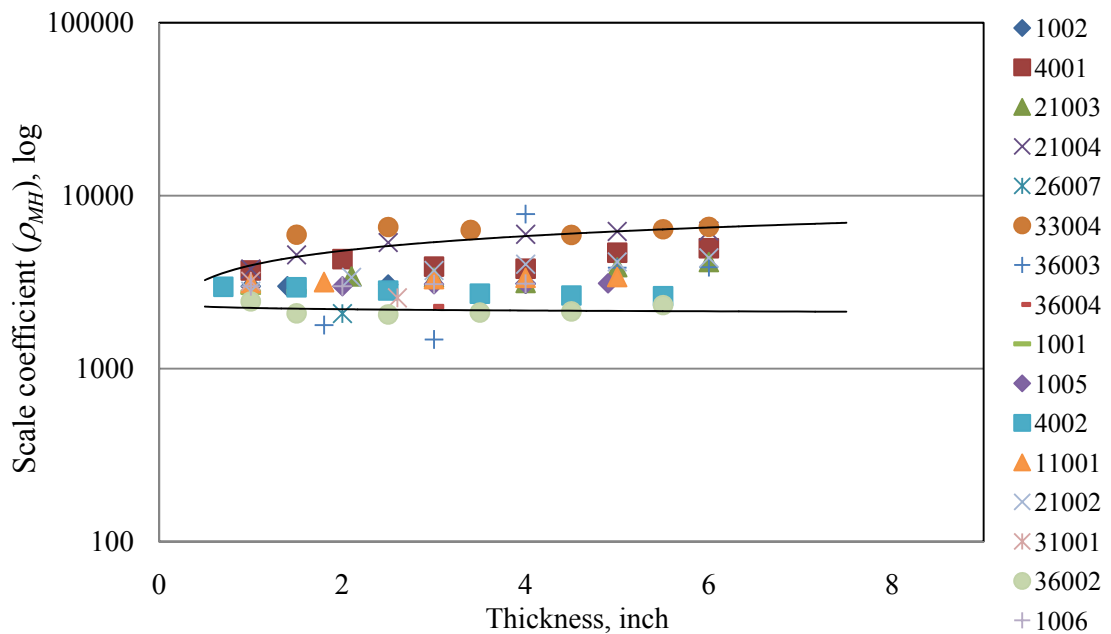


Figure 5.43. Sensitivity analysis of ρ_{MH} for AC over AC pavement structure in a Wet-No Freeze climatic zone.

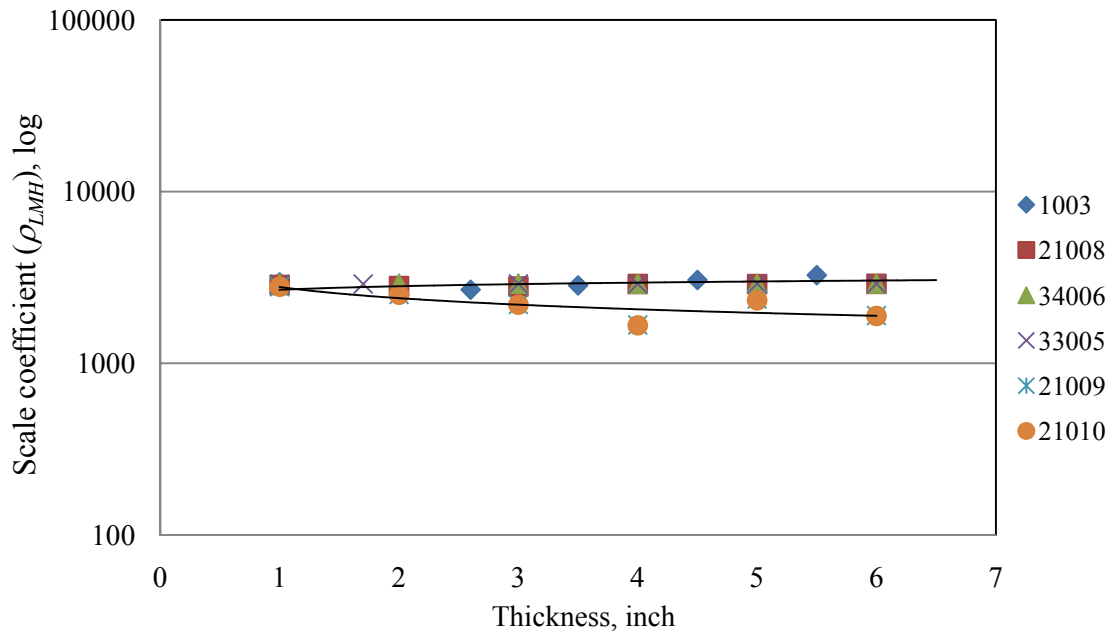


Figure 5.44. Sensitivity analysis of ρ_{LMH} for AC over FC (SC) pavement structure in a Wet-No Freeze climatic zone.

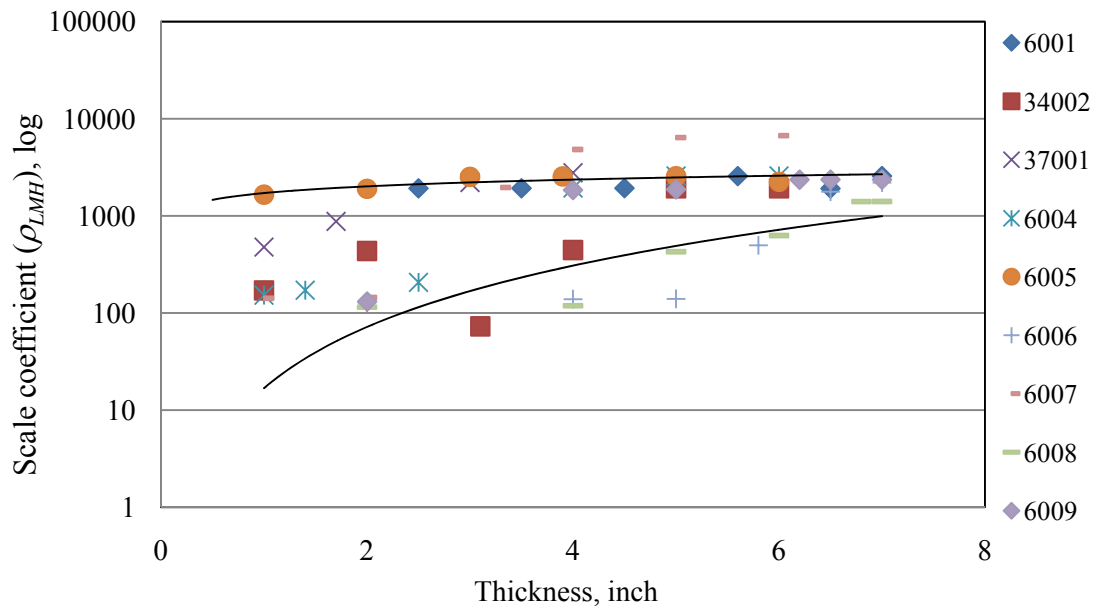


Figure 5.45. Sensitivity analysis of ρ_{LMH} for AC over AC pavement structure in a Dry-Freeze climatic zone.

Figures 5.45, 5.46, and 5.47 show a sensitivity analysis for an AC overlay over an AC pavement structure in a Dry-Freeze climatic zone for three different severity levels (ρ_{LMH} , ρ_{MH} , and ρ_H). All three severity levels show a larger ρ -value range in the thin overlay pavement, and the range decreases with overlay thickness. The three severity levels for an AC overlay over an AC pavement structure in a Dry-No Freeze climatic zone appear in Figures 5.48, 5.49, and 5.50. This model presents a clear pattern for the scale coefficient (ρ), and both the upper bound and lower bound increase with overlay thickness. Furthermore, the ρ -value band width at each severity level is close to constant.

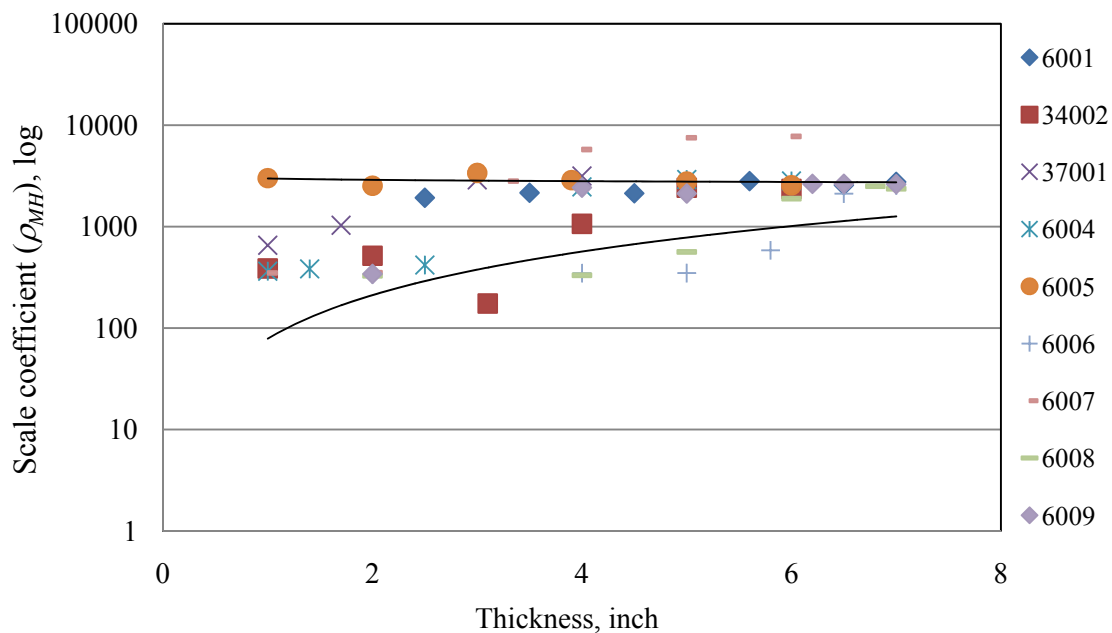


Figure 5.46. Sensitivity analysis of ρ_{MH} for AC over AC pavement structure in a Dry-Freeze climatic zone.

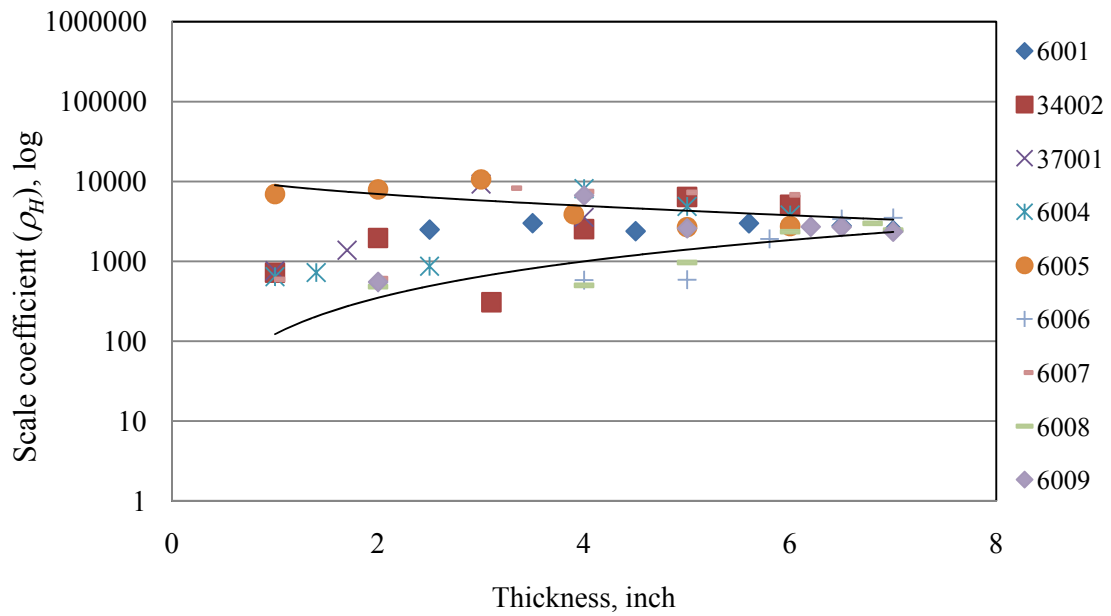


Figure 5.47. Sensitivity analysis of ρ_H for AC over AC pavement structure in a Dry-Freeze climatic zone.

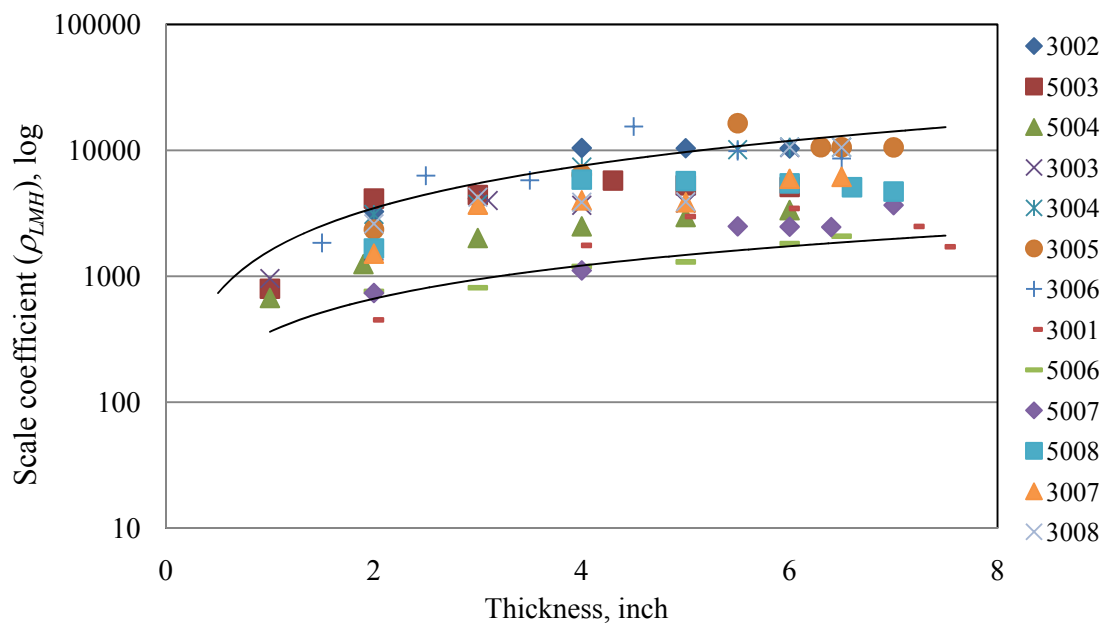


Figure 5.48. Sensitivity analysis of ρ_{LMH} for AC over AC pavement structure in a Dry-No Freeze climatic zone.

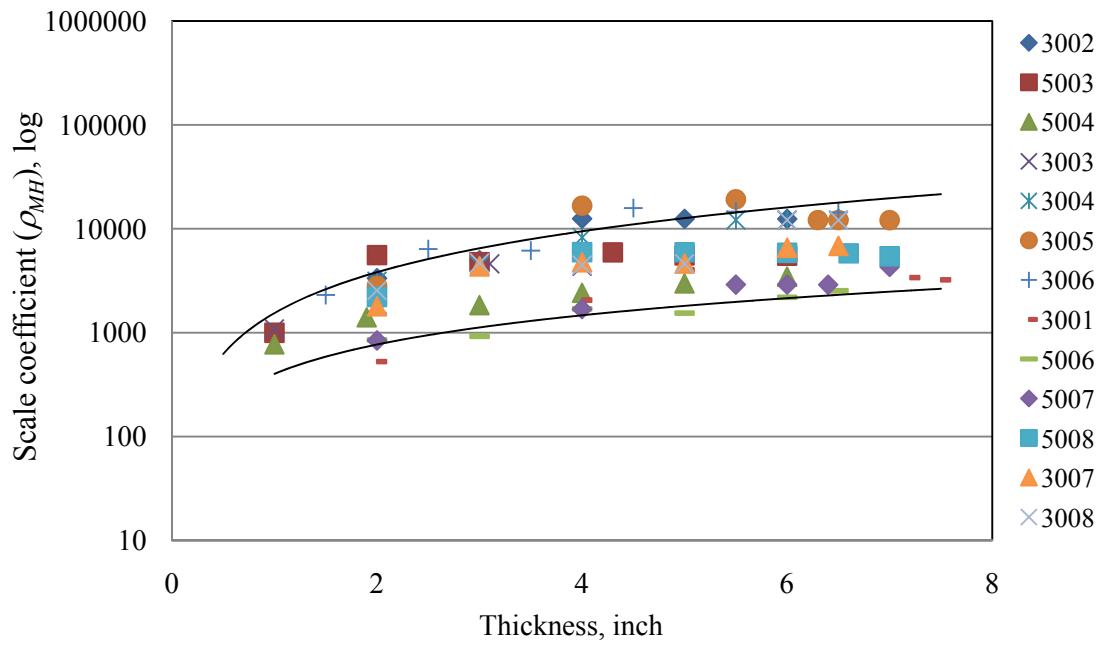


Figure 5.49. Sensitivity analysis of ρ_{MH} for AC over AC pavement structure in a Dry-No Freeze climatic zone.

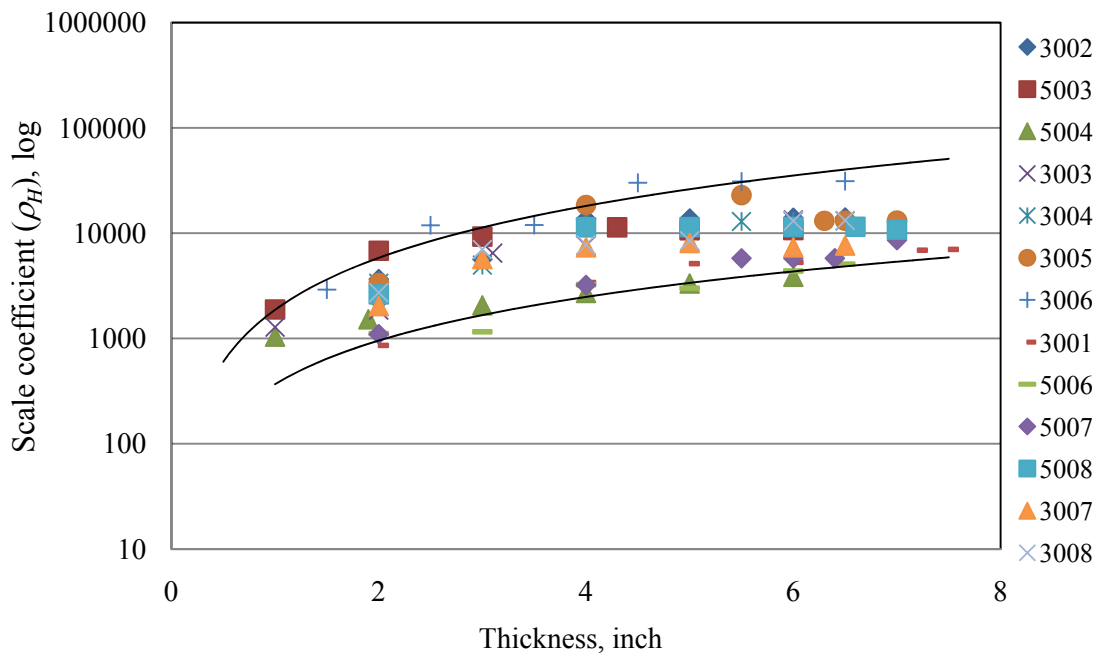


Figure 5.50. Sensitivity analysis of ρ_H for AC over AC pavement structure in a Dry-No Freeze climatic zone.

The sensitivity analyses of an AC overlay with a reinforcing layer are presented in Figures 5.51 to 5.54. The summary of these results is that the range of the scale coefficient, ρ , increases with overlay thickness. Figures 5.51 and 5.52 show the sensitivity analysis of ρ_{LMH} and ρ_{MH} for an AC overlay over a reinforcing layer over a PCC pavement structure in New York City (Wet-Freeze climatic zone). The upper bound for both ρ_{LMH} and ρ_{MH} severity levels show a direct relationship with overlay thickness, but the lower bound of ρ_{LMH} shows an inverse relationship with overlay thickness. The data for the same pavement structure in Waco, Texas (Wet-No Freeze climatic zone) for ρ_{LMH} is presented in Figure 5.53. The range of ρ -values increases with overlay thickness in this model, and the wide band is caused by one outlier section. Figure 5.54 shows a sensitivity analysis of ρ_{LMH} for an AC overlay over a reinforcing layer over an AC pavement structure in a Dry-Freeze climatic zone (Amarillo, Texas). The same ρ -value range patterns exist in this case as well. The outlier sections are the reason for the larger ρ -value ranges with the larger overlay thickness.

Most of the models show less variation in a thin overlay layer, and the ρ -value range increases with overlay thickness. Two models show an inverse ρ -value range pattern which are the AC overlay over an FC(SC) in a Wet-Freeze climatic zone and an AC overlay over an AC pavement in a Dry-Freeze climatic zone. In addition, only one model shows no significant variance in ρ -values with overlay thickness Figure 5.41.

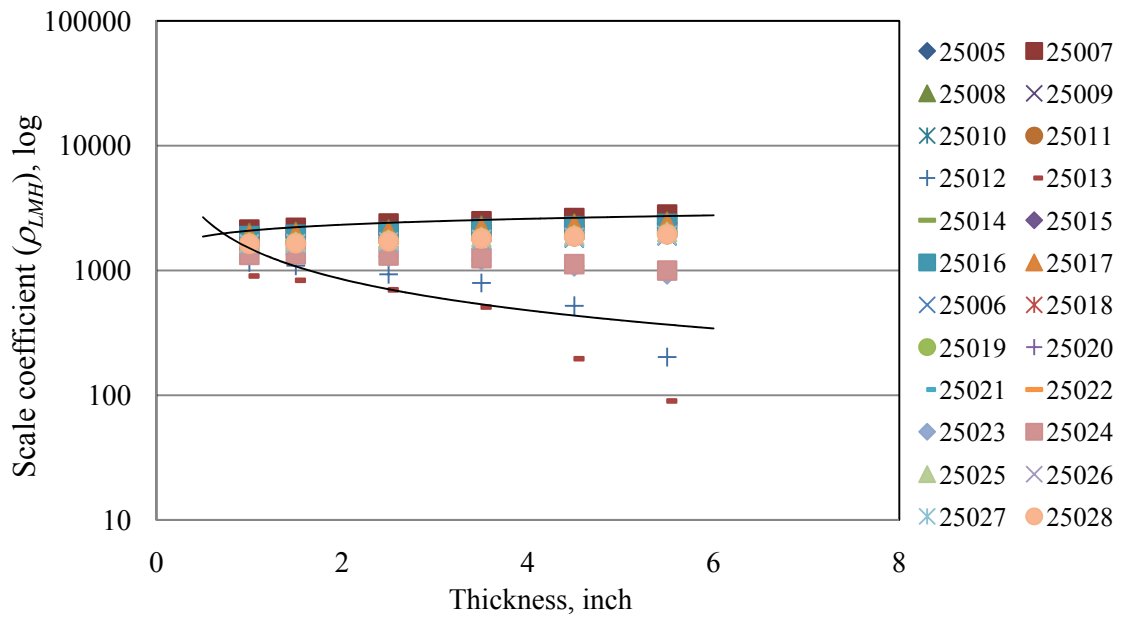


Figure 5.51. Sensitivity analysis of ρ_{LMH} for AC over Reinforcing over PCC pavement structure in a Wet-Freeze climatic zone.

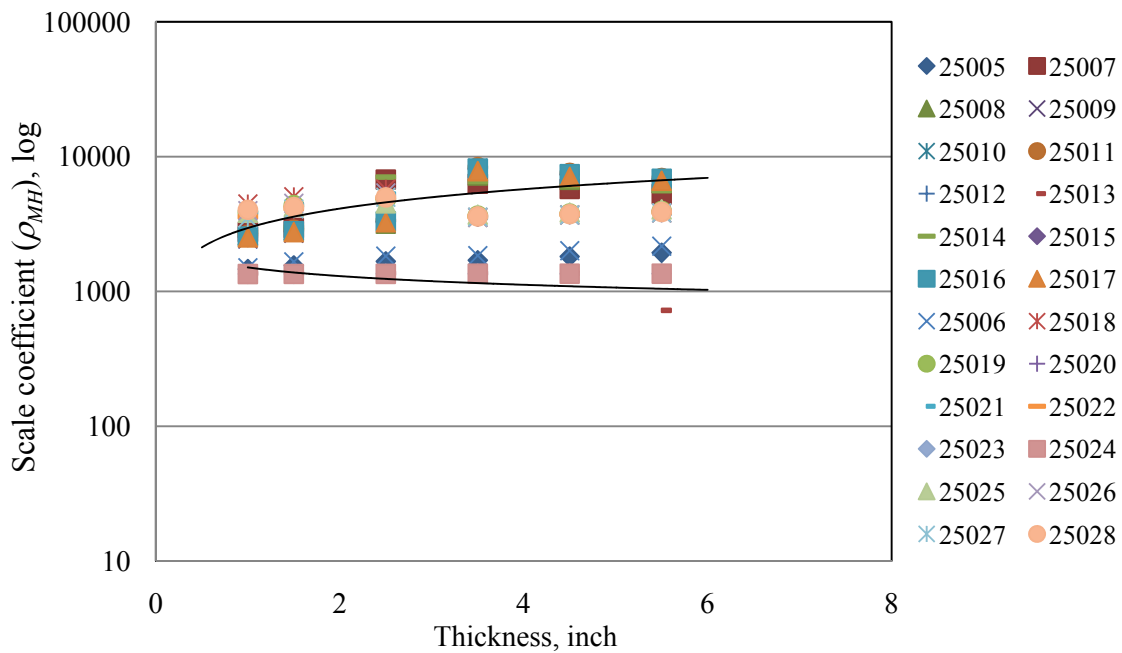


Figure 5.52. Sensitivity analysis of ρ_{MH} for AC over Reinforcing over PCC pavement structure in a Wet-Freeze climatic zone.

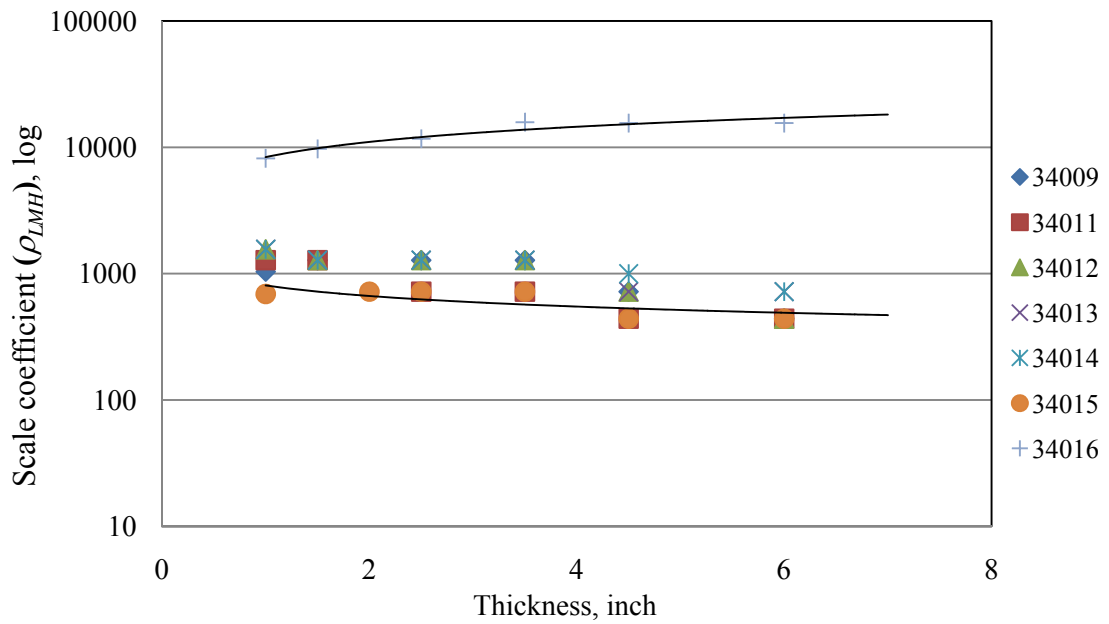


Figure 5.53. Sensitivity analysis of ρ_{LMH} for AC over Reinforcing over PCC pavement structure in a Wet-No Freeze climatic zone.

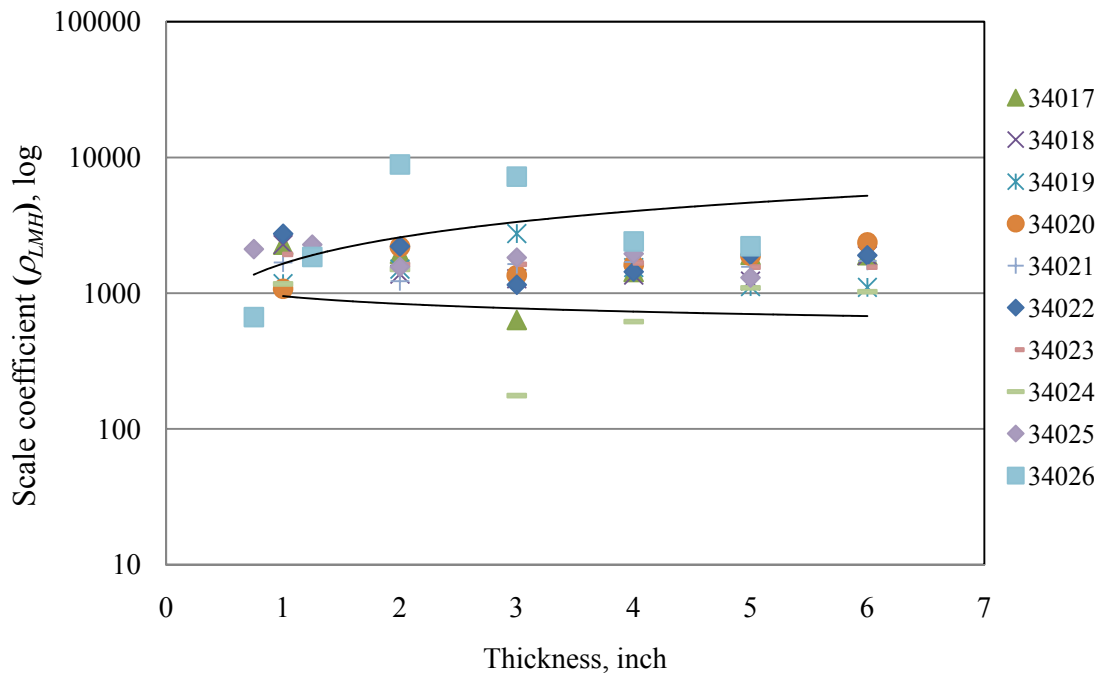


Figure 5.54. Sensitivity analysis of ρ_{LMH} for AC over Reinforcing over AC pavement structure in a Dry-Freeze climatic zone.

CHAPTER VI

CONCLUSION AND FUTURE WORK

6.1 Summary and Conclusion

A Reflection Cracking Overlay Design Program was calibrated using field data for over 400 pavement test sections in 28 states and all of the four climatic zones of the United States. The program uses a mechanistic model that predicts the reflection cracking lives of a specified hot mix asphalt overlay due to bending and shearing traffic stresses and thermal stresses. The relationship between the computed lives and the field conditions in terms of the extent and severity of reflection cracking depends upon the characteristics of the pavement structure and overlay and of the climate at the location. This relationship is expressed as sets of calibration coefficients. The Design Program is designed to run independently or to be incorporated as a subprogram of the MEPDG software.

A total of eleven sets of calibration coefficients were developed from the available data. The overlay performances that can be predicted with these different sets of calibration coefficients represent the four climatic zones in the United States. Eleven different pavement structure and overlay combinations were identified in the preliminary surveys. These overlays include hot mix asphalt overlays over cracked asphalt pavement surfaces, jointed concrete pavement as well as asphalt overlays that use strain-absorbing membrane interlayers and reinforcing geosynthetics. When considering the four climatic zones, there is a total of thirty six possible sets of calibration coefficients. The methods

of developing sets of calibration coefficients for overlays that are described in this dissertation make it possible to develop sets of calibration coefficients for a specific type of overlay and to design overlays using these sets of calibration coefficients. A Calibration Program has been provided to facilitate this independent calibration process. Both the Design Program and the Calibration Program have the same internal 150 location weather databases that can be called up by the user.

The objective of the calibration coefficients developed in this project was to match the field observations as closely as possible; i.e., the Reflection Cracking Overlay Design Model will generally reproduce the field experience of the more commonly used overlays. The program runs quickly enough to allow speedy trials of several overlay thicknesses and asphalt mixes in order to find the design that best matches the project objectives. The computational speed is achieved partially by the use of Artificial Neural Network (ANN) algorithms to perform the computations that must be done many times in the course of a simulated time period of ten to twenty years. The ANN algorithms are used to compute the mixture modulus at different temperatures and loading rates and to calculate the stress intensity factors which drive the growth of cracks.

Several examples of predicted reflection cracking performance of various overlays in different parts of the United States are presented in Chapter V. These examples illustrate the reproduction of the field observations of the growth of the extent and severity of reflection cracking. The assumed form of these distress growth curves was chosen because it gives realistic predictions and remains within reasonable bounds.

However, extreme designs that are well outside the range of the types of overlays that were used for calibration may not produce credible results.

6.1.1 The Model Development Process

The application of mechanics to the prediction of reflection cracking through hot mix asphalt concrete overlays involves a number of very detailed steps including the use of finite element analysis of crack growth and the modeling of those results with an ANN algorithm in order to speed up the computational time. The second step is the computational task of determining the material properties of the overlay under a variety of loading conditions and temperatures, including traffic and thermal stresses, must be done rapidly in order to make the Design Model a practical tool for design. A third step is to generate accurate weather characteristics that can be used to provide realistic material properties and stresses throughout each day and over the observed service life of an overlay. A fourth step of the assembly of this model is to develop a consistent means of describing the distress that was observed in the field. The fifth part was to devise a means to relate the predicted distress to the observed distress in a simple way, and produce predicted distress that matched well with what was actually observed in the field. A discussion of these five steps follows.

6.1.2 Mechanistic Prediction of Crack Growth

The model was selected for the Design Program based on several factors. One of the most important factors was the speed with which daily crack growth could be computed to facilitate consideration of several material, thickness, and reinforcing options in the overlay. This led to the decision to use ANN algorithms to compute both the changing modulus of the overlay mix and the growth of the cracks up from the cracks in the existing pavement, and to develop mechanistic data with which to train the ANN algorithms for crack growth. This was done by calculating a large set of stress intensity factor data for a variety of overlay and pavement structures using a two-dimensional finite element approach with the transverse third dimension being represented by a series solution. When the calculated results were compared to the correct answers generated by a full three-dimensional set of computational results, the errors were acceptable. The ANN models fit all 18 sets of computed data bases very well. Neither the two- nor the three-dimensional finite element analysis was used within the Design Program because of the long computational time that each requires.

6.1.3 Hot Mix Asphalt Overlay Material Properties

The ANN algorithms were also used for generating the material properties of a hot mix asphalt overlay material as it responds to traffic and thermal stresses. It was also necessary to use a well constituted and widely available database of hot mix asphalt material properties to represent these properties. The database assembled and modeled by Witczak in 1999 and 2006 (2, 3) satisfied these criteria. Representing both models by

an ANN algorithm provided two models that were computationally fast with a better coefficient of determination (R^2) than Witzak's regression models. By input binder properties, some aggregate gradation, volumetric composition of the mix, and frequency of loading and temperature into these ANN algorithms; a very satisfactory database of mixture properties over a wide range of loading times and temperatures can be generated quickly. The binder properties that were used as reference properties within the program were binder properties that were extracted from field cores and reported earlier (4). Although the user may input other binder properties at the detailed Level 1 input, binder data from actual constructed pavements may be used for Level 2 or 3. The Performance Grade (PG) of the binder and the internal reference data may be used for Level 2 to generate the remainder of the required data.

The fracture properties of an asphalt mixture depend on simpler and more fundamental properties of that mixture as shown by Schapery (55, 56) and confirmed in other studies (4) which calibrated to field fatigue cracking data. The calibration coefficients that were developed in these studies were used in this project without any alteration, even though the type of distress was different.

6.1.4 Climatic Data and Temperature Prediction

Accurate temperature prediction is a key to making accurate predictions of thermal crack growth, especially in an overlay. Comparisons between the temperature predictions and actual temperatures measured in the field demonstrated the need for a higher degree of accuracy in calculating the temperature within the overlay. Such a

temperature model (70) was incorporated into the Design Program. The temperatures calculated by this program and those measured in the field rarely differed by more than 2° C. A complete set of weather data was assembled from databases that are available to the public for about 150 different locations within the United States and Canada for use in the Design Program.

6.1.5 Consistent Description of Reflection Cracking Distress

The S-shaped curve for the accumulation of reflection cracking that was adopted in this project matches well with the pattern that is observed in the progressive development of many kinds of distress. There are three curves that represent the extent and severity of the reflection cracks as they are observed in the field. Each curve is plotted against the percent of the original length of transverse cracks in the old pavement surface. The curves show the growth of the high severity reflection cracks; the sum of the percentages of the high and medium severity cracks; and the sum of the percentages of the high, medium, and low severity cracks. The difference between the curves represents the percentages of the individual levels of distress severity. This S-shaped curve is defined by two parameters: ρ , the scale parameter, and β , the shape parameter. The scale parameter (ρ) is the number of days required for the percentage of reflected cracks to reach 36.8 percent, $1/e$, of the original length of the transverse cracks or joints in the old pavement surface. The shape parameter (β) determines how steep the growth of the curve is as it reaches the 36.8 percent mark.

This method allows a simple, consistent, and comprehensive description of the distress history of an overlay. It also made the task of calibrating the calculated reflection cracking lives due to traffic and thermal stresses to the field observations possible.

6.1.6 Calibration of Calculated Overlay Life to the Observed Distress

Linear regression was used to develop calibration coefficients ρ and β . It is a convenient and efficient function in Microsoft Excel. The user can easily learn and use it to determine the calibration coefficients (ρ_i, β_i). The coefficient of determination (R^2) was acceptable, and the scatter of the data was clustered around the line of equality in most of the models. However, the quality and accuracy of the field data may cause a higher degree of scatter.

6.1.7 Sensitivity Analysis of Scale Parameter, ρ

Over hundreds test sections were ran the sensitivity analysis of scale parameter (ρ), and separated into eleven models. Nine of these eleven models were presented in the same trend which was the variance of scale parameter (ρ) increased with increasing overlay thickness. The variance was defined by the upper bond and lower bond which most of the data point dropped. There were only two exceptions which are AC over FC (SC) over AC in Wet-Freeze climatic zone and AC over AC in Dry-Freeze climatic zone.

6.2 Future Work

Another twenty five sets of pavement structure-overlay and climatic zone combinations remain to be developed, some of which may not be possible because they are simply not built. However, the process of developing calibration coefficients for a particular type of overlay described in this report can be applied to any overlay in any region or even within a state or other political subdivision. There are several more types of overlay designs that should be developed using this same approach and making use of the computational tools that are provided here. For example, sets of calibration coefficients for overlays incorporating geosynthetic reinforcing products need to be developed (only three were developed in the dissertation). It would also be desirable if the manufacturers of these products would develop guidelines or standards for designers to use that would provide realistic estimates of the generic reinforcing stiffness of their products.

The fit between the predicted and the observed reflection cracking distress can be improved by reducing the error in both the predicted and observed performance. The observed field data were fitted with an S-shaped curve with two parameters: ρ , the scale parameter, and β , the shape parameter. Both of these parameters were fitted by linear regression analysis with mechanistically-predicted numbers of days for traffic and thermal stresses to cause a reflection crack to grow to the surface of an overlay. There are errors that are inherent in both the observed and the predicted values. The error in the observed field data can be reduced by recording mean values of the observed distress from a sampling survey. The error in the mechanistically-predicted numbers of days of

crack propagation can be reduced by having more accurate recorded pavement structure and materials properties, traffic, and weather and by having as realistic a mechanistic model of the cracking process as is possible. This project models the asphalt mixture as a viscoelastic material and applies viscoelastic crack growth concepts. Together with the use of the ANN algorithms for reducing program execution time, this is the most realistic mechanistic model that is currently available for use in design.

A sensitivity analysis of the mechanistic model of the crack growth process will identify those material properties which are the most sensitive predictors of overlay performance. It is expected that a small number of these sensitive properties will be identified. Making improvements in these most sensitive material properties will extend the service lives of overlays and increase the predictive accuracy of the models that are developed. Performance-based specifications which are focused on these most sensitive material properties will make construction quality control and quality assurance more effective and will extend the service lives of overlays.

The Design Program was designed to be able to be incorporated within the MEPDG software framework as well as having the capability to stand alone. Experience with using the Design Program in designing overlays will show which sets of calibration coefficients need to be improved and, in addition, will reveal those features of a design that make the greatest extension of an overlay's service life.

An evaluation of available reflection cracking models was performed in this dissertation, and a number of promising approaches were in the development stage at that time. Most of these models proved to require extensive computational times that

would make them impractical to use in design. However, as computer speeds increase, the mechanics-based methods will require less running time and should be considered for the next version of this overlay design function to reduce the systematic errors and simplify the calibration effort.

REFERENCES

1. NCHRP (National Cooperative Highway Research Program) 1-37A. (2007), *Mechanistic Empirical Design of New and Rehabilitated Pavement Structures*. Available: <http://www.trb.org/mepdg/guide.htm>. Accessed July 20, 2008.
2. Andrei, D., M. Witczak, and M. Mirza, *Development of a Revised Predictive Model for the Dynamic (Complex) Modulus of Asphalt Mixtures*, NCHRP 1-37 A Inter Team Report, University of Maryland, 1999.
3. Bari, J. and M. Witczak, Development of a New Revised Version of the Witczak E* Predictive Model for Hot Mix Asphalt Mixtures, *Journal of the Association of Asphalt Paving Technologists*, vol. 75, pp. 381-423, 2006.
4. Lytton, R., J. Uzan, E. Fernando, R. Roque, D. Hiltunen, and S. Stoffels, *Development and Validation of Performance Prediction Models and Specifications for Asphalt Binders and Paving Mixes*, Strategic Highway Research Program (SHRP A-357), 1993.
5. Paris, P. C., E. Erdogan, A Critical Analysis of Crack Propagation Laws, *Journal of Basic Engineering, Transaction of the American Society of Mechanical Engineering*, vol. 85, pp. 528-883, 1963.
6. Nunn, M., An Investigation of Reflection Cracking in Composite Pavements in the United Kingdom, *Proceedings of 1st International RILEM Conference on Reflective Cracking in Pavements, Assessment and Control*, Liege, Belgium, 1989, pp. 146-153.
7. Lytton, R., Use of Geotextiles for Reinforcement and Strain Relief in Asphalt Concrete, *Geotextiles and Geomembranes*, vol. 8, pp. 217-237, 1989.
8. Gary, B. E., G. E. Martin, Resurfacing with Bituminous Types of Surfaces, *Proceedings of Highway Research Board, National Research Council*, vol. 12, pp. 177-192, 1932.
9. Hall, K., J. Connor, M. Darter, and S. Carpenter, *Rehabilitation of Concrete Pavements, Vol. 3: Concrete Pavement Evaluation and Rehabilitation System*, Publication FHWA-RD-88-073. FHWA, US Department of Transportation, 1989.

10. Eckman, B., *ESSO MOEBIUS Computer Software for Pavement Design Calculations*, User's manual. Centre de Recherche ESSO. Mont Saint Aignan. France. June, vol. 19, pp. 190-198, 1990.
11. Van Gurp, C. and A. Molenaar, Simplified Method to Predict Reflective Cracking in Asphalt Overlays, in *RILEM Conference on Reflective Cracking in Pavements*, Leige, Belgium, pp. 190-198, 1989.
12. Treybig, H., B. McCullough, P. Smith, and H. Von Quintus, *Overlay Design and Reflection Cracking Analysis for Rigid Pavements, Volume 1 and 2*, Report FHWA-RD-77-66 and 67. FHWA, US Department of Transportation, 1977.
13. McCullough, B.F., and S.B. Seeds, Field Validation of an Overlay Design Procedure to Prevent Reflection Cracking, *Proceedings 5th International Conference on Structural Design of Asphalt Pavements*, vol. I, pp. 780-791, 1982.
14. Seeds, S., B. Mc Cullough, and F. Carmichael, Asphalt Concrete Overlay Design Procedure for Portland Cement Concrete Pavements, *Transportation Research Record*, vol. 1007, pp. 26-36, 1985.
15. Monismith, C. and N. F. Goetzee, Reflection Cracking: Analysis, Laboratory studies and Design Considerations, *Proceedings of Association of Asphalt Paving Technologists*, vol. 49, pp. 268-313, 1980.
16. Coetzee, N. and C. Monismith, Analytical Study of Minimization of Reflection Cracking in Asphalt Concrete Overlays by Use of a Rubber-Asphalt Interlayer, *Transportation Research Record*, pp. 100-108, 1979.
17. Chen, N., J. D. Vito, and R. Gene, Finite Element Analysis of Arizona's Three-Layer Overlay System of Rigid Pavements to Prevent Reflective Cracking, *Proceedings of Association of Asphalt Paving Technologists*, vol. 51, pp. 150-168, 1982.
18. Francken, L. and A. Vanelstraete, Interface Systems to Prevent Reflection Cracking, *Proceedings of 7th International Conference on Asphalt Pavement*, Nottingham, UK, vol. 1, pp. 45-60, 1992.
19. Vanelstraete, A. and L. Francken, Numerical Modelling of Crack Initiation under Thermal Stresses and Traffic Loads, *Proceedings of the 2nd International RILEM Conference on Reflective Cracking I Pavements*, 1993, pp. 136-145.

20. Kim, J. and W. Buttlar, Analysis of Reflective Crack Control System Involving Reinforcing Grid over Base-Isolating Interlayer Mixture, *Journal of Transportation Engineering*, vol. 128, pp. 375-384, 2002.
21. Sousa, J., J. Pais, R. Saim, G. Way, and R. Stubstad, Mechanistic-Empirical Overlay Design Method for Reflective Cracking, *Transportation Research Record: Journal of the Transportation Research Board*, vol. 1809, pp. 209-217, 2002.
22. Sousa, J., J. Pais, and G. Way, A Mechanistic-Empirical Based Overlay Design Method for Reflective Cracking, *International Journal of Road Materials and Pavement Design*, vol. 6, pp. 339-363, 2005.
23. Sousa, J., J. Pais, R. Saim, G. Way, and R. Stubstad, *Development of a Mechanistic Overlay Design Method Based on Reflective Cracking Concepts*, Final Report for Rubber Pavements Association, Consulpav International, 2001.
24. Majidzadeh, K., E. Kauffmann, and D. Ramsamooj, Application of Fracture Mechanics in the Analysis of Pavement Fatigue, *Journal of Association of Asphalt Pavement Technologists*, vol. 40, pp. 227-246, 1970.
25. Chang, H., R. Lytton, and S. Carpenter, *Prediction of Thermal Reflection Cracking in West Texas*, Texas Transportation Institute, Texas A & M University 1976.
26. Jayawickrama, P. and R. Lytton, Methodology for Predicting Asphalt Concrete Overlay Life Against Reflection Cracking, *Proceedings 6th International Conference on Structural Design of Asphalt Pavements*, pp. 912-924, 1987.
27. Germann, F. and R. Lytton, *Methodology for predicting the reflection cracking life of asphalt concrete overlays*, FHWA/TX 79/09+207-5, 1979.
28. Pickett, D., R. Lytton, *Laboratory Evaluation of Selected Fabrics for Reinforcement of Asphaltic Concrete Overlays*, Texas Transportation Institute, The Texas A&M University System, 1983.
29. Button, J. and R. Lytton, Evaluation of Fabrics, Fibers, and Grids in Overlays, in *Proceedings of the Sixth International Conference on Structural Design of Asphalt Pavements*, The University of Michigan, vol. 1, pp. 925-934, 1987.
30. Eltahan, A. and R. Lytton, Mechanistic-Empirical Approach for Modeling Reflection Cracking, *Transportation Research Record: Journal of the Transportation Research Board*, vol. 1730, pp. 132-138, 2000.

31. Cleveland, G., R. Lytton, and J. Button, Reinforcing Benefits of Geosynthetic Materials in Asphalt Concrete Overlays Using Pseudo Strain Damage Theory, *TRB CD*, 2003.
32. Owusu-Antwi, E., L. Khazanovich, and L. Titus-Glover, Mechanistic-Based Model for Predicting Reflective Cracking in Asphalt Concrete-Overlaid Pavements, *Transportation Research Record: Journal of the Transportation Research Board*, vol. 1629, pp. 234-241, 1998.
33. Al-Qadi, I., M. Elseifi, and D. Leonard, Development of an Overlay Design Model for Reflective Cracking with and without Steel Reinforcing Nettings, *Journal of the Association of Asphalt Paving Technologists*, vol. 72, pp. 388-423, 2003.
34. Elseifi, M. and I. Al-Qadi, A Simplified Overlay Design Model against Reflective Cracking Utilizing Service Life Prediction, *Road Materials and Pavement Design*, vol. 5, pp. 169–192, 2004.
35. Miner, M., Cumulative Damage in Fatigue, *Journal of applied mechanics*, vol. 12, pp. 159-164, 1945.
36. LTPP. *Long Term Pavement Performance, LTPP Data Base*. Available: <http://www.ltpm-products.com/index.asp>. Accessed June 12, 2008
37. (BRRC), B. R. R. C., *Design of Overlaid Cement Concrete Pavements Reinforced with Bitufor® Traffic Loading*, Research Report EP5035/3544, 1998
38. Joseph, P., W. A. P. Haas, and L. Rothenburg, Low Temperature Reflection Cracking through Asphalt Overlays, in *Proceedings 6th International Conference on Structural Design of Asphalt Pavements*, pp. 935-945, 1987.
39. Bažant, Z. and J. Planas, *Fracture and Size Effect in Concrete and Other Quasibrittle Materials*, CRC Press, pp. 616, 1998.
40. Rashid, Y., Ultimate Strength Analysis of Prestressed Concrete Pressure Vessels, *Nuclear Engineering and Design*, vol. 7, pp. 334-344, 1968.
41. Bažant, Z. and B. Oh, Crack Band Theory for Fracture of Concrete, *Materials and structures*, vol. 16, pp. 155-177, 1983.
42. Bažant, Z., *Mechanics of Fracture and Progressive Cracking in Concrete Structures*, Kluwer Academic, 1985.

43. Uzan, J. and E. Levenberg, Strain Measurements in Asphalt Concrete Specimens Towards the Development of a Fracture Model, *International Journal of Pavement Engineering*, vol. 2, pp. 243-258, 2001.
44. Jenq, Y., C. Liaw, and P. Liu, Analysis of Crack Resistance of Asphalt Concrete Overlays-a Fracture Mechanics Approach, *Transportation Research Record*, vol. 1388, pp. 160-166, 1993.
45. Dugdale, D., Yielding of Steel Sheets Containing Slits, *Journal of the Mechanics and Physics of Solids*, vol. 8, pp. 100-108, 1960.
46. Barenblatt, G., The Mathematical Theory of Equilibrium Cracks in Brittle Fracture, *Advances in applied mechanics*, vol. 7, p. 104, 1962.
47. Hillerborg, A., M. Modéer, and P. Petersson, Analysis of Crack Formation and Crack Growth in Concrete by Means of Fracture Mechanics and Finite Elements, *Cement and concrete research*, vol. 6, pp. 773-782, 1976.
48. Petersson, P.E., *Crack Growth and Development of Fracture Process Zone in Plain Concrete and Similar Materials*, Report No. TVBM-1006, Lund Institute of Technology, Lund, Sweden. 1981.
49. Paulino, G., S. Song, and W. Buttlar, Cohesive Zone Modeling of Fracture in Asphalt Concrete, in *Proceedings of the 5th International Conference on Cracking in Pavements*, Lemoges, France, pp. 63-70, 2004.
50. Kim, H. and W. Buttlar, Micromechanical Fracture Modeling of Hot-Mix Asphalt Concrete based on a Disk-Shaped Compact Tension Test, *Journal of the Association of Asphalt Paving Technologists*, vol. 74, 2007.
51. Wagoner, M., W. Buttlar, and G. Paulino, Development of a Single-Edge Notched Beam Test for Asphalt Concrete Mixtures, *Journal of Testing and Evaluation*, vol. 33, pp. 1-9, 2005.
52. Wagoner, M., W. Buttlar, and G. Paulino, Disk-Shaped Compact Tension Test for Asphalt Concrete Fracture, *Journal of Society for Experimental Mechanics*, vol. 45, pp. 270-277, 2005.
53. Wu, R., J. Harvey, and C. Monismith, Towards a Mechanistic Model for Reflective Cracking in Asphalt Concrete Overlays, *Journal of the Association of Asphalt Paving Technologists*, vol. 75, pp. 491-534, 2006.

54. Peerlings, R., R. De Borst, W. Brekelmans, and J. De Vree, Gradient Enhanced Damage for Quasi-Brittle Materials, *International Journal for Numerical Methods in Engineering*, vol. 39, pp. 3391-3403, 1996.
55. Schapery, R., U. S. O. o. N. Research, and A. Texas, *A Theory of Crack Growth in Viscoelastic Media*, Mechanics and Materials Research Center, Texas A & M University, 1973.
56. Schapery, R., A Theory of Crack Initiation and Growth in Viscoelastic Media; I: Theoretical Development, II: Approximate Methods Of Analysis, III: Analysis of Continuous Growth, *International Journal of Fracture*, vol. 11, pp. 141-159, 1975.
57. Wu, R., *Finite element analyses of reflective cracking in asphalt concrete overlays*, University of California, Berkeley, 2005.
58. Liu, W., T. Scullion, *MODULUS 6.0 for Windows: User's Manual*, Texas Transportation Institute, Texas A&M University System, 2001.
59. NCHRP, *Guide for Mechanistic-Empirical Design of New and Rehabilitated Pavement Structures; Part 2. Design Inputs, Chapter 4, Traffic*, National Cooperative Highway Research Program, 2004.
60. FHWA, *Traffic Monitoring Guide*. FHWA-PL-01-021, US Dept. of Transportation, Federal Highway Administration, Office of Highway Information Management, 2001.
61. Sridhar, B., *Characterization and Development of Axle Load Spectra to Enhance Pavement Design and Performance on the Basis of New Mechanistic-empirical Design Guide in Louisiana*, Department of Civil and Environmental Engineering, Louisiana State University, 2008.
62. Hajek, J., O. Selezeva, G. Mladenovic, and J. Jiang, *Estimating Cumulative Traffic Loads*, Federal Highway Administration, 2008.
63. Garber, N. and L. Hoel, *Traffic and Highway Engineering*. Pacific Grove, California, Brooks/Cole, 2002.
64. Fernando, E., W. LIU, D. MUSANI, and D. PARK, *Summary Report: Evaluation of Effects of Tire Size and Inflation Pressure on Tire Contact Stresses and Pavement Response*, Technical Report 0-4361-1. College Station, Texas, Texas Transportation Institute, 2006.

65. Ratkowsky, D. and D. Giles, *Handbook of Nonlinear Regression Models*. New York: M. Dekker, 1990.
66. Ahmed, Z., I. Marukic, S. Zaghoul, and N. Vitillo, Validation of Enhanced Integrated Climatic Model Predictions with New Jersey Seasonal Monitoring Data, *Transportation Research Record: Journal of the Transportation Research Board*, vol. 1913, pp. 148-161, 2005.
67. Hermansson, A., Simulation Model for Calculating Pavement Temperatures Including Maximum Temperature, *Transportation Research Record: Journal of the Transportation Research Board*, vol. 1699, pp. 134-141, 2000.
68. Gui, J., P. Phelan, K. Kaloush, and J. Golden, Impact of Pavement Thermophysical Properties on Surface Temperatures, *Journal of Materials in Civil Engineering*, vol. 19, pp. 683-690, 2007.
69. Hermansson, A., Mathematical Model for Paved Surface Summer and Winter Temperature: Comparison of Calculated and Measured Temperatures, *Cold Regions Science and Technology*, vol. 40, pp. 1-17, 2004.
70. Han, R., X. Jin, and C. J. Glover, Modeling of Pavement Temperature History for Pavement Performance Prediction, presented at the Submitted to 88th Annual Meeting of the Transportation Board, Washington, D.C., 2009.
71. Natke, H., *Identification of Vibrating Structures*. Vienna, Springer-Verlag(CISM International Centre for Mechanical Sciences. Courses and Lectures, 1982.
72. Wang, F. and R. Lytton, System Identification Method for Backcalculating Pavement Layer Properties, *Transportation Research Record 1384*, pp. 1-7, 1993.
73. Zollinger, D.G., S. Lee, J. Puccinelli, and N. Jackson, *LTPP Computed Parameter: Moisture Content*, FHWA-HRT-08-035, Federal Highway Administration. 2008.
74. Hiltunen, D. and R. Roque, A Mechanics-Based Prediction Model for Thermal Cracking of Asphaltic Concrete Pavements, *Journal of the Association of Asphalt Paving Technologists*, vol. 63, pp. 81-117, 1994.
75. Monismith, C.L.F. Long, and J.T. Harvey, California's Interstate-710 Rehabilitation: Mix and Structural Section Designs, Construction Specifications, *Journal of the Association of Asphalt Paving Technologists*, Vol. 70, 2001, pp. 762-795.

76. Scarpas, A. and J. Blaauwendraad, CAPA: A Modern Tool for the Analysis and Design of Pavements, *Proceedings of the 2nd International Conference on Reflective Cracking in Pavements*, pp. 121-128, 1993.
77. Scarpas, A., A. De Bondt, and G. Gaarkeuken, Reflective Cracking Control Via Reinforcing Systems: FE Modelling of Reinforced Overlays, *Proceedings of the 3rd International RILEM Conference*, Maastricht, the Netherlands, pp. 344-353, 1996.
78. Zienkiewicz, O.C. *The Finite Element Method for Engineers*, McGraw-Hill, London, 1977.
79. Henshell, R. and K. Shaw, Crack Tip Elements Are Unnecessary, *International Journal for Numerical Methods in Engineering*, vol. 9, pp. 495-507, 1975.
80. Barsoum, R., On the Use of Isoparametric Finite Elements in Linear Fracture Mechanics, *International Journal for Numerical Methods in Engineering*, vol. 10, pp. 25-37, 1976.
81. Ingraffea, A. R., and P. A. Wawrzynek. *Finite Element Methods for Linear Elastic Fracture Mechanics*, Elsevier Science Ltd., Oxford, England, 2003.
82. Lytton, R., D. E. Pufahl, C. H. Michalak, H. S. Liang, and B. J. Dempsey, *An Integrated Model of The Climatic Effects on Pavements*, Report No. FHWA-RD-90-033, Federal Highway Administration, 1990.
83. Larson, G. and B. Dempsey, *Enhanced Integrated Climatic Model, Version 2.0*, United States. Federal Highway Administration Minnesota. Dept. of Transportation, Report No. DTFA MN/DOT 72114, 1997.
84. Rumney, T. N. and R. A. Jimenez, Pavement Temperatures in the Southwest, *Highway Research Record*, vol. 361, pp. 1-13, 1969.
85. Dempsey, B., A Heat-transfer Model for Evaluating Frost Action and Temperature Related Effects in Multilayered Pavement Systems, *Highway Research Record*, vol. 342, pp. 39-56, 1970.
86. Solaimanian, M. and T. Kennedy, Predicting Maximum Pavement Surface Temperature Using Maximum Air Temperature and Hourly Solar Radiation, *Journal of the Transportation Research* vol. 1417, pp. 1-11, 1993.
87. Klein, A. and J. Stroeve, Development And Validation of a Snow Albedo Algorithm for the Modis Instrument, *Annals of Glaciology*, vol. 34, pp. 45-52, 2002.

88. Viswanadham, Y. and R. Ramanadham, Estimation of Long Wave Radiation by an Empirical Method, *Pure and Applied Geophysics*, vol. 81, pp. 272-278, 1970.
89. Ceylan, H., K. Gopalakrishnan, and S. Kim, Looking to the Future: the Next-Generation Hot Mix Asphalt Dynamic Modulus Prediction Models, *International Journal of Pavement Engineering*, vol. 10, pp. 341-352, 2009.
90. Williams, M., R. F. Landel, and JD Ferry, *Journal of the American Chemical Society*, vol. 77, p. 3701, 1955.

VITA

Fang-Ling Tsai was born in Hualien, Taiwan. In September 2003, she received her B.S. in civil engineering from China University of Science and Technology (Taipei, Taiwan). In September 2005, she received her M.S. also in civil engineering, with emphasis in road infrastructure, from I-Shou University. Her masters' thesis topic is "Dynamic Elasto-Plasticity Analysis of Pavement under Vehicle Loading". This research studied the behavior of elasto-plasticity finite element model under different dynamic vehicle loads.

From January 2006 to December 2010, she attended Texas A&M University to pursue her doctoral degree. She received a graduate research assistantship at the second semester from Texas Transportation Institute (TTI), and later from the Benson Chair Foundation, and she received her Ph.D. in Civil Engineering in December 2010. She participated in the Nation Cooperative Highway Research Program (NCHRP) with the objective of predicting reflection cracking in Hot-Mix Asphalt (HMA) overlays.

Her permanent address is:

No. 16, Lane 53, Ming-ren 1 St., Young-an Village, Gi-an Township

Hualien, Taiwan

Her e-mail address is: lynne5280@yahoo.com.tw